ELECTRONIC COLLECTIVE MODES IN TWO DILUTE CONDUCTORS WITH MOMENTUM-RESOLVED ELECTRON ENERGY-LOSS SPECTROSCOPY

BY

SAMANTHA ILENE RUBECK

DISSERTATION

Submitted in partial fulfillment of the requirements
for the degree of Doctor of Philosophy in Physics
in the Graduate College of the
University of Illinois Urbana-Champaign, 2021

Urbana, Illinois

Doctoral Committee:

Professor Jim Eckstein, Chair
Professor Peter Abbamonte, Director of Research
Assistant Professor Lucas Wagner
Associate Professor Bryce Gadway

Abstract

Much of modern condensed matter research tries to understand strongly correlated electron systems. These materials exhibit a variety of interesting quantum phenomena that stem from strong electron interactions and the emergent quasiparticles that define the system. Understanding the collective mode dynamics of these particles is key to understanding the macroscopic behavior of these materials. One quantity that contains fundamental information about the about these boson collective modes is the charge susceptibility $\chi(\mathbf{q}, \omega)$ which contains information about the propagation of density fluctuations that are mediated by bosonic excitations. Until recently though, it was not possible to measure $\chi(\mathbf{q}, \omega)$ at low energy (< 100 meV) and with the momentum resolution and accuracy needed to see interesting phenomena. With the development of momentum-resolved electron energy-loss spectroscopy (M-EELS) in the Abbamonte Group at UIUC, $\chi(\mathbf{q}, \omega)$ can now be probed at low energy scales of interest. Here we use M-EELS to study the collective modes of several strongly correlated materials with interesting low energy physics.

Bose condensed phases of excitons have the potential to realize macroscopic quantum phenomena at unprecedented high temperatures [1, 2]. When excitons Bose condense in a real material, however, some rearrangement of the charge density inevitably results, leading to a distortion of the crystal lattice [3–6]. This raises the question of whether there can ever be a distinction between a Bose condensate of excitons and a conventional, structural phase transition that breaks the same symmetry. Here, we use inelastic electron scattering (M-EELS) to study copper-intercalated $TiSe_2$, in which exciton condensation can be directly observed as a soft electronic mode at the exciton condensation temperature, T_{XC} [7]. While the lattice distortion in Cu_xTiSe_2 persists to $x > 0.10$ [8], we find the exciton condensate is fully suppressed by $x = 0.014$, which is short of the semimetal-metal transition we identify at $x = 0.025$. Our observations indicate that the excitonic and lattice instabilities split as x is increased, showing that structural and excitonic subsystems can exhibit separate transitions and may be distinct subsystems that break different symmetries. In addition we found that although exciton condensation is suppressed, exciton fluctuations remain for most of the doping phase diagram. These fluctuations have been theorized to aid in superconducting pairing in

this system [9, 10].

$SrTi_{1-x}Nb_xO_3$, is an electron doped ionic semiconductor that exhibits aborted ferroelectricity due to quantum fluctuations [11], dilute (unconventional) superconductivity that survives even when the plasmon energy (ω_p) is lower than the Fermi energy (E_F) [12], and charge transport properties that suggests bad metal behavior [13]. In general, the polar nature of ionic semiconductors leads to coupling of the longitudinal optical (LO) phonons to collective charge modes, such as plasmons, due to long range polarization fields. Understanding the dynamics of these collective modes, which have been implicated in superconducting pairing [14] [15] [16], can provide insight into the nature of these unusual properties. Here, we use inelastic electron scattering (M-EELS) with a fracturing surface preparation technique to study the doping, temperature, and momentum dependence of the charge collective modes in $SrTi_{1-x}Nb_xO_3$. We measure propagating and diffusive acoustic phonons, Fuchs-Kliewer optical phonons and overtones that get suppressed with doping due to metallic screening, a 93 meV phonon mode that becomes highly damped and asymmetric at x=0.002, and a very broad plasmon that blue-shifts with decreasing temperature. We find that the plasmon in $SrTi_{1-x}Nb_xO_3$ remains dispersion-less at all temperatures and dopings even with other propagating collective modes (acoustic phonon), contrary to RPA predictions and dispersions in other polar doped semiconductors [17]. The width of the plasmon deviates from RPA predictions by an order of magnitude. In addition, the energy of the plasmon measured in M-EELS is less than that of other techniques like infrared spectroscopy for samples of comparable carrier densities.

Acknowledgements

There are a plethora of people who made this dissertation possible. First and foremost, I want to thank my advisor Professor Peter Abbamonte for his guidance and support throughout my graduate career. You had confidence in me even when I didnt have confidence in myself. Working with you has made me a better scientist, researcher, and mentor. I would also like to thank Professors Jim Eckstein, Lucas Wagner, and Bryce Gadway for providing feedback on my proposed research projects and for evaluating my defense.

Next I want to thank all my labmates. First to all the labmates who made such a large impact early in my graduate career - Mindy Rak, Matteo Mitrano, and Ali Husain. Mindy you taught me how to run an EELS experiment and always kept me entertained with interesting conversation whether it be in our office corner or at 1 am realigning samples. Thank you for including me in the Cu_xTiSe_2 project and teaching me the day-to-day responsibilities of working in the lab. I am so thankful for all the positive feedback you gave in your cards and thoughtful words, which always boosted my confidence (especially when everything was failing). Matteo, you gave the lab group so much life and character! There was never a dull moment with you around. I have such an appreciation for how you think about science and the academic process. Thank you for always providing good ideas and resources, for all the coffee/chai day Fridays, and most importantly thank you for all the gossip. I could not imagine my graduate career without you. Ali, you were the source of creativity and out-of-the-box thinking in the group! Thank you for always helping me with SPEC, for coming up with clever solutions to my problems, for instigating lab social gatherings, and for your wise words of wisdom - "In the end, you don't take data with money, you take data with your heart."

To the next generation of the EELS team - Cat Kengle, Jin Chen, Simon Bettler, Faren Hoveyda Marashi, and Xuefei Guo. I know you will be able to make the EELS great again! Specifically thanks to Cat and Jin who were great mentees and who always patiently put up with me learning how to teach. Cat, thank you for all the help on the $SrTiO_3$ project, for all the coffee breaks, and for all the great conversation!

To my other amazing lab/office mates over the years: Stella Sun, Sangjun Lee, Sean Vig, Gilberto de la Pena Munoz, Yizhi Fang, and Yingying Peng, thank you for always keeping the office lively and full of

discussion.

To my Chicago family - Jenna Goldberg, Mary McGrath, Krista Evensen, Larry Rubeck, Hilary Rubeck, Leo Rubeck, Warren Rubeck, and AJ - thank you for always being there and letting me stay with you when I needed a short getaway from Urbana-Champaign. Many of my favorite moments in the last six years were when I spent time with all of you!

To all of my amazing roommates throughout the years - all inhabitants of 404 house, Sandra Chiacchiari, Jola, Whitney Sinclair, Eddalee Hochwalt Naumann, and Caroline Owen thank you for making Urbana feel like home and making sure that life was never boring.

Lance and Wendy, I could not imagine my graduate experience without the support and mentorship from you! Lance, you advocated for me throughout my research and throughout my time in leadership positions in PGSA, GradSWE, and Allies in STEM, and all the way to the end of my degree when you wrote such a thoughtful and detailed recommendation letter.

To my CU Boulder physics family, thank you for all the support and encouragement and poker throughout these years. I am so thankful to have you all in my life and that these relationships were truly larger than just the camaraderie of surviving undergrad problem sets.

To the horseshoe boys - Luke Slattery, Christian Boyd, and Alex Munox - my experience in the physics department would not have been the same without you all (even if I am still bitter about being excluded from the official horseshoe boys group).

To all the wonderful women of GradSWE, being a part of this group has made me grow professionally and socially. It provided an outlet for research frustrations as well as leadership opportunities and time to spend with women outside of my department.

To Alexandra Cote and Whitney Sinclair, my two greatest grad school partners and friends for life. Alex, my grad school wifey and partner in crime, you (and Sally) were always there for all the highs and lows of this experience. We ate, we drank, we shopped, we laughed, and we cried (well mainly me for the first few years and then mainly you towards the end)! Whitney, you were my rock throughout this entire thesis writing process. The words to express how grateful and appreciative I am towards you are too much to write on this page. Everyday I try to be more like you.

Finally and most importantly, to my parents, brother, and grandmother. Thank you for always having the confidence in me to do this! I can't even count how many times I wanted to quit but your support, unconditional love, and reality checks kept me going! I would not be here without any of you.

This work was supported by the Center for Quantum Sensing and Quantum Materials, an Energy Frontier Research Center funded by the U. S. Department of Energy, Office of Science, Basic Energy Sciences under

Award DE-SC0021238. Additional support was provided by the Gordon and Betty Moore Foundation EPiQS grant GBMF-9452 and by NSF Graduate Research Fellowship DGE-1746047.

Table of Contents

List of Figures

Chapter 1

Introduction

In the field of condensed matter physics, systems can be classified based on the interaction strength between the free particles that make up the material. In the case of weak interactions, the energy of the interactions between particles (such as Coulomb energy for electrons) is a lot smaller than the energy of the particles themselves (kinetic energy of electrons) so we can describe individual particles as non-interacting. This is the case for most textbook metals and semiconductors, whose microscopic and macroscopic properties can be explained using Fermi liquid theory. In strongly correlated systems, the energy between particles is no longer negligible and this gives rise to interesting collective phenomenon such as superconductivity, magnetism, and density waves. Measuring, quantifying and understanding these emergent phenomena and their microscopic origins is the basis for almost all the research in the field, including this thesis.

1.1 Characterizing Materials with Scattering Techniques

In order to characterize a many-body system we need to understand both the single particle or quasiparticle dynamics (i.e. fermions) as well as the dynamics associated with a collection of these particles or quasiparticles (i.e. bosons). Examples of bosons in material systems include plasmons (collective mode of electron oscillation), phonons (collective mode of lattice vibrations), and magnons (collective mode of spin oscillation).

For the case of fermions, quasiparticles are characterized by the one-electron Green's function,

$$G(r, r', t - t') = -i\langle\{\psi^\dagger(\mathbf{r}, t), \psi(\mathbf{r}', t')\}\rangle \frac{\theta(t - t')}{\hbar} \tag{1.1}$$

which describes the probability that an electron at location, r, and time, t, will propagate to location

r' and time t'. $G(r, r', t - t')$ contains information about the energy band structure and lifetimes of the quasiparticles [18]. Examples of spectroscopic techniques that measure single particle excitations is angle-resolved photoemission spectroscopy (ARPES) and scanning tunneling microscopy (STM).

For the case of bosons, the collective excitations (also known as collective modes) are characterized by the density Green's functions that describe the density response due to a perturbation. These "dynamic response functions" contain information about the interactions that drive collective behavior. In other words, we can measure the disturbance in bosonic collective modes created by the probe particle interacting with the material. Such techniques can use neutrons, photons, or electrons as the probe that interacts with the system of interest.

Photons

Two common techniques using photons as the probe particle are infrared (IR) spectroscopy and inelastic X-ray scattering (IXS). IR spectroscopy measures the reflectively from which one can extract the dielectric response function, $\epsilon(\omega)$. The dielectric response function is related to the dynamic susceptibility, $\chi(\omega)$ [19]. IR spectroscopy is a great technique due to its high energy resolution however it is limited to just measuring at $q = 0$ (i.e. Brillouin zone Γ point) in momentum space.

Inelastic X-ray scattering has the benefits of high energy resolution as well as measuring across the Brillouin zone. However due to the fact that photons couple to the electron density as compared to the charge density, this method is less sensitive to charge collective modes such as plasmons [20]. This is due to the fact that the electron density is composed of electrons from the valence plus the core states. In many highly correlated materials, the lattice is composed of elements that have a high Z number, so the majority of the electrons in these system come from core states. This means that photon probe techniques are very sensitive to lattice excitations, such as phonons, and have a weaker signal from valence electron excitations, such as plasmons [21].

Neutrons

Neutrons are neutral particles and are not sensitive to the charged dynamics in the system. Inelastic neutron scattering is an example of a technique that can measure the spin dynamic response function with meV energy resolution across the Brillouin zone. Therefore this technique is used to measure spin collective excitations, such as magnons, but can also be sensitive to lattice excitation's through the displacement of the nucleus of individual atoms on a crystal lattice [22].

Electrons

Unlike neutrons, electrons are not neutral and are therefore sensitive to charged particles in materials. Unlike photons, electrons are sensitive to all charge (electrons + protons). This means that the core electrons cancel the positive charge in the nuclei of the atoms, so inelastic electron scattering primarily sees the valence electrons and is sensitive to valence collective modes such as plasmons. In addition, since the nucleus of atoms is coupled to electrons, if there is a lattice displacement, the electrons will feel the effects of that too, making electron scattering also sensitive to lattice dynamics. Inelastic electron scattering (also known as electron energy loss spectroscopy) can be used in a transmission geometry that has good momentum resolution but poor energy resolution (100 milli-electron Volt (meV)) or it can be done in a reflection geometry that has excellent energy resolution (on the order of several meV).

For this thesis, we focus on the dynamic response function that describes the charge collective excitations. This is also known as the dynamic charge density response or the dynamic charge susceptibility and is represented in Equation 1.2. Which describes the probability that a disturbance in the charge density at location,r, and time, t will propagate to location, r', and time, t'.

$$\chi(r, r', t - t') = -i\langle[\hat{\rho}(\mathbf{r}, t), \hat{\rho}(\mathbf{r}', t')]\rangle \frac{\theta(t - t')}{\hbar} \tag{1.2}$$

This is a similar statement to Equation 1.1 except that this describes the bosonic response as compared to the fermionic response.

For decades there have been techniques to probe energy and momentum dependence (dispersions) of spin collective excitations in materials however there lacked a probe to measure dispersions of charge collective modes at low energies. This gap in knowledge led to the development of a technique that measures dispersions of the dynamic charge density response function at meV scales known as momentum-resolved electron energy loss spectroscopy (M-EELS). It is important to note that the quantity M-EELS aims to measure is the dynamic charge response function, however experimentally the dynamic structure factor, also known as the dynamic correlation function, $S(\mathbf{q}, \omega)$, is what is measured [21]. The two quantities are directly related and this will be discussed further in Chapter 2.

1.2 Collective Excitations in the Density Response Function of Highly Correlated Systems

The development of M-EELS allows us to measure the energy and momentum dependence of the charge response function in highly correlated systems with interesting emergent phenomena. This thesis will fo-

cus on the collective excitations in two specific systems - Cu_xTiSe_2 and $SrTi_{1-x}Nb_xO_3$. Cu_xTiSe_2 and $SrTi_{1-x}Nb_xO_3$ are both doped semiconductors that exhibit strongly correlated phenomena.

1.2.1 Strongly Correlated Phenomena in Cu_xTiSe_2

Cu_xTiSe_2 exhibits several interesting quantum phenomena such as charge density waves (CDW) and superconductivity [23]. In addition, it has recently been shown that undoped $TiSe_2$ realizes exciton condensation [7].

A CDW is a periodic modulation of the electric charge with an accompanying periodic lattice distortion (PLD) that occurs below a critical temperature, T_C [24]. In Cu_xTiSe_2 for dopings $x < 0.05$, the wave vector of the CDW, $\mathbf{q_0}$, is a rational fraction of the reciprocal lattice vector making it commensurate with the lattice. For dopings $x > 0.05$, the CDW wave vector is incommensurate [8].

Superconductivity is another example of a system that attributes its unique properties to electron interactions. The superconducting phase is a low temperature phase that is characterized by perfect diamagnetism (expulsion of magnetic fields from the solid) and perfect conductivity (zero resistivity). These properties of superconductivity result from the fact that electrons in the system, which normally repel one another, experience an attractive force that dominates at low temperature making it energetically favorable for these electrons to pair into Cooper pairs.

In 1957, Bardeen, Cooper, and Schrieffer developed the first microscopic theory of superconductivity, BCS theory [25], which was able to describe all known superconductors at the time. In these materials, Cooper pairs form through the mediation of crystal lattice vibrations. As electrons pass through the lattice, they are attracted to the positive ions of the lattice. This attraction creates a potential well that attracts another electron forming a single Cooper pair, mediated by the phonon.

It was shown that undoped $TiSe_2$ also exhibits exciton condensation [7], which can contribute to a PLD and CDW formation. If cooled to low temperature, a collection of bosons will condense into a single quantum-mechanical state known as a Bose condensate. Bose condensation is seen in many macroscopic quantum phenomena, including superconductivity. In $TiSe_2$ the bosons that condense are excitons, or electron-hole pairs bound together by the Coulomb interactions. A condensate of excitons can also modulate the charge density and can create a PLD. The origins of CDW formation - from a PLD or from exciton condensations - was a long debated topic in condensed matter research.

An experimental signature that differentiates CDW formation due to exciton condensation from that of a PLD is the observation of a soft electronic collective mode at $T = T_{\mathrm{XC}} = T_{\mathrm{PLD}}$ and $\mathbf{q} = \mathbf{q_0}$ as well as a $\mathbf{q} = 0$ electronic mode that decreases in energy with decreasing temperature until it reaches $T = T_{\mathrm{XC}} = T_{\mathrm{PLD}}$. This

key finding was experimentally proven by using M-EELS [7], which measures dispersions of charge collective modes at low energies. However, the exciton condensate and PLD in $TiSe_2$ share the same symmetry and occur at the same temperature. Determining if these two phases are distinct from one another can give us more insight into the nature of the electronic interactions in this system.

Intercalating $TiSe_2$ with copper suppresses the PLD and induces a superconducting dome [23]. X-ray scattering has shown that the PLD is suppressed in Cu_xTiSe_2 [8, 26], but a separate measurement of the exciton condensate as a function of x is still needed. In this work we use M-EELS to measure how the soft electronic mode evolves with copper intercalation to investigate whether the exciton condensate and PLD behave independently.

1.2.2 Strongly Correlated Phenomena in $SrTi_{1-x}Nb_xO_3$

$SrTi_{1-x}Nb_xO_3$ also exhibits several interesting quantum phenomena such as quantum paraelectric behavior and unconventional superconductivity [27].

Unlike its periodic table neighbor $BaTiO_3$, $SrTiO_3$ never reaches the ferroelectric ordered phase. As temperature decreases, the dielectric constant increases as if the system is about to transition into a ferroelectric state, but then plateaus at around 20,000 times the vacuum permittivity [28] [11]. This deviation from ferroelectricity is due to quantum fluctuations causing the system to remain in a quantum paraelectric phase.

What makes $SrTi_{1-x}Nb_xO_3$ particularly interesting is that it is a dilute metal. Due to the proximity to quantum fluctuations, this material exhibits strong screening of static Coulomb interactions. As a result of this, unique charge transport properties emerge such as mobility that changes several orders of magnitude with temperature [13], resistivity at high temperatures that goes as T-cubed and resistivity that surpasses the Mott–Ioffe–Regel limit [29] (the limit in which the length between electron collisions is comparable to the mean distance between the electrons).

In addition, $SrTi_{1-x}Nb_xO_3$ has a superconducting dome that exists at exceptionally low carrier densities and therefore can no longer can be explained by the BCS theory of superconductivity. Since BCS theory was developed, there have been many discoveries of materials that cannot be explained by BCS theory. Such systems include high Tc superconductors, heavy fermion systems, ruthanates, dilute carrier systems, and more. The condensed matter community is still trying to understand the microscopic pairing mechanism that drives these "unconventional" superconductors.

In 1964, superconductivity was discovered in electron doped $SrTiO_3$ with a critical temperature of 0.3 K [30]. This system was the first oxide perovskite superconductor found, decades before the cuprates (high

T_c superconductor) [31]. In addition, this material exhibits a relationship between the critical temperature and carrier density that is shaped like a dome. Many other systems with superconducting domes have since been discovered and the dome's proximity to other electronic phases is considered pertinent to understanding the microscopic behavior in the system [32].

Electron doped $SrTiO_3$, which includes $SrTi_{1-x}Nb_xO_3$, falls into the subclass of materials known as dilute superconductors because it becomes superconducting at densities as low as 5.5×10^{17} cm^{-3} [12]. Due to the low carrier density, the screening of the Coulomb repulsion is weak and therefore BCS theory does not apply. Understanding these dilute systems has become of increasing interest as more materials in this category have been discovered including Bismuth, which has recently been discovered as the lowest density superconductor [33].

Although $SrTiO_3$ and $SrTi_{1-x}Nb_xO_3$ have been studied for over half a century, until recently there had not been a technique that could measure the dispersions of charge collective modes at low energies. The dilute-ness of $SrTi_{1-x}Nb_xO_3$ makes it particularly interesting to measure its collective excitations because the energy of lattice excitations is comparable to that of electronic excitations. This prompted us to explore how these collective modes behave.

1.3 Overview

My Ph.D. work has furthered our understanding of collective excitations in highly correlated materials. In particular, I have explored the normal state properties of lattice and electronic collective modes for two interesting systems - Cu_xTiSe_2 and $SrTi_{1-x}Nb_xO_3$

In Chapter 2, I provide an overview of the theory behind the M-EELS experiment. I include calculations of the scattering cross section as well as other quantities such as the density-density correlation function, S(q,w), the density response function, $\chi(\mathbf{q}, \omega)$, and the dielectric loss function. I also address an unsolved issue related to assumptions in the cross section calculation and provide one avenue for a potential solution.

In Chapter 3, I will present the M-EELS experimental implementation at UIUC. I give a brief description of the M-EELS setup followed by an explanation of what makes M-EELS distinct from HR-EELS. Next I will describe the electron optics of M-EELS as well as the new procedures I implemented for characterizing the electron beam behaviour. The later is compared to theoretical calculations and will be useful for optimizing the electron trajectory. Following that, I will discuss sample preparation, including a novel preparation technique for non-2D layered materials that I established. Finally I will address several of the instrumentation upgrades that I have designed and implemented over the course of my graduate degree.

In Chapter 4, I discuss the results of the M-EELS study on Cu_xTiSe_2. I first address the condensed matter interest in understanding and observing exciton condensation in undoped $TiSe_2$ - a system that realizes exciton condensation at the same temperature and with the same symmetries as a lattice distortion. This motivates the M-EELS experiment on Cu_xTiSe_2. Can copper intercalation determine if the exciton condensation and lattice distortion phases are distinct from one another? Measurements of the periodic lattice distortion order parameter and calculations of effective doping on each sample are presented. Next I present the momentum, doping, and temperature dependent results along with the fitting scheme used to quantify this data. Finally, I end with a discussion and revised phase diagram showing that the effects of copper doping quickly suppress the exciton condensate phase and that there exist excitonic fluctuations that describe the unusual temperature dependence seen across the phase diagram.

In Chapter 5, I discuss the results of the M-EELS study on $SrTi_{1-x}Nb_xO_3$. I first discuss the interesting properties exhibited by this unconventional material both in its undoped and electron doped states. Specifically I will touch on the importance of the electronic collective modes in this material due to their proximity in energy with the lattice collective modes. Next I will address how the novel wiresaw sample preparation impacts the M-EELS measurements. I present the momentum, doping, and temperature dependent results. These results show a lack of dispersion of the electronic collective mode, strong phonon overtones, and unusual electronic mode temperature dependence. Finally, I end with a discussion about how this data deviates from both RPA calculations and infrared spectroscopy measurements.

1.4 Summary of Accomplishments

Below is a summary of the work I have accomplished during the course of my Ph.D.

- **Development of M-EELS hardware and sample prep techniques to increase M-EELS measurements of more diverse materials.** I have designed, implemented and tested several ultra high vacuum (UHV) components to increase the classes of materials that M-EELS can study. Previously, M-EELS could only measure samples that are 2D - layered materials that can easily be cleaved in an UHV chamber. This severely limits the types of materials and physics that we can study with M-EELS. To overcome this, I created a vacuum suitcase chamber that can attach to both the M-EELS chamber as well as MBE and ARPES chambers and achieve UHV pressures. This allows for the growth of thin films in MBE to be transported to M-EELS without ever being exposed to air and in turn not requiring a way to clean the surface for scattering. I also developed an annealing stage that can heat materials in UHV which can be used to evaporate dirt off sample surfaces as well as electron

dope materials (by removing oxygen) and evaporate selenium caps on thin films. I introduced a UHV fracturing technique as a way to cleave samples that are not 2D layered. The vacuum suitcase was developed in collaboration with Guannan Chen (UIUC, Madhavan Group) and Waclaw Swiech (MRL Research Scientist) who assisted with making the vacuum suitcase compatible with MBE instruments. The final CAD design of the annealing stage was implemented by undergraduate student, Reka Manton, under my guidance.

- **New characterization tools for in-situ optimization of electron beam trajectory.** I helped develop methods to characterize the behavior of the electron beam at multiple points in the electron trajectory. Originally electron throughput and resolution were only characterized and optimized by varying a single parameter at a time. Due to the fact that the phase space of the electron optics parameters is so large (40+ parameters), this approach often led to being stuck at a local minimum in parameter space. An alternative approach is to vary a few parameters simultaneously to more accurately determine the parameter space. This approach was previously implemented by characterizing the phase space at the detector [34, 35]. In this work, I extend on the phase space characterization by looking at multiple points along the electron trajectory not just at the detector. These characterization tools will be especially important for implementing next iterations of the M-EELS spectrometer. The work of this characterization was a collaboration with labmates Cat Kengle, Jin Chen, Faren Hoveyda Marashi, and Simon Bettler.

- **Modifying M-EELS cross section calculation to include experimental momentum resolution.** Calculating the M-EELS cross section uses assumptions that in the regime near-Bragg conditions breaks down [34–36]. This is problematic when calculating physical quantities such as $S(\mathbf{q}, \omega)$ and $\chi''(\mathbf{q}, \omega)$ which entails dividing out the cross section matrix elements and creates an artificial distortion of the spectral weight at near-Bragg momentum. One approach to solving this is to include the experimental resolution of the spectrometer in the matrix element calculations. The derivations and simulations of this approach, specifically for the material Bi2212, is work done by Christian Boyd and Luke Yeo (UIUC, Phillips Group). The work presented in this thesis is a collaboration with Christian and Luke using their calculations applied to materials of interest in this thesis, namely $SrTiO_3$.

- **Using M-EELS to determining if the exciton condensate and periodic lattice distortion phases in $TiSe_2$ are distinct from one another.** This was done by measuring the soft plasmon (a signature of exciton condensation) as a function of copper intercalation, Cu_xTiSe_2, which introduces coulomb screening of the valence electrons. Our results show that exciton condensation is quickly

suppressed by the added coulomb screening while the periodic lattice distortion survives well beyond the point where the exciton condensation is suppressed. In addition we found that although exciton condensation is suppressed, exciton fluctuations remain for most of the doping phase diagram. These fluctuations have been theorized to aid in superconducting pairing in this system [9, 10]. The suppression of exciton condensation and introduction of excitonic fluctuations have never been shown before this M-EELS study. This project is the culmination of work in Mindy Rak's [35] PhD thesis. I participated in this project by collecting all the data alongside Mindy, assisting in analysis, writing and editing the manuscript and revising the phase diagram. The work presented in this chapter of my thesis is taken from our manuscript to be submitted:

1cm M. S. Rak, S. I. Rubeck, A. A. Husain, M. Mitrano, et al., Distinct lattice and excitonic instabilities in Cu_xTiSe_2, (to be submitted)

- **Using M-EELS to measure the behavior of electronic collective mode, identified as a plasmon, in systems that have dilute metallicity and that exhibits dilute superconductivity.** The dispersion of the electronic collective mode is important in $SrTi_{1-x}Nb_xO_3$ due to its proximity in energy to the lattice collective modes and its implication in mediating the superconducting pairing [14–16]. Our results show a non-dispersive plasmon that deviates from RPA predictions and infrared spectroscopy measurements. This study touches on several important features that have never been measured before including the momentum dependence of the bulk plasmon, doping dependence of the Fuchs-Kliewer phonon overtones, and an unidentified dispersive mode at 1 eV. I spearheaded the data collection, data analysis, and manuscript (in progress) of this project. Labmates Cat Kengle, Jin Chen, and Mindy Rak assisted in data collection. Cat Kengle also contributed to the analysis of this project. The work presented in this chapter of my thesis is included in our upcoming manuscript:

  1cm S. I. Rubeck, C. Kengle, M. S. Rak, J. Chen, et al., Probing Finite-Momentum Charge Collective Modes in Electron Doped $SrTiO_3$, (in preparation)

Chapter 2

The Theory Behind M-EELS

2.1 Cross Section

The scattering cross section of the reflection M-EELS technique is calculated from the matrix element of the Coulomb interaction from the probe electron interacting with the valence electrons in the sample. In the derivation by Mills and others [37–41] several key assumptions are made:

1. In low-energy, reflection EELS geometry, the probe electron does not penetrate into the material.

2. Multiple scattering of electrons primarily occurs in the elastic channel.

The former is a statement of multiple scattering; that strong interactions with the sample surface causes the electrons to scatter off the surface more than once. The latter is a statement of the type of multiple scattering that occurs. Multiple scattering in the elastic channel means that electrons scatter more than once elastically, but they only scatter inelastically once. From these approximations, the cross section can by calculated using the distorted wave Born approximation (DWBA) [40].

In the work of the Abbamonte group [21,34–36], the scattering cross-section (using the same assumptions as Mills) was calculated for a periodic system. In other words, this calculation takes into account elastic Bragg scattering from a periodic structure instead of assuming a translationally invariant system. In the following I will give a brief summary of the results shown in these previous works.

In the DWBA, the wave functions of the incident and scattered electron, model the reflectively from the sample surface given by:

$$\psi_i = N_i \left[e^{i\mathbf{k_i}\cdot\mathbf{r}} e^{ik_i^z z} + \sum_{\mathbf{G}_1} R_{\mathbf{G}_1} e^{i(\mathbf{k_i}+\mathbf{G_1})\cdot\mathbf{r}} e^{-i\kappa_i z} \right] \theta(z), \tag{2.1}$$

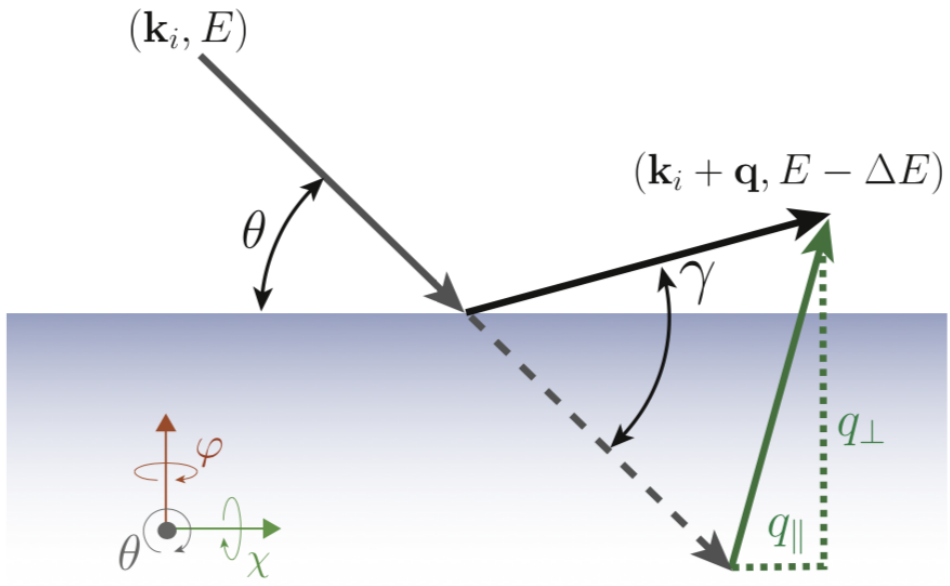

Figure 2.1: **M-EELS Scattering Geometry**
Diagram of the scattering geometry of M-EELS. This shows the incident electron momentum, $\mathbf{k_i}$, and energy, E_i, the scattered electron momentum, $\mathbf{k_s} = \mathbf{k_i} + \mathbf{q}$, and energy, $E_s = E_i - \Delta E$, the scattering angles θ and γ, the in-plane momentum transfer $q_\parallel$, and out-of-plane momentum transfer $q_\perp$. Figure reproduced from [42].

$$\psi_s = N_s \left[e^{i\mathbf{k_s}\cdot\mathbf{r}} e^{ik_s^z z} + \sum_{\mathbf{G}_2} R_{\mathbf{G}_2} e^{i(\mathbf{k_s}+\mathbf{G_2})\cdot\mathbf{r}} e^{-i\kappa_s z} \right] \theta(z), \tag{2.2}$$

where ψ_i and ψ_s are the wave functions for the incident and scattered electron, respectively. $N_{i,s}$ are the normalization constants and the coordinate $\mathbf{R} = (\mathbf{r}, z)$ consists of the in-plane coordinate, $\mathbf{r}$, and the out-of-plane coordinate, z, with respect to the surface. $\mathbf{G}$ is the reciprocal lattice wave vector. $\mathbf{G}$ is equal to zero when an electron undergoes elastic specular reflection, $\mathbf{G}$ is equal to $(2\pi/a, 0)$ when an electron undergoes Bragg reflection in the next Brillouin zone. $\mathbf{k_{i,s}}$ is the in-plane component of momentum and $k_{i,s}^z$ is the out-of-plane component of momentum before Bragg scattering. θ(z) is the step function defining the sample surface. $\kappa_{i,s}$ is the out of plane momenta of the electron after Bragg scattering and is given by,

$$\kappa_{i,s} = \pm\sqrt{(k_{i,s}^z)^2 - \mathbf{G}^2 - 2\mathbf{k}_{i,s}\cdot\mathbf{G}}. \tag{2.3}$$

In order to maintain conservation of energy, if the in-plane momentum takes $\mathbf{G}$ into account, then the out-of-pane momentum must also take the $\mathbf{G}$ wave vector into account.

The M-EELS cross section comes from calculating the matrix element for the Coulomb interaction of the

probe electron with the valence electrons in the sample:

$$M = -\frac{ie^2}{2\hbar}\int d\mathbf{R}_1 d\mathbf{R}_2 \frac{\langle n|\,\hat{\rho}(\mathbf{R}_1)\,|m\rangle\,\psi_s^*(\mathbf{R}_2)\psi_i(\mathbf{R}_2)}{|\mathbf{R}_1-\mathbf{R}_2|} \tag{2.4}$$

where $|n\rangle$ and $|m\rangle$ denote the final and initial states of the sample, $\mathbf{R}_1$ is the location of the valence electron, and $\mathbf{R}_2$ is the location of the probe electron.

Inserting the wave functions from Eqs. 2.1 and 2.2 into Eq. 2.4, we find that there are four different terms:

$$\begin{aligned}\psi_s^*(\mathbf{R}_2)\psi_i(\mathbf{R}_2) = N_s N_i \Big[& e^{i(\mathbf{k}_i-\mathbf{k}_s)\cdot\mathbf{r_2}} e^{i(k_i^z-k_s^z)z_2} \\ & + \sum_{\mathbf{G}_2} R^*_{\mathbf{G}_2} e^{i(\mathbf{k}_i-\mathbf{k}_s-\mathbf{G}_2)\cdot\mathbf{r_2}} e^{i(k_i^z+\kappa_s)z_2} \\ & + \sum_{\mathbf{G}_1} R_{\mathbf{G}_1} e^{i(\mathbf{k}_i-\mathbf{k}_s+\mathbf{G}_1)\cdot\mathbf{r_2}} e^{-i(\kappa_i+k_s^z)z_2} \\ & + \sum_{\mathbf{G}_1,\mathbf{G}_2} R^*_{\mathbf{G}_2} R_{\mathbf{G}_1} e^{i(\mathbf{k}_i-\mathbf{k}_s+\mathbf{G}_1-\mathbf{G}_2)\cdot\mathbf{r_2}} e^{-i(\kappa_i-\kappa_s)z_2} \Big] \theta^2(z_2).\end{aligned} \tag{2.5}$$

Each term represents a scattering process that is illustrated in Fig 2.2. Since this calculation is taken in the DWBA and we are only considering single scattering events, we can neglect all terms that contribute to multiple scattering (e.g. terms that are not linear in R).

Plugging the matrix element with only the single scattering terms into Fermi's golden rule, yields a transition rate

$$\omega_{n\leftarrow m} = 2\pi\hbar|M|^2. \tag{2.6}$$

$$\begin{aligned}\omega_{n\leftarrow m} = \frac{\pi^2 N^4}{\hbar}\sum_{\mathbf{G}} |R_{\mathbf{G}}|^2 V_{\text{eff}}^2(\mathbf{q}-\mathbf{G}) \\ \times \int_{-\infty}^{0} dz_1 dz_2 \,\langle m|\,\hat{\rho}^*(\mathbf{q}-\mathbf{G},z_1)\,|n\rangle\,\langle n|\,\hat{\rho}(\mathbf{q}-\mathbf{G},z_2)\,|m\rangle\, e^{-|\mathbf{q}-\mathbf{G}||z_1+z_2|}\end{aligned} \tag{2.7}$$

where $\mathbf{q} = \mathbf{k_i} - \mathbf{k_s}$ and $V_{\text{eff}}^2(\mathbf{q}-\mathbf{G})$ is a Coulomb matrix element given by

$$\begin{aligned}V_{\text{eff}}^2(\mathbf{q}-\mathbf{G}) = \frac{V_{2D}^2(\mathbf{q}-\mathbf{G})}{2} \\ \times \left[\frac{4|\mathbf{q}-\mathbf{G}|^2 + (k_s^z - k_i^z + \kappa_i - \kappa_s)^2 + (k_i^z + k_s^z + \kappa_i + \kappa_s)^2}{\left(|\mathbf{q}-\mathbf{G}|^2 + (\kappa_i + k_s^z)(k_i^z + \kappa_s)\right)^2 + |\mathbf{q}-\mathbf{G}|^2(k_s^z - k_i^z + \kappa_i - \kappa_s)^2}\right].\end{aligned} \tag{2.8}$$

$V_{\text{eff}}(\mathbf{q}-\mathbf{G})$ describes the interaction between the probe electron and the electrons near the surface of the sample and will be discussed in more depth in the following section.

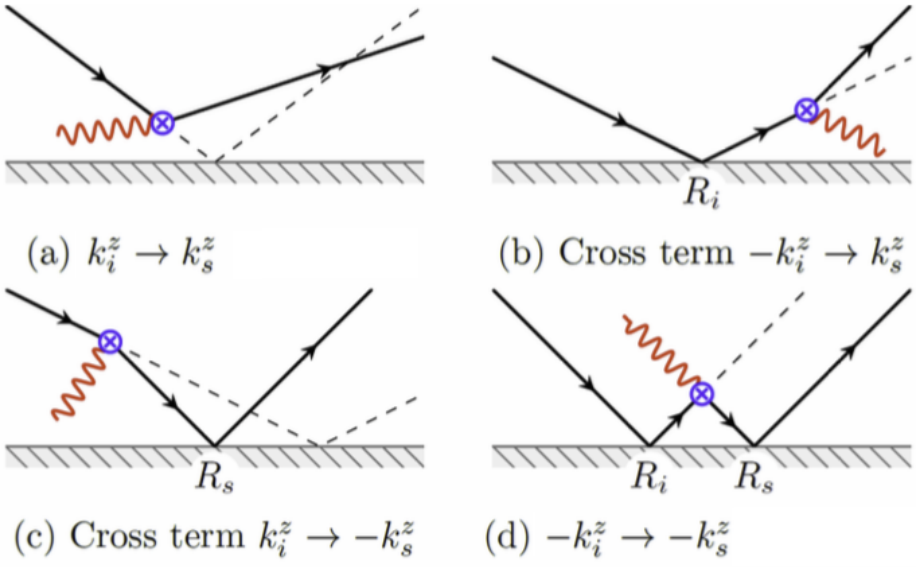

Figure 2.2: **Electron Scattering Channels**
Representation of the four different quantum mechanical processes shown in Mills' theory of surface EELS using the distorted wave Born approximation. Due to multiple scattering arguments, the cross section is dominated by terms that are linear in R (b) and (c) while terms that are not-linear in R (a) and (d) can be neglected. Figure reproduced from [21].

Using this transition rate from Fermi's Golden Rule to calculate the double-differential cross section,

$$\frac{\partial^2\sigma}{\partial\Omega\partial E} = \frac{1}{\Phi}\sum_{n,m}\omega_{n\leftarrow m}P_m\frac{\partial^2 N}{\partial\Omega\partial E} \tag{2.9}$$

where $\Phi = \sqrt{2E_i/m}/V$ is the incident electron flux, $P_m = e^{-E_m/k_BT}/\mathcal{Z}$ is the Boltzmann factor, and the last term is the density of final states,

$$\frac{\partial^2 N}{\partial\Omega\partial E} = \frac{V}{8\pi^3}\left(\frac{2m}{\hbar^2}\right)^{3/2}\sqrt{E_f} \tag{2.10}$$

where $E_f = E_i - \hbar\omega$ is the energy of the scattered electron.

Following the algebra and assumptions in [21, 34, 35], we arrive at the generalized M-EELS cross section for scattering from a periodic surface,

$$\frac{\partial^2\sigma}{\partial\Omega\partial E} = \sum_{\mathbf{G}}\sigma_0 V_{\text{eff}}^2(\mathbf{q}-\mathbf{G})\int_{-\infty}^{0}dz_1dz_2e^{-|\mathbf{q}-\mathbf{G}||z_1+z_2|}\sum_{m,n}P_m \times\langle m|\,\hat{\rho}^*(\mathbf{q}-\mathbf{G},z_1)\,|n\rangle\,\langle n|\,\hat{\rho}(\mathbf{q}-\mathbf{G},z_2)\,|m\rangle\,\delta(E-E_n+E_m) \tag{2.11}$$

where

$$\sigma_0 = \frac{m^2 V^2 N^4 |R_{\mathbf{G}}|^2}{2\pi\hbar^4} \sqrt{\frac{E_f}{E_i}}. \tag{2.12}$$

In the limit where $\mathbf{G} = 0$ (i.e. $\mathbf{q} \sim 0$), the above equations reduce to

$$\frac{\partial^2 \sigma}{\partial \Omega \partial E} = \sigma_0 V_{\text{eff}}^2(\mathbf{q}) \int_{-\infty}^{0} dz_1 dz_2 e^{-|\mathbf{q}||z_1+z_2|} \sum_{m,n} P_m \langle m| \hat{\rho}^*(\mathbf{q}, z_1) |n\rangle \langle n| \hat{\rho}(\mathbf{q}, z_2) |m\rangle \times \delta(E - E_n + E_m) \tag{2.13}$$

where

$$V_{\text{eff}}(\mathbf{q}) = \frac{4\pi e^2}{\mathbf{q}^2 + (k_i^z + k_s^z)^2}, \tag{2.14}$$

which matches the result from [39].

There are several important implications that arise from these results.

1. **The probe depth of M-EELS is $1/|\mathbf{q}|$ when assuming we are in the limit where $\mathbf{G} = 0$ term dominates.** Charge fluctuations create a dipole electric field extending both into the vacuum and into the material a distance $1/|\mathbf{q}|$. For the materials studied in this thesis, the probe depth is on the order of hundreds of $\mathring{A}$ or less. This means, while generally considered a surface probe, M-EELS is much more bulk sensitive than surface techniques like ARPES or STM.

2. **Scattered electrons do not penetrate the material, they only interact with electrons near the surface.** The incident electrons probe the surface collective modes that couple to density fluctuations below the surface. This coupling comes about from the probe electrons long-ranged coulomb potentials. Therefore, M-EELS can see both surface and bulk excitations.

3. **Even though M-EELS is a surface sensitive probe, it can still measure bulk phenomena.** The ability to couple to the bulk density fluctuations gives M-EELS its sensitivity to bulk modes. This is different compared to other surface sensitive spectroscopy techniques such as ARPES and STM, that only measure the top layer [41].

4. **The Coulomb matrix element, $V_{\text{eff}}^2(\mathbf{q} - \mathbf{G})$, diverges when a Bragg condition is met, $\mathbf{q} = \mathbf{G}$).** The implications of this is an enhancement of intensity at the Bragg condition. The details of this will be address in section 2.3.

2.2 Physically Relevant Quantities Calculated From M-EELS Cross Section

The cross section is what we measure as raw intensity in electrons per second from the M-EELS spectrometer. However in order to compare to other spectroscopy techniques we need to convert the raw intensity to more physically relevant quantities. This includes the density-density correlation function, $S(\mathbf{q},\omega)$, the surface density response function, $\chi_S(\mathbf{q},\omega)$, and the dielectric loss function.

2.2.1 Density-Density Correlation Function

As discussed in the introduction, M-EELS is unique because it allows us to measure the dynamic charge response function of the surface, $\chi''_S(\mathbf{q},\omega)$. More directly though, the M-EELS cross section is related to the density-density correlation function, or the dynamic structure factor [43, 44] written as

$$S(\mathbf{q},z_1,z_2,\omega)=\sum_{m,n}\left[\langle m|\,\hat{\rho}(\mathbf{q},z_1)\,|n\rangle\,\langle n|\,\hat{\rho}(-\mathbf{q},z_2)\,|m\rangle\,P_m\right]\delta(E-E_n+E_m). \tag{2.15}$$

The density-density correlation function describes density fluctuations with in-plane wave vector $\mathbf{q}$ that are correlated between the depths z_1 and z_2 below the surface of the material. Substituting Equation 2.15 into Equation 2.13 we can rewrite the cross section in terms of the density-density correlation function:

$$\frac{\partial^2\sigma}{\partial\Omega\partial E}=\sum_{\mathbf{G}}\sigma_0 V_{\text{eff}}^2(\mathbf{q}-\mathbf{G})\int_{-\infty}^{0}dz_1dz_2e^{|\mathbf{q}-\mathbf{G}||z_1+z_2|}S(\mathbf{q},z_1,z_2,\omega). \tag{2.16}$$

Since the probe electrons are just interacting with electrons near the surface, we can write this as a surface density-density correlation function,

$$S_S(\mathbf{q},\omega)=\int_{-\infty}^{0}dz_1dz_2e^{-|\mathbf{q}-\mathbf{G}||z_1+z_2|}S(\mathbf{q},z_1,z_2,\omega)\approx S(\mathbf{q},0,0,\omega). \tag{2.17}$$

This leaves the cross section in its final simplified form,

$$\frac{\partial^2\sigma}{\partial\Omega\partial E}=\sum_{\mathbf{G}}\sigma_0 V_{\text{eff}}^2(\mathbf{q}-\mathbf{G})S_S(\mathbf{q},\omega). \tag{2.18}$$

The above statements makes the assumption that the correlation function exhibits the same periodicity as the lattice such that

$$S(\mathbf{q}-\mathbf{G},z_1,z_2,\omega)=\alpha S(\mathbf{q},z_1,z_2,\omega), \tag{2.19}$$

where α is the ratio of intensities at each Bragg reflection $\mathbf{G}$, such that $\alpha = I_{\mathbf{G_1}}/I_{\mathbf{G_2}} > 1$ since the intensity from lower order Bragg peaks is always larger than higher order Bragg peaks. This is important because it means that the experimental spectra repeat in each Brillouin zone, only differing by a scale factor.

For M-EELS experiments at 50eV incident beam energy, measurements are usually restricted to the first and second Brillouin zone. Therefore the cross-section becomes

$$\frac{\partial^2\sigma}{\partial\Omega\partial E} = [V^2_{\text{eff}}(\mathbf{q}) + \alpha V^2_{\text{eff}}(\mathbf{q}-\mathbf{1})]\sigma_0 S_S(\mathbf{q},\omega) \tag{2.20}$$

where $\alpha = I_{\mathbf{G}=0}/I_{\mathbf{G}=1}$, and $V^2_{\text{eff}}(\mathbf{q}-\mathbf{1})$ can be calculated from Equation 2.8.

2.2.2 Density Response Function

Using the quantum mechanical fluctuation-dissipation theorem [18, 41, 43, 44], we can relate $S_S(\mathbf{q},\omega)$ to the surface density response function, $\chi''_S(\mathbf{q},\omega)$, which represents the perturbation in the charge density created by the incident electrons interacting with the surface electrons.

$$S_S(\mathbf{q},\omega) = -\frac{1}{\pi}\frac{1}{1-e^{-\hbar\omega/k_BT}}\chi''_S(\mathbf{q},\omega), \tag{2.21}$$

where $\chi''_S(\mathbf{q},\omega)$ is the imaginary part of the surface density propagator, $\chi_S(\mathbf{q},\omega)$. The correlation function and density response function are related by the Bose factor, $(1-e^{-\hbar\omega/k_BT})^{-1}$.

In order to calculate $\chi''_S(\mathbf{q},\omega)$, the Bose factor needs to be extracted. This process is not as straight forward as dividing the Bose factor out because it is singular at ω=0. Instead we antisymmeterize the correlation function using a procedure analogous to the symmetrization procedure used in ARPES [45]. The details of this process are outlined in Vig [21, 36] and result in the following:

$$\chi''_S(\mathbf{q},\omega) = \pi[S_S(\mathbf{q},-\omega) - S_S(\mathbf{q},\omega)]. \tag{2.22}$$

2.2.3 Dielectric Loss Function

The conventional 3D density response function $\chi(\mathbf{q},\omega)$ is related to the inverse dielectric function, -Im$[1/\epsilon(\mathbf{q},\omega)]$ via the relationship [46]:

$$\text{Im}\left(\frac{1}{\epsilon(\mathbf{q},\omega)}\right) = V(\mathbf{q})\chi''(\mathbf{q},\omega), \tag{2.23}$$

where

$$V(\mathbf{q}) = \frac{4\pi e^2}{\mathbf{q}^2}. \tag{2.24}$$

The inverse dielectric function can be measured by other techniques like optical spectroscopy for $\mathbf{q} = 0$.

Although M-EELS measures the surface density response function, if the in-plane surface response and the in-plane bulk response do not differ dramatically, then it may be possible to relate the surface response function to the bulk dielectric function. We can assess the similarity between the surface and bulk response functions on an individual basis by comparing the M-EELS spectra at $\mathbf{q} = 0$ for a particular material to the dielectric loss function measured with infrared spectroscopy for that same material.

In the limit of 2D materials (i.e. materials that that have weak Van der Waal forces between its layer making it easy to cleave such as $TiSe_2$) it has been shown in [34] that

$$\left(\frac{\partial^2\sigma}{\partial\Omega\partial E}\right)_{M-EELS} \propto \mathrm{Im}\left(\frac{1}{\epsilon(\mathbf{q},\omega)}\right). \tag{2.25}$$

However, for semi-infinite homogeneous systems such as $SrTiO_3$,

$$\left(\frac{\partial^2\sigma}{\partial\Omega\partial E}\right)_{M-EELS} \propto \mathrm{Im}\left(\frac{1}{\epsilon(\mathbf{q},\omega)+1}\right). \tag{2.26}$$

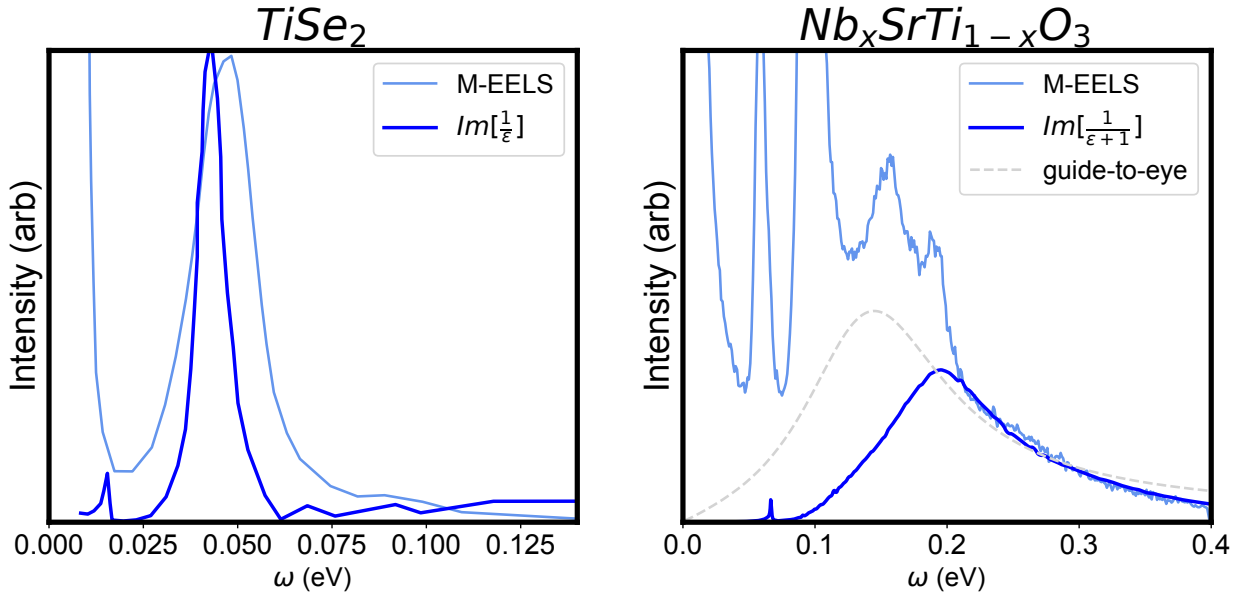

Figure 2.3: **Collective Modes of Bulk versus Surface Techniques**
Comparison of the electronic collective mode from IR spectroscopy (loss function calculated from optical conductivity and reflectivity measurements) and the electronic collective mode seen in M-EELS for two materials - $TiSe_2$ and $SrTi_{1-x}Nb_xO_3$. $TiSe_2$, a 2D layered transition metal dicalcagenide, shows good agreement between IR loss function [47] and M-EELS data [7] at 17 K and q=0, demonstrating that the surface response function is similar to the bulk dielectric function. $SrTi_{1-x}Nb_xO_3$,a 3D ionic material, shows poorer agreement between IR loss function [48] and M-EELS data (this work) at 23 K and q=0. A guide-by-eye is provided to show the by eye estimate of the plasmon in the $SrTi_{1-x}Nb_xO_3$ background.

Figure 2.3 shows a comparison of $TiSe_2$ and $SrTi_{1-x}Nb_xO_3$ using both M-EELS and IR spectroscopy. For $TiSe_2$, the $\mathrm{Im}\left(\frac{1}{\epsilon(\mathbf{q},\omega)}\right)$ is calculated from IR data from [47] and the q=0 M-EELS data is taken from [7].

Both data sets were taken at 17 K. The two techniques show comparable spectra for the electronic collective mode at 50 meV. The M-EELS peak is broader than that from IR due to the fact that IR spectroscopy is truly a q=0 technique, while for M-EELS, q=0 is an integrated measurement of all q within the momentum resolution. Therefore, for the case of $TiSe_2$, the in-plane surface response is similar to the in-plane bulk response meaning that the surface response function is similar to the bulk dielectric function and Equation 2.25 holds.

Figure 2.3 also compares the response of bulk and surface probes for $SrTi_{1-x}Nb_xO_3$, both measured at 23 K. In this case, the bulk, IR spectroscopy response is calculated using $\mathrm{Im}\left(\frac{1}{\epsilon(\mathbf{q},\omega)+1}\right)$ with data taken from [48] and compared to the M-EELS surface response in this work. Both techniques show a broad electronic collective mode. The M-EELS plasmon mode is shown with a guide to the eye line for clarity. The mode seen by M-EELS is at lower energy compared to that measured with IR spectroscopy. The discrepancy between the in-plane surface response and the in-plane bulk response indicates that M-EELS is measuring a superposition of bulk and surface effects most likely due to the polar nature of $SrTi_{1-x}Nb_xO_3$. This will be discussed in more detail in Chapter 5.

2.3 Coulomb Matrix Element

An issue that arises from the scattering cross-section calculation is that the Coulomb matrix element, V_{eff}, is strongly momentum dependent and diverges when the momentum coincides with a Bragg peak. This effect has to do with the breakdown of the Born approximation and is known as "Bragg enhancement" due to the fact that it amplifies inelastic scattering periodically with the lattice. It is interesting to note that although M-EELS matrix elements are strongly momentum-dependent, they do not strongly depend on energy for most momentum except for at low energy and low momentum where it does become largely dependent on energy. This is in stark contrast to other techniques such as ARPES, whose matrix elements always depend strongly on energy [49].

The Coulomb matrix element is written in its full form in Equation 2.8 however for this section let us just look at the case where $\mathbf{G} = 0$,

$$V_{\mathrm{eff}}(\mathbf{q}) = \frac{4\pi e^2}{\mathbf{q}^2 + (k_i^z + k_s^z)^2} \tag{2.27}$$

$\mathbf{q}$ is the in-plane momentum transfer referred to as $q_\parallel$ in Figure 2.1.

$q_\parallel$ can be rewritten as:

$$\mathbf{q}_\parallel = \mathbf{k}_\mathbf{s}^\parallel - \mathbf{k}_\mathbf{i}^\parallel = k_s \cos(\gamma - \theta) - k_i \cos(\theta) \tag{2.28}$$

where $k_{i,s} = \sqrt{2mE_{i,s}}/\hbar$, E_i is the energy of the incident electrons set to 50 eV for the experiments in this work, $E_s = E_i - \omega$ is the energy of the scattered electrons. The out-of-plane momentum transfer is $q_\perp$ is written as:

$$q_\perp = k_s^\perp - k_i^\perp = k_s \sin(\gamma - \theta) + k_i \sin(\theta). \tag{2.29}$$

Its important to note that the Coulomb matrix element does not depend on $q_\perp$ but instead on $k_s^\perp + k_i^\perp$. This term is defined as:

$$k_s^\perp + k_i^\perp = k_s \sin(\gamma - \theta) - k_i \sin(\theta) \tag{2.30}$$

The sign of $k_i^\perp$ depends on how you define your coordinate system. For these calculations our coordinate system is defined in Figure 2.1 where +z is normal to the same surface extending into vacuum, such that $k_s^\perp$ and $k_i^\perp$ have opposite sign.

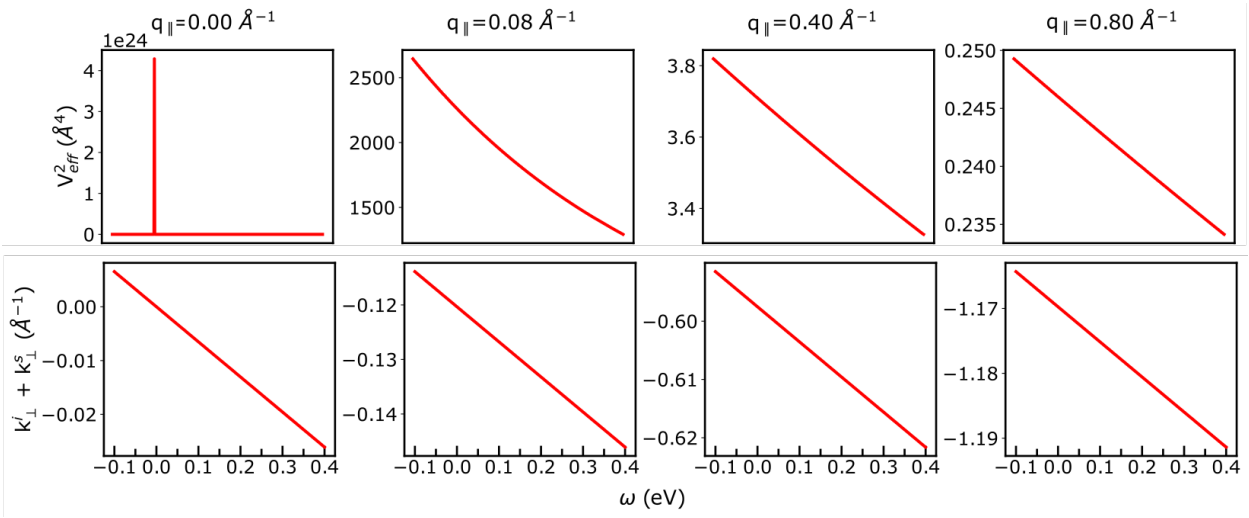

Figure 2.4: **Effective Coulomb Matrix Components Calculated with M-EELS Experimental Geometries**
Using $SrTiO_3$ geometries (θ and γ) from lattice parameters (a=b=c=3.905 $\mathring{A}$), and fixed out-of-plane momentum, $q_\perp = 4.02\mathring{A} = 2.5 r.l.u.$, we calculated the Coulomb matrix element, $V^2_{\text{eff}}(\mathbf{q})$, and $k_s^\perp + k_i^\perp$. These terms were calculated at different points in momentum space from $\mathbf{q}_\parallel = 0$ $\mathring{A}^{-1}$ (first column) the center of the Brillouin zone to $\mathbf{q}_\parallel = 0.8$ $\mathring{A}^{-1} = 0.5$ $r.l.u$ (last column), the Brillouin zone boundary.

Figure 2.4 highlights the energy and momentum dependence of these terms. These were calculated using the $SrTiO_3$ lattice parameters (a=b=c=3.905 $\mathring{A}$), fixed out-of-plane momentum, $q_\perp = 4.02$ $\mathring{A} = 2.5$ $r.l.u.$ and variable θ, γ, and ω. Each column is a different point in momentum space from $\mathbf{q}_\parallel = 0$, the center of the Brillouin zone to $\mathbf{q}_\parallel = 0.8$ $\mathring{A}^{-1} = 0.5$ $r.l.u$, the Brillouin zone boundary.

There are several key features to note from Figure 2.4:

1. **M-EELS is working in a fixed momentum transfer configuration.** Comparatively, HR-EELS

which works in a fixed angle configuration. By varying θ, γ, and ω, $q_\perp$ and $q_\parallel$ remain fixed in an energy loss scan. This is demonstrated in the second and third row of Figure 2.4.

2. V_{eff}^2 **diverges at low transferred energy when** $q_\parallel = 0$**.** Specifically, as $q_\parallel$ and $k_s^\perp + k_i^\perp$ go to zero, the Coulomb matrix element diverges with ω^{-4} behavior. This comes about due to the fact that $k_s^\perp + k_i^\perp$ is not a fixed quantity in M-EELS.

3. V_{eff}^2 **depends on** $k_s^\perp + k_i^\perp$ **which is linear in** ω **for fixed** $q_\perp$ **and** $q_\parallel$**.** Due to conservation of momentum and conservation of energy, $k_s^\perp + k_i^\perp$ must go through zero as $q_\parallel$ and ω go to zero.

Although the functional form of the Coulomb matrix element diverges, the experimental intensity does not. Therefore the approximations in which the matrix elements were derived (DWBA) break-down near Bragg conditions. The effect of V_{eff}^2 becomes apparent when dividing the M-EELS intensity by Coulomb matrix element to calculate $S(\mathbf{q}, \omega)$ as defined in Section 2.2. Figure 2.5 shows the M-EELS intensity of $SrTiO_3$ at low momentum transfer compared to the calculated $S(\mathbf{q}, \omega)$ for the same spectra.

There are two effects from the matrix elements. One being that in the raw intensity, the matrix elements suppress high energy excitations which is why low energy excitations (i.e. phonons) are very strong compared to other collective modes. This is a real effect that comes about due to Bragg enhancement. The second effect is seen by dividing out the Coulomb matrix element and in doing so, increasing spectral weight at high energies and suppressing spectral weight at low energies. This effect is artificial and comes from dividing by a diverging V_{eff}^2 at low momentum and not from multiple scattering in the elastic channel.

An imperfect solution to this problem would be to use an f-sum rule to correct for momentum scaling in the majority of the Brillouin zone, assuming that the matrix elements are energy-independent in this region, and exclude regions where the matrix elements show strong energy dependence near Bragg conditions. Excluding this data in calculation of the dynamic structure factor and dynamic response function is not ideal since q=0 measurements are how we can compare to bulk techniques like IR spectroscopy. There has been a push in recent years to solve this problem by using a matrix elements that have been broadened to account for the finite momentum resolution of the experiment and do not diverge at low q as discussed in the next section.

2.3.1 Resolution-Broadened Coulomb Matrix Elements

There has been some effort to try to circumvent the matrix element issue for near-Bragg-peak momentum. The cross section that we measure is actually a combination of physics from the material (e.g., widths of excitations) plus effects of the instrument itself (momentum and energy resolution). The larger the resolution

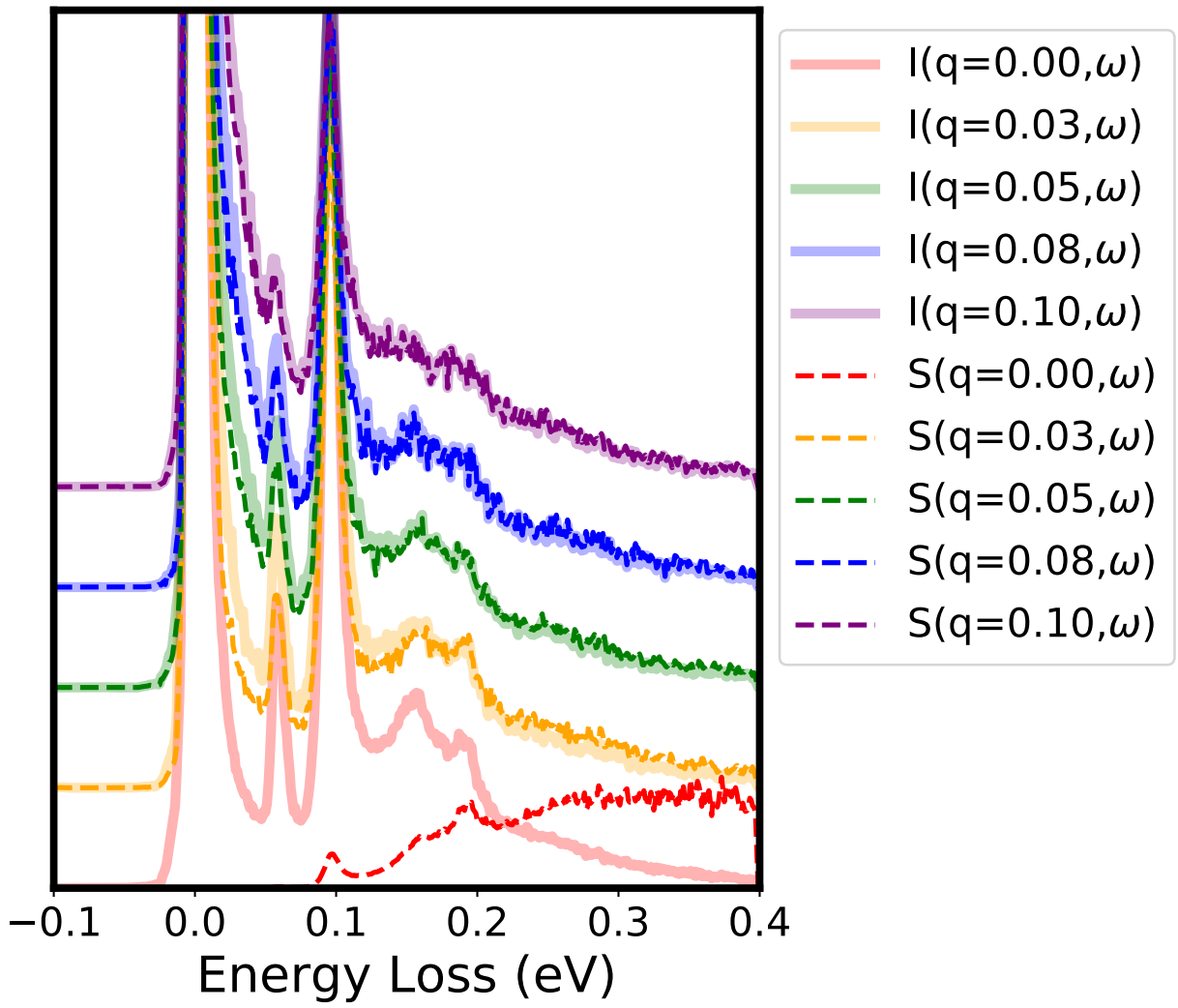

Figure 2.5: **Dividing Out the Coulomb Matrix Element**
Raw M-EELS intensity, $I(q,\omega)$, and calculated charge response, $\chi''(q,\omega)$, as a function of momentum along (1,0) in $SrTiO_3$. The response function is obtained by dividing out the Coulomb matrix element. For q near the Bragg condition (q=0 r.l.u), dividing out the matrix element creates an artificial suppression of spectral weight at low energy and an artificial enhancement of spectral weight at high energy. For momenta not near the Bragg condition, the effect of dividing out the coulomb matrix element is negligible.

from the instrument, the broader the collective excitation peaks. Because we can not separate the instrument effects from the intrinsic physics, we can instead determine a convolved prefactor in the cross section that accounts for both effects. This method was briefly touched upon in [50] and has been developed further by Christian Boyd and Luke Yeo in Phillips Philips group at UIUC. I have worked in collaboration with Christian and Luke to implement this resolution-broadened cross section for M-EELS data. This is still a work in progress, however I will provide a summary of what has been done thus far.

This modification takes a convolution of the original coulomb propagator with the energy and momentum

resolution of the instrument as shown by:

$$\frac{\partial^2\sigma}{\partial\Omega\partial E} = \int_{-\infty}^{\infty}\int_{-\infty}^{\infty} f(\mathbf{q}',\omega')\sigma_{\mathbf{0}}(\omega-\omega')\mathbf{V}^{\mathbf{2}}_{\text{eff}}(\mathbf{q}-\mathbf{q}',\omega-\omega')\mathbf{S}_{\mathbf{S}}(\mathbf{q}-\mathbf{q}',\omega-\omega')\,\mathbf{dq}'\,\mathbf{d}\omega' \tag{2.31}$$

where the momentum resolution, Δq, and the energy resolution, $\Delta\omega$, are contained in the resolution function, $f(\mathbf{q},\omega)$.

This can be rewritten in terms of the surface density response function using Equation 2.21

$$\frac{\partial^2\sigma}{\partial\Omega\partial E} = \int_{-\infty}^{\infty}\int_{-\infty}^{\infty} f(\mathbf{q}',\omega')\sigma_{\mathbf{0}}(\omega-\omega')\mathbf{V}^{\mathbf{2}}_{\text{eff}}(\mathbf{q}-\mathbf{q}',\omega-\omega')\eta(\omega-\omega')\chi''_{\mathbf{S}}(\mathbf{q}-\mathbf{q}',\omega-\omega')\,\mathbf{dq}'\,\mathbf{d}\omega' \tag{2.32}$$

where $\eta(\omega) = 1/\pi(1-e^{-\hbar\omega/k_BT})$ is the Bose factor.

There are many assumptions we can make to simplify this statement. The first is that we can assume that $V^2_{\text{eff}}(\mathbf{q},\omega)$ does not depend on energy, which is true for most of the Brillouin zone far from the Bragg conditions. We also assume that the resolution function is separable, $f(\mathbf{q},\omega) = \mathbf{h}(\mathbf{q})\mathbf{g}(\omega)$, i.e., that the energy resolution is not dependent on the momentum resolution and vice versa.

To normalize $\chi''_S(\mathbf{q},\omega)$ at all momenta, we use an f-sum rule. The charge response function f-sum rule is defined as,

$$\int d\omega\ \omega\chi''(\mathbf{q},\omega) = -\frac{\hbar^{\mathbf{2}}\mathbf{q}^{\mathbf{2}}\mathbf{N}}{\mathbf{m}} \tag{2.33}$$

where N is the electron number density and m is the mass of electrons. Or written another way,

$$\int d\omega\ \omega\frac{\chi''(\mathbf{q},\omega)}{\mathbf{q}^{\mathbf{2}}} = \int \mathbf{d}\omega\ \omega\chi''_{\mathbf{sumrule}}(\mathbf{q}=\mathbf{0},\omega) = \mathbf{Constant} \tag{2.34}$$

In addition we can say that $\chi''_{sumrule}(\mathbf{q},\omega)$ is not rapidly changing in $\mathbf{q}$ such that $\chi''_{sumrule}(\mathbf{q}\neq 0,\omega) \sim \chi''_{sumrule}(\mathbf{q}=0,\omega)$ and can be factored out of the integral. Rewriting Equation 2.32 with these assumptions:

$$\frac{\partial^2\sigma}{\partial\Omega\partial E} = \int_{-\infty}^{\infty}\eta(\omega-\omega')\sigma_0(\omega-\omega')\chi''_{S,sumrule}(\omega-\omega')g(\omega')\,d\omega'\int_{-\infty}^{\infty}\mathbf{V}^{\mathbf{2}}_{\text{eff}}(\mathbf{q}-\mathbf{q}')|\mathbf{q}-\mathbf{q}'|^{\mathbf{2}}\mathbf{h}(\mathbf{q}')\,\mathbf{dq}' \tag{2.35}$$

We can further simplify this by recognizing that $\Delta\omega/\omega << 1$. On average, the energy resolution off a sample is approximately 6 meV. However we measure features in $\chi''_{S,sumrule}(\omega)$ that are larger than the resolution and that do not radically change on the scale of 6 meV. Therefore the effect of convolving the energy resolution with $\chi''_{S,sumrule}(\omega)$ is negligible for the energy ranges of interest in experiments. For momentum, this is not the case. At low momentum close to the Bragg condition, $V_{\text{eff}}(\mathbf{q},\omega)$ does not vary slowly and cannot be factored out the way $\chi_{S,sumrule}$ can. Therefore a convolution of the resolution with the matrix elements is needed to take into account true experimental factors.

Finally, we have the form,

$$\frac{\partial^2\sigma}{\partial\Omega\partial E} = \eta(\omega)\sigma_0(\omega)\chi''_{S,sumrule}(\omega)\int_{-\infty}^{\infty} V_{\text{eff}}^2(\mathbf{q}-\mathbf{q}')|\mathbf{q}-\mathbf{q}'|^2 h(\mathbf{q}')\,\mathbf{dq}' \tag{2.36}$$

where $h(\mathbf{q})$ is the momentum resolution function given by a Lorentzian. This momentum resolution function is measured off each sample surface along one direction (see Figure 2.7 $\omega = 0$ momentum scan along (H,0) momentum direction). It is assumed that the resolution is isotropic so we can use the same resolution function along the (K,0) momentum direction. The FWHM of the Lorentzian represents the momentum resolution of experiment since it incorporates the effect of the sample surface quality.

From this, we have defined a resolution-broadened Coulomb matrix element which is a convolution of the DWBA Coulomb matrix element with a resolution function which smears the near-Bragg momentum divergence.

$$V_{broadened}^2 = \int_{-\infty}^{\infty} V_{\text{eff}}^2(\mathbf{q}-\mathbf{q}')|\mathbf{q}-\mathbf{q}'|^2 h(\mathbf{q}')\,\mathbf{dq}' \tag{2.37}$$

Using $SrTiO_3$ lattice parameters (a=b=c=3.905 $\mathring{A}$), and fixed out-of-plane momentum, $q_\perp = 4.02\mathring{A} = 2.5 r.l.u.$ and variable θ, γ, and ω, Figure 2.6 shows what happens to the Coulomb matrix element when resolution effects are taken into account, specifically for the q = 0 case for a variety of Δq.

The effect is significant at q=0, where the non-resolution-broadened Coulomb matrix element scales as ω^{-4}. When convolved with lortentzian resolution functions, this scaling deviates from a ω^{-4} power law behavior to behavior that has a weaker dependence on energy and doesn't diverge as ω approaches zero. For finite q we expect this resolution broadening to have a smaller effect. This is because V_{eff}^2 is a slower function of ω at larger q, so broadening has less of an effect. For most sample surfaces, the momentum resolution will range from 0.03-0.07 r.l.u (0.05-0.11 $\mathring{A}^{-1}$ for $SrTiO_3$). As shown in Figure 2.6, this range of resolutions correspond to a regime where $V_{\text{broadened}}^2$ is weakly energy dependent.

Figure 2.7 is an example of $SrTiO_3$ data both with the resolution-broadened and non-resolution-broadened matrix elements divided out. From this it is evident that the resolution-broadened matrix elements dampen the divergence at q=0. For small finite q, the resolution-broadened Coulomb matrix elements continues to have a small energy dependence as compared to the non-resolution-broadened term. At large finite q, the raw data, Coulomb matrix element, and resolution-broadened Coulomb matrix elements are all identical which is expected.

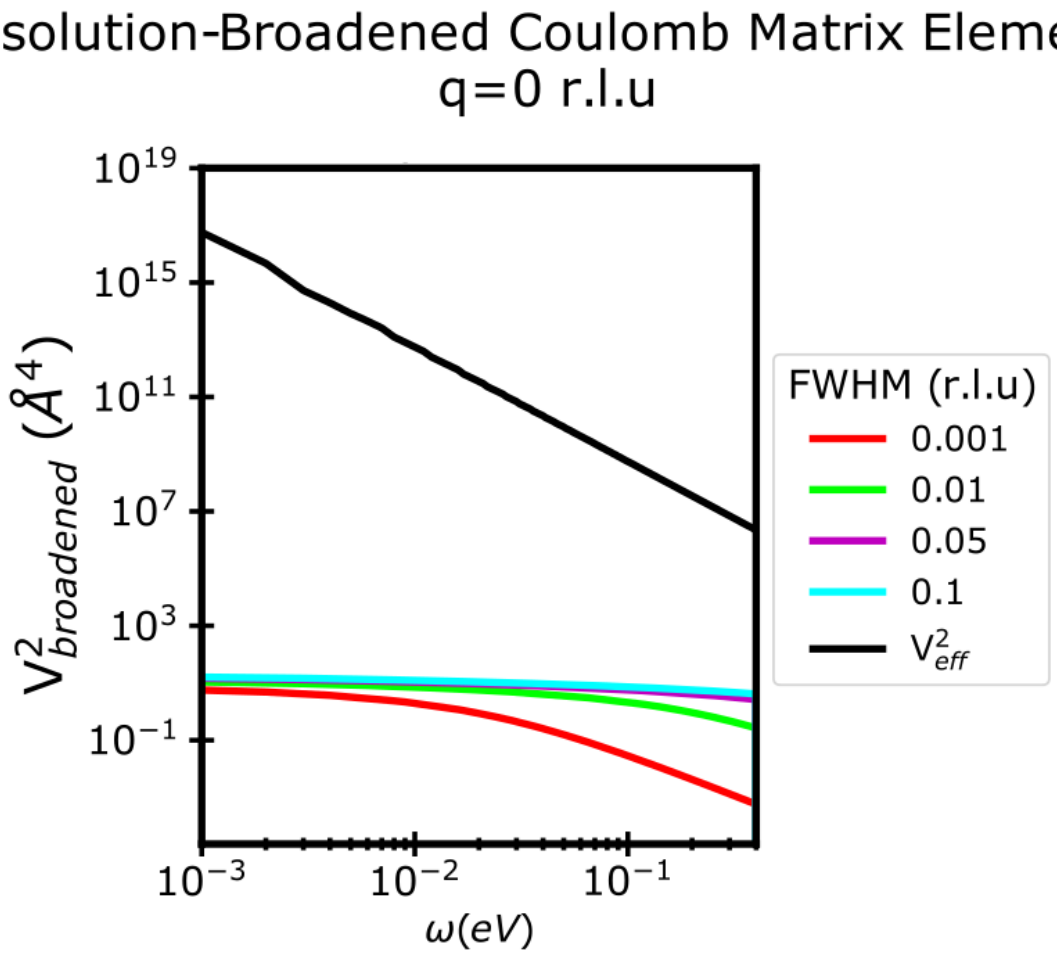

Figure 2.6: **Resolution-Broadened Coulomb Matrix Elements**
Resolution-broadened Coulomb matrix elements at q=0 for several values of momentum resolution (as determined by the FWHM of the Bragg peak) plot on a log-log scale. The non-resolution-broadened Coulomb matrix element is shown in black and diverges as ω goes to zero with ω^{-4} dependence. In most experiments, the resolution off a sample has a FWHM in the range of 0.03-0.07 r.l.u. The resolution-broadened Coulomb matrix elements is less energy dependent than the unbroadened case.

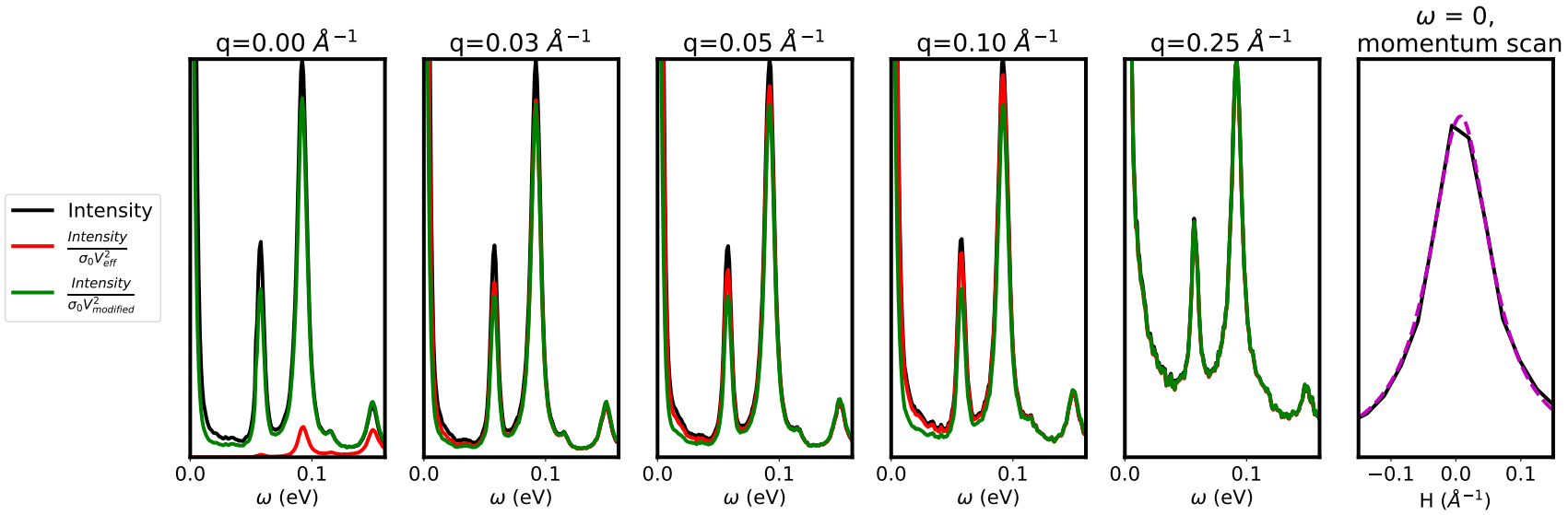

Figure 2.7: **Resolution-Broadened Coulomb Matrix Elements Applied to M-EELS Data**
Here we show the effect that the Coulomb matrix element has on $SrTiO_3$ data at several momentum in the Brillouin zone. The spectra in black is the raw M-EELS intensity, the red spectra is the M-EELS $SrTiO_3$ data divided by the Coulomb matrix element, the green spectra is the M-EELS $SrTiO_3$ data divided by the resolution-broadened Coulomb matrix elements. The subplot on the right is a scan of the (0,0) Bragg peak, the FWHM of which is the momentum resolution off the sample and is used in convolving the matrix elements with the resolution function as shown in 2.37.

Chapter 3

Experimental Setup

To test the concepts addressed in the introduction, we need a technique that can measure the momentum dependence of the collective electronic modes with meV resolution. To do this, we employ the technique of momentum-resolved electron energy loss spectroscopy (M-EELS). Unlike inelastic x-ray scattering or neutron scattering, which are most sensitive to lattice excitations, inelastic electron scattering is highly sensitive to valence charge excitations [21] and is therefore an ideal technique to study the electronic collective modes. **Using M-EELS, we aim to identify the role of electronic collective modes in a selection of materials exhibiting strong electron-electron interaction by measuring their dispersions as a function of temperature and carrier density.**

In this chapter, I give a brief description of the M-EELS setup followed by an explanation of what makes M-EELS distinct from HR-EELS. Next I will describe the electron optics setup as well as the new procedure that I implemented for optimizing the electron beam. The electron optics discussion will also include a detailed characterization of our in-lab instrument as compared to theoretical expectations. Following that, I will discuss sample preparation, including a novel preparation technique for non-2D layered materials. Finally I will address several of the instrumentation upgrades that I have designed and implemented over the course of my graduate degree.

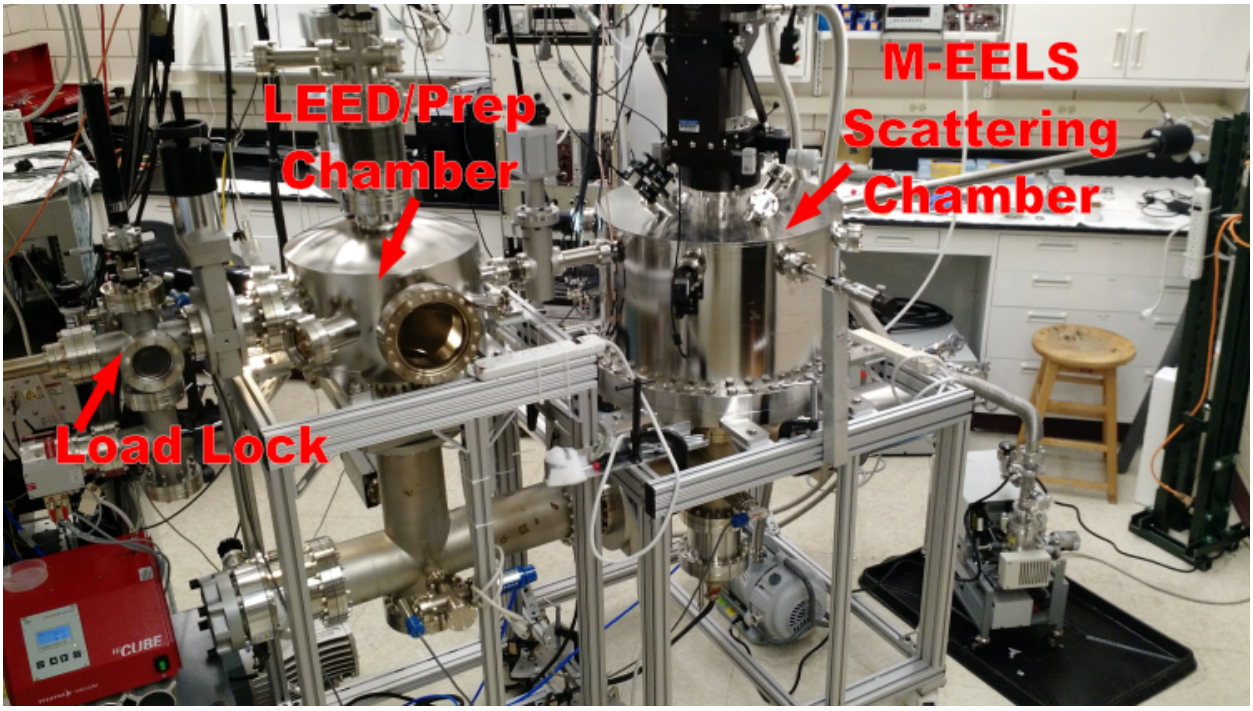

Figure 3.1: **M-EELS Laboratory Setup**
Photograph of the M-EELS experimental setup circa 2017. The M-EELS setup consists of three ultra high vacuum chambers: loadlock, LEED/prep chamber, and the main M-EELS chamber.

3.1 M-EELS Experimental Setup

3.1.1 Physical Setup

Our M-EELS system uses an Ibach-like electrostatic spectrometer that is commercially available (LK Technologies ELS5000) and is most commonly used for HR-EELS surface science measurements (3.2). By mating this spectrometer to a multi-axis sample goniometer (Figure 3.2) and properly aligning all the rotation axes with the sample orientation (as is done in other momentum resolved techniques such as inelastic x-ray scattering and neutron scattering), we can achieve a true momentum-resolved inelastic electron scattering measurement.

The left side of Figure 3.2 shows, the main components of the Ibach style spectrometer [51]: a LaB_6 filament, double pass monochromator, single pass analyzer, and Channeltron point detector. When current is passed through the filament, the LaB_6 material heats up and emits electrons that then pass through a double monochromator - setting the incident beam energy - before scattering off the sample. After scattering, the electrons pass through an analyzer that selects the final energy to measure. The scattered electrons with that final energy are then detected as pulses by a Channeltron point detector. The pulses are converted into intensity (counts) for each energy loss value. Electrostatic lenses are used to focus the incident electron

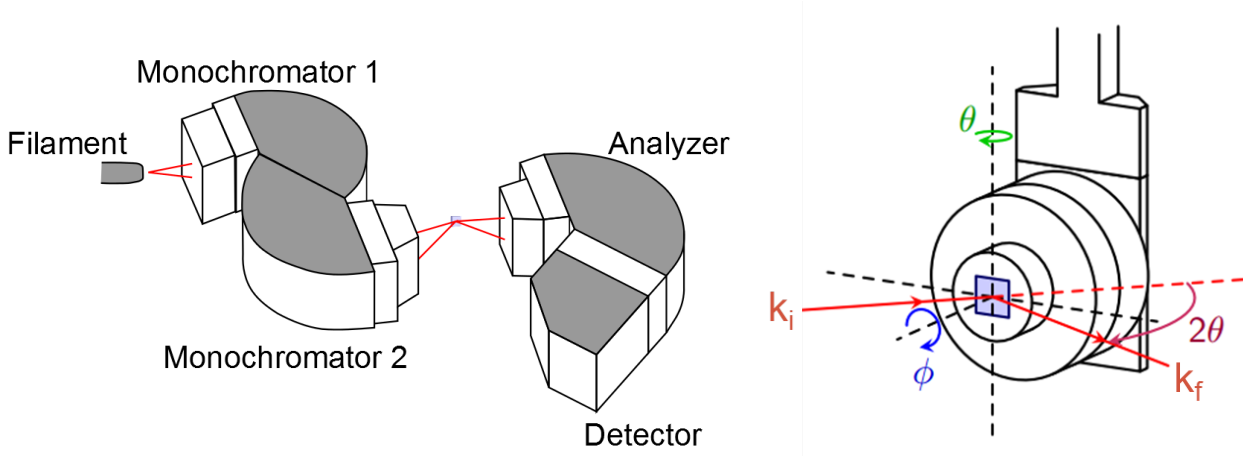

Figure 3.2: **Spectrometer and Goniometer Cartoon**
Cartoon representation of the M-EELS Spectrometer (on left) and the five-axis sample goniomenter (on right). The EELS Spectrometer is composed of electrostatic lenses that steer the beam, set the energy of the incident and scattered electrons, adjusts the energy and momentum resolution of the beam, and sets the rotation of the analyzer (γ). The five-axis goniometer rotates the sample and defines the scattering angles (θ,ϕ). θ, γ set the incident and scattered momenta ($k_{i,s}$) and ϕ sets the scattering direction (H,K) of the crystal. Figure from [36] [35].

beam on the sample and the scattered electrons on the detector. These lenses get tuned every day to account for small drifts in the beam. The energy resolution of this instrument can be as low as 0.5 meV however for the experiments in this thesis, the energy resolution at 50eV incident beam energy is around 5meV.

The HR-EELS system and goniometer have been modified to motorize the rotation of the analyzer (γ) and the rotation of the sample (θ, ϕ). The motorization of γ, θ, and ϕ improve the reproducibility and accuracy of the momentum transfer as compared to HR-EELS.

The entire spectrometer and goniometer setup operates inside an ultra-high vacuum (UHV) chamber that is lined with double mu-metal shielding to reduce the magnitude of external magnetic fields in the scattering chamber to less than 10 mG. In addition, the multi-axis goniometer is attached to a liquid-helium cryostat currently allowing us to cool a sample to 22 K. For the data shown in this thesis, the UHV pressure is on the order of 10^{-11} Torr.

Figure 3.1 is a photo of the M-EELS system at the University of Illinois. There are three vacuum sections of this experimental apparatus:

Load lock

The load lock chamber is where we load the prepped samples into the instrument and pump down from atmospheric pressure to high vacuum (on the order of 10^{-8} Torr). This chamber includes a sample magazine, that I designed and implemented, which enables us to pump down five prepped samples at one time. In

addition, the load lock has also been upgraded to transfer thin film samples using a vacuum suitcase that attaches to a molecular beam epitaxy (MBE) chamber. More information on this hardware can be found in Section 3.2

Sample Prep Chamber

Once the prepped samples are pumped down to 10^{-8} Torr in the loadlock, they can then be transferred to the LEED/prep chamber using magnetic UHV grippers. This chamber is further pumped on to obtain an UHV pressure of 5x10^{-10} Torr. In this chamber, prepped samples are cleaved to expose a clean surface. The chamber also includes a Low-Energy Electron Diffraction (LEED) unit which is used to check the crystallographic quality of the surface, informing us of the quality of the cleave.

One future upgrade to this chamber is an annealing stage which will allow us to prepare clean sample surfaces without cleaving. The design for an annealing stage is discussed in Section 3.2.

M-EELS Chamber

After cleaving, the sample is transferred to the main experimental chamber that contains the M-EELS spectrometer. The sample is placed in a copper seat that sits on a attocube peizo motor (for ϕ rotation) at the bottom of the cryostat. This chamber is also equipped with a cyropump and titanium sublimation pump achieving pressures of 8x10^{-11} Torr.

Electronics

The control electronics residing outside these vacuum chambers are used to scan the M-EELS lens voltages, amplify and count the single electron pulses, and control the sample motions. For detailed description of electronics see other theses from the Abbamonte Group [34, 36].

3.1.2 Sphere of Confusion

What differentiates M-EELS from conventional HR-EELS instruments is its high momentum accuracy. In order to achieve the most accurate momentum measurements, the incident electron beam, γ (detector), θ (sample), and ϕ (the sample orientation) must all intersect at a single point. Deviations from this point, map out a "sphere of confusion" whose volume sets the momentum accuracy of the instrument (see Figure 3.3). Common sample manipulators do not take into account whether the sample lies in the center of rotation, therefore the sample moves in space as it rotates. This misalignment can be as large as several

millimeters [34]. The motorized degrees of freedom allow us to minimize the volume of the sphere of confusion distinguishing this technique from HR-EELS.

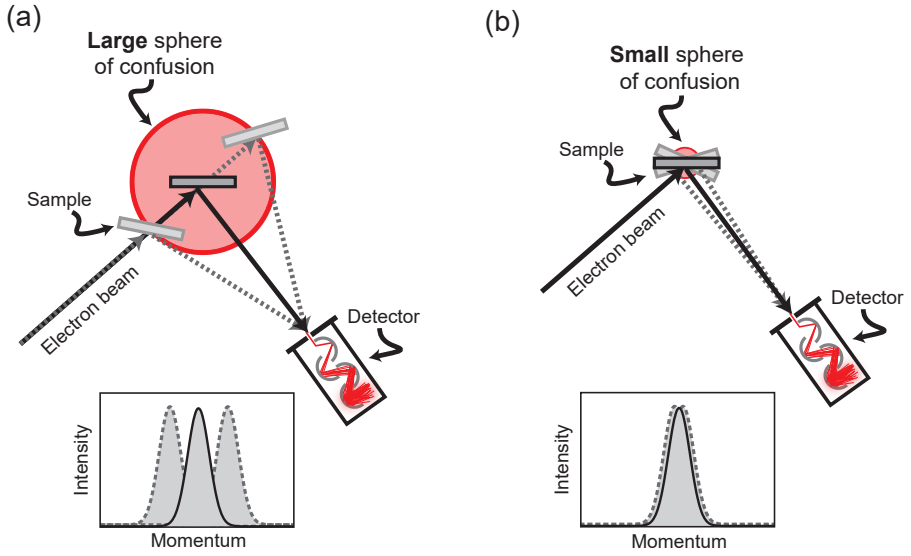

Figure 3.3: **Sphere of Confusion**
If a sample is not located in the center of rotation of the goniometer (θ) and analyzer (γ), it will move in space as it rotates, mapping out a "sphere of confusion". (a) When the sphere of confusion is large, the momentum inaccuracy is large meaning that it is difficult to know where you are in momentum space. This is common in HR-EELS experiments. (b) As you reduce the size of the sphere of confusion, the momentum transfer becomes more accurate. This momentum accuracy is unique to M-EELS and differentiates it from HR-EELS techniques. Figure reproduced from [34]

The theoretical momentum resolution is 0.03 $\mathring{A}^{-1}$. Additionally, we identify two non-collinear Bragg peaks (e.g. (1,0) and (0,1)) from a sample and construct an *in situ* orientation matrix that translates between the motor angles and reciprocal space. This is what makes our M-EELS system "momentum-resolved".

These motorized rotations and sample alignment method determine the momentum accuracy of the instrument. However the momentum precision and resolution are determined by the electron optics. In the next section, we will discuss the details that go into optimizing the electron optics in order to improve the energy and momentum resolution of the device.

3.1.3 Electron Optics Characterization

The electron optics that steer and focus the electrons from the source to the detector consists of an emission system, premonochromator, monochromator, focusing lens system, energy analyzer, and electron detector as shown in Figure 3.4. Theoretical calculations and numerical simulations of the electron optics components can be found in [52]. In addition to the theory associated with electron spectrometers, it is useful to have

a detailed characterization of the electron optics configuration that is specific to our laboratory M-EELS set-up. Characterizing the electron optics can help us systematically optimize our in-lab spectrometer to improve electron throughput, energy resolution, and momentum resolution.

In this section, I will provide a detailed description of all the electron optics components. Specifically, I will provide calculations and reference data to characterize the electron beam at various points along the electron path. These characterization tools can be used in the future to optimize, document, and streamline the beam tuning process.

Throughout this section, I include data from both an ideal electron optics configuration (which I refer to as the "aligned" configuration) as well as data from a non-ideal electron optics configuration (which I refer to as the "misaligned" configuration). In the aligned setup, the electron beam is focused on the entrance slit of the pre-monochromator. In the misaligned setup, the electron beam focus is not positioned at the entrance slit of the pre-monochromator. This is represented in Figure 3.4, which points out the different paths the electron beam can take for the aligned and misaligned voltage configurations. In both of these configurations, we optimize for current and energy resolution at the detector. However in the misaligned configuration, electron throughput and energy resolution are negatively impacted by the non-ideal voltage configuration. Although this section defines a non-ideal voltage configuration as misalignment of the focus on the pre-monochromator slit, this is just one example of a non-ideal configuration. In reality there can be many non-ideal voltage configurations that have different adverse effects on the electron behaviour.

In addition to discussing the general behavior of the electron optics system, I have included lens reference scans for two different tuning optimizations. These figures can be found in Appendix A and provide a guide to how the electrostatic lenses behave with the hope that they can be a useful reference for future M-EELS spectrometers and lens tuning procedures.

Table 3.1 lists the currents obtained at various points along the electron path (relays) for three different beam tuning configurations. The manufacturer settings used a beam energy of 100 eV, while the tune configurations measured by our group in 2018 and 2020 were taken with a beam energy of 50 eV. All of the tuning configurations in this table were taken with the filament power set to approximately 5 W (1.7 A, 3.0 V).

Emission System

The emission system consists of a LaB_6 filament, repeller, and Einzel lens system. As shown in the electron optics diagram of Figure 3.4, the Einzel lens have three, split lenses that are labeled as A1, A2, A3, and that set the mean voltage on each lens. Each of those voltages also has a Δ value that sets the spread of

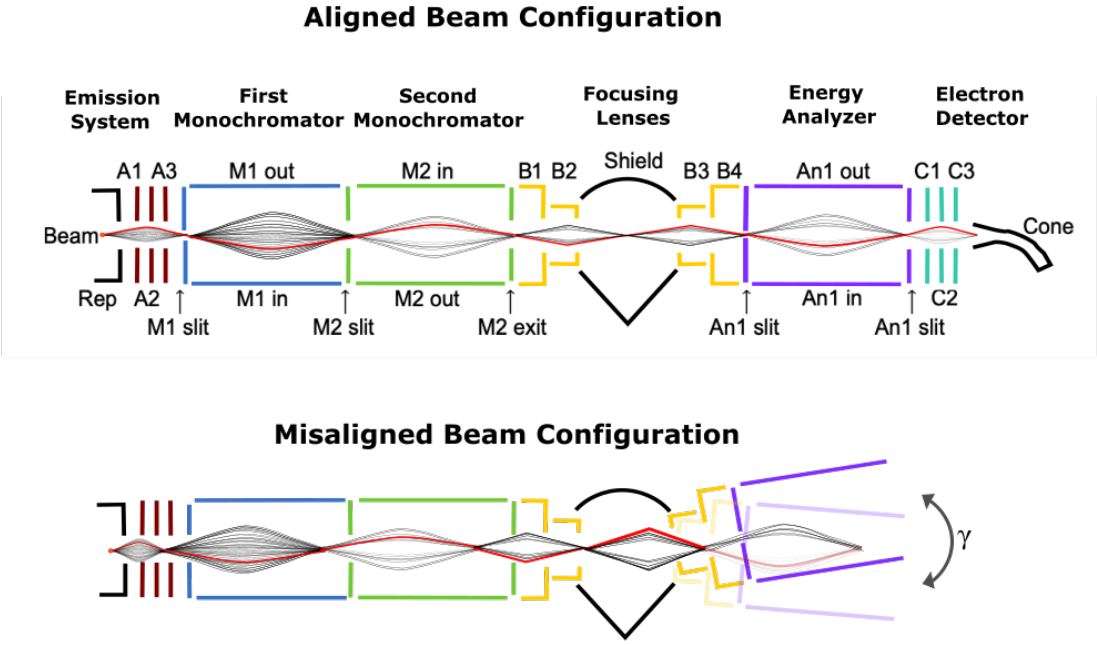

Figure 3.4: **Electron Optics Cartoon**
Cartoon of the electron trajectory for two different lens configuration. In the aligned configuration, the electron beam is focused on all the lens slits, starting from the A lenses focusing the beams on the entrance to the premonochromator. The misaligned cartoon is an example of voltage configuration where the electron beam is not focused on the lens slits. In this configuration, the A lenses do not focus on the premonochromator entrance slit and this can lead to multiple beam profiles when rotating the analyzer (γ).

Table 3.1: **Current Along Electron Path**

Relay	Manufacturer Settings (100eV)	2018 (50eV)	2020 (50eV)
Premonochromator entrance slit	10 μ A	6.6 μ A	-
Premonochromator outer plate	500 nA	700 nA	390 nA
Monochromator outer plate	1 nA	1 nA	860 pA
Monochromator exit slit	0.98 nA	1 nA	-
Analyzer entrance slit	-	-	164 pA
Analyzer outer plate	102 pA	400 pA	79 pA
Detector entrance	35 pA	40-80 pA	30 pA

voltages on the lens, which is used to steer the beam. The A lenses have delta voltages that steer the beam vertically (ΔA2) and horizontally (ΔA1 and ΔA3).

When current is passed through the filament, the LaB_6 material heats up and emits electrons. We can characterize the temperature of the filament by measuring the energy distribution leaving the premonochromator. Using the first sector of the monochromator, we can measure the kinetic energy spread of the electrons emitted by the filament. Figure 3.5 shows the energy distribution leaving the first monochromator both for

a beam energy of 100 eV and 7 eV, fit with a Maxwell Boltzman- equation. From this we determine the filament temperature to be 1800K which is comparable to the manufacturer's specifications.

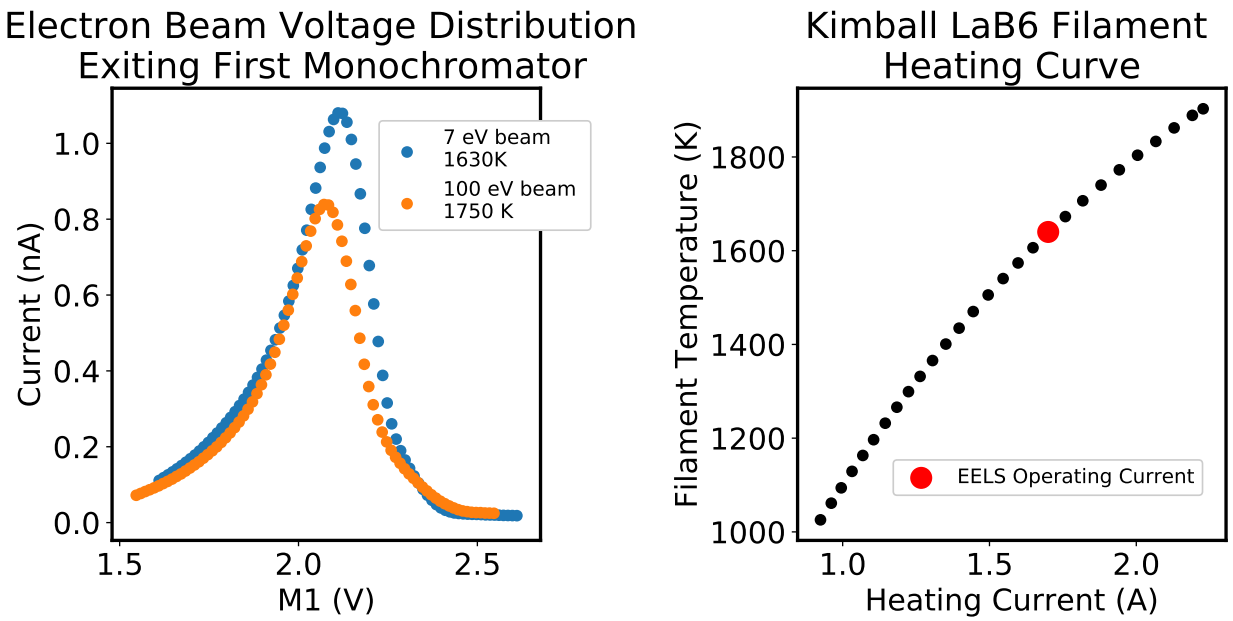

Figure 3.5: **Filament Emission**
Energy distribution leaving the first monochromator (left figure) both for a beam energy of 100 eV and 7 eV, fit with a Maxwell-Boltzman equation. From the fits we determine the filament temperature to be 1750 K and 1630 K respectively. These fit values are comparable to the manufacturer's specifications (right figure) adapted from [53]. For a heating current of 1.75 A, the filament temperature is approximately 1665 K.

The electrons that are emitted from the filament get accelerated by the repeller lens and focused onto the entrance slit of the premonochromator with the A lenses. These lenses play two major roles in the electron optics system. Firstly they focus the electrons onto the entrance slit of the premonochromator which effects the profile of the beam downstream. Secondly, the Einzel A lenses compensate for any tilt or offset in filament placement. Throughout this section, the tilt/filament offset will be represented by the angle in which electrons enter the premonochromator, α, shown in Figure 3.6.

The entrance angle of the beam is important in determining the energy resolution of the pre-monochromator as determined from Equation 3.6. Minimizing this angle improves the resolution. This angle can be non-zero due to the inaccuracy of the filament placement. The filament seat has slack to allow for an easier installation however this can create difficulties due to electrostatic lenses needing to compensate for the error in placement. The first Einzel lens, A1, can take on a large range of values from 0-70 V in order to compensate for the tilt and offset. For reference, prior to a filament replacement, A1 = 31 V but after the filament replacement A1 = 57 V. This demonstrates the large variability in voltages needed to compensate

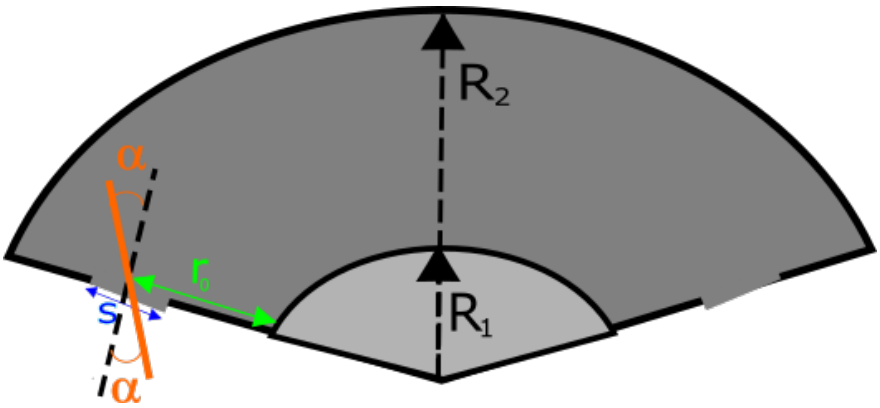

Figure 3.6: **Monochromator Geometry**
Cartoon of the cylindrical geometry of the monochromator. The angle in which electrons enter the monochromator is defined as α, the inner and outer radius of the monochromator are R_1 and R_2 respectively, the entrance slit to the monochromator has a width, s, and the mean trajectory of the electrons in the cylinder is at some radius, r_0.

for filament placement.

Following Ibach's theoretical simulations [52], the A Einzel lenses should have the following relation: $A1 < A2$, and $A3 << A2, A1$. However, this does not account for the error in filament position as our setup does. Therefore our spectrometer follows a different relation: $A3 < A2 << A1$.

Monochromator

The thermal energy distribution of s from the cathode gets fed into an antisymmetric toroidal pre-monochromator which feeds into a second monochromator. The double pass monochromator setup is the most effective way of achieving a highly monochromatic current. This has to do with the fact that the pre-monochromator reduces the space charge between electrons as well as decreases the number of spurious electrons, deflected off of the voltage plates, from going into the second monochromator.

Each monochromator consists of voltage lenses that set the pass energy (M1 for pre-monochromator, and M2 for second monochromator), control the horizontal spread of energies (ΔM1,ΔM2), Steer the electrons vertically (M1cover, M2cover), control the vertical spread of energies(ΔM1cover,ΔM2cover) and set the entrance/exit slit voltages (M1slit,M1exit=M2slit,M2exit).

For the case of cylindrical deflectors [52], the electric field between two cylindrical metal plates with an applied voltage is

$$\varepsilon_r = \frac{\Delta V}{ln(R_2/R_1)}\frac{1}{r} \tag{3.1}$$

where ε_r is the radial component of the electric field, ΔV is the voltage difference between the two plates,

R_2 is the radius of the outer cylindrical plate, and R_1 is the radius of the inner cylindrical plate as defined in Figure 3.6. Therefore an electron moving in the electric field produced by these cylindrical plates will travel along a circular path with radius r as described by

$$\frac{m\nu^2}{r} = \frac{2E_0}{r} = e\varepsilon_r \tag{3.2}$$

where E_0 is the pass energy of the electron and e is the elementary charge.

The above equations can be rearranged to get the pass energy of the electron as a function of the delta voltage between the cylindrical plates:

$$E_0 = \frac{e\Delta V}{2ln(R_2/R_1)}. \tag{3.3}$$

The coefficient, $\frac{1}{2ln(R_2/R_1)}$, is what we refer to as the geometric constant,C_{geom}, and for the values in Ibach's calculations, $\mathrm{C}_{geom} = 0.849$.

The trajectory of electrons with angle, α, starting from a radial position, y_1 (a small deviation from the center path of the cylinder, r_0), will arrive to a position y_2 such that

$$y_2 = -y_1 + r_0\frac{\delta E}{E_0} - \frac{4}{3}r_0\alpha^2 \tag{3.4}$$

where δE is the deviation from the pass energy and is directly related to the resolution of the monochromator. The energy dispersion of electrons in a cylinder with a mean trajectory around the radius, r_0 can be calculated from

$$E_0\frac{dy}{dE} = r_0. \tag{3.5}$$

Using the above equations and assumptions made in [52] we arrive at

$$\frac{\Delta E_{1/2}}{E_0} = \frac{s}{r_0} + \frac{2}{3}\alpha^2 \tag{3.6}$$

where $\Delta E_{1/2}$ is the FWHM of the transmitted beam, s is the entrance/exit slit width, r_0 is the radial position of the entrance or exit slits, the pre-factor of $\frac{2}{3}$ is due to the angular aberration due to space charge in the cylindrical geometry, and α is the angle that electrons enter the monochromator slit. Equation 3.6 defines the resolution of the monochromator in terms of the pass energy and initial angle of the electrons. Baseline resolution is determined from the geometry, $\frac{s}{r_0}$, but the resolution is worsened depending on the A lenses which set α of the incoming beam.

For cylindrical deflectors, we can analytically calculate what the voltage field that the electrons experience in their trajectory. Using Gauss's law, the electric field inside a cylindrical geometry with height, h, is

$$E = \frac{q}{2\pi h\epsilon_0 r}\hat{r} = \frac{R_1^2\sigma_1}{2\epsilon_0 r}\hat{r} \tag{3.7}$$

where σ_1 is the charge density on the inner voltage plate such that $\sigma_1 = q/\pi R_1^2 h$. The voltage difference between the inner and outer cylindrical plates is

$$\Delta V = V(R_2) - V(R_1) = -\int_{R_1}^{R_2} \frac{R_1^2\sigma_1}{2\epsilon_0 r'}\, dr' \; = -\frac{R_1^2\sigma_1}{2\epsilon_0} ln\Big(\frac{R_2}{R_1}\Big) \tag{3.8}$$

In the M-EELS setup, the voltage lens are defined as $\Delta M = V_{M,in} - V_{M,out} = V_{R_1} - V_{R_2}$. Therefore

$$\Delta M = \frac{R_1^2\sigma_1}{2\epsilon_0} ln\Big(\frac{R_2}{R_1}\Big) \tag{3.9}$$

For a radial distance, r, inside the two cylindrical plates,

$$V(r) = V(R_1) - \Delta V = V(R_1) - \frac{\Delta M ln(r/R_1)}{ln(R_2/R_1)} \tag{3.10}$$

For a toroid geometry, it is not analytically possible to calculate the voltage in the deflector. An alternative approach is to numerically solve the Laplace equation,

$$\nabla^2 V = 0 \tag{3.11}$$

given that we know the voltages at the boundary conditions (i.e. M1slit, M1in, M1out, M2slit, M2in, M2out, M2exit). Figure 3.7a and 3.8a are the numerical solutions to the Laplace equation for a cylindrical geometry given boundary conditions from our M-EELS setup. The values we get from the numerical simulation are similar to the values from the analytical solution.

We will use Equation 3.3 and Equation 3.6 and the solutions to Laplace's equations to characterize the monochromators in our M-EELS instrument. However, all the calculations above do not provide a direct comparison to the in-lab instrument due to the fact that they were derived for a cylindrical geometry while our M-EELS instrument has a toroid geometry. While analytically solving for V(r) for a toroid is not feasible, we could solve this numerically. This is more complicated than the procedure for a cylinder and is not covered in the scope of this work.

Even though it is not a direct comparison, we will still use the cylindrical equations above as a qualitative guide in characterizing the monochromators of our in-lab M-EELS. In addition to the geometric discrepancy, Ibach's calculations for pass energy and resolution are derived only for the symmetric monochromator (slit voltage = exit voltage). However, our lab instrument has both a symmetric monochromator and an asymmetric (also refered to as retarding) monochromator (slit voltage $\neq$ exit voltage), which is not accounted for in the the following characterization.

Simulating the monochromators is still a work in progress. The next steps entail numerically solving the Laplace equation for a toroid geometry and using this to ray-trace trajectories of electrons for various voltage configurations. In addition, deriving the pass energy and resolution functions for a toroid symmetric deflector and a toroid asymmetric deflector.

Premonochromator

The first stage of the double pass monochromator is the premonochromator. The premonochromator is an asymmetric deflector in that the entrance slit has a larger voltage than the exit slit. The effect of having a higher potential at the entrance slit is to provide a higher target potential for the electrons from the cathode emission system. By doing this, the amount of space charge is reduced so more current can pass through the monochromator stages [52].

Figure 3.7a is a 2D map of the voltage field for an asymmetric cylindrical deflector using voltage values used in experiments (M1slit = 0.873, M1 = 2.541, M1d = 2.998, M2slit = M1exit = -0.007). This was calculated using the numerical simulator by solving the Laplace equation in a cylindrical geometry.

Figure 3.7b shows the relationship between the pass energy and energy distribution/spread of the electrons passing through the asymmetric monochromator. The slope of which is the geometric constant as defined in equation 3.3. These data were collected for both the aligned configuration and the misaligned configuration. Fitting to a line, $C_{geom} = 0.457 \pm 0.027$ for when the electron beam is focused on the slits of the monochromator and $C_{geom} = 0.560 \pm 0.025$ when the electron beam focus is not aligned with the slits.

The value of C_{geom} deviates from Ibach's calculation of 0.85 possibly due to the fact that we have a toroidal deflector and because of the asymmetric entrance/exit slits. In addition, the value of C_{geom} changes when we change the alignment of the A lenses. This implies that the geometric constant is not just dependent on the geometry of the monochromator but also on information about the incoming electron beam. This deviates from Ibach's calculations and should be explored further but most likely has to due with the asymmetric aspect of the lenses not taken into account.

Figure 3.7c is a plot of the FWHM of the transmitted beam versus the energy distribution/spread of the electrons passing through the asymmetric monochromator, the slope of which is $\frac{s}{r_0} + \frac{2}{3}\alpha^2$ as defined in equation 3.6. In theory one can solve for α to back track the incoming angle of the electron beam. Again, equation 3.6 was derived for the case of the symmetric cylindrical deflector so calculating α using these equations does not make sense. Below 2.6V in the energy distribution, we see that the slope reverses sign. This is not understood and deviates from Ibach's equations.

Asymmetric Monochromator

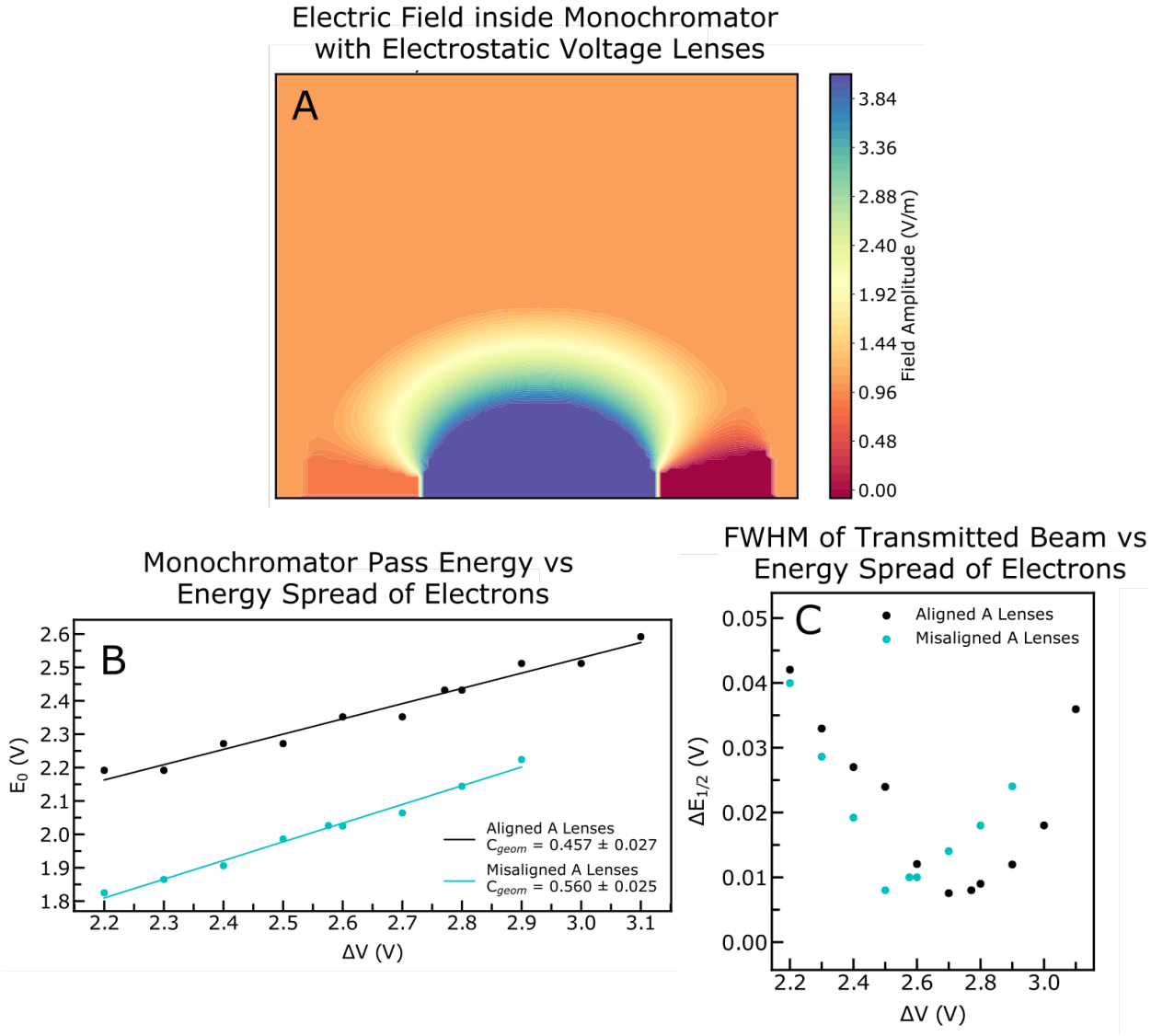

Figure 3.7: **Asymmetric Monochromator**
In an asymmetric deflector, the entrance slit has a larger voltage than the exit slit. This helps to reduce space. (A) 2D map of the voltage field for an asymmetric cylindrical deflector calculated using the numerical simulator for solving the Laplace equation in a cylindrical geometry. The boundary conditions used in this simulation are M1slit = 0.873, M1 = 2.541, M1d = 2.998, M2slit = M1exit = -0.007. (B) To determine the geometric constant, we meausure the slope of the pass energy vs energy distribution/spread of the electrons passing through the asymmetric monochromator (Equation 3.3). When the A lenses are aligned, $C_{geom} = 0.457 \pm 0.027$. When the A lenses are misaligned, $C_{geom} = 0.560 \pm 0.025$. (C) Measured FWHM of the transmitted beam versus the energy distribution of the electrons passing through the asymmetric monochromator. This relationship can be compared to Equation 3.6 to determine the angle α.

Second Monochromator

The second stage of the double pass monochromator is a symmetric deflector meaning that the entrance slit has the same voltage as the exit slit. Since the asymmetric pre-monochromator reduced the space charge,

this is no longer an issue for the second monochromator. This monochromator therefore serves the sole purpose of better refining the energy bandwidth and in turn improving the resolution.

Figure 3.8a is a 2D map of the voltage field for an symmetric cylindrical deflector using voltage values used in experiments (M1slit = -0.007, M1 = 1.604, M1d = 1.500, M2slit = M1exit = -0.007).

Figure 3.8b shows the relationship between the pass energy and energy distribution/spread of the electrons passing through a symmetric monochromator, the slope of which is the geometric constant as defined in equation 3.3. These data were collected for both the aligned configuration and the misaligned configuration. Fitting to a line, $C_{geom} = 0.367 \pm 0.004$ for when the electron beam is focused on the slits of the monochromator and $C_{geom} = 0.392 \pm 0.005$ when the electron beam focus is not aligned with the slits. C_{geom} does not change much with energy distribution (or α), implying that this toroidal monochromator has a C_{geom} that is solely based on geometry as indicated in Ibach. This can be compared to the theoretical calculation from Ibach's Equation 3.3 using r_0 and s taken from our geometry (red line). Our measured value of C_{geom} is different from theoretical value of 0.851 most likely due to the fact that we have a toroid geometry and this theoretical line is for the cylindrical geometry. For the symmetric monochromator, the alignment of the A lenses has a smaller effect on the value of C_{geom} than it did for the asymmetric deflector. This could be because the second monochromator is further down the electron path so the effect of misalignment is felt less or corrected for by previous lenses.

Figure 3.7c is a plot of the FWHM of the transmitted beam versus the energy distribution/spread of the electrons passing through the asymmetric monochromator the slope of which is $\frac{s}{r_0} + \frac{2}{3}\alpha^2$ as defined in equation 3.6. This is plotted against the theoretical expectation when assuming that α is very small for the cylindrical geometry. The magnitude of $\Delta E_{1/2}$, matches the value from Ibach and is more comparable to the theory than for the asymmetric deflector.

To summarize, the equations derived in a cylindrical goemetry are more consistent with a toroidal geometry in a symmetric monochromator. For the symmetric toroid monochromator, the resolution behaved comparably to the expected behavior in Equation 3.6. In addition, the geometric constant remained independent of geometry. These were not the case for the asymmetric toroid monochromator. This implies that either the equations capture the symmetric case despite the geometry or that the order of the monochromators (asymetric first, symmetric second) matters (i.e. we can correct for these deviations along the electron path).

Symmetric Monochromator

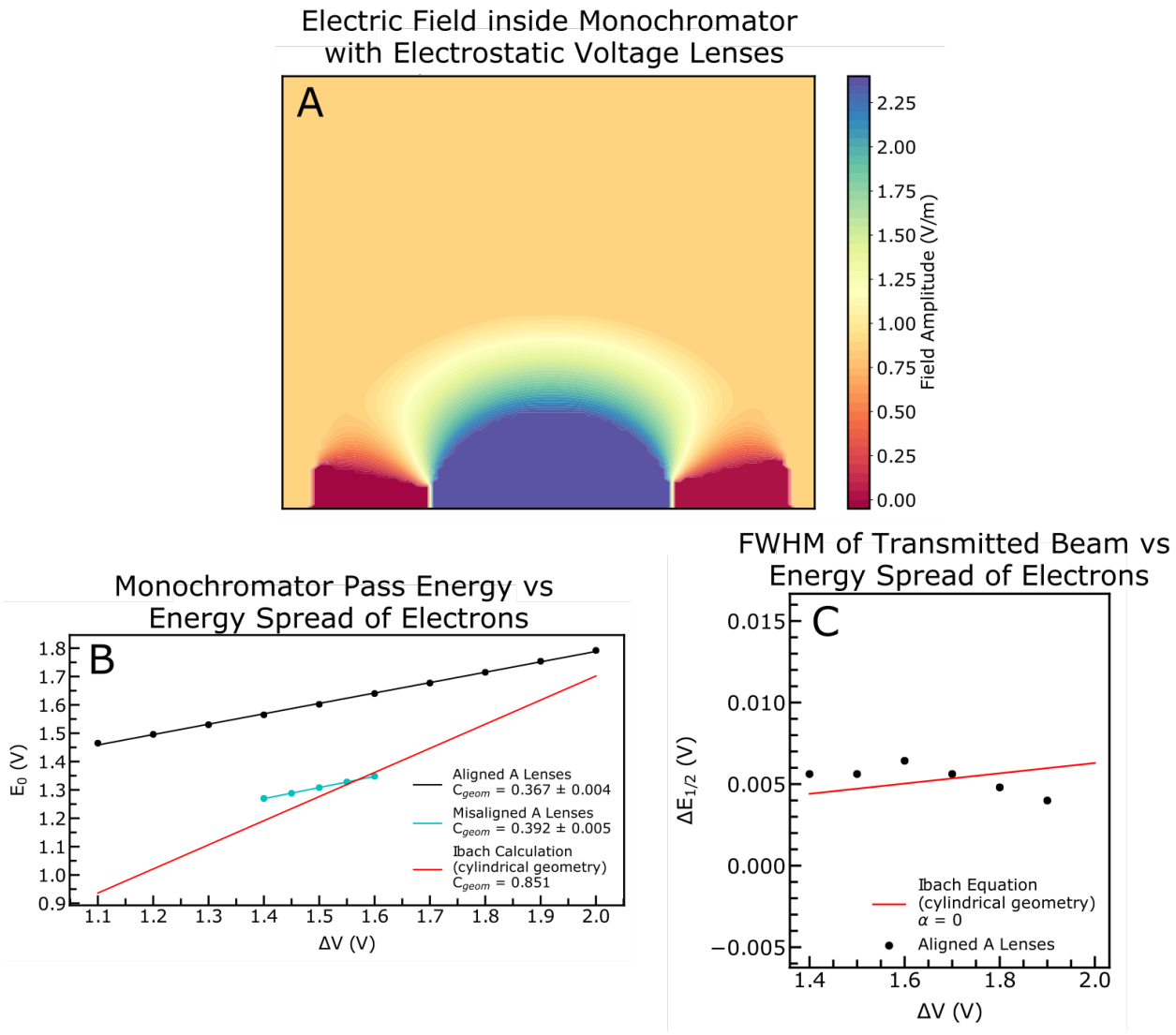

Figure 3.8: **Symmetric Monochromator**
In an symmetric deflector, the entrance slit voltage is equal to the exit slit voltage. (A) 2D map of the voltage field for an symmetric cylindrical deflector calculated using the numerical simulator for solving the Laplace equation in a cylindrical geometry. The boundary conditions used in this simulation are M1slit = -0.007, M1 = 1.604, M1d = 1.500, M2slit = M1exit = -0.007. (B) To determine the geometric constant, we measure the slope of the pass energy vs energy distribution/spread of the electrons passing through the symmetric monochromator (Equation 3.3). When the A lenses are aligned, $C_{geom} = 0.367 \pm 0.004$. When the A lenses are misaligned, $C_{geom} = 0.392 \pm 0.005$. These are compared to the theoretical value of $C_{geom} = 0.851$ [52]. (C) Measured FWHM of the transmitted beam versus the energy distribution of the electrons passing through the symmetric monochromator. This relationship can be compared to Equation 3.6 to determine the angle α. This is compared to theory for the case where $\alpha = 0$ [52].

Focusing Lenses

The focusing lenses (i.e. zoom lenses) come in two sets: B1 and B2 which accelerate and focus the outgoing monochromator beam onto the sample and B3 and B4 which decelerates the electrons and focuses the beam on the entrance to the analyzer. For this work, the electrons are accelerated to reach a beam energy of 50 eV.

Figure 3.9 is a 2D mapping of the beam as γ is rotated for various configurations of the zoom lenses. This measurement was taken for both the aligned and misaligned geometries with current measured at the entrance to the analyzer. For the misaligned configuration, there are two beams paths in the γ profile. This is expected behavior when an electron beam in not focused on the entrance/exit slits of various electron optics components just as demonstrated by the cartoon Figure 3.4.

Tuning the focusing lenses can partially compensate for the poor imaging from the Einzel A lenses. Decreasing B1(and B4) shifted the center of the two electron paths to become closer together in *gamma* until they formed a very broad peak.

In an ideal imaging configuration with aligned A lenses, adjusting the focusing lenses can increase counts and resolution without affecting the beam path. This is what is expected behavior of these lenses.

Energy Analyzer

The electron optics of the energy analyzer are identical to that of the second monochromator. The scattered beam from the sample is dispersed and the exit slit sets the electron energy that will traverse the analyzer and arrive at the detector.

The analyzer consists of voltage lenses that set the pass energy (An1), control the horizontal spread of energies (ΔAn1), Steer the electrons vertically (An1cover), control the vertical spread of energies(ΔAn1cover) and set the entrance/exit slit voltages (An1slit,An1exit).

As part of the daily tuning procedure, the beam current as a function of γ and energy loss is measured that the entrance of the detector. The phase-space tuning method [34,35], dictates the true energy resolution of the beam as compared to just measuring the resolution for a single value of γ.

Fig 3.10 is an example of these γ-eloss map for both the aligned and misaligned configurations. In the aligned scenario the resolution of the beam is 6meV (taken from the integrated FWHM of the beam profile) and does not have a large dependence on γ as is expected [34, 35]. In the misaligned case, the integrated FWHM is 12meV (Figure 3.10) due to the large dependence of energy onγ. This behavior is described as a

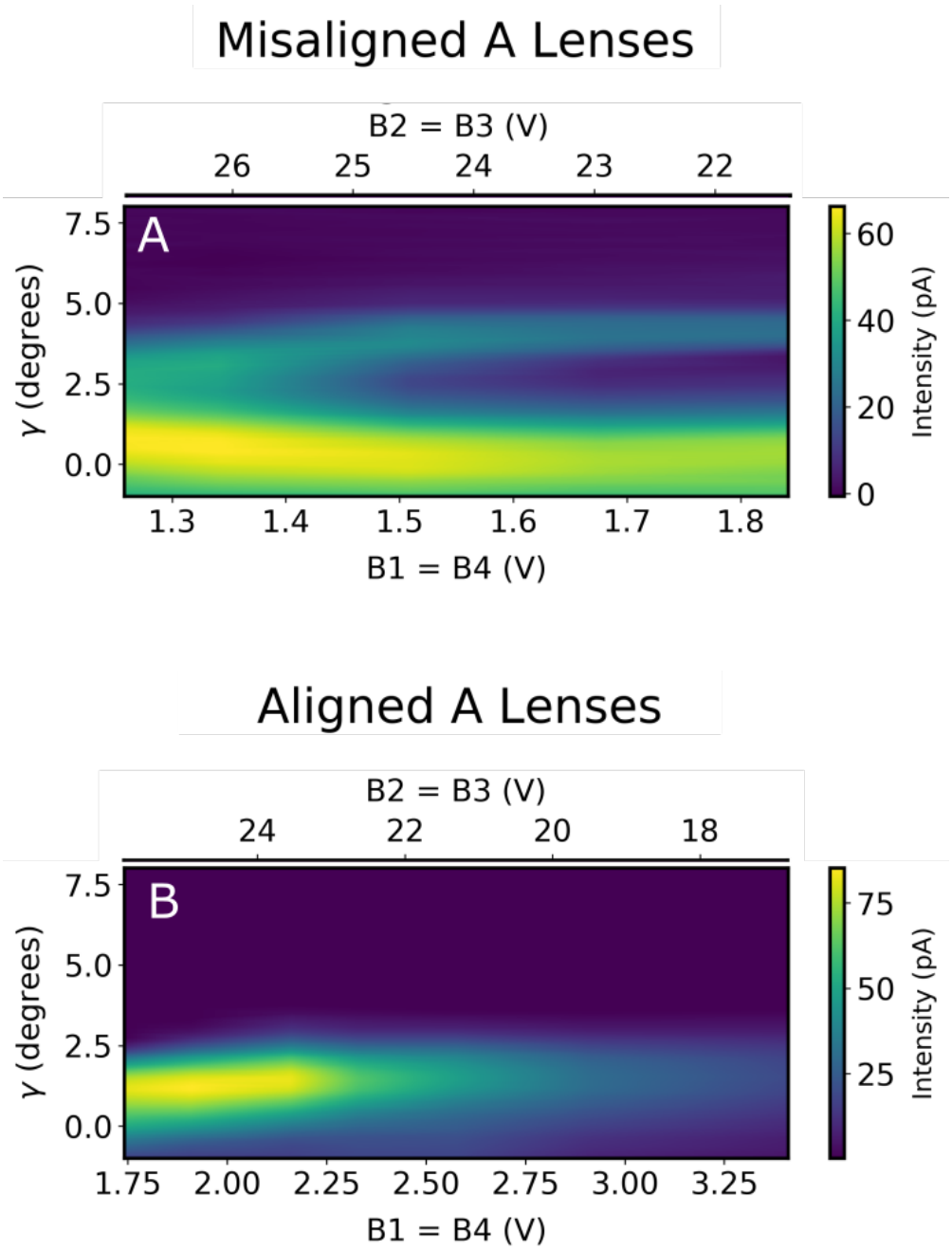

Figure 3.9: **Beam Profile at the Analyzer**
2D mapping of the beam profile as measured at the entrance to the analyzer. The profile is measured as a function of analyzer angle, γ and zoom or B lenses. (A) In the misaligned configuration, the electron beam forms two paths that enter the analyzer at different γ. The zoom lenses can slightly compensate for this by changing the focus on the analyzer entrance. (B) In the aligned configuration, the electron beam only enters the analyzer at one γ. The zoom lenses can increase or decrease the throughput of electrons here but does not change the entrance angle.

chirp and and is a product of aberrations of the electron beam. For example, if the electron beam entering the monochromators has large value of tilt angle, α then we would expect aberrations of the beam due to coupling between the energy and angle of the electrons. Ideally we can assume this coupling is negligible but this is only the case if α is small [52].

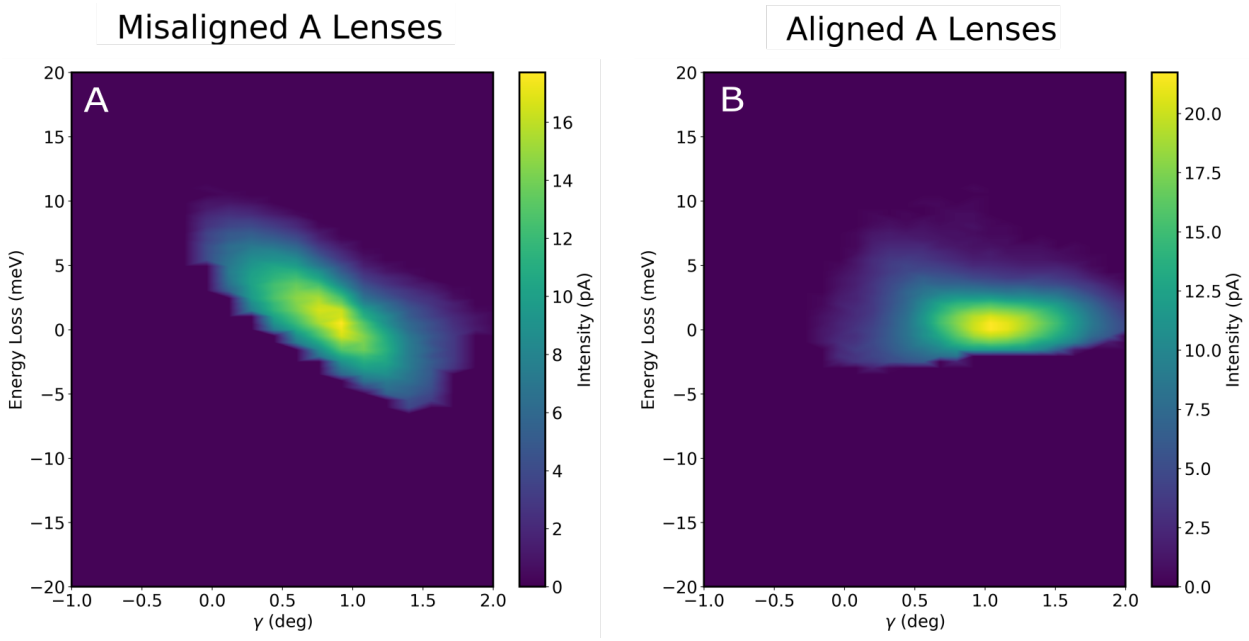

Figure 3.10: **Beam Profile at the Detector**
2D mapping of the beam profile as measured at the detector. The profile is measured as a function of analyzer angle, γ, and electron energy. The angle-integrated energy determines the energy resolution. (A) In the misaligned configuration, the energy profile is chirped resulting in a large angle-integrated energy and therefore bad energy resolution. (B) In the aligned configuration, the energy profile is not chirped resulting in a smaller energy resolution (approximately 5 meV).

This once again highlights the importance of optimally tuning the A lenses as its effects can be seen throughout the entire path of the electron optics.

Electron Detector

The final stage of the electron optics is another set of Einzel that reject any stray electrons due to aberrations, etc. These Einzel lenses are labeled as C1, C2, C3 and each of these voltage lenses have a Δ value that set the spread of voltages on the lens used to steer the beam. The C lenses have delta voltages that steer the beam vertically (ΔC1 and ΔC3) and horizontally (ΔC2).

The C lenses focus the beam onto the Channeltron electron multiplier. The pulses from the Channeltron are counted outside the UHV system using an Ortec discriminator (Ortec model 9302) and amplifiers to

produce TTL pulses to count. Figure 3.11 is what the expected amplified channeltron pulse and TTL signal should look like after the going through the Ortec discriminator.

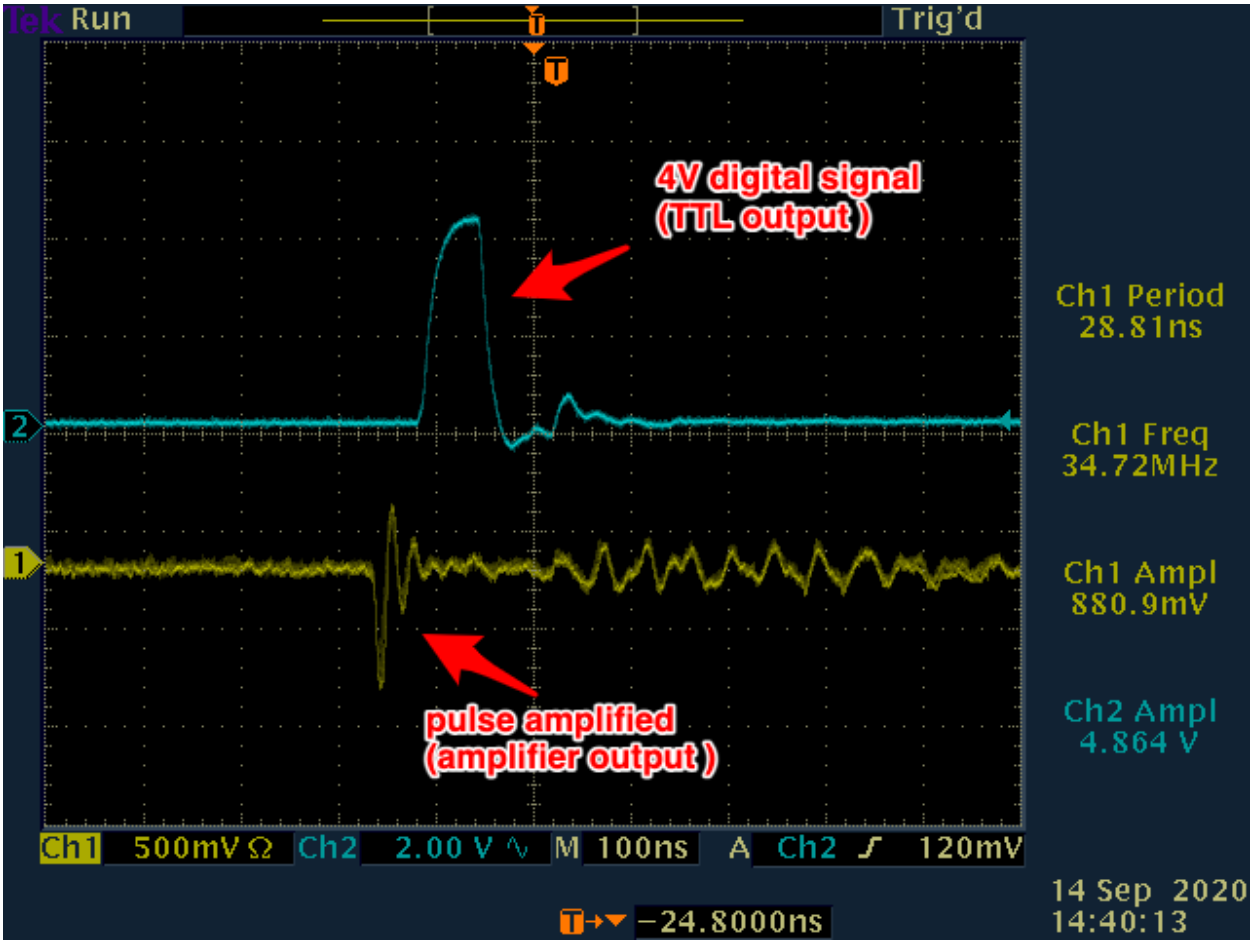

Figure 3.11: **Detector Output**
Oscilloscope measurement of the expected amplified Channeltron pulse and TTL signal after passing through the Ortec discriminator.

The Channeltron electron multiplier is made of an insulating material that is coated with a high resistance semi-metal. When high voltage is applied (2.5-3.0 kV), a voltage gradient induces an electric field. When an electron strikes the detector this is registered as a current pulse. The current pulses get converted to voltage pulses before entering a voltage discriminator. The voltage discriminator works by only passing though pulses that are above the set lower voltage threshold. Therefore we can define the voltage threshold to be just above the electronics/background noise but below the experimental signals from M-EELS (Figure 3.12).

As the Channeltron ages however, the gain on the multiplier decreases and the peak height gets shifted to lower allowed voltages until it gets very close to the background noise (see Figure 3.12). If the lower voltage

threshold on the discriminator is lowered further to allow for more data pulses to pass through, then we start to see the noise background in our data. If we increase the lower voltage threshold then we are losing pulses of data. One way to fix this is to increase the high voltage on the Channeltron which will increase the gain on the multiplier and shift the pulse height distribution to higher voltage. This process is repeated as the Channeltron continues to age until the Channeltron completely dies from the high voltage.

As part of this electron optics characterization process, it is also important to characterize the pulse height distribution of the Channeltron detector as a way to gauge the state of the instrument.

The traditional way to measure a pulse height distribution from an electron detector using a multi-channel analyzer (MCA), which can simultaneous bin the number of pulses at each voltage and therefore directly measure the pulse height distribution. Unfortunately, the pulses from our Channeltron detector, which are less than 10 ns in duration, are too fast to be counted by commercially available MCA instruments. As a way to get around this, we use the high bias voltage (related to the gain) of the Channeltron to characterize the state of the detector as outlined in Figure 3.12. When the discriminator voltage threshold optimized between the electronics noise and Channeltron signal (blue curve in Figure 3.12c), the bias voltage curve has a signature shoulder feature. In the optimized state, the Channeltron bias voltage should be set 50-100 V above this shoulder [54]. As the discriminator voltage threshold moves to higher voltage values, the shoulder feature in the bias voltage curves moves to higher bias voltage (green and yellow curves in Figure 3.12b). Therefore as the Channeltron ages and the pulse height distribution moves to lower voltages, the once optimized discriminator threshold will look more like above the optimized voltage. Hence, if we measure the Channeltron bias voltage curves over time, the shoulder will move to higher bias voltage in time. Each time the Channeltron is replaced, a new set of bias voltage curves needs to be measured. This will be used as a baseline comparison for how that detector behaves over time.

Tuning Best Practices

The following procedure has been developed to optimize the tuning process in direct beam configuration (not off a sample). This procedure is a culmination of this work as well as building off of previous phase-space tuning procedures [34, 35]. Reference scans for individual voltage scans can be found in Appendix A.

1. **Get current from the filament to the detector.** As a first pass, get some current from the filament all the way to the detector. This is done by tuning the pass energy and cover plate voltages of monochromators and analyzer. If there is some current at each point (relay) along the path, then move onto the next step to optimize the resolution. If there is no current at relay M1 or relay M2,

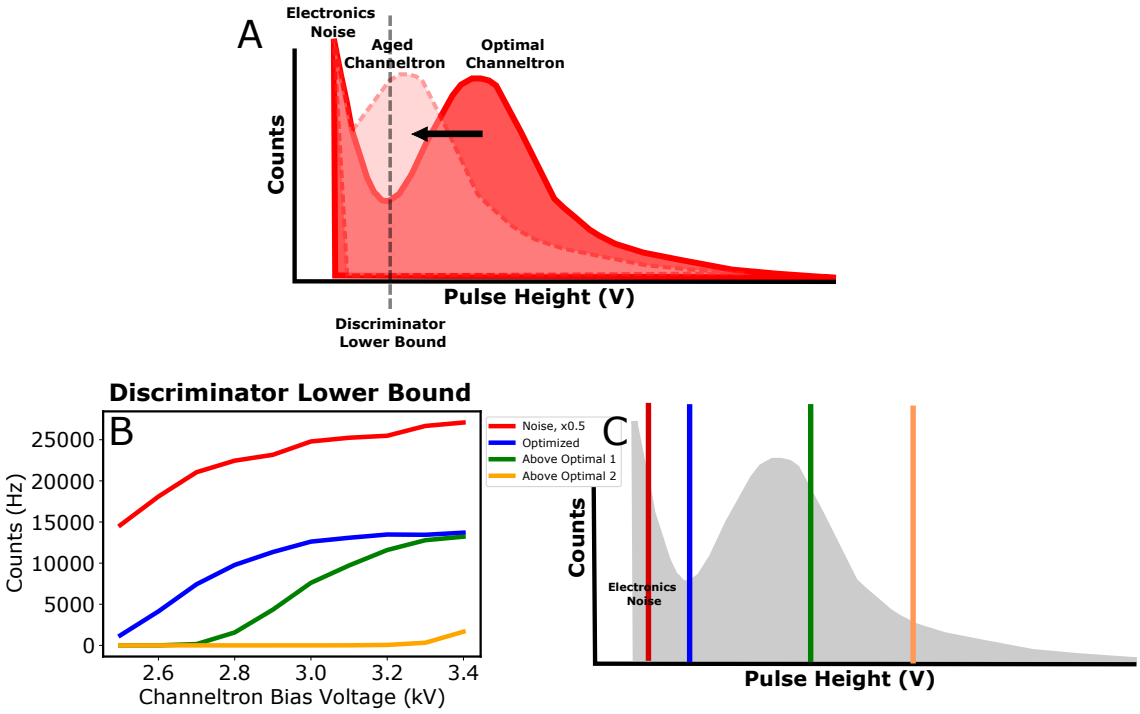

Figure 3.12: **Determining the State of the Channeltron Detector using a Voltage Discriminator** (A) Cartoon of a pulse height distribution from a Channeltron electron multiplier. As the detector ages, the peak of the pulse height distribution merges with counts from the electronics noise. (B) and (C) The lineshape of counts versus Channeltron bias voltage changes depending on where the discriminator lower voltage threshold is set. This can be used to determine the state of the detector by such that the shoulder in the bias voltage lineshape will move to higher voltage as the Channeltron ages.

the filament is probably off-center or tiled which can be compensated with the A lenses. Increase the value of the A1 lens and steer the beam horizontally with $\Delta A1$ and $\Delta A3$.

2. **Characterize what the beam looks like along its trajectory.** As long as there is some current at all points along the path, we can use the characterization tools described in the previous sections to identify the best ways to improve throughput and resolution. The characterization tools are as follows:

   - At the second monochromator, measure the resolution and pass energy of the pre-monochromator as demonstrated in Figure 3.7.
   - At the analyzer entrance, measure the resolution and pass energy of the second monochromator as demonstrated in Figure 3.8.
   - At the analyzer entrance, measure the profile of the beam path as a function of γ and the focus

lenses (B lenses) as demonstrated in Figure 3.9.

- At the detector entrance, measure the energy and angle distribution of the beam as a function of γ and eloss (voltage lens that selects the electron energy into the detector) as demonstrated in Figure 3.10.

3. **Use the characterizations to optimize the beam.** The results of the above characterization will determine the next steps to optimize the beam. For example, if the profile of the beam path at the analyzer entrance has multiple electron paths and the energy/angle distribution is chirped, it is most likely that the A lenses are not focused properly. However, if at the analyzer entrance, the beam passes through at one value of γ but the energy/angle distribution is still chirped, then this might indicate an issue of aberrations from the monochromator or analyzer. If this is the case, adjusting the pass energy to resolution ratio (i.e. Δ/M1) would be a good place to start.

4. **Iterate over this process multiple times.** After characterizing the beam trajectory and adjusting lenses accordingly, re-tune the other lenses in order while measuring current at the detector. The goal here is just to increase the throughput in the adjusted tuning configuration. Next, redo the characterization measurements to gauge the state of the tuning process. Repeat this process until you achieve a good electron throughput and resolution (approximately 50 pA at the detector, 5 meV integrated FWHM at the detector).

5. **Characterize the Channeltron detector.** Once the beam trajectory is optimized, it is useful to characterize the state of the detector following the procedure above.

In addition we have found that there are two effective ways to increase counts to the detector (albeit in lieu of resolution). One way to accomplish this is to increase the accepted spread of energies (delta voltages on the monochromators, $\Delta M1$ or $\Delta M2$) and then adjusting the pass energy, M1 or M2, accordingly to re-center the beam on the exit slit. However there is a physical upper limit to this. Another way to increase counts is with the C lenses after the analyzer. Both of these methods allow more electrons through by accepting electrons with higher angles from lens aberrations. Therefore it makes sense that increased counts with these lenses would come at the cost of resolution. Measurements of these methods can be found in Figure 3.13.

Previous methods of tuning involved comparing throughputs at each relay and voltage scans at each lens to previous tuning files. This method isn't ideal since the tuning phase space is so large that measurements of individual voltages could get us stuck in a local minimum. Also, this previous method was solely based

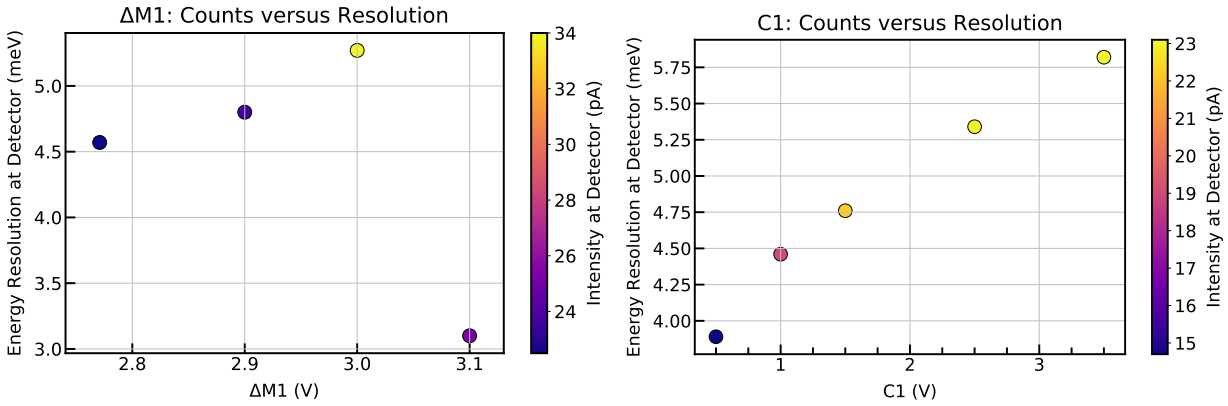

Figure 3.13: **Increasing Electron Throughput**
There are two effective ways to increase counts at the detector: increasing the energy spread of the first monochromator (left figure) and increasing the acceptance angles into the final lenses before the detector (right figure). Both methods increase the number of electrons to the detector at the cost of energy resolution.

on the throughput of electrons and did not account for aberations that effect energy and momentum resolution. With this new method of tuning, we can systematically measure the phase-space of parameters at several points along the electron trajectory. This enables us to measure several parameters of phase-space simultaneously while also taking into account aberations of the beam.

3.2 Updates to Original M-EELS Setup

3.2.1 Load-Lock

This chamber includes a sample magazine, that I designed and implemented, which enables us to pump down five prepped samples at one time. Previously, we were limited to two sample cleaves per day - constrained by the time it takes to load samples into the load lock and pump down to high vacuum. However with the implementation of the sample magazine, sample throughput has increased five-fold - up to ten sample cleaves per day.

3.2.2 Annealing Stage

It is very important in UHV science to be able to have samples with clean surfaces that do not have absorbates or other contaminates from the atmosphere. The current method of developing an *in situ* clean surface for scattering is by cleaving 2-D layered materials. However this severely limits the types of materials that we can study in the M-EELS system. There are alternative ways to create a clean surface such as annealing which evaporates all the contamination off the surface. Implementing this will dramatically increase the

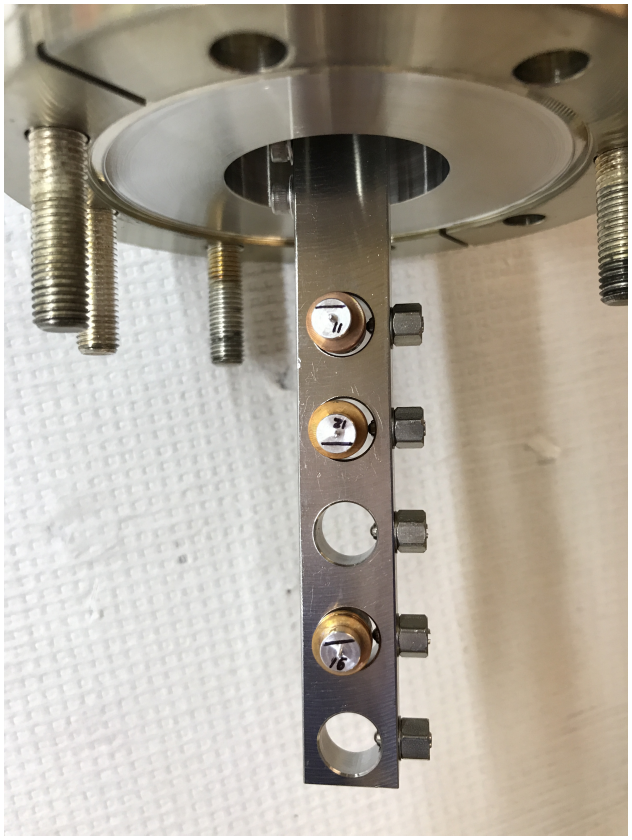

Figure 3.14: **Sample Magazine**
This UHV sample holder allows for us to insert up to five samples into the vacuum chamber at a time.

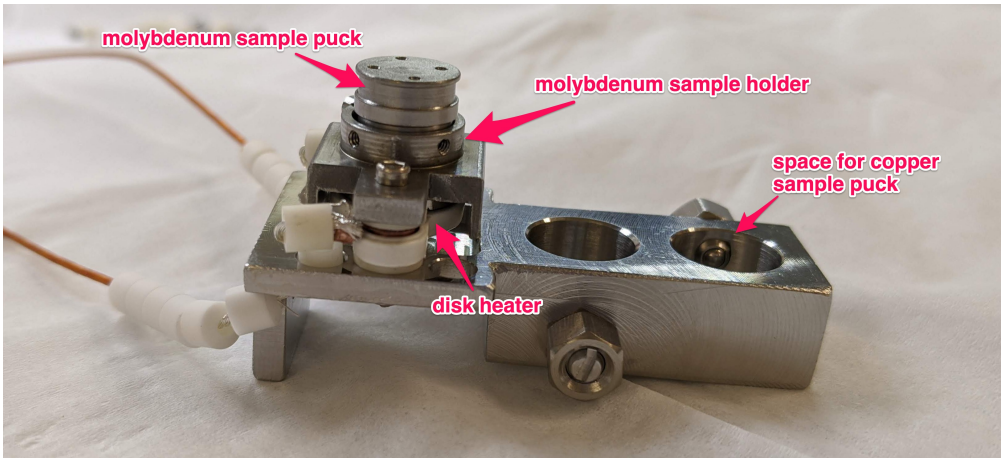

Figure 3.15: **Sample Annealing Stage**
This UHV annealing stage has three sample spots - two for cleaving and one for annealing. The annealing sample spot (at the top) consists of a Momentive disk heater that can heat to higher than 1500 degrees Celsius. On the heater sits a molybdenum puck holder, molybdenum puck, and an inconel spring to hold the puck in place.

types of materials that one can study with M-EELS. In addition, depending on the temperature that the annealing stage can achieve, this method can also be used to electron-dope samples, such as oxygen reduced $SrTiO_3$, or to evaporate selenium caps off of thin films.

Figure 3.15 is the annealing stage to be installed in the prep chamber of Figure 3.1. It is composed of a stainless steel body with two parking spots that holds copper sample pucks with a spring loaded plunger set screw. These spots can be used to cleave samples in the conventional way.

At the top of the stainless steel body sits a Momentive disk heater (voltage 15 V, current 8 A, power 80 W) shown in Figure 3.15 and can achieve temperatures higher than 1500 degrees Celsius. On top of the disk heater sits molybdenum holder for a molybdenum sample puck. In between the molybdenum holder and puck is an inconel spring providing support and thermal conductivity to the puck. Inconel sheet metal is used as the spring because of its high thermal conductivity, high melting point, and its ability to retain its springy-ness over many temperature cycles. The inconel spring is held in with a screw on the molybdenum holder. The remaining screw holes on the holder are to attach leads for a K-type thermocouple.

3.2.3 Vacuum Suitcase

Another avenue of interesting materials to study in M-EELS are thin films. Thin films are grown using techniques such as molecular beam epitaxy in a UHV environment. Due to samples of films only being a few layers thick, it is not feasible to cleave these materials. Annealing the surface is one option to expose a clean scattering plane. Another option is to transport the film from one UHV chamber to another, never exposing the film to air. To do this, I engineered a vacuum suitcase instrument to enable us to transfer samples between labs without ever exposing them to air. This system is compatible with several UHV setups at UIUC including molecular beam epitaxy, scanning tunneling microscopy, angle resolved photoemission spectroscopy, and our M-EELS system. This will enable us to study thin film materials with a variety of techniques without the surface being contaminated.

The vacuum suitcase is composed of a magnetic manipulator, dual ion-getter pump, ion gauge and gate valve. The suitcase can achieve pressures in the 10^{-9} Torr. Inside the suitcase, and at the end of the magnetic manipulator, there is a screw adapter that screws into a sample holder (Figure 3.16a).

Inside the vacuum suitcase chamber is a sample holder whose design is similar (Figure 3.16b) to the annealing stage in the previous section. The sample holder is made of molybdenum and sits on top of a Momentive disk heater (voltage 15 V, current 8 A, power 80 W) shown in Figure 3.16b and can achieve temperatures higher than 1500 degrees Celsius. A molybdenum sample puck sits inside the sample holder, held in by an inconel spring providing support and thermal conductivity to the puck.

When attached to the MBE system in the Madhavan Group, the sample holder plugs into a banana plug UHV feedthrough that connects to the heater power supply. The heater will heat the puck and holder to get the substrate hot enough for material growth. A temperature calibration curve was measured for heater power versus temperature of substrate as shown in Figure 3.16c. This temperature calibration curve was measured using a pyrometer off of a SiC substrate screwed to the molybdenum sample puck over the course of 4.5 hours.

On the M-EELS side, the suitcase attaches to the loadlock chamber. The sample is translated perpendicular to the EELS UHV grippers. The samples are transferred in the same way as samples from the sample magazine except there is no need to cleave the surface.

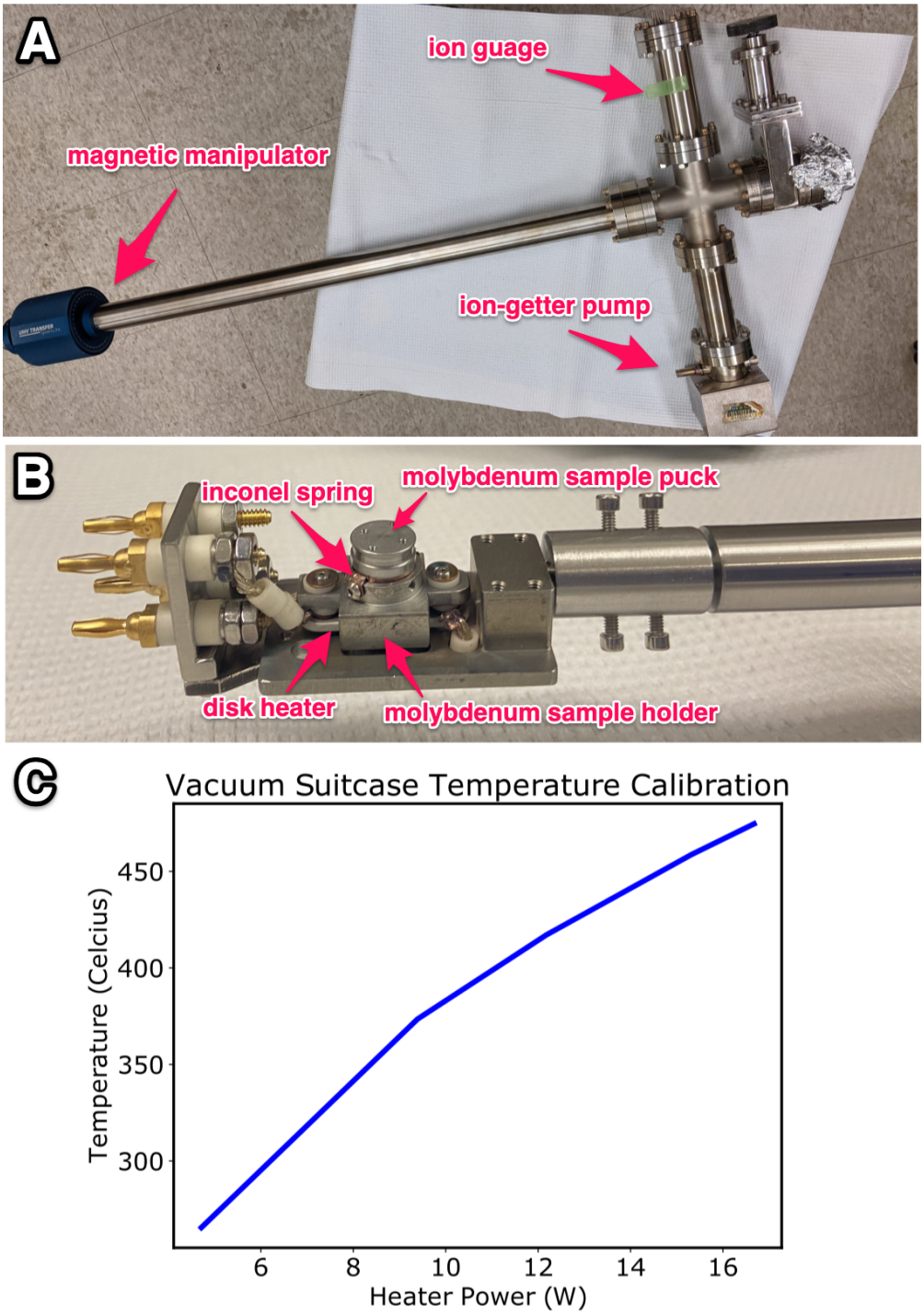

Figure 3.16: **Vacuum Suitcase**
(A) Photo of the vacuum suitcase chamber composed of a magnetic manipulator, dual ion-getter pump, ion gauge and gate valve. (B) Photo of the UHV sample holder that goes inside the vacuum suitcase and is screwed into the magnetic manipulator. UHV feedthrough connect to the Momentive heater power supply used for MBE material growth. On the heater sits a molybdenum puck holder, molybdenum puck, and an inconel spring to hold the puck in place. (C) Calibration curve of the heater power versus temperature of substrate measured using a pyrometer off of a SiC substrate screwed to the molybdenum sample puck over the course of 4.5 hours.

3.3 Sample Preparation

3.3.1 Laue

Samples are oriented using a Laue diffractometer. In Laue diffraction, an X-ray beam is backscattered off a sample to produce a high-symmetry pattern that reflects the symmetry of the lattice. Laue patterns for $TiSe_2$ and $SrTiO_3$ are shown in Figure 3.17. Once a high symmetry pattern is found, a line is then drawn on the sample puck using a diamond scribe to mark the high symmetry directions of the crystal which will be used to orient the sample once in the EELS scattering chamber. This process does not guarantee however the sample will be along the exact crystalographic direction we need for experiments by the time the sample makes it to the EELS spectrometer. The uncertainty of the orientation is both due to human uncertainty in scribing the sample puck and uncertainty from the sample being cleaved and transferred multiple times before making it to the EELS spectrometer. The error in orientation is not significant due to the fact that we can correct for this by rotating ϕ (using an Attocube peizo motor) until we see a (1,0) Bragg peak. On average, the sample orientation is within ± 15 degrees, a range easily reached with our Attocube setup.

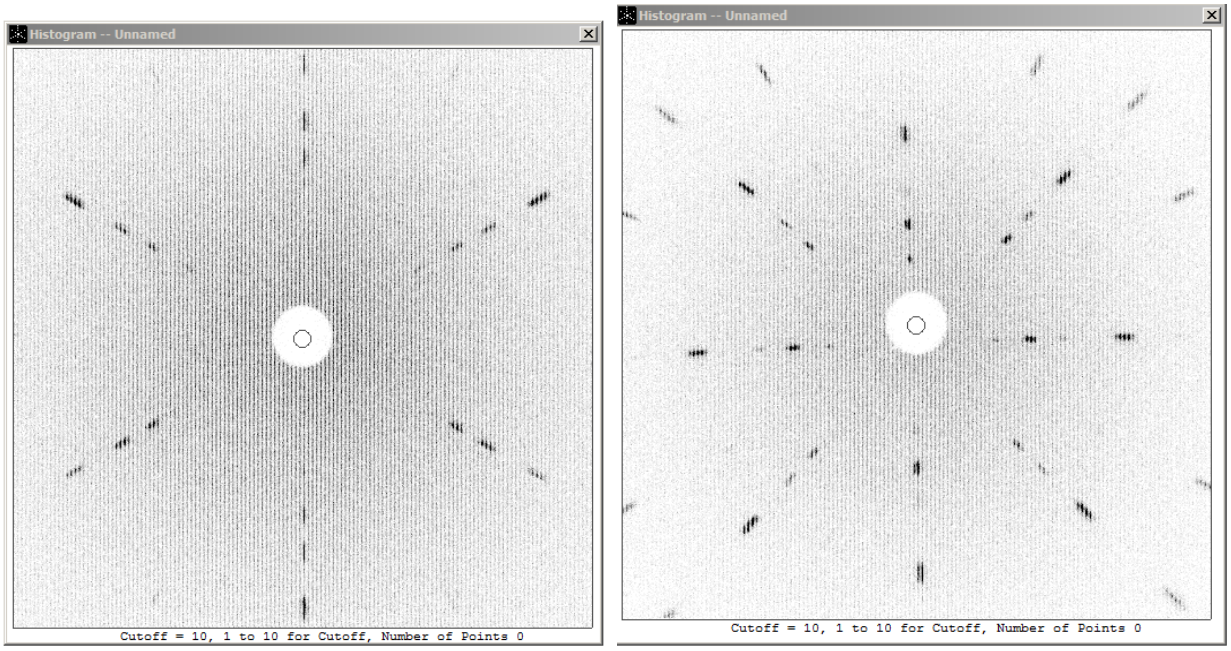

Figure 3.17: **Laue Diffraction to Orient Sample for M-EELS Experiments**
Laue diffraction pattern from Cu_xTiSe_2 (left figure) with hexagonal crystal structure and $SrTi_{1-x}Nb_xO_3$ (right figure) with cubic crystal structure. ‘

3.3.2 Hall

As introduced in intro physics classes, if an electric current flows in a conducting system in the presence of a magnetic field, there will be a transverse force on the charge carriers due to the magnetic field. This will produce a buildup of charge at the edge of the sample that can be measured as a voltage difference from one edge to the opposite edge of the sample. By measuring the voltage difference as a function of applied magnetic field, one can determine the number of carriers (and in turn the carrier density) in a sample. This process is described by the following:

$$V_H = \frac{IB}{nte} \tag{3.12}$$

where I is the applied current, B is the magnetic field, n is the density of carriers, t is the sample thickness, and e is the elementary charge of an electron.

$$R = \frac{V_H}{I} = \frac{B}{nte} \tag{3.13}$$

$$ne = \frac{\Delta B}{\Delta R} t^{-1} \tag{3.14}$$

Therefore the carrier density of a sample can be determined by measuring the change in resistance for some range of magnetic field perpendicular to the sample. These measurements were using a Quantum Design Physical Properties Measurement System (PPMS). Carrier densities were determined at room temperature, scanning a range of magnetic field from -8 to +8 Tesla. For $SrTi_{1-x}Nb_xO_3$, $4mm \times 4mm \times 1mm$ samples were attached to the PPMS holder using double-sided tape. Copper leads are soldered to the PPMS holder and then connected to the four corners with indium dots in a Van der Pauw configuration (Figure 3.18A). To improve the connection of the copper wires with the sample, the indium dots were heated using a soldering iron. Figure 3.18B and 3.18C show a prepped sample and example data, respectively. The slope of the curve determines the carrier density of the sample.

3.3.3 Wiresaw

In systems that are not 2D layered, an alternative to annealing and *in situ* sample growth is to fracture a 3D crystal in order to acheive a clean sample surface. In order to do this, a fracturing weak point needs to be made so that when force is applied, the sample will want to break along a certain direction. This sample prep method is especially important in $SrTiO_3$. $SrTiO_3$ is cubic material that does not naturally cleave and annealing this material introduces oxygen vacancies which alter its carrier density [55]. Therefore a new method of exposing a fresh surface needed to be developed.

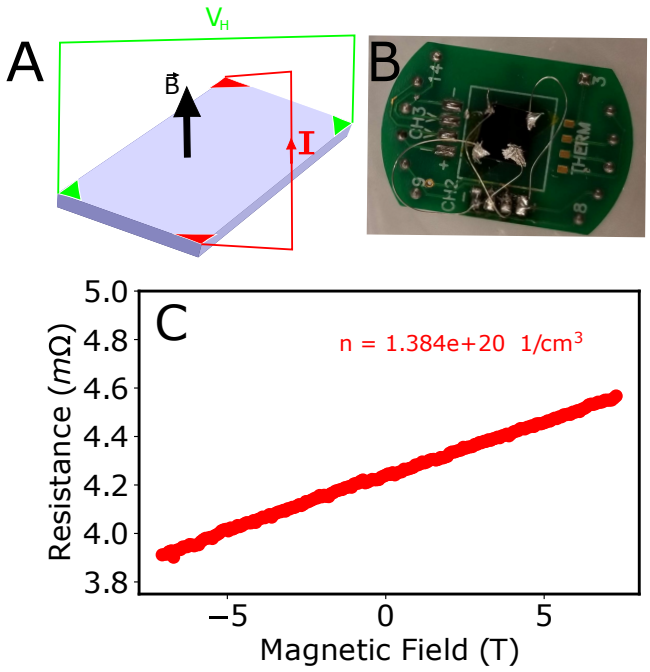

Figure 3.18: **Suitcase Sample Holder**
(A) Cartoon of Van der Pauw Hall configuration. (B) Photo of $SrTi_{1-x}Nb_xO_3$ on the PPMS sample holder. The Copper leads are connected to the sample with indium dots. (C) PPMS measurement of the sample resistance for a range of applied magnetic field. From the slope of the measurement, the carrier density can be calculated as given by Equation 3.14. For this measurement, the carrier density is 1.384 x 10^{20} $1/cm^3$.

Figure 3.19: **Diamond Wiresaw Sample Prep**
Notches are created on four sides of a sample using a Wells diamond wire saw. The wire used is made of tungsten embedded with diamond and has a diameter of 300 microns..

We developed a method of notching the sides of each sample as shown in Figure 3.19 with samples that are 1 mm thick. These notches are created using a Wells wire saw. The wire used is made of tungsten embedded with diamond and has a diameter of 300 microns. By notching the sides of the sample, we introduce a point

of weakness in the sample so that when force is applied (in vacuum) the sample will cleave at the notches. This fracturing technique works would likely not work for ARPES or STM since those technique are more surface sensitive then M-EELS.

This method can be extended to many other cubic structures and other materials that are not easily cleaved. This has the potential to open the door for taking M-EELS measurements on a whole new class of materials.

Chapter 4

Distinct Lattice and Excitonic Instabilities in Cu_xTiSe_2

4.1 Exciton Condensation in $1T$-$TiSe_2$

If cooled to a sufficiently low temperature, a collection of bosons will condense into a single quantum-mechanical state known as a Bose condensate. The physics of Bose condensation is crucial to understanding a variety of macroscopic quantum phenomena, including superconductivity and superfluidity. Excitons are bosons that consist of an electron and a hole bound together by the Coulomb interaction. The light mass and high binding energy of excitons means they should Bose condense at higher temperatures than other condensed phases [1], enabling fundamental studies of exciton condensates.

A system in which a thermally-equilibrated, 3D exciton condensate can form is a semimetal with a small, indirect band gap [3–6]. As the band gap is tuned close to zero, the system becomes unstable to the spontaneous formation of excitons once the carrier density is too low to sufficiently screen electron-hole pairs [4, 6]. The nonzero center-of-mass momentum of the excitons modulates the charge density and a lattice distortion occurs due to the movement of charge. Forming an exciton condensate breaks a spatial symmetry, like in a conventional, structural phase transition. Can there ever be a distinction between an exciton condensate in a material and a structural transition that breaks the same symmetry?

Consider, for example, the semimetal $1T$-$TiSe_2$, whose small, indirect gap is ideal for exciton condensation [3–5, 56]. $TiSe_2$ forms a periodic lattice distortion (PLD) below $T_{\mathrm{PLD}} \sim 200$ K with a wave vector $\mathbf{q_0}$ that connects the valence and conduction band extrema [56,57]. The signature of the PLD is a phonon that softens to zero energy at $T = T_{\mathrm{PLD}}$ and $\mathbf{q} = \mathbf{q_0}$ [58,59]. We recently demonstrated that the PLD in $TiSe_2$ coincides

with an exciton condensate by observing a separate, soft electronic collective mode at $T = T_{\mathrm{XC}} = T_{\mathrm{PLD}}$ and $\mathbf{q} = \mathbf{q_0}$ using momentum-resolved electron energy-loss spectroscopy (M-EELS) [8]. The precursor to this soft mode at temperatures greater than T_{XC} is an electronic, plasmon-like excitation, which decreases toward zero energy at it approaches T_{XC}. Kogar et al. demonstrated that there are two signatures of exciton condensation - electronic mode that softens at $T = T_{\mathrm{XC}} = T_{\mathrm{PLD}}$ and $\mathbf{q} = \mathbf{q_0}$, and an electronic mode that decreases in temperature for $T > T_{\mathrm{XC}} = T_{\mathrm{PLD}}$ and $\mathbf{q} = 0$. Since the exciton condensate and PLD in $TiSe_2$ share the same symmetry and occur at the same temperature, can we determine if the two phases are distinct from one another?

4.2 M-EELS Study of Copper Intercalated $TiSe_2$

Intercalating $TiSe_2$ with copper suppresses the PLD and induces superconductivity [23]. The copper intercalants introduce screening [60], add disorder, and expand the c-axis lattice parameter [23], but these changes may affect the excitonic state and the PLD differently. For example, an increase in metallic screening likely affects electron-hole pairing more than the PLD. X-ray scattering has already determined how the PLD is suppressed in Cu_xTiSe_2 [8, 26], but a separate measurement of the exciton condensate as a function of x is still needed. Here we use M-EELS to measure how the soft electronic mode evolves with copper intercalation to investigate whether the exciton condensate and PLD can act independently.

Previous studies of the lattice distortion in Cu_xTiSe_2 show that the PLD survives far into the metallic superconducting phase centered around $x = 0.08$, but that T_{PLD} decreases as x increases [8, 23]. The PLD exhibits a slight incommensuration away from the $2a \times 2a \times 2c$ superstructure for $x > 0.05$ [8]. The incommensuration coincides with the onset of superconductivity, which has also been seen in $TiSe_2$ by applying pressure [61] or electrostatic gating [62]. While our recent M-EELS measurement of the soft electronic mode at $x = 0$ showed that the exciton condensate and PLD coincide, we now study Cu_xTiSe_2 with M-EELS to determine how the excitonic effect evolves for $x > 0$.

M-EELS measurements were taken with a conventional HR-EELS spectrometer, retrofitted with a custom low-temperature seven-axis ultra-high vacuum compatible goniometer. The goniometer was aligned so that the sample rotation axis intersected the spectrometer rotation axis at a single point. Sample orientation was accomplished by identifying two Bragg peaks (e.g. (0,0) and (1,0)) to construct an *in situ* orientation matrix translating between diffractometer angles and reciprocal space. Samples were cleaved *in situ* at room temperature and then cooled to the desired temperature. Spectra were obtained at an incident beam energy of 50 eV with an energy resolution between 4-6 meV and a momentum resolution of 0.03 inverse Angstroms.

Electron energy-loss scans were accomplished by moving the sample rotation and detector positions to keep the out of plane momentum transfer fixed while simultaneously scanning the voltage on the analyzer. The out-of-plane momentum transfer was fixed to 3.65 reciprocal lattice units to enable the spectrometer to reach the in-plane Brillouin zone boundary at 50 eV beam energy while maintaining an incident beam angle of at least 30 degrees with respect to the sample surface. Further instrumentation-related specifics can be found in Ref. [21].

4.3 Determining Effective Doping

A M-EELS study of Cu_xTiSe_2 requires precise knowledge of the carrier density of each cleaved surface since the electron carriers come from randomly-distributed copper intercalants [60] and an unknown number of selenium vacancies that cause the carrier density to vary by tenths of a percent from cleave to cleave. The plasma frequency, ω_p, depends on the carrier density, n, according to,

$$\omega_p^2 = \frac{4\pi n e^2}{m^*}, \tag{4.1}$$

where m^* is the effective mass of the charge carriers [63]. Knowing the plasma frequency of a surface allows us to determine *in situ* the mean carrier density.

We determine the plasma frequency by fitting our M-EELS spectra at $\mathbf{q} = 0$ and $T = 300$ K to the dielectric loss function, -Im$[1/\epsilon(\mathbf{q},\omega)]$, using the Drude expression for the dielectric constant [63],

$$\epsilon(\omega) = \epsilon_\infty - \frac{\omega_p^2}{\omega^2 + i\omega/\tau}, \tag{4.2}$$

where $\epsilon_\infty = 18$ is the background dielectric constant [64] and $1/\tau$ is the relaxation rate.

If the carrier density of a surface is proportional to the effective doping of that surface, then the square of the plasma frequency (ω_p^2) should increase linearly with x according to equation (4.1). In Fig. 4.1, we see that ω_p^2 does increase approximately linearly with nominal doping. A nonzero plasmon energy at $x = 0$ indicates that the carrier density n is nonzero, with residual carriers from either selenium vacancies or temperature. We do a linear fit to ω_p^2 versus nominal doping x for all cleaves and find the following relationship between the effective doping x_{eff} of a surface and the plasma frequency,

$$x_{\text{eff}}(\omega_p) = \frac{\omega_p^2 - 205,965.40 \text{ meV}^2}{9,436,672.58 \text{ meV}^2}. \tag{4.3}$$

Table 4.1: **Nominal doping, Drude fit parameters, and effective doping of Cu_xTiSe_2 samples.** Nominal doping x of each surface, the Drude fit parameters for the plasma frequency ω_p and relaxation rate τ, and the effective doping x_{eff} determined from ω_p. The uncertainty in each parameter corresponds to the standard deviation.

x	ω_p (meV)	τ (meV^{-1})	x_{eff}
0	437.06 ± 0.79	0.00635 ± 0.00004	0 ± 0.001
0	471.52 ± 0.99	0.00620 ± 0.00005	0.002 ± 0.001
0.004	483.71 ± 1.10	0.00659 ± 0.00006	0.003 ± 0.001
0.004	490.67 ± 0.85	0.00635 ± 0.00004	0.004 ± 0.001
0.004	494.52 ± 1.14	0.00609 ± 0.00005	0.004 ± 0.001
0.004	496.29 ± 1.16	0.00642 ± 0.00006	0.004 ± 0.001
0.004	499.05 ± 1.31	0.00632 ± 0.00006	0.005 ± 0.001
0.01	550.71 ± 1.05	0.00658 ± 0.00005	0.010 ± 0.001
0.01	551.10 ± 1.29	0.00611 ± 0.00006	0.010 ± 0.001
0.01	583.14 ± 1.58	0.00593 ± 0.00006	0.014 ± 0.001
0.02	668.29 ± 1.05	0.00646 ± 0.00004	0.026 ± 0.001
0.04	690.41 ± 1.22	0.00634 ± 0.00004	0.029 ± 0.001
0.07	907.85 ± 2.76	0.00642 ± 0.00009	0.066 ± 0.001
0.07	932.21 ± 2.10	0.00608 ± 0.00006	0.070 ± 0.001
0.109	1133.90 ± 3.70	0.00514 ± 0.00008	0.114 ± 0.001

From this equation, we calculate the effective doping of all surfaces from the plasma frequency determined from the Drude fit to the M-EELS spectra at $\mathbf{q} = 0$ and $T = 300$ K. The effective doping values are recorded in Table 4.1 and these are the values reported as x in the rest of the chapter.

We can check that our Drude model fit parameters are reasonable by computing the carrier density for each effective doping and comparing to values from Hall effect measurements. We can compute the carrier density from the plasma frequency using equation (4.1) if we have the effective mass m^*. We estimate the value for the effective mass from ARPES spectra of the conduction band for $x = 0.04$ and $x = 0.06$ [60] using a fit of the form $E(k) = \hbar^2k^2/2m^*$. The fit gives $m^* = 4.7m_e$ for $x = 0.04$ and $m^* = 4.1m_e$ for $x = 0.06$. We average the two values together to give a final value for the effective mass of $m^* = 4.4m_e$. Using equation (4.1), we find a linear relationship between carrier density n and effective doping as seen in Fig. 4.2.

We can now compare the carrier densities found from our Drude fit parameters to carrier densities found from measurements of the Hall coefficient [65]. The Hall coefficient R_H is related to the carrier density by the equation, $R_H = -1/ne$. Table 4.2 compares the carrier density from our Drude fits to the carrier densities from the Hall coefficient at 300 K for the dopings studied in the Hall experiment [65]. The carrier densities are most consistent for the higher two dopings than for the lower two dopings. The differences at the lower dopings may be due to the two types of carriers contributing to the carrier density. Since our carrier densities differ from the Hall values by a factor of 3 or less, our Drude fit parameters do on the whole seem to be reasonable.

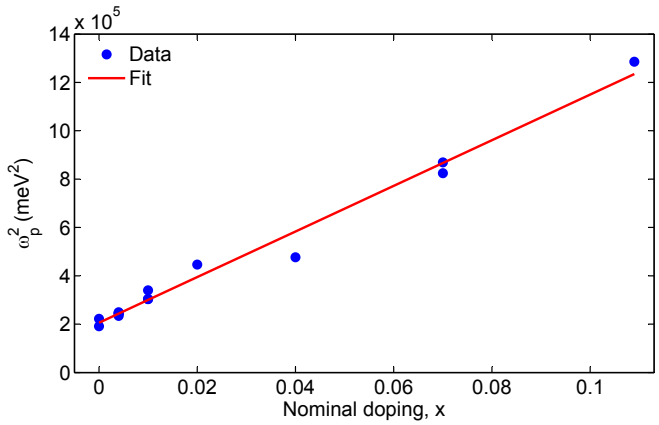

Figure 4.1: **Cu_xTiSe_2 Plasma Frequency versus Nominal Doping**
Plot of plasma frequency squared versus nominal doping x for Cu_xTiSe_2 samples. The linear fit is used to calculate effective doping for each sample from the plasma frequency.

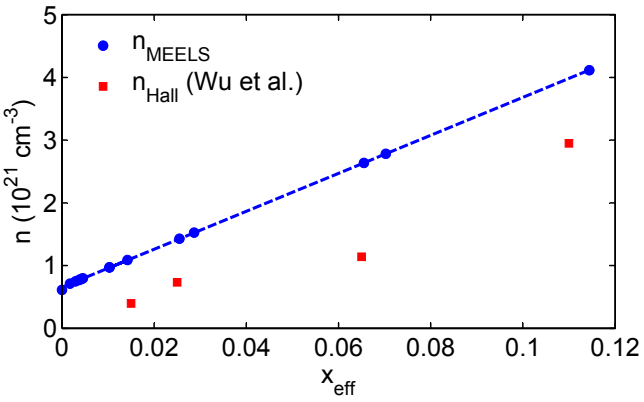

Figure 4.2: **Carrier Density vs Doping**
Carrier density n as a function of effective doping calculated from equation (4.1) using the Drude fit parameters and the effective doping from ARPES spectra [60]. The carrier density is linearly related to the effective doping.

Table 4.2: **Comparing carrier densities from our Drude fits and Hall data from [65].**

x_{eff}	n_{MEELS} (cm^{-3})	n_{Hall} (cm^{-3})
0.014	1.09e21	3.95e20
0.026	1.43e21	7.33e20
0.066	2.64e21	1.14e21
0.109	4.12e21	2.96e21

Copper intercalants electron-dope the Ti-3d conduction band [60] and increase the metallic screening, which should strongly affect the exciton condensate [4,6]. We quantify the screening properties of the normal state, out of which the condensate forms, by computing the real part of the dielectric constant, Re[$\epsilon(\omega)$], using our Drude fit parameters. For a metal, Re[$\epsilon(\omega)$] exhibits a zero-crossing at $\omega = \sqrt{\omega_p^2/\epsilon_\infty - 1/\tau^2}$. We find that Re[$\epsilon(\omega)$] is always positive for $x \leq 0.014$, but that a zero-crossing appears for $x \geq 0.026$ (Fig. 4.3c). For the purposes of this study, we use the appearance of a zero-crossing to define a semimetal-metal transition in Cu_xTiSe_2, which we identify to be at $x = 0.025$ by interpolating Re[$\epsilon(0)$] between $x = 0.014$ and $x = 0.026$.

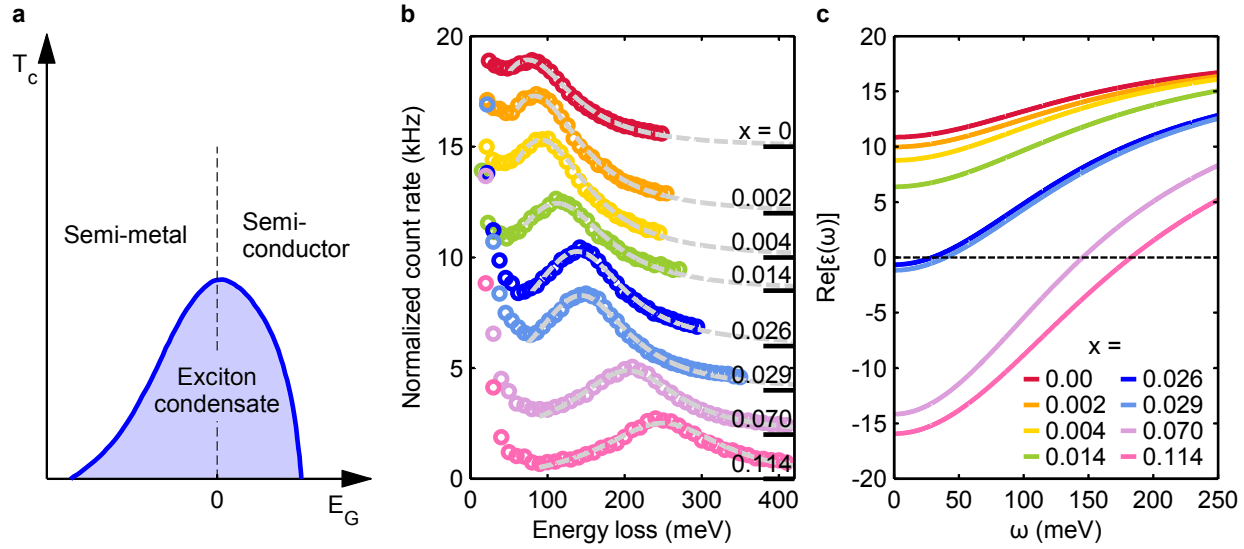

Figure 4.3: **Characterizing Metallic Behavior in Cu_xTiSe_2**
a, Caption goes here. **b**, M-EELS spectra at $\mathbf{q} = 0$ at $T = 300$ K, showing an electronic mode at $\omega = 83$ meV at $x = 0$ that shifts to higher energies as the doping x increases. Spectra have been scaled to the elastic line and offset vertically for clarity. Dashed-gray lines are fits to the dielectric loss function. **c**, The real part of the dielectric constant as a function of energy computed from fits to the M-EELS spectra in **b**. A zero-crossing appears near $x = 0.026$.

4.4 Measurements of the PLD Order Parameter

In elastic scattering ($\omega = 0$) scans taken along the (H,0) direction with M-EELS, we see the development of the PLD order parameter in Cu_xTiSe_2 below the transition temperature, T_{PLD}. The PLD order parameter appears as a peak at the PLD wave vector, $\mathbf{q}_0 = (0.5,0)$. Fig. 4.4 shows the PLD peak at $\mathbf{q}_0$ for samples with effective dopings ranging from $x_{\mathrm{eff}} = 0$ to $x_{\mathrm{eff}} = 0.114$. Within our momentum resolution, the width of PLD peak does not systematically increase with effective doping, indicating that the disorder introduced by the copper atoms does not appreciably broaden the PLD reflections seen with M-EELS. If there were significant

disorder from the copper atoms, our momentum-resolution would worsen and the PLD peak would broaden.

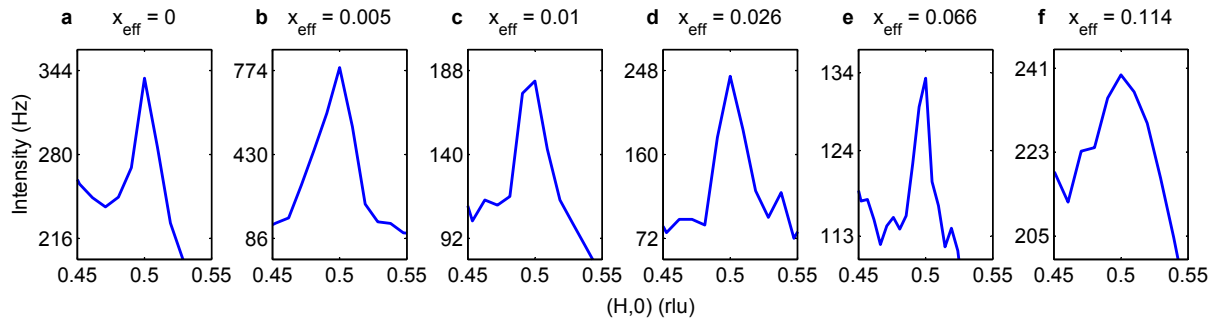

Figure 4.4: **PLD Order Parameter**
a-f, Elastic scattering ($\omega = 0$) data taken along the (H,0) direction showing the PLD order parameter at $\mathbf{q}_0 = (0.5,0)$. Each panel corresponds to a different effective doping. **a-c** were taken at $T = 100$ K and **d-f** were taken at $T = 30$ K, which are all temperatures below T_{PLD} for each doping.

4.5 Temperature Dependence of the Electronic Collective Mode

We investigate the evolution of the exciton condensate with doping by first measuring the temperature dependence of the electronic mode at $\mathbf{q} = 0$ (Fig. 4.5). As demonstrated in Ref. [8], the electronic mode in $TiSe_2$ decreases in energy from $T = 300$ K down to $T_{\mathrm{PLD}} \sim 200$ K, but then shifts up in energy and sharpens dramatically below T_{PLD} (Fig. 4.5a). Here we observe that samples with $x \leq 0.014$ exhibit similar behavior to $x = 0$, although the sharpening of the electronic mode below T_{PLD} is less dramatic (Fig. 4.5b-d). We also find that the electronic mode energy reaches a minimum at $T < T_{\mathrm{PLD}}$ for $x > 0$ (black arrows in Fig. 4.5i).

In the superconducting region of the phase diagram, such as $x = 0.066$ (Fig. 4.5g) and $x = 0.114$ (Fig. 4.5h), the electronic mode energy increases as the temperature decreases. This temperature dependence for a plasmon was also seen in an optical study of $Cu_{0.07}TiSe_2$ [64]. Hall effect measurements show that the carrier density is temperature-independent at these dopings [65], meaning the change in plasma frequency must be due to a change in the effective mass below $T = 300$ K, based on equation (4.1). The change in effective mass indicates significant renormalization of the bands in the normal state for materials in which superconductivity emerges at low temperature. There is some evidence for such renormalization in photoemission spectra on $Cu_{0.065}TiSe_2$ [66]. In addition, this temperature dependence has been seen in materials such as Bi_2Te_3, Sb_2Te_3, and $Cu_xBi_2Se_3$ [67, 68], and has been associated with a temperature dependence of the effective mass - suggesting that this behavior is the normal state for this system.

For $x = 0.026$ (Fig. 4.5e) and $x = 0.029$ (Fig. 4.5f), we discover that the electronic mode energy is approximately independent of temperature suggesting a crossover from excitonic behavior at dopings $x <$

0.026 to the normal behavior for $x \geq 0.066$. These observations suggest that the excitonic effect disappears by $x = 0.026$, which is far short of the PLD suppression that occurs at $x > 0.10$.

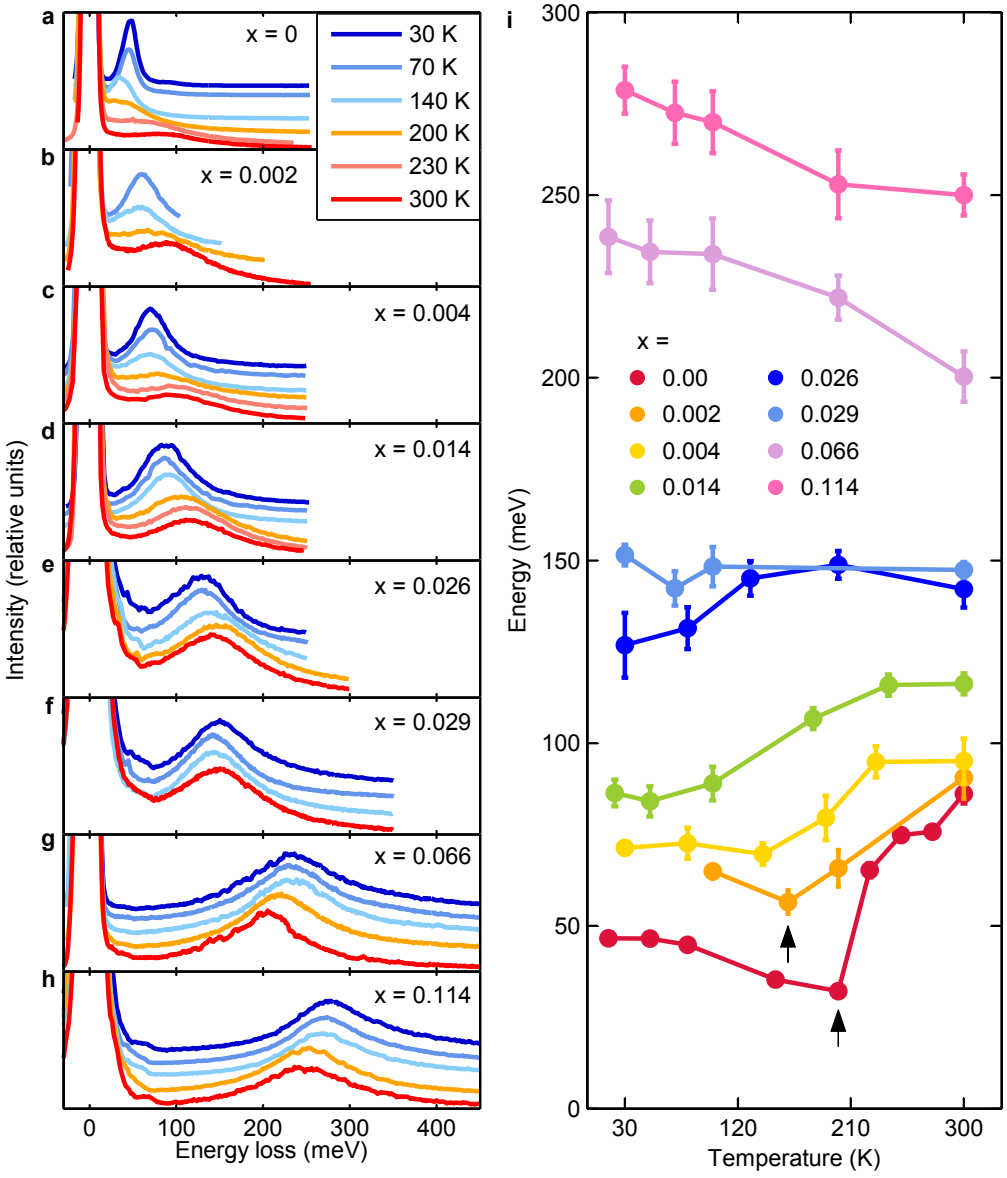

Figure 4.5: **Temperature Dependence of the Electronic Mode at q = 0.** **a**, M-EELS spectra at $\mathbf{q} = 0$ for $x = 0$, showing an electronic mode at 83 meV that shifts and sharpens below T_{PLD} (spectra have been offset for clarity). This data has been reproduced from Ref. [8]. **b-d**, Spectra for $x = 0.002$, 0.004, and 0.014, showing an electronic mode that shifts and sharpens slightly below T_{PLD}. **e-f**, Spectra for $x = 0.026$ and 0.029, showing an electronic mode that is largely temperature-independent. **g-h**, Spectra for $x = 0.066$ and 0.114, showing an electronic mode that shifts to higher energy as the temperature decreases. **i**, Temperature dependence of the electronic mode energy for different dopings, determined from fits to the spectra in **a-h**. The error bars represent statistical and systematic contributions, the latter determined by applying several fit models to the data (discussed in Section 4.7).

4.6 Dispersions of the Electronic Collective Mode

We gain further insight into the suppression of the exciton condensate by measuring the full momentum dependence of the electronic mode. In Ref. [8], we demonstrated that for $x = 0$ the electronic mode behaves as an ordinary plasmon at $T = 300$ K, softens toward zero energy at $T = 185$ K $\sim T_{\mathrm{PLD}}$, and hardens into an amplitude mode of the condensed excitons with $\omega = 47$ meV at $T = 17$ K (Fig. 4.6j). In Fig. 4.6a-c, we present M-EELS data on a semimetallic sample with $x = 0.002$. At $T = 300$ K (Fig. 4.6a), the electronic mode shifts up slightly in energy and broadens as $\mathbf{q}$ increases along the (1,0) direction. Upon cooling to $T = 160$ K $< T_{\mathrm{PLD}}$ (Fig. 4.6b), the electronic mode softens toward zero energy and cannot be distinguished from the elastic line near $\mathbf{q_0} = (0.5, 0)$, as in $x = 0$. At $T = 100$ K (Fig. 4.6c), the mode hardens into an amplitude mode at $\omega = 65$ meV and its energy remains approximately constant for all momenta. We see that the amplitude mode frequency actually *increases* as the exciton condensate is suppressed.

In Fig. 4.6d-f, we find that the dispersion of the electronic mode does not change with temperature for a metallic sample with $x = 0.026$. The energy of the electronic mode is approximately independent of momentum at all temperatures, including those above, near, and below $T_{\mathrm{PLD}} \approx 140$ K. In a superconducting sample with $x = 0.070$ and $T_{\mathrm{PLD}} \approx 70$ K, the electronic mode again remains dispersion-less at all temperatures (Fig. 4.6g-i). The lack of momentum-dependence and damping at $T = 300$ K is unusual when compared to the bulk plasmon dispersion in a metal like aluminum [69]. The absence of a soft electronic mode in these measurements validates that the full excitonic effect is absent by $x = 0.026$, where the PLD is still very pronounced.

To compare the behavior of the electronic mode between different dopings, we quantify its behavior by fitting the M-EELS spectra with a series of Gaussian and Lorentzian functions for the elastic peak, phonon modes, and the electronic mode, including both Stokes and anti-Stokes (energy gain) features. A discussion of this fitting scheme is addressed in the next section. In Fig. 4.6j-n , we see that the soft electronic mode, which signals the formation of a finite population of excitons, only occurs in materials with $x < 0.014$. For $x \geq 0.014$, the electronic mode no longer exhibits soft mode behavior, indicating that the exciton condensate disappears at $x = 0.014$, before the semimetal-metal transition at $x = 0.025$.

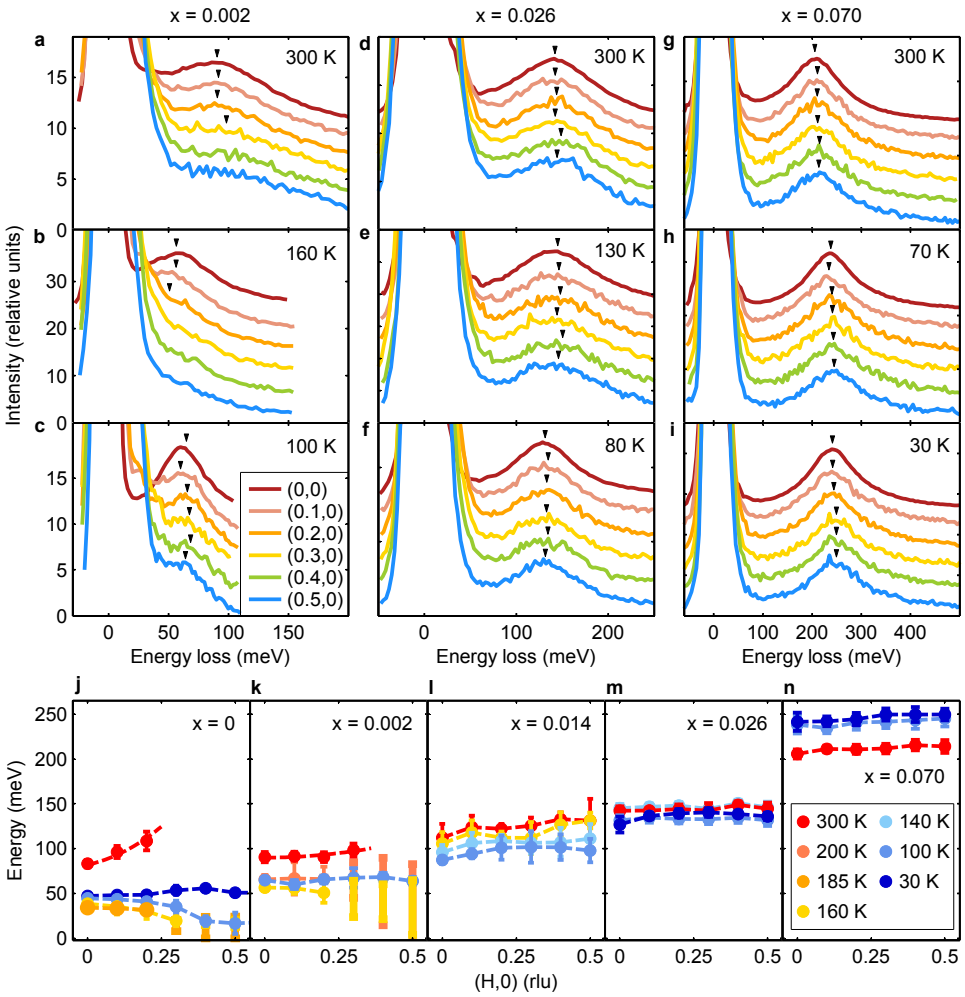

Figure 4.6: **Momentum Dependence of the Electronic Mode in Cu_xTiSe_2.** **a**, Normal state M-EELS spectra for $x = 0.002$, showing a plasmon at $\omega = 90.5$ meV that disperses to higher energy and damps. **b**, $x = 0.002$ spectra at $T = 160$ K, showing the electronic mode reverse its dispersion, softening toward 0 meV at $\mathbf{q_0} = (0.5,0)$. **c**, $x = 0.002$ spectra at $T = 100$ K, showing a hardened, nondispersive electronic mode at $\omega = 65$ meV. **d-f**, Spectra for $x = 0.026$, showing a nondispersive electronic mode at $T = 300$ K, 130 K, and 30 K. **g-i**, Spectra for $x = 0.070$, showing a nondispersive electronic mode at $T = 300$ K, 70 K, and 30 K. Arrowheads indicate the peak energy determined by our data fits (Section 4.7). **j-n**, Dispersion curves along the (1,0) momentum direction for different dopings determined by fitting the raw spectra in **a-i**. The errorbars represent statistical and systematic contributions, the latter determined by fitting the spectra with several different fit models (Section 4.7). Thick, vertical bars denote spectra where the electronic mode is not discernible from the elastic line. Data points in **j** are reproduced from Ref. [8].

4.7 Quantifying the Electronic Mode

This section outlines the method for obtaining the energy points and error bars in Fig. 4.6. The following procedure was repeated at each momentum value and temperature for each x_{eff} value.

There are several main sources of systematic error in the measurement. These include the shift of the elastic line during the experiment due to drifts in the voltages of the M-EELS lens elements, ambiguity in

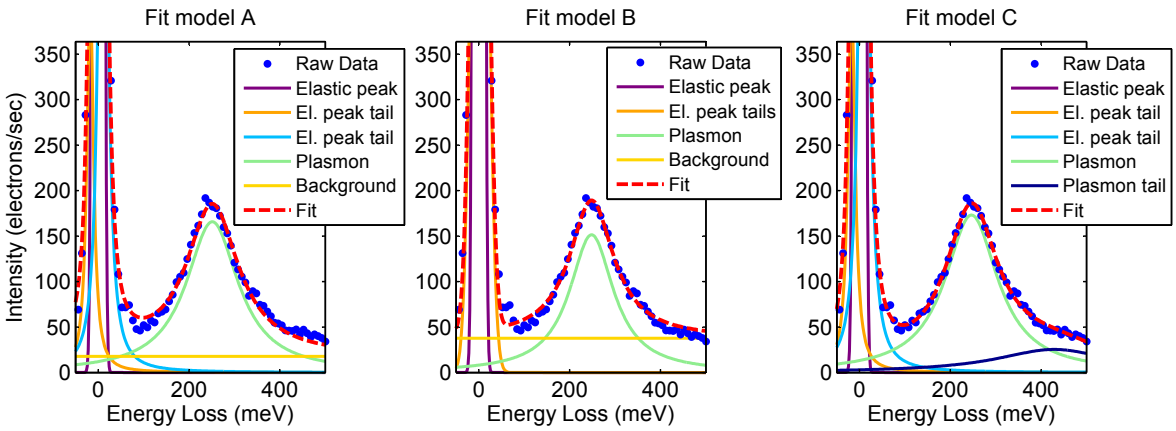

Figure 4.7: **300 K Fits**
Fits to the $T = 300$ K, $\mathbf{q} = (0,0)$ data for an $x_{\text{eff}} = 0.114$ sample. Details of the three fit schemes are given in the text. The plasmon energy for each model is defined to be the plasmon peak position from the fit minus the elastic peak position from the fit. The plasmon energies from each of the three models are averaged together to get the final result for the plasmon energy.

distinguishing the electronic mode from phonon modes (especially for samples with $x_{\text{eff}} < 0.01$ and in the vicinity of the phase transition), and distinguishing the electronic mode from the background continuum.

To estimate these errors, each spectrum was fit using the least squares method according to three different schemes. Scheme A uses a Gaussian profile to fit the elastic peak, two Lorentzian profiles to fit what are either the tails of the elastic peak or low energy phonons, a Lorentzian profile for the plasmon, and a constant background. Scheme B uses a Gaussian profile for the elastic peak, a second Gaussian profile the elastic peak tails, a Lorentzian profile for the plasmon, and a constant background. Scheme C uses a Gaussian profile for the elastic peak, two Lorentzian profiles for the elastic peak tails, a Lorentzian profile for the plasmon, and a second Lorentzian profile for the high-energy tail of the plasmon. If more phonons are visibly present in a spectrum, additional Lorentzian profiles are added to the schemes for each phonon. An example of each fit scheme is shown in Fig. 4.7 for $x_{\text{eff}} = 0.114$ spectra at $\mathbf{q} = 0$ and $T = 300$ K. For low effective dopings ($x_{\text{eff}} < 0.01$), the tail of the plasmon was not pronounced and only fit schemes A and B were used. Fig. 4.8 shows example fits for the $\mathbf{q} = (0.4,0)$ spectra at $T = 200$ K for an $x_{\text{eff}} = 0.002$ sample.

In each fit scheme, the plasmon energy is defined as the difference between its fit value and the position of the elastic peak from the fit,

$$\begin{aligned} E_p^A &= E_{fit}^A - E_0^A \\ E_p^B &= E_{fit}^B - E_0^B \\ E_p^C &= E_{fit}^C - E_0^C \end{aligned} \tag{4.4}$$

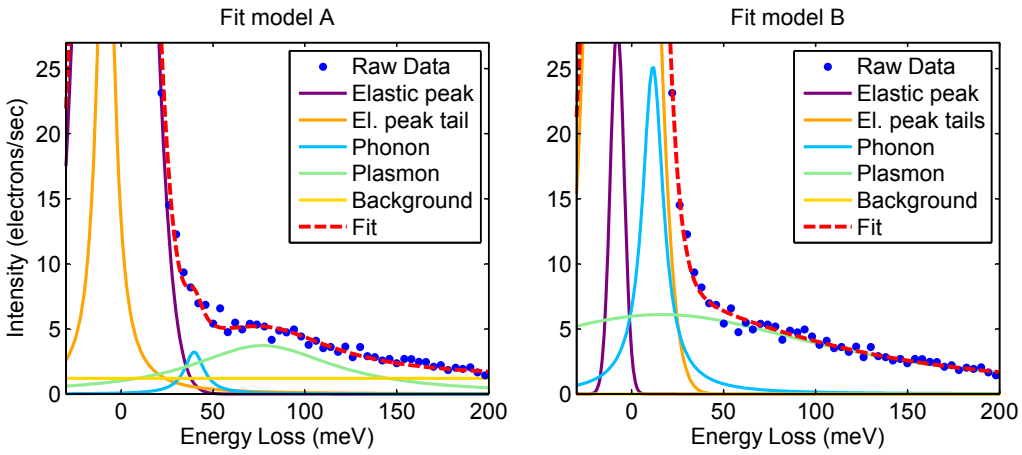

Figure 4.8: **200 K Fits**
Fits to the $T = 200$ K, $\mathbf{q} = (0.4,0)$ data for an $x_{\text{eff}} = 0.002$ sample. Details of the two fit schemes are given in the text. The plasmon energies from the two fit models are averaged together to get the final result for the plasmon energy.

where E_{fit} and E_0 are the fit energies of the plasmon and elastic peak in each of the three fit schemes. The plasmon energy is taken to be the average of these three values,

$$E_p = \frac{E_p^A + E_p^B + E_p^C}{3}. \tag{4.5}$$

The statistical source of error for each scheme is calculated by adding the standard deviations of the plasmon position and the elastic peak position in quadrature,

$$\begin{aligned} \delta_A &= \sqrt{(\delta_{fit}^A)^2 + (\delta_0^A)^2} \\ \delta_B &= \sqrt{(\delta_{fit}^B)^2 + (\delta_0^B)^2} \\ \delta_C &= \sqrt{(\delta_{fit}^C)^2 + (\delta_0^C)^2} \end{aligned} \tag{4.6}$$

where δ_{fit} and δ_0 are the errors in the plasmon energy and elastic peak energy, respectively, in each of the three schemes. The systematic error is estimated as the deviation of the plasmon energy obtained in each of the three fitting schemes from the average value:

$$\begin{aligned} \sigma_A &= |E_p^A - \omega_p| \\ \sigma_B &= |E_p^B - \omega_p| \\ \sigma_C &= |E_p^C - \omega_p|. \end{aligned} \tag{4.7}$$

The final error bars come from adding the statistical and systematic errors in quadrature,

$$\sigma = \sqrt{\delta_A^2 + \delta_B^2 + \delta_C^2 + \sigma_A^2 + \sigma_B^2 + \sigma_C^2}. \tag{4.8}$$

4.8 Exciton Fluctuations

Although the soft mode behavior disappears at $x = 0.014$, the electronic mode q=0 behavior suggests that there are still excitonic effects at play up to $x = 0.066$ at which the system is in its normal state. There has been recent work showing that $TiSe_2$ exhibits excitonic fluctuations above $T > T_{\mathrm{PLD}} = T_{\mathrm{XC}}$ [70, 71]. To quantify the excitonic fluctuations in this work we define a dimensionless parameter, A, such that

$$A = \frac{\omega(T) - \omega(300K)}{\omega(300K)} \tag{4.9}$$

and

$$\delta A = A(T, x) - A(T, x = 0.11) \tag{4.10}$$

The fluctuating region comes from the temperature below which the plasmon energy starts to shift to lower energies at q=0 as shown in Figure 4.5i. δA goes to zero at room temperature and high doping where excitonic fluctuations no longer exist. In addition, these fluctuations are only meaningful once we have lost the soft mode associated with the full exciton condensation state. Table 4.3 is the calculated δ_A values for all the dopings at several temperatures.

Table 4.3: δA

x	30K	70K	100K	200K	300K
0	-	-	-	-	0
0.002	-	-	-	-2.855	0
0.004	-	-	-	-0.1752	0
0.014	-	-0.3664	-0.3142	-0.0936	0
0.026	-0.2230	-0.1653	-0.0593	-0.0348	0
0.029	-0.0874	-0.1245	-0.0737	-0.0118	0
0.066	0	0	0	0	0
0.114	0	0	0	0	0

4.9 Discussion

The overall behavior of the excitonic effect in Cu_xTiSe_2 is summarized in the phase diagram in Fig. 4.9. The phase diagram shows the superconducting dome and PLD phase boundary lines determined in previous

studies [8,23], the semimetal-metal transition defined as the appearance of a zero-crossing in Re[$\epsilon(\omega)$] using our Drude fits, the excitonic phase boundary determined from the temperature at which the electronic mode softens to zero energy at $\mathbf{q_0}$, and the excitonic fluctuation parameter, δ_A, determined from the temperature at which the electronic mode energy starts to shift to lower energies at q=0. We see that the excitonic transition departs from the PLD transition as x increases, falling to zero at $x = 0.014$. The exciton condensate is suppressed even before the semimetal-metal transition at $x = 0.025$, indicating that the excitonic transition is extremely sensitive to screening.

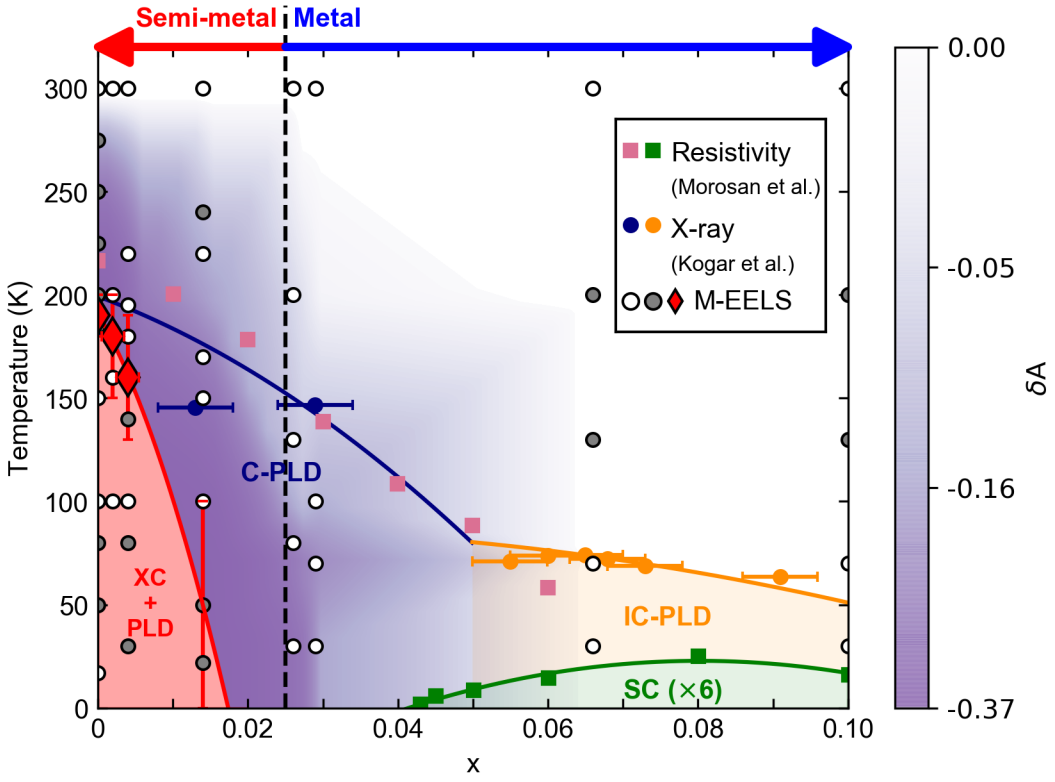

Figure 4.9: **Phase diagram of Cu_xTiSe_2.**
The red diamonds indicate the temperature at which the electronic mode softens most completely toward zero energy, as measured in this study with M-EELS. The black outlined circles are every point that has M-EELS data, where the grey filled circles are M-EELS data will full dispersions. The purple gradient represents the exciton fluctuations parameter and is a linear interpolation of the values found in 4.3. Filled circles are the PLD transition temperature measured with x-ray diffraction, where blue circles indicate a commensuarate PLD (C-PLD) and orange circles indicate an incommensurate PLD (IC-PLD), and are taken from Ref. [8]. The pink squares are the temperature at which the resistivity anomaly associated with the PLD occurs and the green squares are the superconducting transition temperature, both taken from Ref. [23]. The black dashed line indicates the semimetal-metal transition found from Fig. 4.3c.

The separation of the excitonic transition from the commensurate PLD is unexpected. Since the pioneering theoretical work of Kohn and Sherrington [6], the belief has been that there is no distinction between

a Bose condensate of excitons in a semi-metal and a conventional, structural phase transition. The two orders are expected to always coincide in a material, since they break the same symmetries, making them indistinguishable from a symmetry perspective. This is the reason for using the term "excitonic insulator" to refer to this state of matter. Our results show that, at least for $TiSe_2$, the excitonic and structural effects are separate degrees of freedom that can exhibit distinct transitions.

Although the exciton condensate is suppressed at $x = 0.014$, there still exist excitonic fluctuations for most of the phase diagram. These fluctuations compete against the normal state behavior resulting in a temperature independent electronic mode for $x = 0.026$ and $x = 0.029$. The intermediate regime between the excitonic and normal states feels the effects from both and these opposing q=0 behaviors cancel each other. As the material becomes a better conductor, these fluctuations get completely screened out. Experimentally realizing excitonic fluctuations in Cu_xTiSe_2 is an important as it is has already theoretically been demonstrated that excitonic fluctuations can mediate superconductivity [9, 10].

Our study reveals additional important conclusions about the exciton condensate and other properties of Cu_xTiSe_2. The first is that the excitonic transition is extremely sensitive to screening since it is suppressed before the semimetal-metal transition at $x = 0.025$. The amplitude mode frequency increases with doping, also indicating that the energy required to create another electron-hole pair increases as the system more effectively screens the Coulomb interaction that binds the excitons. The second conclusion is that the normal state out of which the superconductivity forms is an anomalous metal. For $x = 0.029$, the plasmon energy is approximately independent of temperature, due to the fact that excitonic fluctuations exist in this region and compete with the normal state behavior. However, for $x > 0.065$, the plasmon is strongly temperature-dependent, suggesting the quasiparticle band structure is renormalizing in an unusual way even far above T_{SC}. The third conclusion is that the electronic mode is not strongly $\mathbf{q}$-dependent at $x > 0.014$ and does not follow the conventional dispersion for a plasmon in a Lindhard metal [44]. We checked that the nondispersive behavior is not a consequence of disorder from copper intercalation by confirming that the PLD superlattice peaks remain sharp at high dopings (Fig. 4.4). Since non-dispersive plasmons are a feature of beyond-RPA effects in strongly interacting metals [72], future studies should consider whether such effects are relevant in Cu_xTiSe_2.

Chapter 5

Probing Finite-Momentum Charge Collective Modes in Nb-doped $SrTiO_3$

Ionic semiconductors, are generically characterized by the interaction of longitudinal-optical (LO) phonons and collective charge carrier modes. Due to their polar nature, long range polarization fields can couple the longitudinal optical (LO) phonons to collective charge modes including plasmons. This is especially important in degenerate systems where the plasmon frequency is comparable to the LO phonon frequencies.

One doped ionic semiconductor that stands out is electron doped $SrTiO_3$, which exhibits aborted ferroelectricity due to quantum fluctuations [11], dilute (unconventional) superconductivity at carrier densities as low as 5.5×10^{17} cm^{-3} [12], and charge transport properties that implicate bad metal behavior [13]. Understanding the charge collective mode dynamics can provide insight into the nature of these unusual properties.

In this work, we use momentum-resolved electron energy loss spectroscopy (M-EELS) to measure the dispersion, temperature, and doping dependence of the collective modes in $SrTi_{1-x}Nb_xO_3$. Experimental work with a fracturing technique for surface preparation, allows us to probe these collective modes in an ultra-high vacuum (UHV) environment. This fracturing technique takes advantage of the fact that M-EELS, while a surface technique, is bulk sensitive, while for other surface techniques (such as ARPES), this sample preparation would not work. Using M-EELS in conjunction with the sample fracturing technique, we show conservation of in-plane momentum achieved using this fracturing technique as demonstrated through the observation of a dispersive acoustic phonon. In addition, we measure a non-dispersive plasmon whose energy and dispersion deviate from infrared spectroscopy measurements and RPA predictions.

5.1 Properties of $SrTiO_3$

In its undoped state, $SrTiO_3$ is an insulator with a 3.22 eV band gap [73]. It has a cubic perovskite structure with a lattice parameter of a = 3.905 $\mathring{A}$. The oxygen atoms form an octahedral cage around a titanium atom as shown in Figure 1a. In addition, this material is a polar crystal so optical phonon vibrations can produce a macroscopic polarization in the material, and in turn, a long range electric field. This results in the well-known splitting of the longitudinal optical (LO) and transverse optical (TO) phonons [74] according to the Lyddane-Sachs-Teller relation:

$$\frac{\omega_{LO}}{\omega_{TO}} = \sqrt{\frac{\epsilon_0}{\epsilon_\infty}} \tag{5.1}$$

Where ϵ_0 is the permittivity of free space and ϵ_∞ is the background dielectric constant.

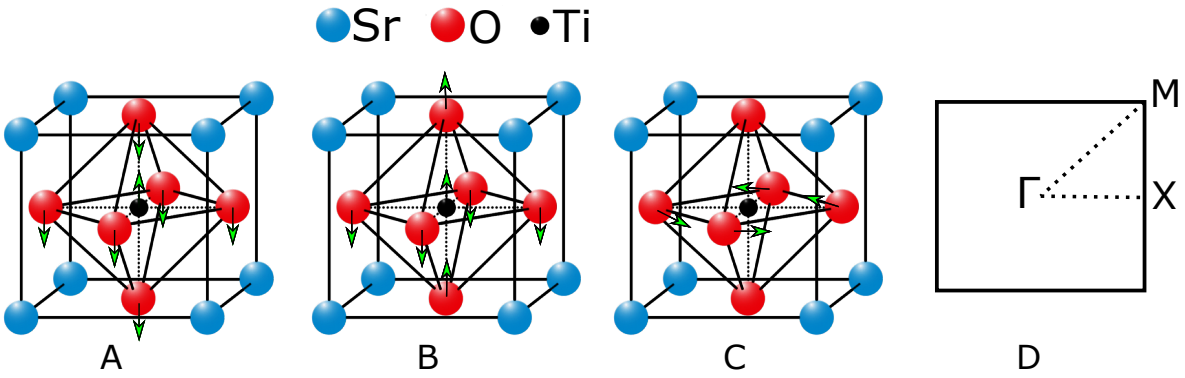

Figure 5.1: **Cubic Perovskite Structure**
(A) and (B) Ionic vibrations of the 58 meV and 93 meV optical phonons [75, 76](C) Cubic lattice structure undergoing an antiferrodistortive transition due to the rotation of the oxygen. (D)Cubic lattice Brillouin zone where all data in this thesis is taken along the Γ-X direction.

At 105 K, the lattice undergoes a structural transition and becomes tetragonal (a = 5.507 $\mathring{A}$, c = 7.796 $\mathring{A}$) [77]. This transition, also known as the antiferrodistortive transition (AFD), comes about due to the rotation of the octahedral oxygen cage around the c axis (Figure 5.1C) [78].

Unlike its periodic table neighbor $BaTiO_3$, $SrTiO_3$ never reaches the ferroelectric ordered phase. As temperature is further decreased below the AFD transition, this system exhibits a ferroelectric instability. The dielectric constant increases as if the system is about to transition into a ferroelectric state, but then plateaus at around 20,000 times the vacuum permittivity [28] [11]. This deviation from ferroelectricity is due to quantum fluctuations causing the system to remain in a quantum paraelectric phase. A signature of

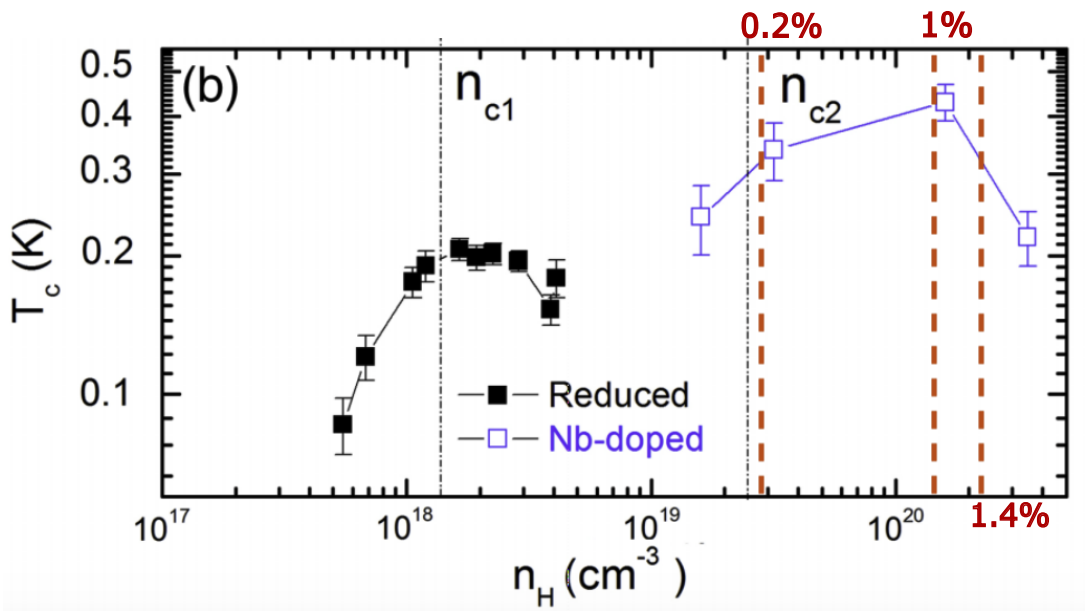

Figure 5.2: **$SrTiO_3$ Phase Diagram**
(a) The superconducting transition temperature as a function of carrier concentration. Figure taken from [80]. Two supercondonducing domes emerge from electron doping with niobium or oxygen reduction. n_{c1} and n_{c2} are critical dopings at which a new band starts to fill. Overlayed on the figure are the dopings measured in this work, with carrier densities that span the range of the Nb doped superconducting dome.

this instability is the incomplete softening of a 12 meV phonon mode at Γ, the center of the Brillouin zone. This instability occurs below 40 K, when the system starts to deviate from Curie law behavior [11].

5.1.1 Electron Doped $SrTiO_3$

Introducing electrons in a very polar material like $SrTiO_3$ forms quasiparticles called polarons. A polaron is a conduction electron that is bound to a lattice due to self-induced polarization from an ionic crystal. For small amounts of electrons, the resulting polarons are localized due to the strong Coulomb nature of the LO phonons. Above the mobility edge, measured as n = 2×10^{16} cm^{-3} [79], electrons fill the conduction band and the strong Coulomb forces get screened making the polarons become mobile in the lattice. [16]

As this material is further doped with electrons, superconductivity emerges. Electrons can be added to the system either by removing oxygen atoms or by replacing titanium atoms with niobium. As seen in Figure 5.2, there are two superconducting domes, one from oxygen deficiency and one from niobium doping. The oxygen deficient samples become superconducting at a lower carrier density than the niobium doped material. In addition, it has been found that electron doped $SrTiO_3$ is a multi-band superconductor [80].

For carrier densities below the critical doping, n_{c1}, electrons fill a single band. As the carrier density is increased, two bands start to fill with electrons (below critical doping n_{c2}) and eventually electrons occupy three bands (above n_{c2}).

The superconductivity that forms in this system from electron doping fails to follow BCS-like phenomenology. In BCS theory, the attraction between electrons only occurs as long as the electrons that are participating are within a narrow range around the Fermi level [81]. In most superconductors, this is satisfied by the fact that the Debye temperature (i.e. the energy scale of the phonons) is much smaller than the Fermi energy. In electron doped $SrTiO_3$, the Debye temperature, measured as 693 K (approximately 60 meV) for undoped $SrTiO_3$ [82], is an order of magnitude larger than the Fermi energy of the oxygen deficient dopings and on the same order of magnitude as the niobium doped samples [83] [12]. Therefore, BCS theory does not hold.

In addition to being a dilute superconductor, $SrTi_{1-x}Nb_xO_3$ exhibits unique charge transport properties such as mobility that changes several orders of magnitude with temperature [13], resistivity at high temperatures that goes as T-cubed and resistivity that surpasses the Mott–Ioffe–Regel limit [29] (the limit in which the length between electron collisions is comparable to the mean distance between of the electrons). These findings can be explained by a changing carrier scattering rate and bad metal behavior or by a changing effective mass of the polarons such that their mass increases with increasing temperature [84]. The nature of these findings is still a highly debated topic [27].

Finally, it was discovered that heterostructures of $SrTiO_3$ with other insulating materials such as LaAlO3 form a metallic two-dimensional electron gas (2DEG) at the interface [85] that exhibits superconductivity [86]. This discovery in the early 2000s renewed interest in understanding the phenomena in this material 40 years after superconductivity was initially discovered. In addition it was found that the 2DEG forms at the interface with vacuum (as vacuum is insulating) [87] for a wide range of dopings from below the mobility edge $n < 10^{13} cm^{-3}$ to highly doped materials $n > 10^{20} cm^{-3}$. This is important for this work because it allows for us to use inelastic electron scattering on insulating undoped $SrTiO_3$ without the surface charging.

5.1.2 The Role of Plasmons in $SrTi_{1-x}Nb_xO_3$

Ionic semiconductors, are characterized by the interaction of LO phonons and collective charge carrier modes. Due to their polar nature, long range polarization fields can couple the LO phonons to collective charge modes including plasmons. This is especially significant in degenerate systems where the plasmon frequency is comparable to the LO phonon frequencies.

The nature of these collective modes has motivated several theories of superconductivity in electron doped

$SrTiO_3$. Specifically these theories implicate a plasmon mediated superconducting pairing mechanism [14] [15] [16]. In doped $SrTiO_3$, superconductivity survives even when the Fermi temperature becomes an order of magnitude lower or of the same magnitude as the Debye temperature. However, the plasmon energy (ω_p) in this system can be lower than the Fermi energy (E_F) especially in the very dilute samples. This motivated theorists to consider a BCS-like model with plasmons mediating the Cooper pairs where $\omega_p < E_F$ [88].

The work in this thesis explores the dynamics of the collective modes in $SrTi_{1-x}Nb_xO_3$ in its normal state. Measurements of the lattice and electronic collective modes (phonons and plasmons) provide insight on how these modes interact in the system. This motivates the need for experiments to study the momentum dependence of the plasmons and phonons. To do this, we need a technique that can measure the momentum dependence of low energy electronic collective modes, also known as M-EELS.

5.2 Collective Modes of $SrTi_{1-x}Nb_xO_3$ Measured with M-EELS

Using the M-EELS setup described in Chapter 3, we aim to study the doping, temperature, and momentum dependence of the electronic modes in $SrTi_{1-x}Nb_xO_3$. For these experiments we use the reciprocal lattice units (H,K,L) to indicate the transferred momentum such that $\mathbf{q} = 2\pi(\frac{H}{a}\hat{x} + \frac{K}{b}\hat{y} + \frac{L}{c}\hat{z})$ where a = b = c = 3.905 Å. The $SrTi_{1-x}Nb_xO_3$ and $SrTiO_3$ crystals were cleaved in ultra high vacuum (10^{-10}) at room temperature and all M-EELS data were collected using an incident beam energy of 50 eV with 6 meV energy resolution, 0.03 $\AA^1$ momentum resolution, and about 40 pA of incident beam current. The samples were cleaved using a fracturing technique discussed in Section 5.2.1. The out-of-plane momentum transfer was fixed at 2.5 reciprocal lattice units (r.l.u.) in order to see the (1,0) Bragg peak while only changing θ and γ. The samples were prepared so that the cleavage plane surface is oriented normal to the (100) plane.

Normalizing of the M-EELS charge susceptibility was done by applying the f-sum rule. The first moment, f-sum rule on the density response relates the integrated intensity over energy to a function of momentum and known physical constants. Using sum rules is common practice in other scattering techniques such as IR spectroscopy and inelastic neutron scattering. The f-sum rule as written here applies to the bulk response function however M-EELS measures the surface response function. For this work however we use the bulk f-sum rule to normalize the data for plotting and comparing to other experiments.

In this work, the f-sum rule is used to scale the data in the following manner:

$$\int_0^{0.4eV} \omega\chi''(q,\omega)\, d\omega = -\frac{\pi q^2 N}{2m} = Cq^2 \tag{5.2}$$

where m is the mass of electron, N is the carrier density, and the bounds of integration go from 0 to the maximum of the energy range of interest. Plugging in the equation for χ'' derived in Chapter 2,

$$\int_0^{0.4eV} \omega\pi[S(\mathbf{q},-\omega) - S(\mathbf{q},\omega)]\, d\omega = Cq^2. \tag{5.3}$$

Relating to dynamic structure factor to the M-EELS cross section,

$$\int_0^{0.4eV} \omega\pi \frac{[I(\mathbf{q},-\omega) - I(\mathbf{q},\omega)]}{\sigma_0 V_{eff}^2}\, d\omega = Cq^2 \tag{5.4}$$

pulling out the terms that do not depend on energy, we end up with a constant at each q point that depends on the integrated intensity and Coulomb matrix elements,

$$C = \frac{\pi}{q^2\sigma_0 V_{eff}^2} \int_0^{0.4eV} \omega[I(\mathbf{q},-\omega) - I(\mathbf{q},\omega)]\, d\omega. \tag{5.5}$$

This constant is then used a scale factor to relate the finite momentum data to q=0 data such that,

$$S(q \neq 0, \omega) = \frac{I(\mathbf{q},\omega)}{\sigma_0 V_{eff}^2} \frac{C_{q=0}}{C_{q\neq 0}} \tag{5.6}$$

Due to the Coulomb matrix element divergence at q = 0 (see Section 2.3), I will show the raw intensity, I(q=0,ω), and for finite q, I show the dynamic structure factor, S(q,ω) scaled to the q=0 spectra.

The samples used in these experiments were all commercially grown from several suppliers. Table 5.1 outlines the samples and carrier density for each doping studied in this thesis. The carrier density is calculated based on the at% stated by suppliers as well as the measured values from Hall data. The Hall measurements were conducted using a Quantum Design Physical Properties Measurement System (PPMS) at room temperature, scanning a range of magnetic field from -8 to +8 Tesla. Figure 5.3 is a summary of the at% from manufacturers versus the Hall carrier density. The carrier density from the manufacturers and that from Hall measurements are consistent within two standard deviations of the mean.

Each Hall measurement was scanned through the range of magnetic field three times. The average of the slopes of these three measurements is taken as the Hall value in both Table 5.1 and Figure 5.3. The error bars are one standard deviation from the mean of the slopes. Several large samples were measured in the PPMS but then later cut to smaller samples for M-EELS measurements. These are indicated in Figure 5.3 legend as a range of sample numbers.

From these numbers we can calculate the expected plasma frequency based on these bulk carrier measurements assuming Drude-like behavior given by,

$$\omega_p = \sqrt{\frac{Ne^2}{\epsilon_0 m^*}} \tag{5.7}$$

Table 5.1: **$SrTi_{1-x}Nb_xO_3$ Carrier Density**

Atomic % of Nb	Manufacturer	At% Carrier Density ($\frac{1}{cm^3}$)	Hall Carrier Density ($\frac{1}{cm^3}$)
0%	MTI Corporation	-	-
Slightly Doped	MSE Supplies	-	$< 10^{16}$
0.2%	Biotain Crystal	-3.36 $\times 10^{19}$	(-2.89±0.26) $\times 10^{19}$
1%	Biotain Crystal	-1.67 $\times 10^{20}$	(-1.49±0.14) $\times 10^{20}$
1.4%	MTI Corporation	-2.35 $\times 10^{20}$	(-2.13±0.07) $\times 10^{20}$

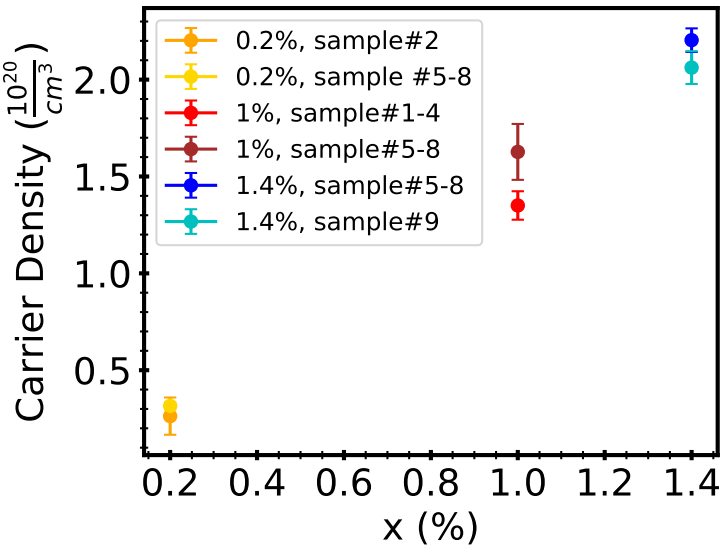

Figure 5.3: **Hall Carrier Density Summary**
Summary of the at% from manufacturers versus the measured Hall carrier density with PPMS. Each data point is the average of three magnetic field sweeps with the errorbars being one standard deviation from the average. Several of these measurements were done on larger samples that were later cut into smaller samples for M-EELS experiments.

where N is the carrier density, m^* is the effective mass of the charge carriers, and ϵ_0 is the permittivity of free space. Due to the fact that the plasma frequency of free carriers is at a lower energy than the inter-band transition (since this is a doped semiconductor), there is a background dielectric constant that the carriers feel. Therefore the plasmon frequency measured in M-EELS is the screened plasma frequency,

$$\omega_{p,screeened} = \frac{\hbar\omega_p}{\sqrt{\epsilon_\infty}} \tag{5.8}$$

where ϵ_∞ is the background dielectric constant.

Calculations of the plasma energy and screened plasma energy are shown in Table 5.2. These values were calculated using m^* and ϵ_∞ using the Hall carrier density values for N. For these calculations we use the reported values for effective mass as $m^* = 0.81m_e$ and $\epsilon_\infty = 5.44$ [89] but these quantities have been shown to be temperature dependent [48].

Table 5.2: **Drude Plasma Energy Calculated from Hall Carrier Density**

Atomic % of Nb	ω_p (eV)	$\omega_{p,screened}$ (eV)
0.2%	0.222±0.067	0.092±0.028
1%	0.503±0.153	0.209±0.064
1.4%	0.603±0.110	0.250±0.046

Figure 5.4 clearly shows the physical change in these materials due to doping with niobium. The undoped, insulating sample is transparent while the highly doped sample is black and shiny. The "slightly" doped sample is less transparent than undoped by eye however there are still not enough carriers to be measured by the Hall effect. Therefore the slightly doped material is presumed to have a carrier density that is below the metal-to-insulator transition, which is experimentally measured as $10^{16}\frac{1}{cm^3}$ [79].

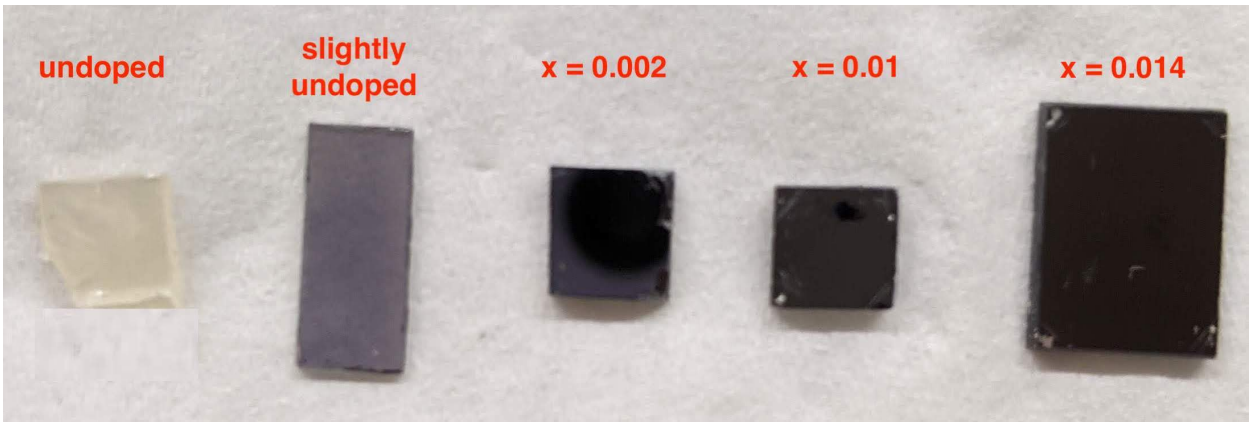

Figure 5.4: **Photo of $SrTiO_3$ and $SrTi_{1-x}Nb_xO_3$ Samples**
The by eye comparison of the effect of niobium doping. The white transparent insulating samples turn black and opaque with niobium doping.

5.2.1 Fracturing Cubic $SrTiO_3$ in Ultra High Vacuum

M-EELS experiments must be carried out in an ultra-high vacuum (UHV) environment. The primary reason for this is that the low-energy electrons (2-200 eV) used in M-EELS make it a surface-sensitive technique that requires sample materials to have pristine, adsorbate-free surfaces. Clean sample surfaces are typically prepared by cleaving the sample in our UHV environment (see Chapter 3). This means that most of the materials we study are cleavable, layered materials. Since $SrTiO_3$ is cubic, it does not naturally cleave and annealing this material introduces oxygen vacancies which alter its carrier density [55]. Therefore a different method of exposing a fresh surface needed to be developed.

We developed a method of notching the sides of each sample as shown in Figure 3.19 (cross section of a sample 1 mm thick). These notches are created using a Wells wire saw. The wire used is made of tungsten

embedded with diamond and has a diameter of 300 microns. Notching the sides of the sample introduces a point of weakness in the crystal so that when force is applied (in vacuum) the sample will fracture. This *in-situ* fracture procedure was implemented by applying a rapid and strong force to the top-post.

Looking at the cleaved samples under an optical microscope shows that the surface is not globally flat but instead has some curvature. This conchoidal fracturing of $SrTiO_3$ has been seen in other perovskite materials [90] and comes about due to the material being brittle with no cleavage plane. Although globally, the surface of fractured $SrTiO_3$ and $SrTi_{1-x}Nb_xO_3$ is not flat, locally, this is not the case. Scanning-tunneling microscopy (STM) experiments have shown that the surface of fractured $SrTiO_3$ exhibits atomically flat terraces that are on the order of tens of nanometers wide [91, 92]. These STM experiments also showed that the atomic surfaces terraces are a mixture of both TiO_2 and SrO surface terminations. The SrO terminations which are prone to oxygen vacancies are wider than the TiO_2 terminations [92]. The surface terminations should not effect interpretations of M-EELS measurements since the electron beam is 0.5mm in diameter, orders of magnitude larger than these terraces. Therefore the electron beam scatters off both TiO_2 and SrO terminated surfaces and the experiment cannot distinguish one from the other. In addition, the M-EELS probe depth, which goes as 1/q, makes this technique not as sensitive to surface features as other techniques like STM.

The globally conchoidal but atomically flat nature of these fractured surfaces are an important distinction to make when using a momentum resolved surface sensitive technique like M-EELS, which requires an atomically flat surface to obtain good momentum resolution. We can see that even though the cleaved surfaces are not flat (Figure 5.2.1), we still see (0,0) and (1,0) Bragg peaks with widths 0.03 r.l.u. (Figure 5.2.1) demonstrating that the surface is crystallographically perfect, and momentum is conserved. This suggests that momentum will be conserved in M-EELS experiments throughout the Brillouin zone.

5.2.2 Multiple Scattering

As discussed in the Chapter 2 the M-EELS cross section is usually described well by the distorted wave born approximation due to the fact that the cross section for elastic scattering is much larger than that for inelastic scattering. Therefore the only multiple scattering that we see acts through the elastic channel and produces the "Bragg enhancement" effect discussed earlier.

However there can be scenarios where multiple scattering occurs during an inelastic scattering process. When this happens, we are in the limit where the scattering cross section is so large we can see multiple scattering events even in the inelastic channel. Therefore the probe electron is scattering multiple times within the sample. This type of scattering is common in a transmission EELS configuration where the

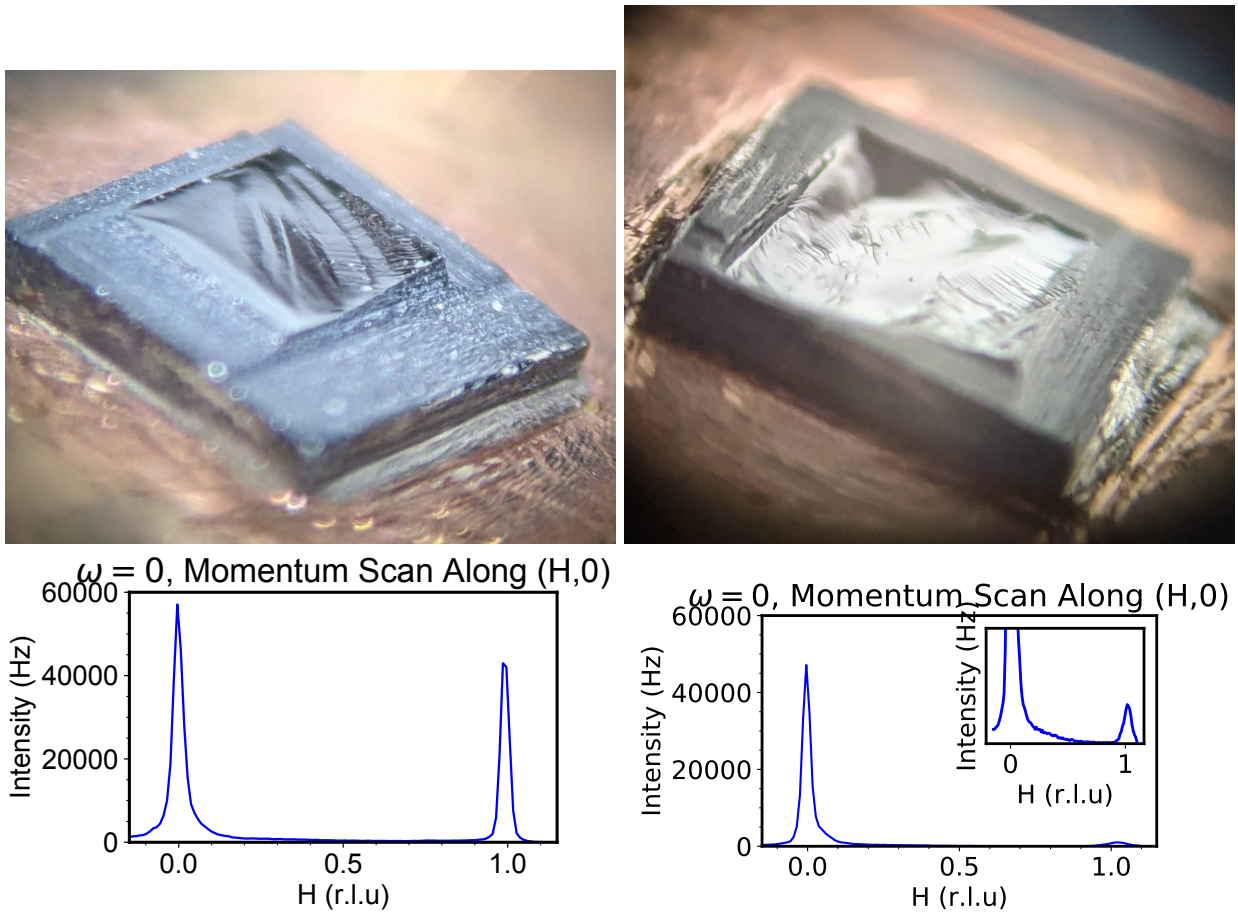

Figure 5.5: **UHV Cleaved $SrTi_{1-x}Nb_xO_3$**
Using the newly developed diamond wiresaw cutting technique, it made it possible to fracture these cubic crystals. The top photos are of $SrTi_{1-x}Nb_xO_3$ samples that were cleaved in UHV at room temperature. The cleaved surfaces are not globally flat however the surface termination has atomically flat terraces. The bottom plots are zero energy momentum scans along the (H,0) momentum direction measured from the above cleaved surfaces respectively. The (0,0) and (1,0) Bragg peaks have widths of about 0.03-0.05 r.l.u. demonstrating that the surface is atomically flat, and momentum is conserved. The inset in the bottom right figure is zoomed into the (1,0) Bragg peak.

multiple scattering is related to the thickness of the sample (i.e. density of scatterers). In the reflection geometry, this multiple scattering is less relevant due to the fact that inelastic features have relatively small spectral weight compared to the elastic spectral weight.

This is not the case for polar materials however such as $SrTiO_3$. $SrTiO_3$ is an ionic crystal that has longitudinal optical phonons that are polarized along the c-axis due to large electric fields produced from moving atoms. The probe electrons can strongly couple to the c-axis polarized optical phonons. In $SrTiO_3$, the optical phonon modes seen in Figure 5.6 at 58 and 93 meV take up a significantly larger percentage of the spectral weight than they do in non-ionic materials such as Sr_2RuO_4 also shown in Figure 5.6. This may

be because EELS measures the longitudinal response, and therefore is more sensitive to c-axis polarized LO phonons than optics, which is more sensitive to the transverse response.

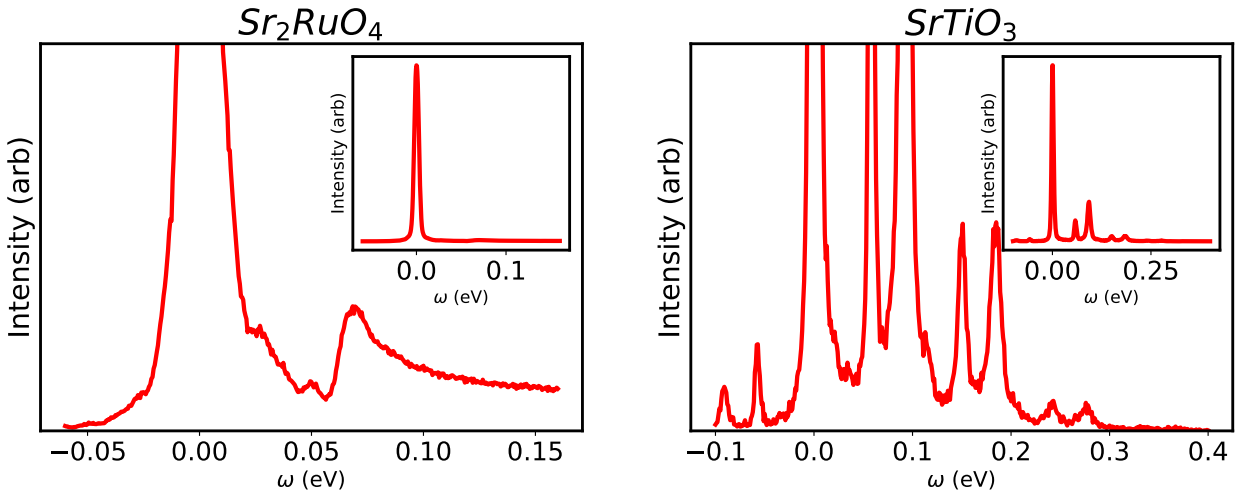

Figure 5.6: **Spectral Weight of Inelastic Features**
The spectral weight of inelastic features varies from sample to sample. On average, the elastic line is orders of magnitude larger than the spectral weight of the inelastic features as seen in the Sr_2RuO_4 data on the left. The inset is zoomed out to show the full elastic line, in doing so, you can not see the inelastic features by eye. There are materials though where the inelastic spectral weight is of comparable order of magnitude to the elastic spectral weight as seen in the $SrTiO_3$ data on the right. When zoomed out to show the full elastic line, the inelastic features are still visible by eye (see inset). In M-EELS this is unique to polar, ionic materials. Due to the strength of the oscillators, multiple scattering overtones are visible and can not be neglected.

Because of the polar nature and strong phonons, overtones due to multiple inelastic scattering are seen in the $SrTiO_3$ M-EELS spectra. There are several mechanisms by which we can see overtones in the inelastic features in M-EELS, as illustrated in Figure 5.7. Figure 5.7a is a representation of electron-phonon interaction where a single electron scatters a single phonon. Figure 5.7b is a representation of multiple scattering in which a single electron scatters multiple phonons (or the same phonon multiple times). In this case, the overtones will be integer multiples of the phonon energies. Figure 5.7c is the case in which an electron scatters and produces two phonons from a single scattering event that are coupled to each other. This occurs if the Hamiltonian that describes the system is non-linear due to anharmonicity. In the scenario where a scattered phonons produces another phonon, the scattered electron is not necessarily at integer multiples of the phonon energy due to the coupling between the phonons.

For $SrTiO_3$, the overtones (up to three harmonics) are clearly visible in the EELS data in this work (Figure 5.8) and in others [93, 94] but are not present in other techniques like IR spectroscopy [48, 95, 96]. In addition, the overtones are integer multiples of the optical phonons such that for the phonons ω_1 and ω_2, the second harmonic energies are $\omega_1 + \omega_2$ and $2\omega_2$, the third harmonic energies are $\omega_1 + 2\omega_2$ and $3\omega_2$, and

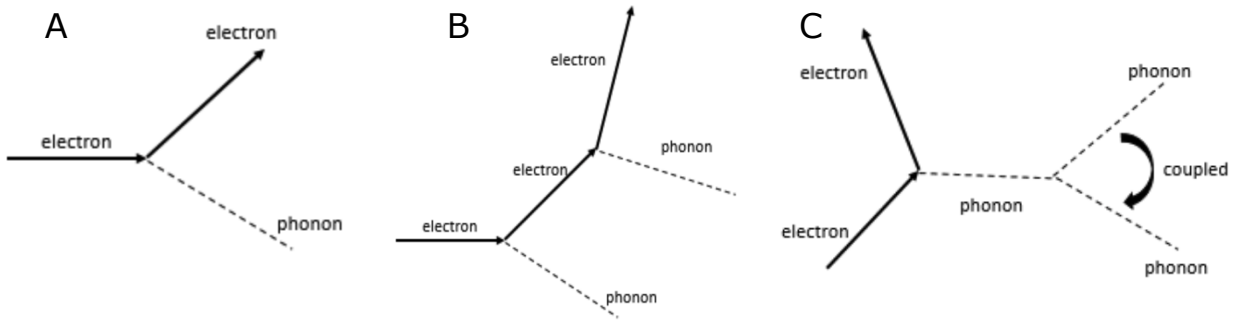

Figure 5.7: **Representations of Multiple Scattering of Electrons**
Multiple scattering can occur via two different mechanisms. (A) Electron-phonon interaction where a single electron scatters a single phonon. This is the dominant interaction for most materials in M-EELS where overtones are not visible. (B) Representation of multiple scattering where a single electron scatters multiple phonons (or the same phonon multiple times). In this case, the overtones will be integer multiples of the phonon energies. (C) Representation of multiple scattering where an electron scatters and produces two phonons from a single scattering event and these phonons are coupled to each other. In this case, the overtones are not necessarily integer multiples of the phonon energy due to the phonon-phonon coupling. This interaction occurs in systems with non-linear Hamiltonians due to anharmonicity.

the forth harmonic energies are $\omega_1 + 3\omega_2$ and $4\omega_2$. We therefore conclude that the overtones of $SrTiO_3$ are due to multiple inelastic scattering of the sort shown in Figure 5.7b.

5.2.3 Collective Modes in $SrTi_{1-x}Nb_xO_3$ for a Range of Carrier Densities

This section will present an in-depth look at what the collective modes of the system look like at different carrier densities. For each doping, first a zero energy momentum scan is presented compared to the dispersion of the low energy acoustic phonon that is well established in this material [97–101]. An acoustic phonon is a propagating collective mode that, in a perfect crystal, will exhibit a clear dispersion. However, this dispersion could be suppressed in a crystal with defects or near a rough surface. The acoustic mode is therefore a good first indication of whether momentum is conserved in the M-EELS measurement. Next we present the momentum dependence of the acoustic phonon, optical phonons, and plasmons at 23K and room temperature. These dispersions are along the (H,0) direction, are scaled by the sum rule as discussed previously, and are offset for clarity. Black arrows indicate significant features such as the dispersing acoustic phonon energy, LO phonon energy, and plasmon energy. Due to the nature of the plasmon being broad and

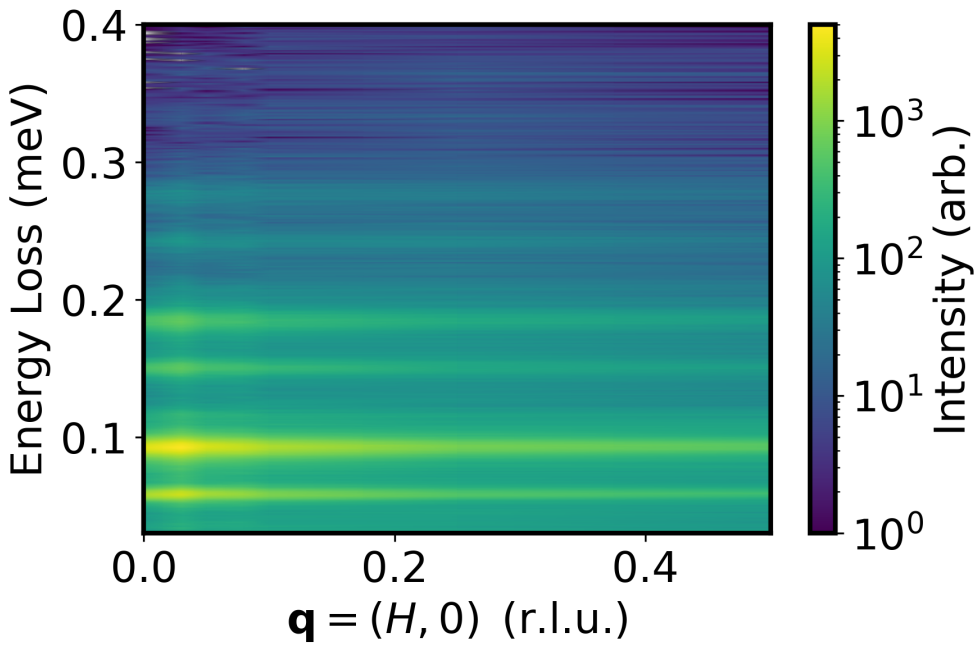

Figure 5.8: **2D Momentum Map of the 2nd, 3rd, and 4th Harmonics in $SrTiO_3$**
Due to its very polar nature, overtones of optical phonons are very visible in M-EELS measurements of $SrTiO_3$, while not visible in other techniques [48, 95, 96]. The $SrTiO_3$ spectrum shows strong optical phonons at 58 meV and 93 meV (note log intensity scale), second harmonics of these phonons are seen at 151 meV and 186 meV, third harmonics at 244 and 279 meV, and forth harmonics at 337 and 372 meV. These modes are constant throughout the Brillouin zone, as expected from optical phonons.

in the background of strong phonon excitations, a guide to the eye is provided to identify this mode. Finally for each doping we present a q=0 temperature dependence compared to that from IR spectroscopy.

Undoped

At x=0, $SrTi_{1-x}Nb_xO_3$ is insulating, which for electron scattering can cause charging on the sample, impeding the M-EELS measurement. In $SrTiO_3$ however, the interface of the surface with vacuum forms a 2DEG and has oxygen vacancies from the fracturing process (as discussed in sections above). The charge that forms on the surface is enough to get scattering data from the collective modes at least for a short amount of time before charging (i.e. on the order of a day or two as compared to a week of measurements that can be done on non-insulating materials). The small amount of surface charge, measured in ARPES as $2 \times 10^{14} cm^2$ [87] is not enough to see any discernible effect, such as formation of plasmons, in the M-EELS spectra. Three different fractured surfaces were studied in this doping that all reproduced the same inelastic behaviors. The data presented in this section is from one sample that was chosen based off the quality of the zero energy (H,0) scan, the momentum resolution off the surface (FWHM of (0,0) Bragg peak), the number

of temperature/momentum points measured, and the overall scattered intensity off the sample.

Figure 5.9 shows the zero energy momentum scan along the (H,0) direction from a fractured undoped sample. The (0,0) and (1,0) Bragg peaks are visible although slightly broadened (0.13 r.l.u.). The dispersion of the low energy acoustic phonon appears as a shoulder to the elastic scattering line that reaches its maximum energy at the Brillouin zone boundary, q=0.5 r.l.u. This is a propagating mode and has a lorentzian lineshape. We conclude that momentum is conserved when scattering off this surface at finite momentum. In other words, if there is another dispersing collective mode, we should be able to measure its dispersion.

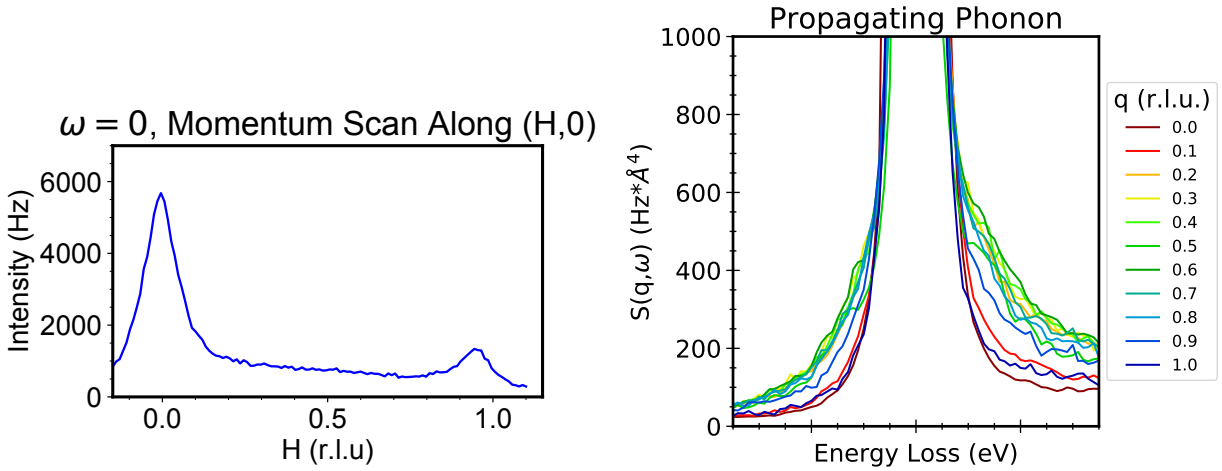

Figure 5.9: **Undoped Fractured Surface**
The left figure shows the zero energy momentum scan showing (0,0) and (1,0) Bragg peaks with 0.13 r.l.u. momentum resolution (determined from the FWHM of (0,0)). We can measure a propagating low energy acoustic phonon mode off this fractured surface (on right).

Figure 5.10 shows the S(q,ω) dispersions of all the collective modes in this material at 300k and 23K. Again, we see the acoustic phonon disperse at both temperatures. Fits to the phonon with a lorentzian function will be discussed in Section 5.3 however for clarity, a best fit of the dispersion of the lorentzian fits is shown with black arrows. There are two Fuchs-Kliewer phonons at $\omega_1 = 57$ meV and $\omega_2 = 93$ meV that are the surface manifestation of the bulk optical phonons and therefore do not disperse. In addition we see overtones at 114 meV ($2\omega_1$), 151 meV ($\omega_1+\omega_2$), and 186 meV ($2\omega_2$) that do not disperse. The presence and dispersions of even higher order overtones is shown in Figure 5.8.

Next we can compare what happens with temperature at q=0 and compare this to infrared spectroscopy (Figure 5.11. The q=0 M-EELS data show nearly identical spectra at room temperature and low temperature. At 300 K, there is a small amount of spectral weight around 30 meV which comes about due to the Bose factor. This data is compared to HR-EELS q=0 data at 470K from [94] which was scaled to fit

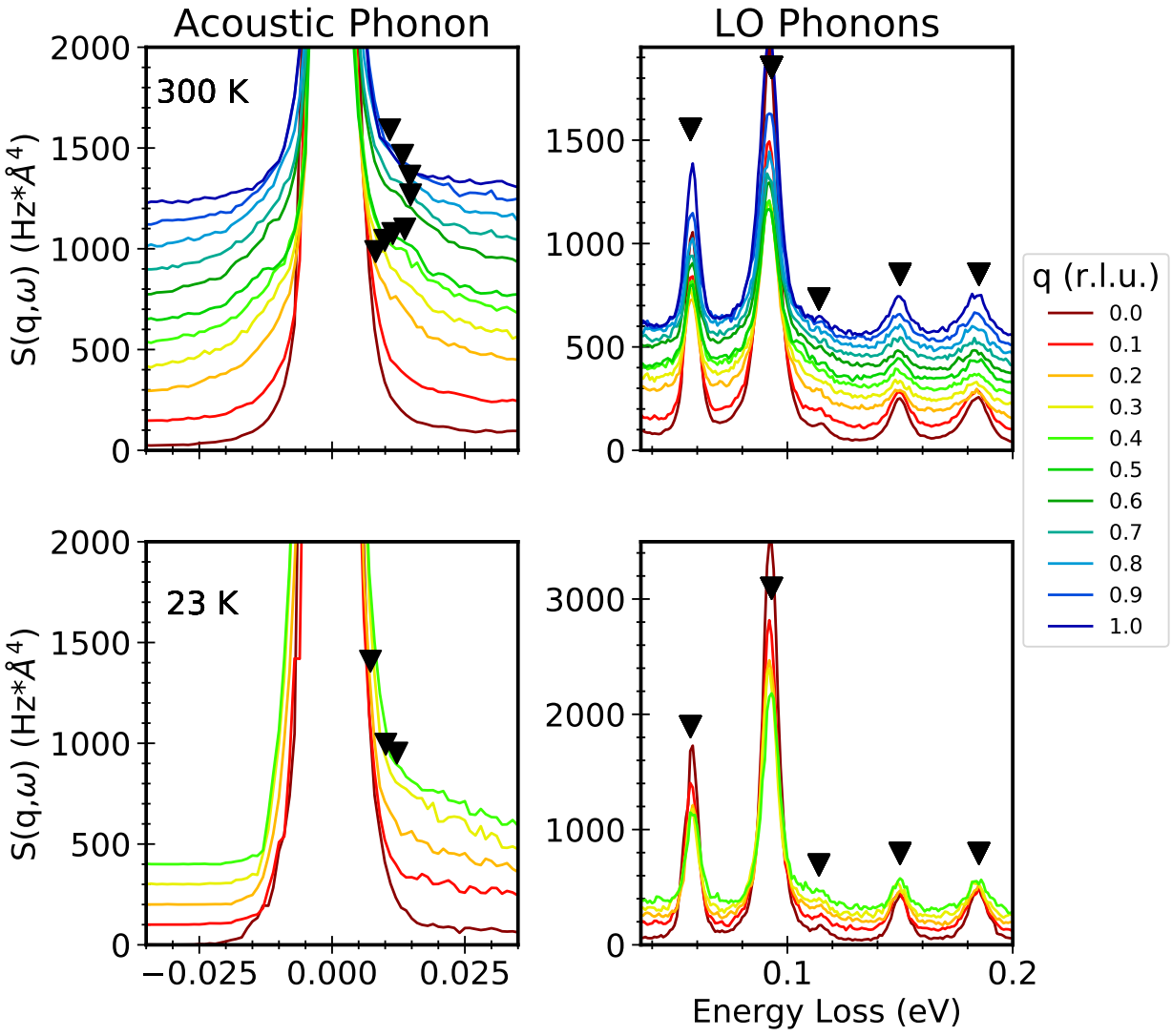

Figure 5.10: **Undoped Dispersions**
Dispersions along the (H,0) for different energy regions at 300 K and 23 K. All spectra are scaled with sum rule and offset for clarity. The q=0 spectra are raw M-EELS intensities to avoid the Coulomb matrix element divergence when calculating S(q,ω). Low energy region shows a propogating dispersing phonon, black arrows are the best fit to the lorentzian fits as described in Section 5.3.3. In the region of 35-200 meV we see two optical phonons and three overtones, black arrows are guide to the eye for each LO mode.

on the same plot. The HR-EELS data is also in good agreement with all the collective mode energies and lineshapes although our M-EELS data has more spectral weight in the phonons and overtones. Comparing this to -Im$[1/(\epsilon(\omega)+1]$, where $\epsilon(\omega)$ was determined from reflectivity and optical conductivity measurements given to us by the authors of [48], we see a good agreement of the data. The phonon energy and lack of temperature dependence are consistent between the two techniques. M-EELS measurements however have broader modes due to a worse resolution than IR spectroscopy and M-EELS sees the presence of the multiple scattering overtones that do not take place in IR measurements.

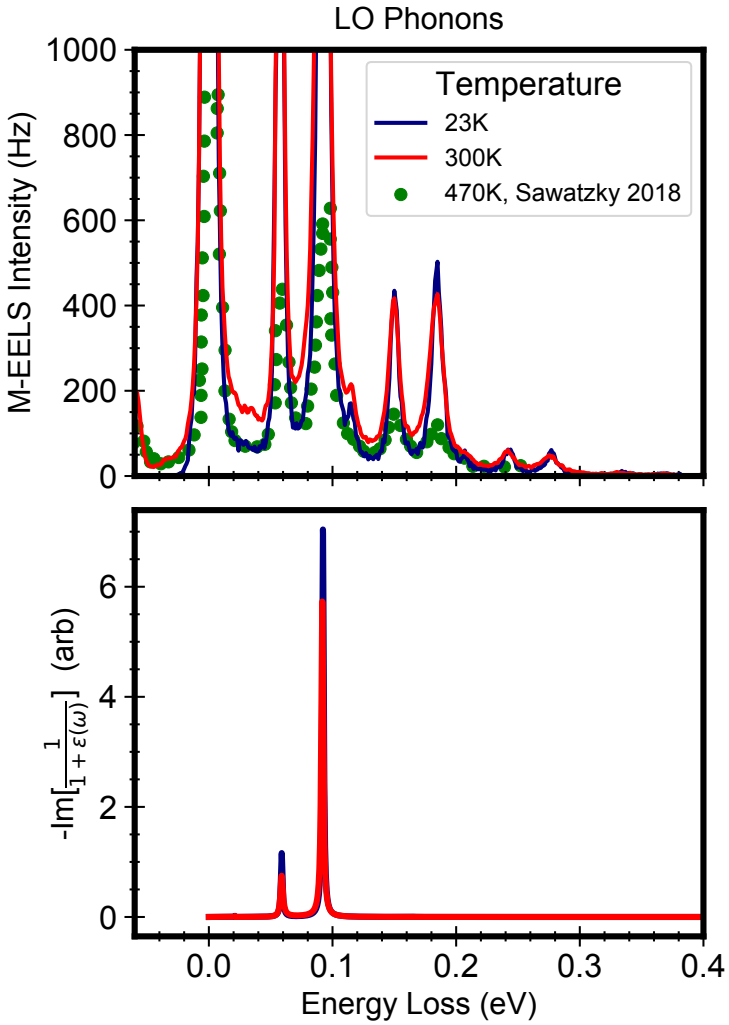

Figure 5.11: **Undoped Temperature Dependence**
Temperature dependence of the optical phonons from M-EELS (top) at q=0 and IR spectroscopy (bottom). Spectra are scaled to elastic line and are not offset. M-EELS data is compared to HR-EELS data on undoped $SrTiO_3$ from [94]

x=0.002

For this composition, the zero energy momentum scan shows (0,0) and a weak (1,0) Bragg peaks (Figure 5.12). The momentum resolution off this sample is 0.037 r.l.u. as determined from the FWHM of the specular peak. The low energy acoustic phonon is broad and does not take on a lorentzian lineshape. This shows a diffusive behavior in momentum that increases in energy up to the Brillouin zone boundary. This means that even though the collective excitation is not propagating on this sample surface we can still get some momentum dependent information. If there is another dispersing collective mode, it should also exhibit this dispersing behavior. Three different fractured surfaces were studied in this doping that all reproduced the same inelastic behaviors including a diffusive acoustic phonon. The data presented in this section is from one sample that was chosen based on the quality of the zero-energy (H,0) scan, the momentum resolution off the surface (FWHM of (0,0) Bragg peak), the number of temperature/momentum points measured, and the overall scattered intensity off the sample.

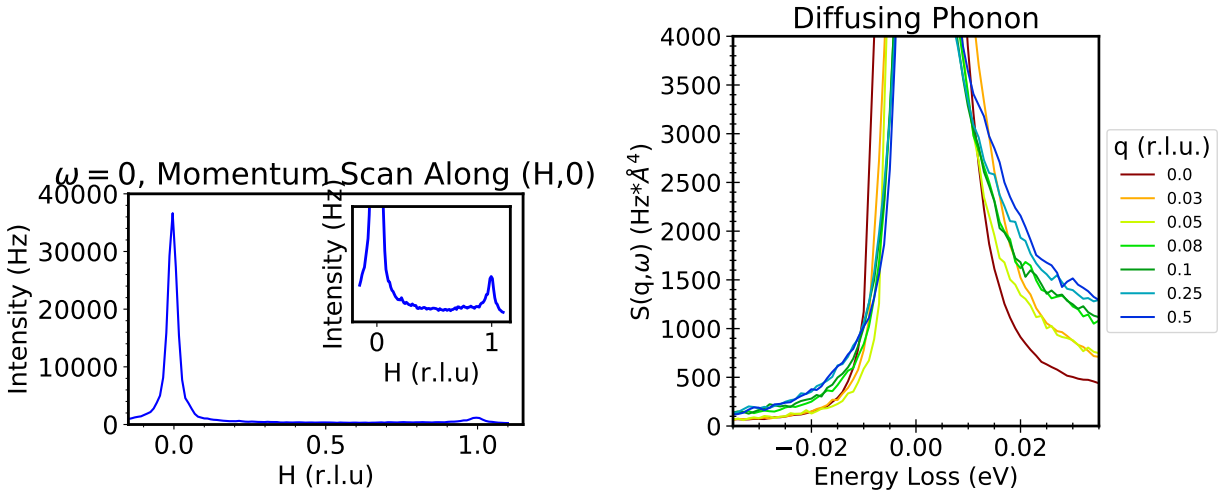

Figure 5.12: **x = 0.002 Fractured Surface**
The left figure shows the zero energy momentum scan showing (0,0) and (1,0) Bragg peaks with 0.037 r.l.u. momentum resolution (determined from the FWHM of (0,0)). We can measure a diffusing low energy acoustic phonon mode off this fractured surface (on right).

At, x=0.002, the carrier density is measured from Hall data as $2.89 \pm 0.26 \times 10^{19} cm^{-3}$. For this doping, we observe the Fuchs-Kliewer phonons and overtones at comparable energies to the undoped material and find that they do not disperse (5.13). The higher order overtones (3rd and 4th harmonics) are almost completely screened, most likely because of the metallic character of this material, and the 93 meV mode has a broad tail. Finally, we see a plasmon that emerges with the addition of carriers. The plasmon is the broad (on the order of 100 meV) background weight that sits underneath the phonons around 100 meV. This energy

agrees well with the calculated screened plasma frequency of 92 ± 28 meV (Table 5.2). Arrows and a guide to the eye are shown to help identify the plasmon mode. At 300 K and 23 K the plasmon remains at a fixed energy throughout the Brillouin zone and does not disperse, in contrast to the acoustic phonon. This suggests the plasmon does not propagate as well as the lattice degrees of freedom.

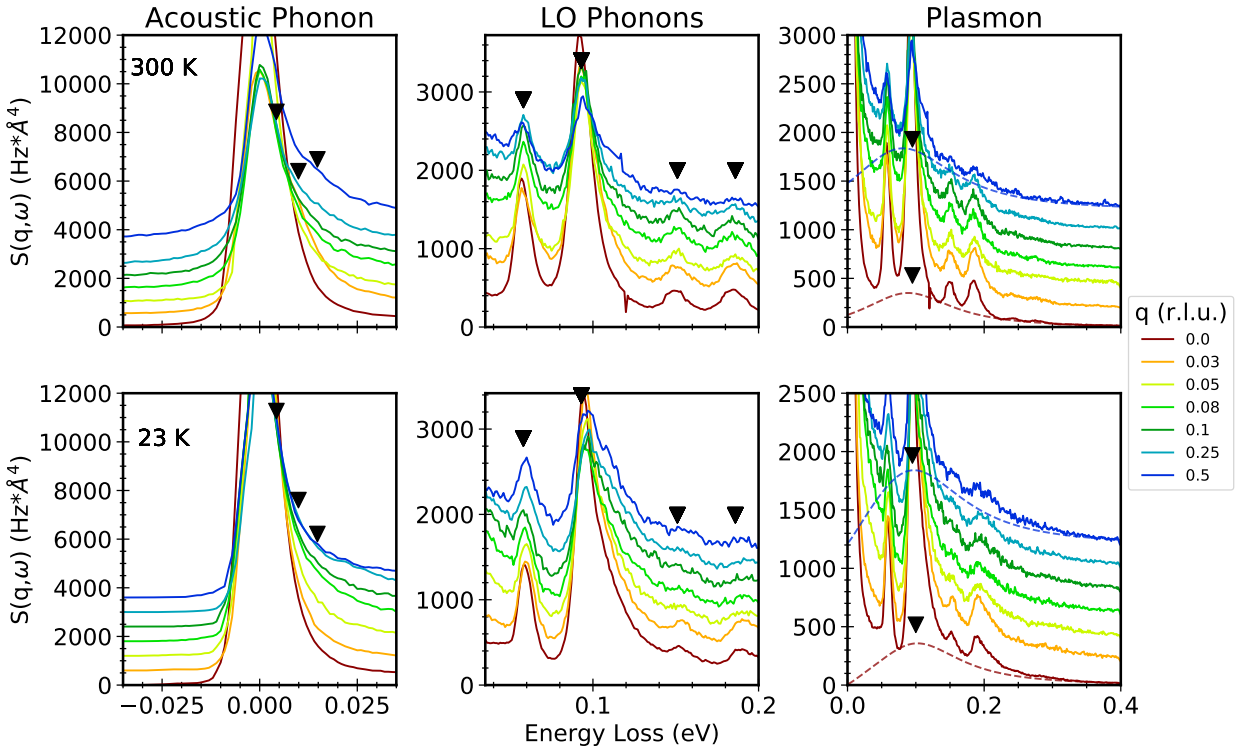

Figure 5.13: **x = 0.002 Dispersions**
Dispersions along the (H,0) for different energy regions at 300 K and 23 K. All spectra are scaled with sum rule and offset for clarity. The q=0 spectra are raw M-EELS intensities to avoid the Coulomb matrix element divergence when calculating S(q,ω). Low energy region shows a diffusive dispersing phonon, black arrows are the best fit to the lorentzian fits as described in Section 5.3.3. In the region of 35-200 meV we see two optical phonons and two overtones, black arrows are guide to the eye for each LO mode. In the energy range out to 400 meV, we see a broad background under the phonons which is the plasmon mode. Dashed lines and black arrows provide guide to the eye for this non-dispersing mode. The dashed lines are by-eye fits using the Drude formulation.

Figure 5.14 shows that the M-EELS optical phonons are independent of temperature which contrasts with the optical spectroscopy measurements that show an increase of approximately 10 meV when cooled from room temperature to 23K. In addition, the IR data also seeing the broadening tail of the 93 meV LO phonon just like in M-EELS, this suggests that the coupling between the 93 meV mode and the plasmon is particularly strong at this composition. In M-EELS, the broad plasmon becomes slightly temperature dependent however it is difficult to quantify this temperature dependence due to the fact that this mode is very broad and weak compared to the Fuchs-Kliewer phonons that sit on top of it.

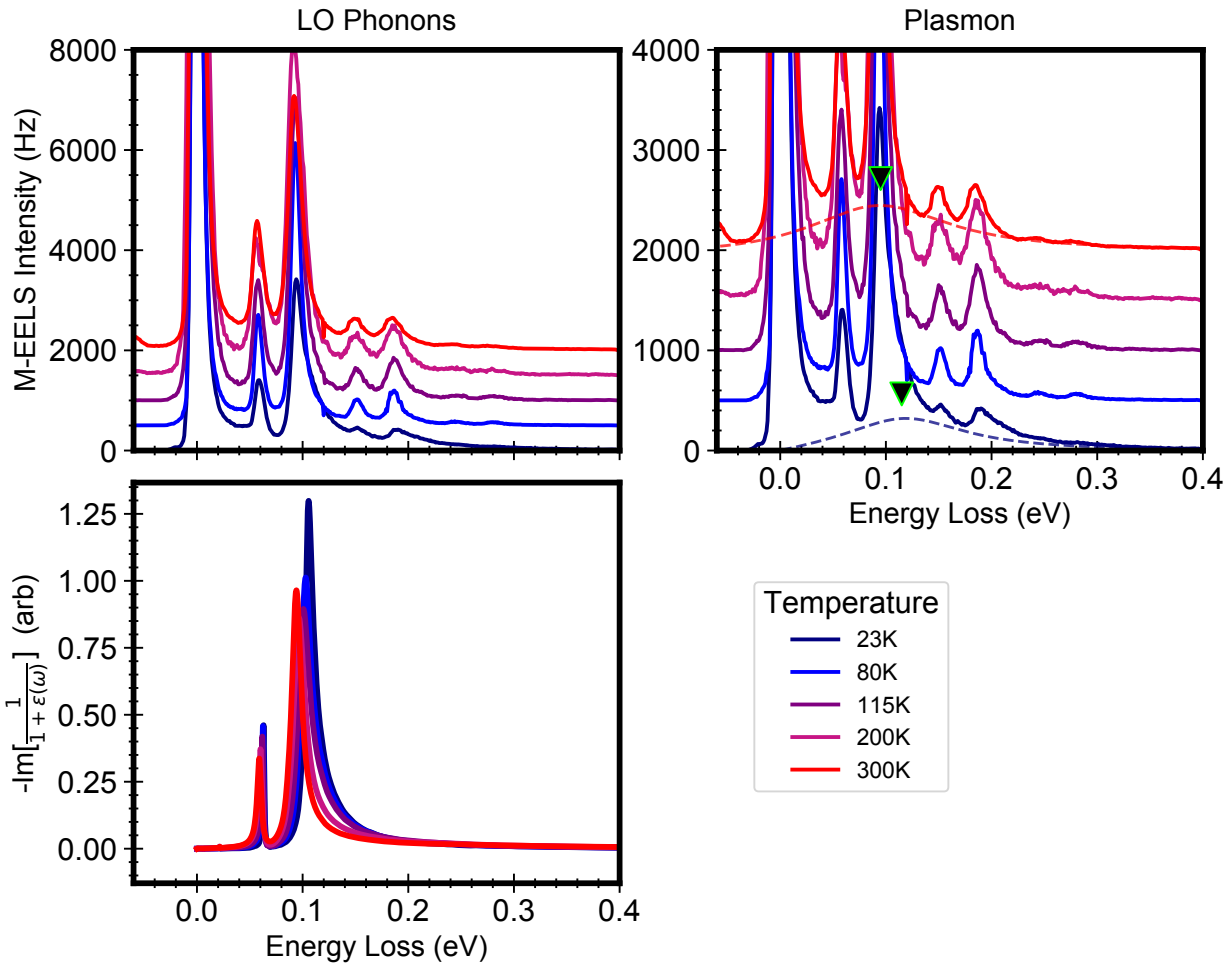

Figure 5.14: **x = 0.002 Temperature Dependence**
Temperature dependence of the optical phonons and plasmon from M-EELS (top) at q=0 and IR spectroscopy (bottom). Spectra are scaled to elastic line and are offset for clarity. Dashed lines and black arrows provide a guide to the eye for the temperature dependent plasmon mode. The dashed lines are by-eye fits using the Drude formulation.

x=0.01

For this measurement, the zero energy momentum scan shows (0,0) and a weak (1,0) Bragg peaks (Figure 5.15). The momentum resolution off this sample is 0.032 r.l.u. as determined from the FWHM of the specular peak. The dispersion of the low energy acoustic phonon looks comparable to the x=0.002 doped samples. The low energy acoustic phonon is broad and does not take on a lorentzian lineshape. This shows a diffusive behavior in momentum that increases in energy up to the Brillouin zone boundary and then decreases. The diffuseness of this dispersion maintains information about the crystal lattice as seen by the fact that it reaches its maximum in energy at the Brillouin zone boundary. This means that even though the collective excitation is not propagating on this sample surface we can still get momentum dependent information. If

there is another dispersing collective mode, it will also exhibit this dispersing behavior. Three different fractured surfaces were studied in this doping that all reproduced the same inelastic behaviors including a diffusive acoustic phonon. The data presented in this section is from one sample that was chosen based on the quality of the zero-energy (H,0) scan, the momentum resolution off the surface (FWHM of (0,0) Bragg peak), the number of temperature/momentum points measured, and the overall scattered intensity off the sample.

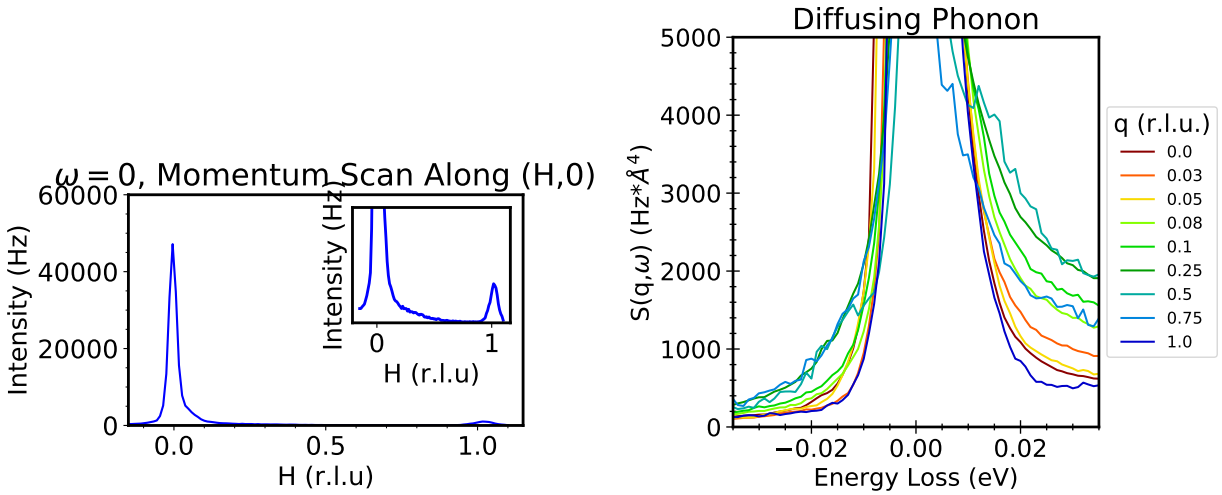

Figure 5.15: **x = 0.01 Fractured Surface**
The left figure shows the zero energy momentum scan showing (0,0) and (1,0) Bragg peaks with 0.032 r.l.u. momentum resolution (determined from the FWHM of (0,0)). We can measure a diffusing low energy acoustic phonon mode off this fractured surface (on right).

At, x=0.01, the carrier density is measured from Hall data as $1.49 \pm 0.14 \times 10^{20} cm^{-3}$. For this doping, we observe the Fuchs-Kliewer phonons and overtones at comparable energies to the x=0.002 doped material and these do not disperse (5.16). The tail of the 93 meV LO phonon, as seen in the x=0.002 data, is no longer present and there remains a sharp peak again. All phonons and overtones have weaker intensity than the x=0.002 and undoped materials but the plasmon mode has increased in intensity and energy. This mode remains very broad and doesn't disperse throughout the Brillouin zone at any temperatures. The energy of the plasmon starts to deviate from the expected value our calculation in Table 5.2, although is still within the large error bars from the Hall measurement. The broad mode sits at around 150 meV (at 23 K) and 100 meV (at 300 K) while the calculated screened plasma energy is 209 ± 64 meV.

Next we look at the temperature dependence of these modes compared to infrared spectroscopy as shown in Figure 5.17. Note that the optical data was measured from a x=0.009 Nb doped material. Once again, M-EELS measurements do not show any LO phonon temperature dependence. The plasmon however does become temperature dependent such that at room temperature there is a broad mode that sits under the

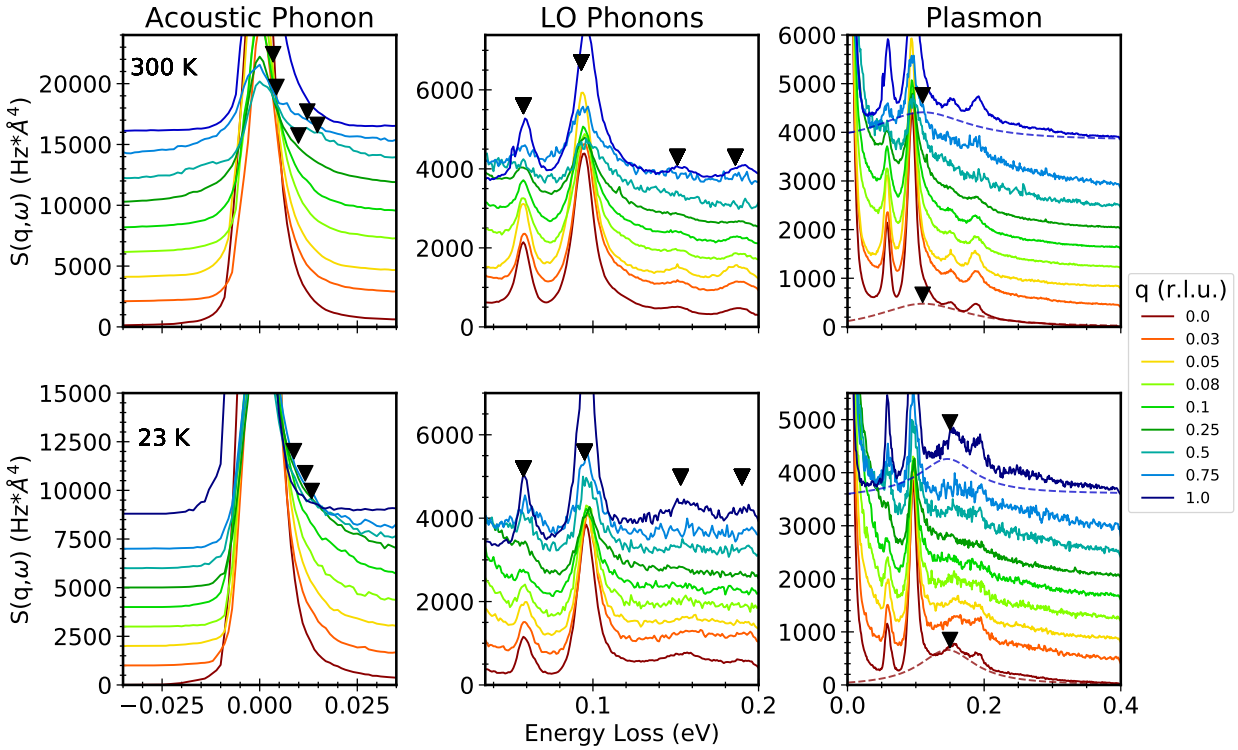

Figure 5.16: **x = 0.01 Dispersion**
Dispersions along the (H,0) for different energy regions at 300 K and 23 K. All spectra are scaled with sum rule and offset for clarity. The q=0 spectra are raw M-EELS intensities to avoid the Coulomb matrix element divergence when calculating S(q,ω). Low energy region shows a diffusive dispersing phonon, black arrows are the best fit to the lorentzian fits as described in Section 5.3.3. In the region of 35-200 meV we see two optical phonons and two overtones, black arrows are guide to the eye for each LO mode. In the energy range out to 400 meV, we see a broad background under the phonons which is the plasmon mode. Dashed lines and black arrows provide guide to the eye for this non-dispersing mode. The dashed lines are by-eye fits using the Drude formulation.

phonons around 100 meV and as temperature decreases, the mode becomes sharper and shifts to about 150 meV. In the optical data the same temperature dependent trend is seen - with cooling the plasmon blue-shifts and its lineshape becomes sharper. The magnitude of the plasmon energy shift in IR is almost double to what is seen in M-EELS where IR sees an energy shift from approximately 115 meV (at room temperature) to 200 meV at low temperature. The calculated screened plasma energy (209 ± 64 meV) for this doping agrees better with IR measurements than it does with M-EELS. This observation suggests that the fractured $SrTiO_3O$ surfaces are more hole doped than the bulk. This is very surprising, since most well-known defects in $SrTiO_3$ (such as oxygen vacancies or electronic reconstruction) electron-dope the system. We will discuss this more in a later section. In addition, with added carriers, IR spectroscopy sees a large screening of the phonons such that the plasmon consumes the majority of the spectral weight. In M-EELS, we see a similar

trend of decreased phonon spectral weight with doping however the phonons we see are still significantly stronger than the plasmon mode. This may be because M-EELS measures the longitudinal response, so it is actually the longitudinal phonons that we are seeing.

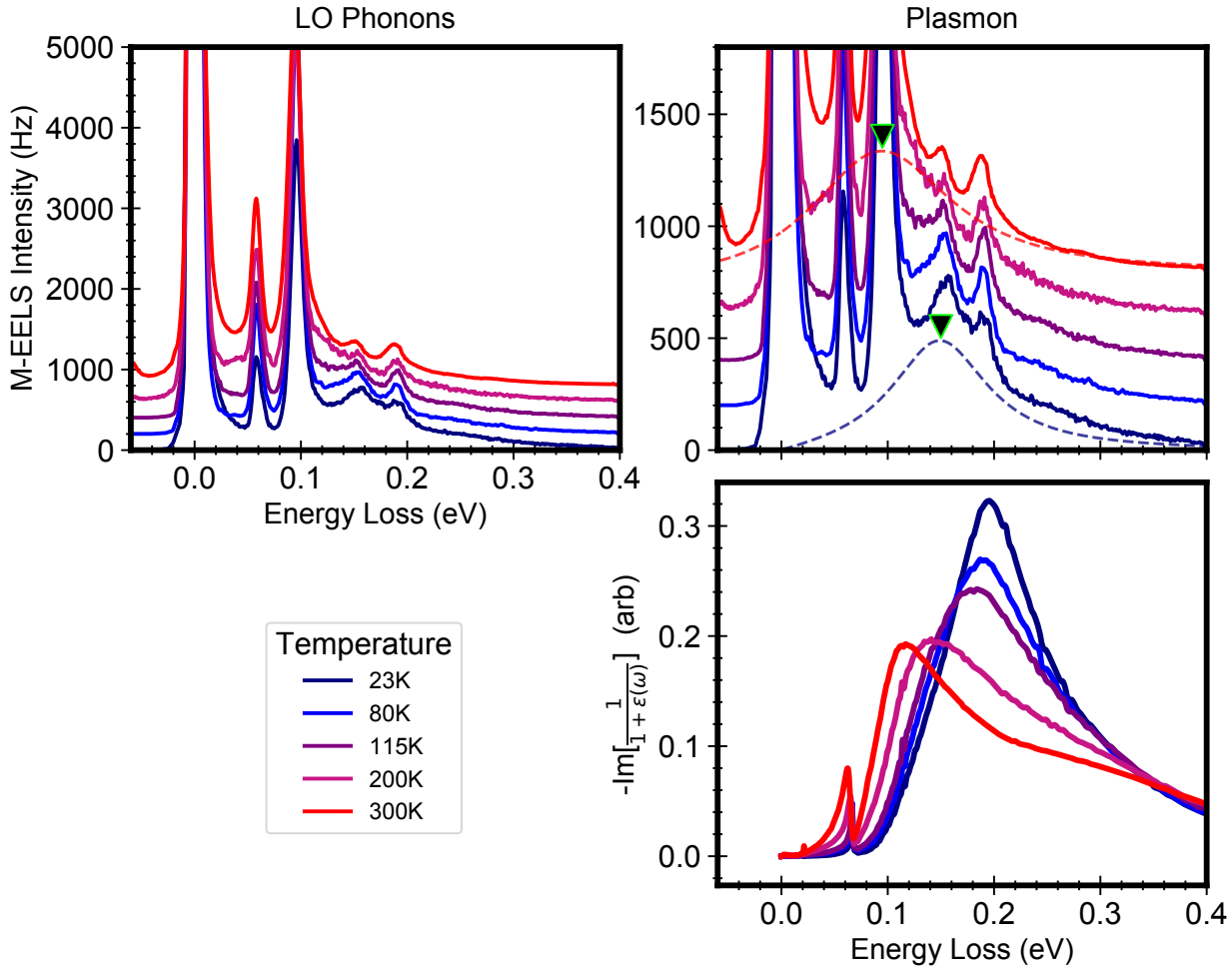

Figure 5.17: **x = 0.01 Temperature Dependence**
Temperature dependence of the optical phonons and plasmon from M-EELS (top) at q=0 and IR spectroscopy (bottom). Spectra are scaled to elastic line and are offset for clarity. Dashed lines and black arrows provide guide to the eye for the temperature dependent plasmon mode. The dashed lines are by-eye fits using the Drude formulation.

x=0.014

The final doping that was studied is a x=0.014 Nb doped material. For this measurement, the zero energy momentum scan shows (0,0) and a very strong (1,0) Bragg peak (Figure 5.18). The momentum resolution off this sample is 0.037 r.l.u. as determined from the FWHM of the specular peak.

The low energy acoustic phonon has a lorentzian lineshape and disperses to 14 meV at the Brillouin

zone boundary. This is strong evidence that momentum should is conserved in these measurements. Six different fractured surfaces were studied at this doping that had varying cleave quality - several showed a propagating acoustic phonon while others showed a broad diffusive phonon. All measurements however reproduced the same inelastic behaviors at energies higher than the acoustic phonon regardless of cleave quality. The data presented in this section were taken from a sample that was chosen based off the quality of the zero energy (H,0) scan, the momentum resolution off the surface (FWHM of (0,0) Bragg peak), the number of temperature/momentum points measured, and the overall scattered intensity off the sample.

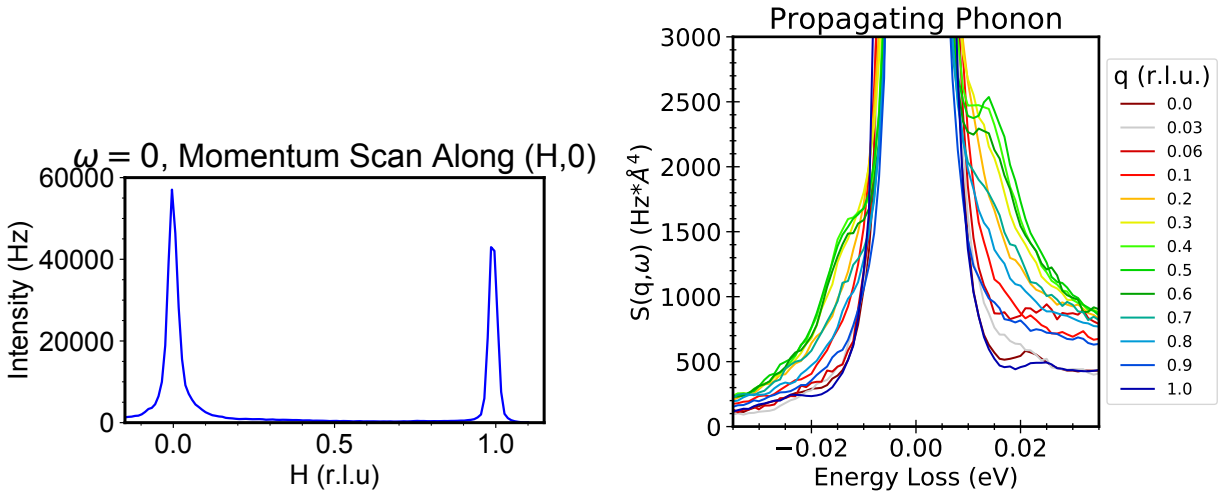

Figure 5.18: **x = 0.014 Fractured Surface**
The left figure shows the zero energy momentum scan showing (0,0) and (1,0) Bragg peaks with 0.037 r.l.u. momentum resolution (determined from the FWHM of (0,0)). We can measure a propagating low energy acoustic phonon mode off this fractured surface (on right).

For x=0.014, the carrier density as measured from Hall data is $2.13 \pm 0.07 \times 10^{20} cm^{-3}$. For this doping, we observe the Fuchs-Kliewer phonons and overtones at comparable energies to the x=0.01 doped material and these do not disperse Figure 5.16. The 93 meV LO phonon remains sharp. All phonons and overtones have weaker intensity than the lighter dopings and the overtones are almost completely screened out, which is consistent with the expectation that this most doped material exhibits the strongest metallic screening. The plasmon mode is very comparable to that seen in x=0.01 in terms of its energy, linewidth, and non-dispersive behavior throughout the Brillouin zone. The energy of the plasmon continues to deviate from the expected value our calculation in Table 5.2. M-EELS measures the plasmon mode around 150 meV (at 23 K) and 100 meV (at 300 K) while the calculated screened plasma energy is 250 ± 46 meV. This again suggests that the fractured surface region of this material is hole-doped compared to the bulk.

Figure 5.20 shows the temperature dependence of the optical phonons and plasmon compared to that seen in IR spectroscopy. The optical phonons are temperature independent while the plasmon continues to

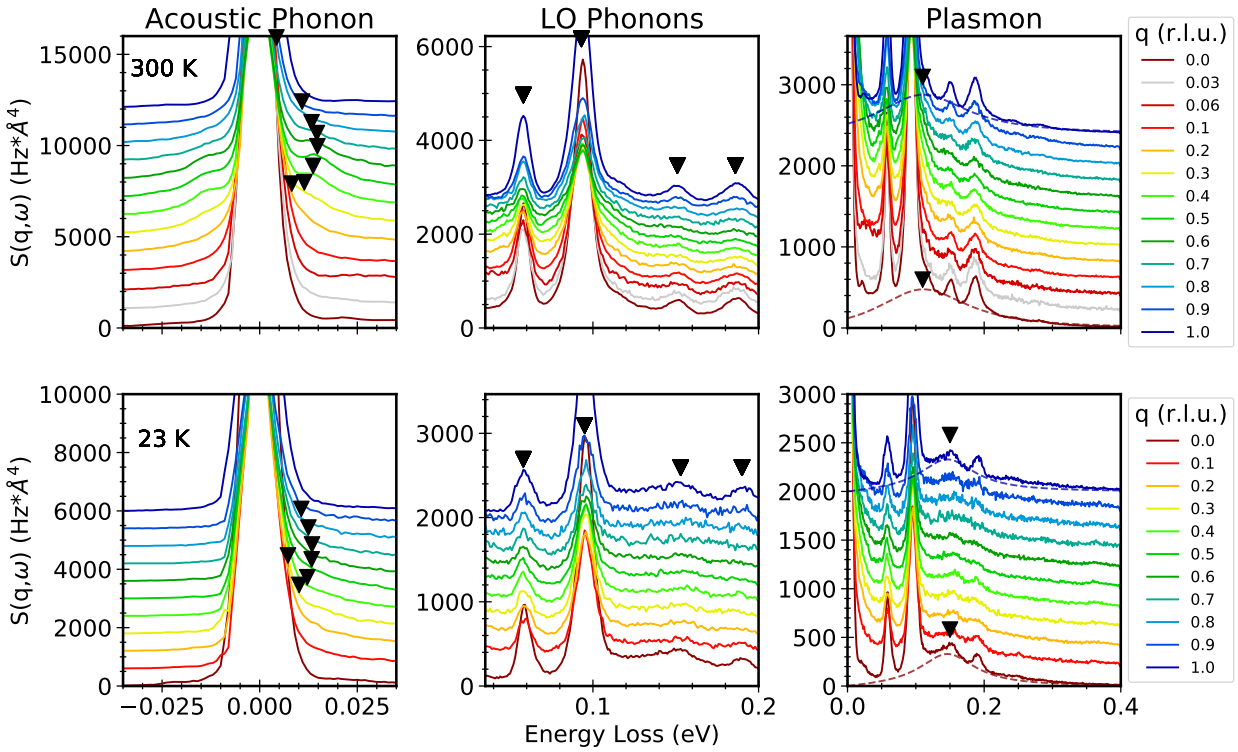

Figure 5.19: **x = 0.014 Dispersions**
Dispersions along the (H,0) for different energy regions at 300 K and 23 K. All spectra are scaled with sum rule and offset for clarity. The q=0 spectra are raw M-EELS intensities to avoid the Coulomb matrix element divergence when calculating S(q,ω). Low energy region shows a diffusive disperssing phonon, black arrows are the best fit to the lorentzian fits as described in Section 5.3.3. In the region of 35-200 meV we see two optical phonons and two overtones, black arrows are guide to the eye for each LO mode. In the energy range out to 400 meV, we see a broad background under the phonons which is the plasmon mode. Dashed lines and black arrows provide guide to the eye for this non-dispersing mode. The dashed lines are by-eye fits using the Drude formulation.

exhibit a large blue-shift with decreasing temperature. At room temperature there is a broad mode that sits under the phonons around 100 meV and as temperature decreases, the mode becomes sharper and shifts to about 150 meV. The optical data presented is an interpolation of the data at x=0.009 and x=0.02 from [48]. In the optical data the same temperature dependent trend is seen - with cooling the plasmon blue-shifts and its lineshape becomes sharper. The magnitude of the plasmon energy shift in IR is double that seen in M-EELS where IR sees an energy shift from approximately 150 meV (at room temperature) to 250 meV at low temperature. The calculated screened plasma energy (250 ± 46 meV) for this doping agrees better with IR measurements than it does with M-EELS.In addition, the optical phonons are completely screened by the plasmon while in M-EELS, these modes still exist but with lower intensity than the lighter doped samples. Once again, this may be because optics couples to the LO and TO phonon modes differently then M-EELS.

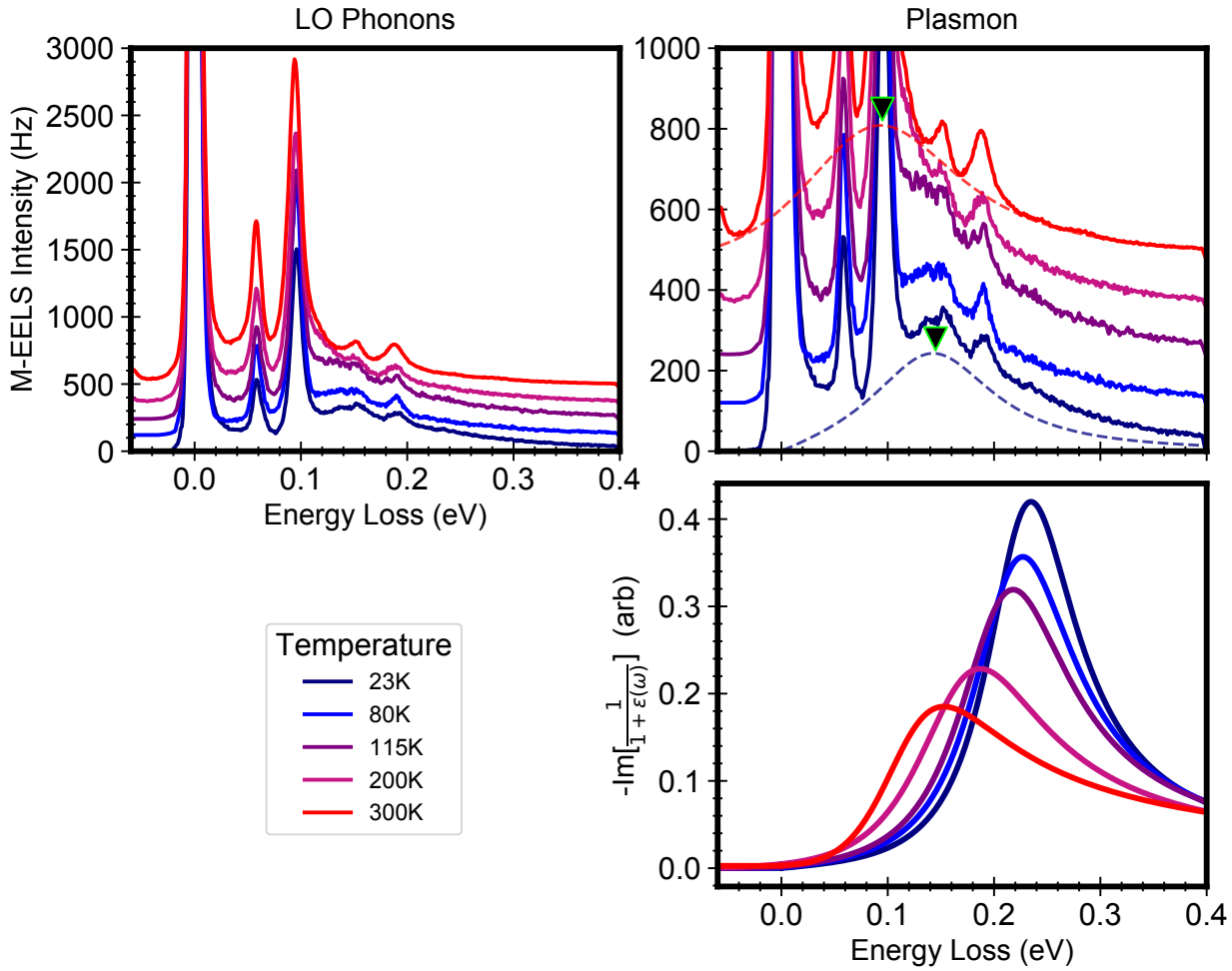

Figure 5.20: **x = 0.014 Temperature Dependence**
Temperature dependence of the optical phonons and plasmon from M-EELS (top) at q=0 and IR spectroscopy (bottom). Spectra are scaled to elastic line and are offset for clarity. Dashed lines and black arrows provide guide to the eye for the temperature dependent plasmon mode. The dashed lines are by-eye fits using the Drude formulation.

Unidentified Mode

In addition to phonons and plasmon, we see a broad mode at higher energies in the range of 0.8 - 1.2 eV (Figure 5.21). This mode appears in all dopings, its energy is doping independent and temperature independent. This mode does exhibit a dispersion at low momentum. At very low momentum (0.02 r.l.u.) the mode decreases in energy by approximately 0.1 eV and its width sharpens. As we go to higher momentum the mode disperses back to higher energy and broadens until it gets overly damped into a particle-hole continuum.

This mode is not seen in other techniques such as optical spectroscopy but is highly reproducible in M-EELS, appearing in all compositions studied. One possibility is that this is a d-d excitonic mode that

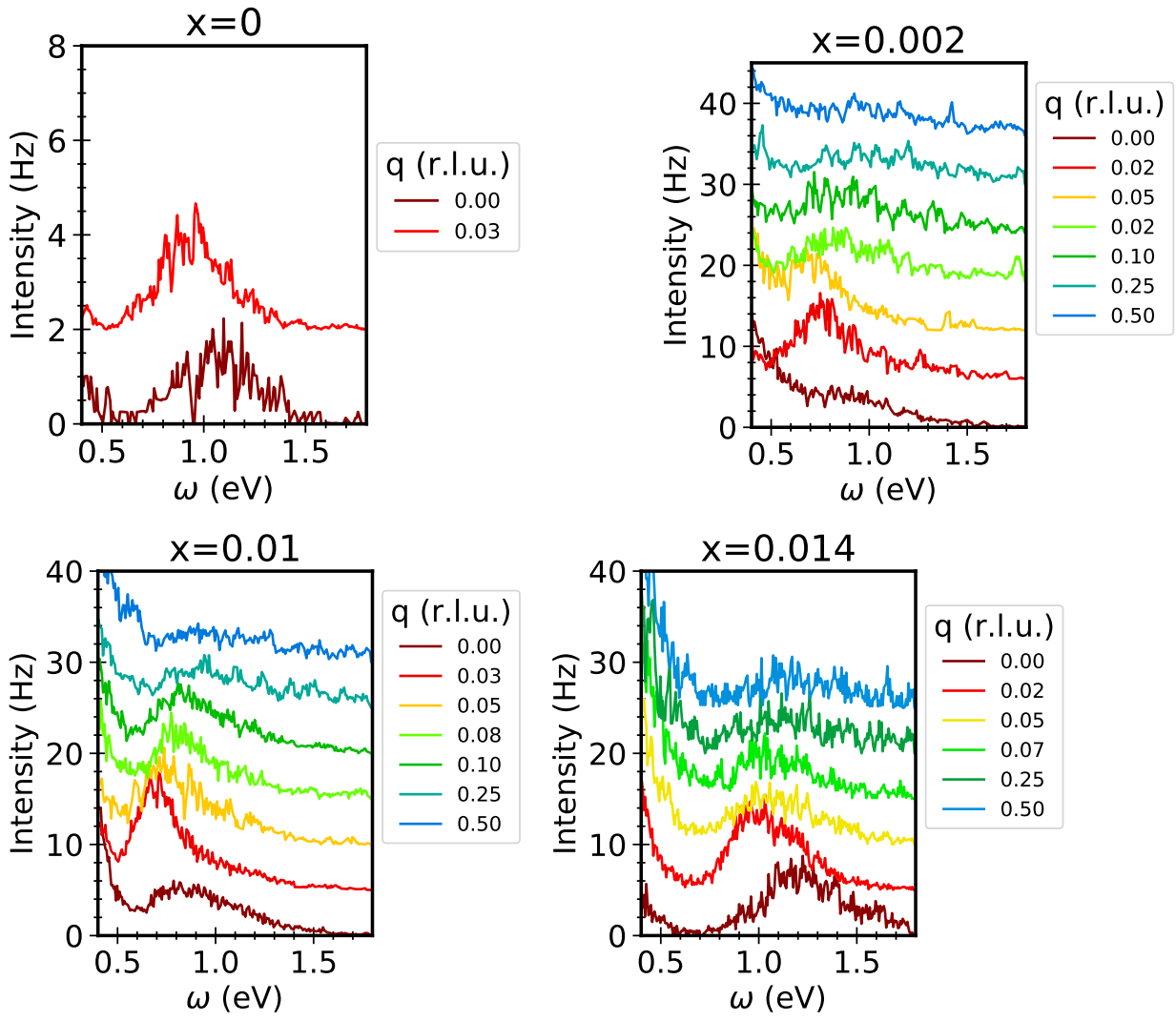

Figure 5.21: **Unidentified Mode**
Unidentified mode seen in all dopings that exhibits a low momentum dispersion.

is not visible in IR spectroscopy [48] due to its even parity and not currently seen in Raman spectroscopy literature which only has data at much lower energies [102–104].

5.3 Discussion

5.3.1 q=0 Doping Dependence

To summarize the doping effect from the above observations, Figure 5.22 shows the q=0, 23 K doping spectra for both M-EELS measurements and optical measurements. The left column of Figure 5.22 is zoomed out to show the effect of doping on the optical phonons, while the right column is zoomed in to show the effect

of doping on the plasmon. Two additional dopings are included in this plot that were not discussed in the previous section: x=0.02 in the IR plots from which the interpolated x=0.014 spectra were calculated, and the "slightly" doped sample in M-EELS which was measured to have a carrier density less than the metal-to-insulator transition (see above discussions).

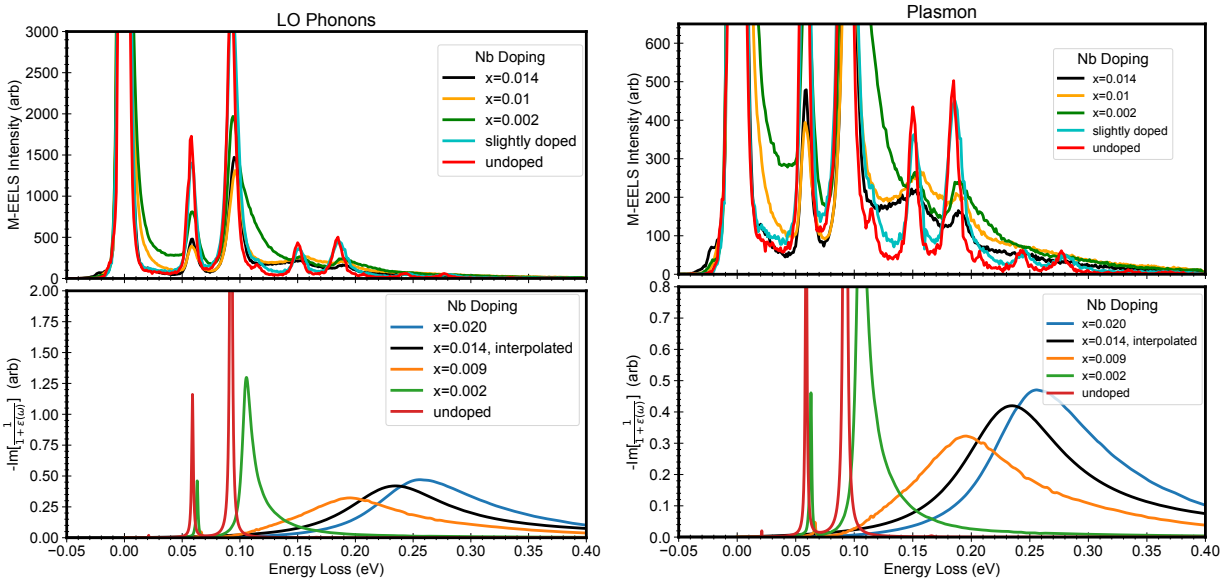

Figure 5.22: **Doping Dependence at q=0, 23 K**
Doping dependence of the optical phonons and plasmon from M-EELS (top) and IR spectroscopy (bottom). Spectra are scaled to elastic line and are not offset. The data is zoomed out to show the optical phonons (left) and zoomed in to show the plasmon (right).

Several important observations from this doping dependence are that

1. Introducing electrons screens the phonons,

2. In M-EELS, the optical phonons only shift by a few meV with added carriers,

3. A broad plasmon emerges with doping,

4. The 93 meV phonon mode becomes highly damped and asymmetric at x=0.002.

The first observation is exactly what is expected as a material becomes more metallic. In the M-EELS data, the screening of the phonons is demonstrated by a decrease in spectral weight and lack of higher order, 3rd and 4th harmonic, overtones. In optical data, the screening is demonstrated by the complete suppression of the strong phonons for carrier densities larger than x=0.002.

The second observation is quantified in Table 5.3. This phonon energy doping dependence is different than what is measured in optical spectroscopy, possibly because M-EELS and IR are couple to the LO and

TO phonons differently. In IR, the 93 meV phonon shifts on the order of 10 meV at the smallest doping (x=0.002) before it gets completely screened out. In addition, the phonon energy shift has been simulated in the supplement of [94] using a Lorentz model dielectric function with an added Drude term. In this EELS simulation, there is large increase in energy (25 meV) of the optical phonons from undoped to x=0.015 doping. They explain this to be the result of coupling between the free-electron plasmon and the Fuchs-Kliewer phonon. This theoretical prediction is not observed in the M-EELS data which only shift by several meV across orders of magnitude change in carrier density.

The third observation is seen in both M-EELS and optical spectroscopy. At x=0.002, both techniques show a phonon that has a broad tail due to mixing with the plasmon. As doping is further increased, the plasmon shifts to higher energy and the phonons become more screened (completely disappearing in IR and weakening in intensity in M-EELS). The plasmon in M-EELS is also at lower energies than that of IR data for comparable carrier densities. This suggests that our samples might be more hole doped than what was measured with optical data.

Table 5.3: **Doping Dependence of LO Phonon Energies**

Doping	ω_1 (meV)	ω_2 (meV)	$\omega_{overtone,1}$ (meV)	$\omega_{overtone,2}$ (meV)
undoped	58	93	150	185
0.2%	58	94	152	190
1%	58	96	157	191
1.4%	58	95	153	190

The overall doping dependence seen in M-EELS qualitatively has the same features that is seen in IR (broad plasmon, screened phonons), however the results from the two techniques are quantitatively different. One explanation for this could be that M-EELS is measuring a superposition of the surface and bulk effects where as IR is only measuring the bulk effects. The Fuchs-Kliewer nature of the phonons remain even beyond the point where the bulk phonon gets screened from the added carriers. This describes the situation where the strong phonon modes remain in M-EELS for the higher doping but get completely screened in IR data. Another explanation of the doping dependence could be that we are actually measuring a carrier density that is in-between the x=0.002 and x=0.01 dopings of IR. Although the IR and M-EELS carrier densities match from Hall measurements, the incomplete screening of the LO modes and the lower energy plasmon seen in M-EELS suggest that we just have fewer carriers in the system. This is not the expected trend since these materials are well known for developing oxygen vacancies at the surface, especially when fractured, which would shift the plasmon energy to higher energy not lower.

5.3.2 q=0 Temperature Dependence

The temperature dependence seen in the x=0.01 and x=0.014 doped materials both in M-EELS and IR is unusual behavior for a plasmon. In most metals, the plasmon is temperature independent or slightly red-shifted due to thermal effects. Assuming a drude-like plasmon as described in Equation 5.7 and 5.8, a blue-shifted plasmon energy suggests that the carrier density, effective mass, or background dielectric constant are changing with decreasing temperature. It has already been shown that carrier density remains mostly independent of temperature [48,105,106]and the effective mass is very temperature dependent [107]. However there still remain open questions about the origin of this behavior. Some suggest that the temperature dependence is related to the scattering rate of carriers which exhibit bad metal properties [13]. Others suggest that the effective mass of the polaronic carriers changes and becomes heavier with warming [84].

5.3.3 Acoustic Phonon Dispersion

In order to determine the effectiveness of the UHV fracturing surface preparation, it needs to be established that momentum is conserved throughout the Brillouin zone. We determined this by quantifying a collective mode whose dispersion is well known in the literature. For the case of $SrTiO_3$ it is the low energy acoustic phonon, which has been calculated with DFT and measured with neutron scattering, that disperses to approximately 14 meV at the Brillouin zone boundary (q=0.5 r.l.u) [97–101]. We fit the low energy data with a voigt function for the elastic line and a antisymmetric lorentzian for the low energy, acoustic phonon weight as shown in Figure 5.23. A summary of these fits is also shown in Figure 5.23. For each doping in the summary plot, the energy loss is the mean of the fit value for all the cleaves in that doping. The error bars are the statistical errors from each fit that are added in quadrature for all the cleaves of that doping. The fits from all the dopings were then fit with a sine function and compared to DFT calculations [97]. The dispersion agreement between different dopings as well as compared to DFT, is within the error bars.

This procedure was done for all cleaves regardless of whether the acoustic mode was propagating (i.e. lorentzian lineshape) or diffusive. The idea behind that was that fitting with a lorentzian, even if the excitation is behaving more diffusively, will at least give an estimate to the shift in spectral weight in that energy region. The fact that we get comparable dispersions for fits of propagating acoustic mode and diffusive acoustic mode suggests that we can still obtain in-plane momentum conservation and information about the q-dependence of collective modes regardless of the global quality of the surface fracture.

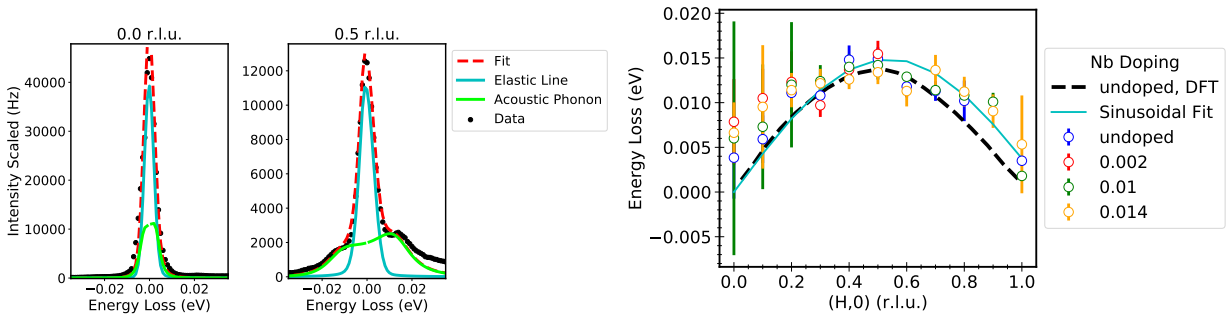

Figure 5.23: **Summary of Acoustic Phonon Dispersion at 300K**
Fits used to quantify the acoustic phonon dispersion for both propagating and diffusive phonon behavior. An example of the fitting scheme is shown on the left. Fits include a voigt function for the elastic line and an antisymmetric lorentzian for the acoustic phonon. Summary of these fits are shown on the right. Each point is an average of all fits (multiple cleaves) for each doping and error bars are the statistical errors from each fit that are added in quadrature for all the cleaves of that doping. The fits from all the dopings were then fit with a sine function and compared to DFT calculations [97]

5.3.4 Plasmon Dispersion

As shown above, the plasmon that emerges from electron doping is not observed to disperse for any doping at any temperature. This finding is unexpected since plasmons in metallic materials are traditionally described by Linhard theory which has a plasmon mode that increases in energy with increasing q and broadens due to the increased Landau damping, rapidly damping away into the particle-hole continuum [44]. This behavior has been theorized and measured in other doped, polar semiconducting materials such as GaAs [17,108]. An RPA calculation of $SrTi_{1-x}Nb_xO_3$ done by Alex Edelman and Peter Littlewood (University of Chicago) find that the plasmon in $SrTi_{1-x}Nb_xO_3$ should be sharp and exhibit q^2 dispersion. A 2D calculation of -Im[$1/\epsilon$] dispersion using RPA and compared to M-EELS data is shown in figure 5.24. The RPA calculation shows a plasmon width of 15 meV FWHM with a plasma frequency of 220 meV that sharply disperses into the particle-hole continuum at q=0.115 r.l.u. and damps away. However in M-EELS and optics, the plasmon that is an order of magnitude broader than the RPA calculation and that is momentum-independent. These features suggest that we are in regime in which RPA is not valid. [72]

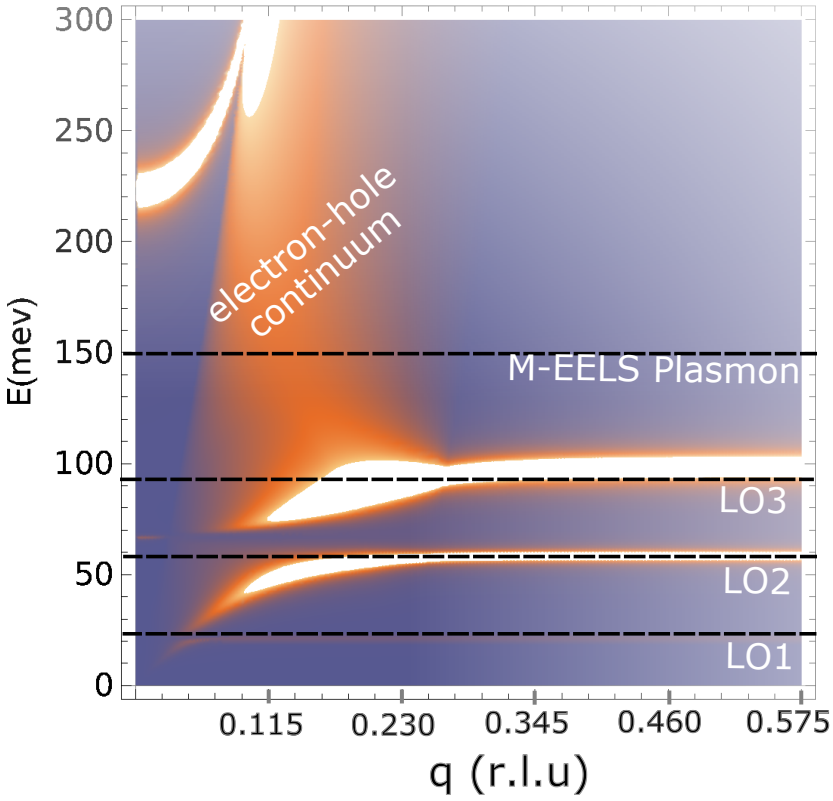

Figure 5.24: **RPA Dispersion of -Im$[1/\epsilon]$ for x=0.014**
RPA calculation done by Alex Edelman and Peter Littlewood which shows a strongly dispersing plasmon and three optical phonons. This is compared to the energy and non-dispersive behavior of the plasmon and optical phonons that we see in M-EELS (black dashed lines).

5.4 Summary and Future work

The work in this chapter explores the dynamics of the collective modes in $SrTi_{1-x}Nb_xO_3$ in its normal state. We used M-EELS to study the doping, temperature, and momentum dependence of the low energy lattice and electronic collective modes. Our findings show that

1. We measure an acoustic phonon that sometimes propagates and sometimes moves diffusively. This depends on the quality of the fractured surface. Therefore, using the fracturing technique means that we can still get in-plane momentum conservation and information about the momentum dependence of the plasmon, even when the surface is not globally flat.

2. The 93 meV phonon mode becomes highly damped and asymmetric at x=0.002.

3. Metallic screening in doped samples suppresses phonons in the data (particularly the overtones), though not as much as in optical data.

4. The plasmon energy blue-shifts with decreasing temperature which follows the same trend as seen in other techniques like optical spectroscopy.

5. The M-EELS plasmon is seen at lower energy than that of IR for comparable carrier densities as measured by the Hall effect. We explain this as a result of M-EELS measuring the surface response rather than the bulk response function or that the samples are hole doped.

6. The plasmon width, as measured in M-EELS and optics, is an order of magnitude larger than predicted by RPA.

7. The plasmon exhibits non-dispersive behavior even though there are other dispersive features that are measured such as the acoustic phonon.

From these conclusions, there still remain several questions that need to be addressed such as, why is the plasmon at lower energies compared to other techniques for the same carrier density, what is making the plasmon so broad, and is the damping of the plasmon preventing it from propagating?

In addition, obtaining quantitative values of the M-EELS plasmon energy, width, and phonon-plasmon couplings can better inform how the modes are behaving. Preliminary work has not been able to provide a consistent method of fitting that works for all temperatures, dopings, and momenta. This is due to the large number of parameters, the proximity in energy of all the collective modes, and the non-drude-like shape of the plasmon (which has prompted us to explore the double-damped extended drude model). Figure 5.25a is an example of a fit that captures the low energy (acoustic phonon) and higher energy (optical phononss and plasmons) behavior. This fit uses a voigt function for the elastic line, anti-symmetetric lorentzian for the acoustic phonon and all the overtones, Fano function for the strong Fuchs-Kliewer phonons, and a double-damped extended Drude for the plasmon. This fit works because the plasmon is at an energy larger than the optical phonons (at 23 K) and the low energy excitations remain below 35 meV (q=0 so acoustic mode

is at a minimum energy). Figure 5.25b is an example of a spectra with features that are not captured by the model used in Figure 5.25a. In this spectra, the low energy diffusive behavior (q=0.5, maximum energy of dispersion), the broad LO phonon tails, and the broad plasmon (at 200 k) all overlap in energy and are ill-defined. Finding local minimums in converging fits for this spectra can lead to un-physical parameters. A consistent fitting method for all temperature, dopings, and momentum is currently being developed to quantitatively understand the collective modes in $SrTi_{1-x}Nb_xO_3$.

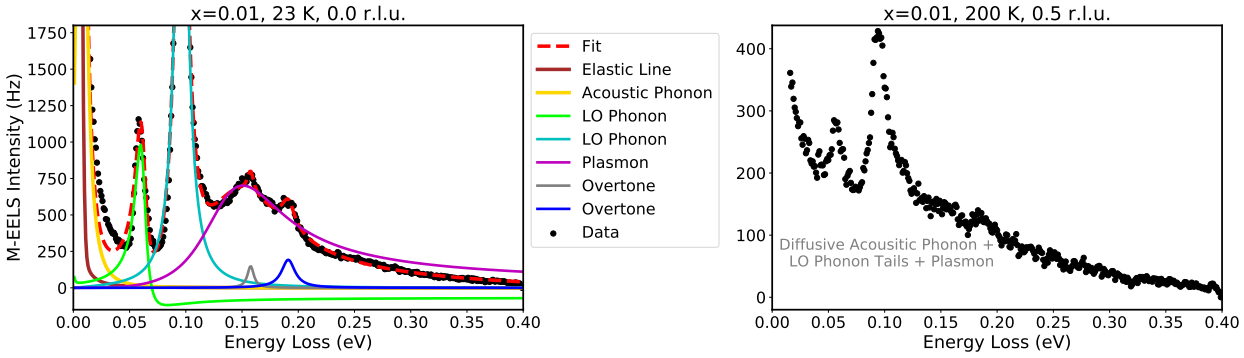

Figure 5.25: **Example Fit Scheme on x = 0.01**
On the left is a fit to 23K, q=0 data where excitations don't significantly overlap in energy. This fit uses a voigt function for the elastic line, anti-symmetetric lorentzian for the acoustic phonon and all the overtones, Fano function for the strong Fuchs-Kliewer phonons, and a double-damped extended Drude for the plasmon. On the right is 200K, q=0.5 r.l.u. data where the collective excitations all overlap in energy and look like one large background.

Chapter 6

Conclusion

M-EELS is a versatile technique used to study the low energy collective modes in strongly correlated electron systems. In this thesis, we summarized M-EELS cross section for a periodic system. From this derivation, we related the cross section to the density-density correlation function, $S(\mathbf{q}, \omega)$, the density response function, $\chi(\mathbf{q}, \omega)$, and the dielectric loss function. The density response function contains information about the propagation of density fluctuations near the surface that are mediated by bosonic excitations. The dielectric loss function is a quantity that we can use to compare to infrared spectroscopy at q=0. We address a limitation of the matrix elements in the near-Bragg condition regime that comes about from assumptions made in deriving the M-EELS cross section and discuss a potential solution of including experimental momentum resolution in the matrix element calculations.

We also addressed the experimental implementation of the M-EELS technique. Specifically we discussed methods to improve electron throughput and energy/momentum resolution by phase-space tuning (i.e. multiple parameters simultaneously) of the electron trajectory and compared this to theoretical calculations [52]. In addition we developed multiple routes to studying materials beyond 2D Van der Waal layered materials. This includes a vacuum suitcase, that can transport thin films without being exposed to air, an annealing stage to clean samples surfaces and electron dope materials, and a UHV fracturing technique for 3D materials using a diamond wiresaw.

Using M-EELS we investigated the low energy excitations of several highly correlated electron systems. Our study of Cu_xTiSe_2 addressed the question of whether there can ever be a distinction between a Bose condensate of excitons and a conventional, structural phase transition that breaks the same symmetry. Using inelastic electron scattering (M-EELS) to study copper-intercalated $TiSe_2$, we can determine if the excitonic phase is distinct from the structural phase by observing what happens to the soft electric collective mode

with doping, a key signature of exciton condensation. We find that the excitonic transition is extremely sensitive to screening since it is suppressed before the semimetal-metal transition at $x = 0.025$. Another conclusion is that the normal state out of which the superconductivity forms is an anomalous metal. For $x = 0.029$, the plasmon energy is approximately independent of temperature, due to the fact that excitonic fluctuations exist in this region and compete with the normal state behavior. However, for $x > 0.065$, the plasmon is strongly temperature-dependent, suggesting the quasiparticle band structure is renormalizing in an unusual way even far above T_{SC}. Lastly the electronic mode is not strongly **q**-dependent at $x > 0.014$ and does not follow the conventional dispersion for a plasmon in a Lindhard metal [44].

Our study of electron doped $SrTiO_3$ explored the dynamics of the collective modes in $SrTi_{1-x}Nb_xO_3$ in its normal state. This material exhibits many interesting phenomena including quantum paraelectric behavior and dilute (unconventional) superconductivity. In particular, the dilute nature of $SrTi_{1-x}Nb_xO_3$ means that the energy of lattice excitations is comparable to that of electronic excitations, leading to coupling between these modes. Measuring the dynamics of the collective modes can provide insight on how these modes interact in the system. Here, we use inelastic electron scattering (M-EELS) with a fracturing surface preparation technique to study the doping, temperature, and momentum dependence of the charge collective modes in $SrTi_{1-x}Nb_xO_3$. We measure propagating and diffusive acoustic phonons, Fuchs-Kliewer optical phonons and overtones that get suppressed with doping due to metallic screening, a 93 meV phonon mode that becomes highly damped and asymmetric at x=0.002, and a very broad plasmon that blue-shifts with decreasing temperature. We find that the plasmon in $SrTi_{1-x}Nb_xO_3$ remains dispersion-less at all temperatures and dopings even with other propagating collective modes (acoustic phonon), contrary to RPA predictions and dispersions in other polar doped semiconductors [17]. The width of the plasmon deviates from RPA predictions by an order of magnitude. In addition, the energy of the plasmon measured in M-EELS is less than that of other techniques like infrared spectroscopy for samples of comparable carrier densities.

Appendix A

M-EELS Electron Optics Lens Voltage Scans

In order to understand the general behavior of the electron optics system, it can be useful to have a reference of how the electrostatic lenses behave in the current M-EELS experimental setup. This appendix includes lens reference scans for two different tuning optimizations.

Figures A.1-A.6 are scans of each electrostatic lens measured at the closest relay to that lens. Therefore the emissions (A) lens profiles were measured at the first monochromator (relay M1), the first monochromator (M1) lens profiles were measured at the second monochromator (relay M2), the second monochromator (M2) lens profiles were measured at the analyzer (relay An1), the focusing (B) lens profiles were measured at the analyzer (relay An1), the analyzer (An1) lens profiles were measured at the detector (relay cone), and the electron detector system (C) lens profiles were measured at the detector (relay cone). Each figure has lens profiles from 2018 and 2020. The 2018 data was based on the phase-space tuning process as discussed in Section 3.1.3. The 2020 data is taken off of the same spectrometer as the 2018 data but in a different voltage configuration. The 2020 emission system lens profiles were measured in the "aligned" beam configuration while the rest of the 2020 data were measured in a "misaligned" beam configuration also discussed in Section 3.1.3.

Finally, each figure includes the voltage value that optimized counts and resolution at the detector. The voltage value for the respective lens is represented by a vertical dashed line. This demonstrates that in an optimized lens tuning, the lens profile maximum and the optimized detector value vary significantly for lenses that are furthest from the detector. For lenses close to the detector along the beam path, the peak of the lens profile corresponds to the optimized voltage at the detector. This signifies that both of these

tuning configurations are just optimized to some local minimum. If optimized at the global minimum in phase space, then the optimized detector voltage should equal the maximum of the profile of each individual lens.

Emission System - A Lenses

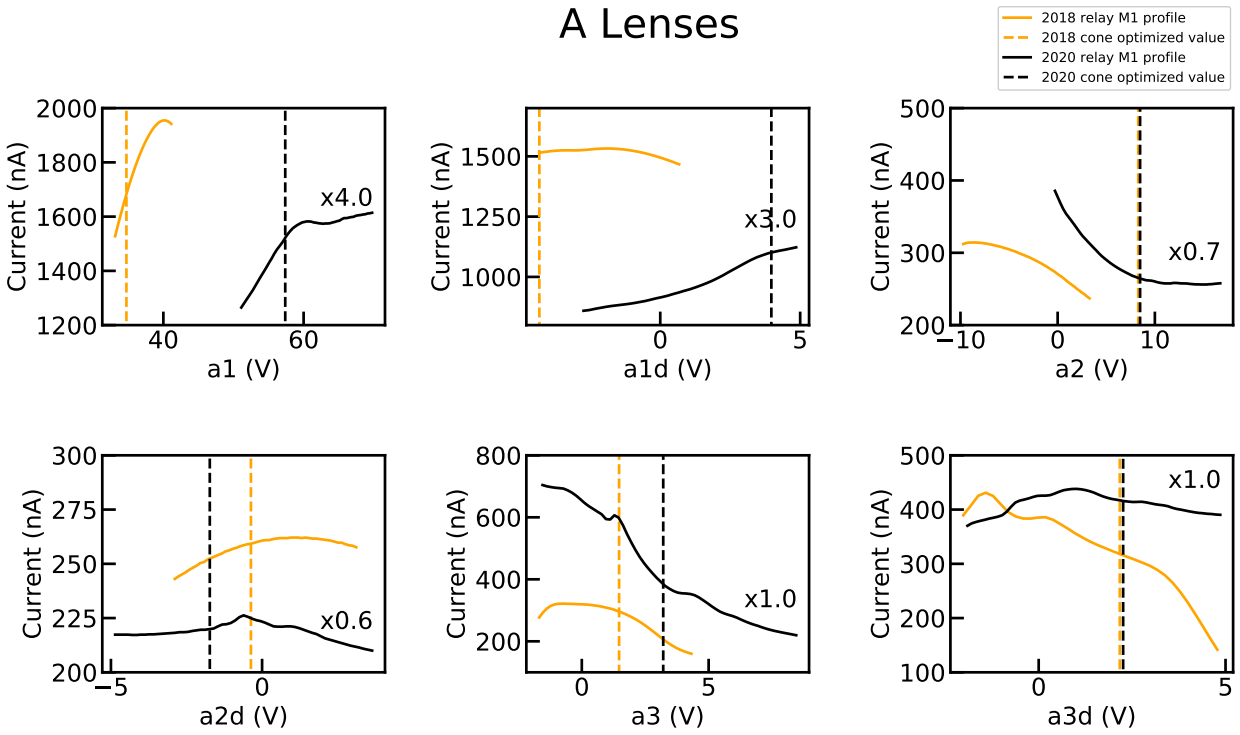

Figure A.1: **Emission System Lens Voltage Profiles**
Emission system (a1, a1d, a2, a2d, a3, a3d) lens profiles measured at the first monochromator (relay M1) for two different optimized voltage configurations. The 2020 data is in an "aligned" beam configuration. The dashed lines represent the voltage value of each respective lens that produces an optimized tuning at the detector. The 2020 data is scaled to see on the same plot as the 2018 data and the scale factor is noted next to each profile.

Premonochromator - M1 Lenses

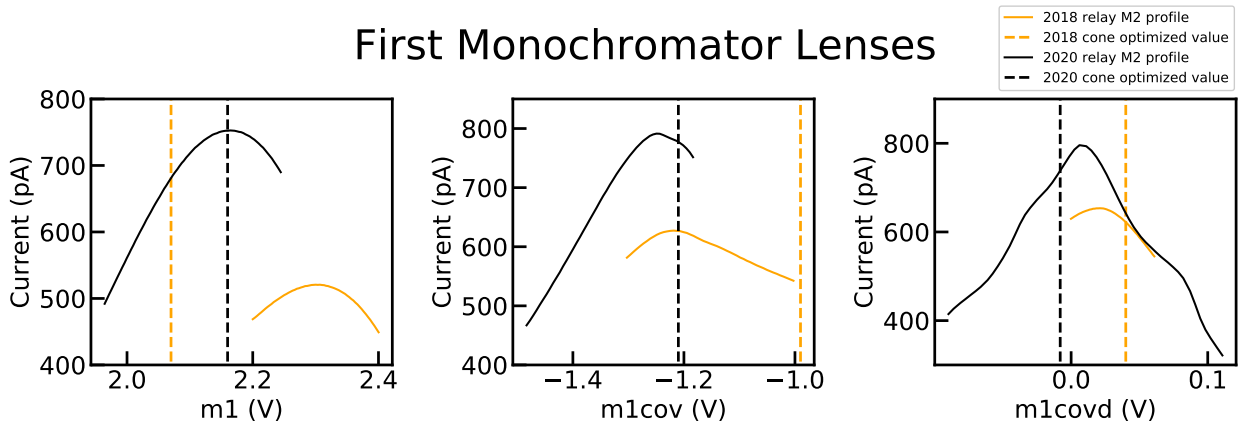

Figure A.2: **Premonochromator Lens Voltage Profiles**
Premonochromator (M1, M1 cover, M1 cover delta) lens profiles measured at the second monochromator (relay M2) for two different optimized voltage configurations. The 2020 data is in a "misaligned" beam configuration. The dashed lines represent the voltage value of each respective lens that produces an optimized tuning at the detector.

Second Monochromator - M2 Lenses

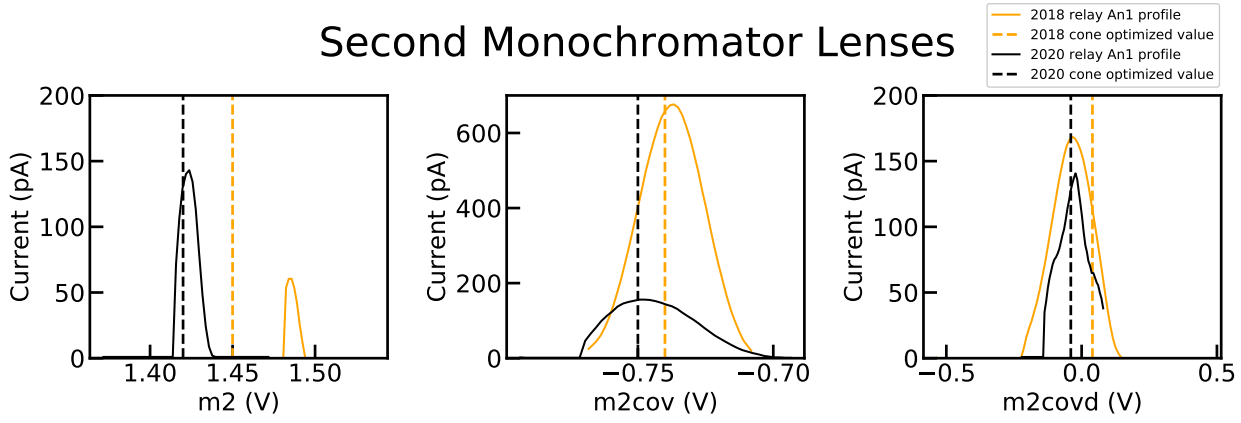

Figure A.3: **Second monochromator Lens Voltage Profiles**
Second monochromator (M2, M2 cover, M2 cover delta) lens profiles measured at the energy analyzer (relay An1) for two different optimized voltage configurations. The 2020 data is in a "misaligned" beam configuration. The dashed lines represent the voltage value of each respective lens that produces an optimized tuning at the detector.

Focusing Lens System - B Lenses

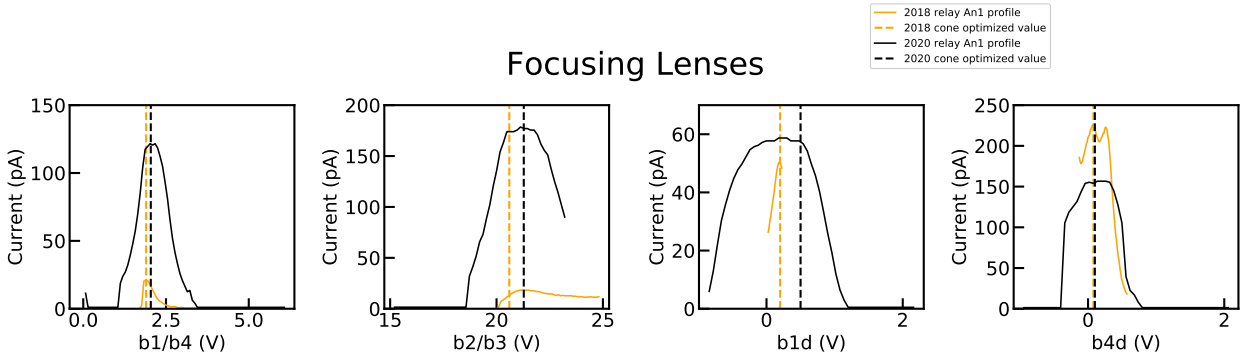

Figure A.4: **Focusing Lens Voltage Profiles**
Focusing (B1/B4, B2/B3, B1d, B4d) lens profiles measured at the energy analyzer (relay An1) for two different optimized voltage configurations. The 2020 data is in a "misaligned" beam configuration. The dashed lines represent the voltage value of each respective lens that produces an optimized tuning at the detector.

Energy Analyzer - An1 Lenses

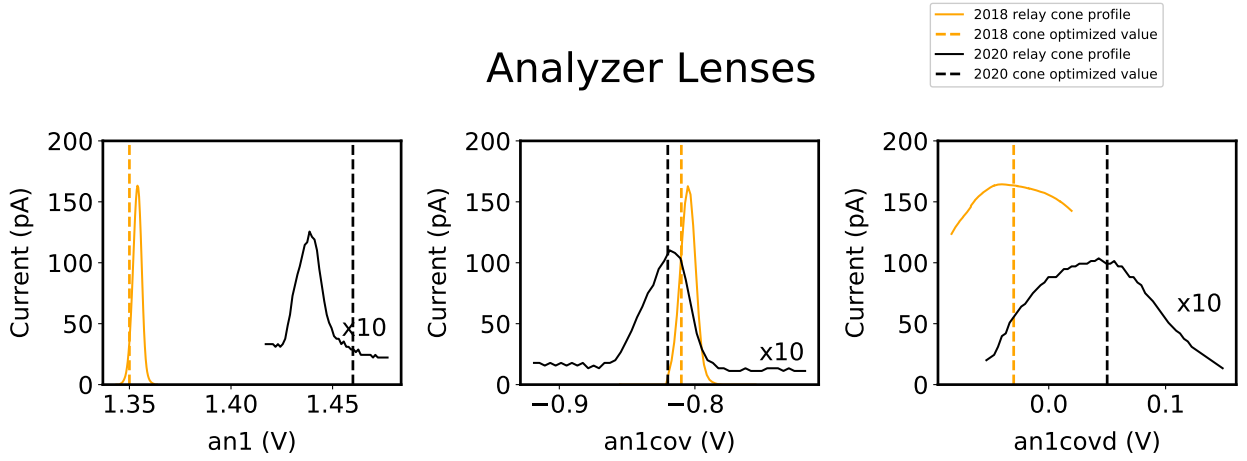

Figure A.5: **Energy Analyzer Lens Voltage Profiles**
Energy analyzer (An1, An1 cover, An1 cover delta) lens profiles measured at the detector (relay cone) for two different optimized voltage configurations. The 2020 data is in a "misaligned" beam configuration. The dashed lines represent the voltage value of each respective lens that produces an optimized tuning at the detector. The 2020 data is scaled to see on the same plot as the 2018 data and the scale factor is noted next to each profile.

Electron Detector System - C Lenses

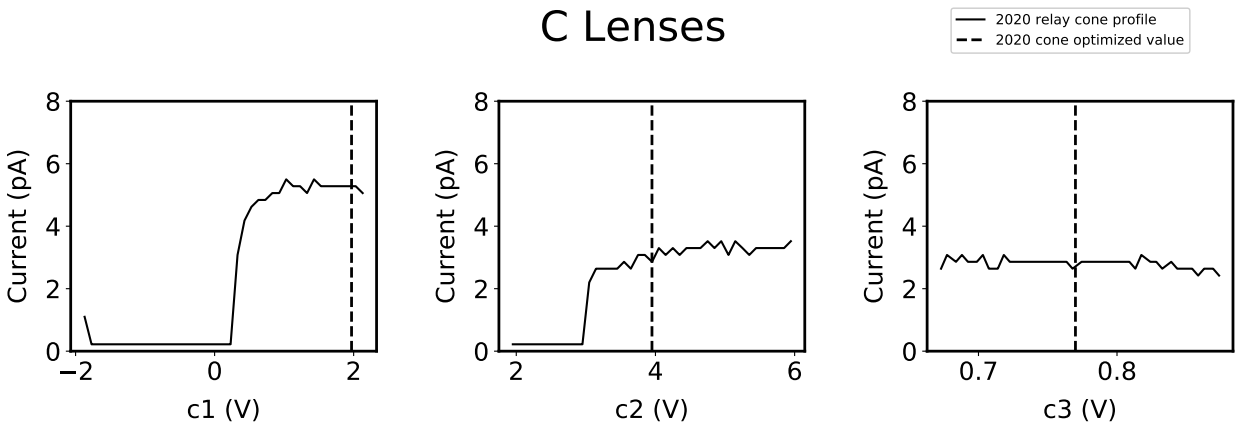

Figure A.6: **Electron Detector System Voltage Profiles**
Electron detector system (C1, C2, C3) lens profiles measured at the detector (relay cone) for two different optimized voltage configurations. The 2020 data is in a "misaligned" beam configuration. The dashed lines represent the voltage value of each respective lens that produces an optimized tuning at the detector.

Appendix B

$SrTi_{1-x}Nb_xO_3$ Raw Data

The data sets in Section 5.2.3 of the main manuscript were measurements taken off of a single cleaved surface and that were representative of the behaviors seen by other measurements of the same doping. This was abbreviated to simplify the presentation of the data. Complete data sets for those dopings measured with M-EELS are given here. Each of the following sections contains all the data measured off of each UHV cleaved surface - the q=0 temperature dependence spectra and the q=0 sample reproducibility spectra were all scaled to the elastic line, the momentum dispersions were all scaled based on the f-sum rule as described in Section 5.2. The spectra are zoomed in to focus on the low energy acoustic phonon and plasmon, specifically, and none of the data is offset from each other to emphasize spectral weight changes. Sample numbers are used to compare to Hall data of figure 5.3.

Undoped

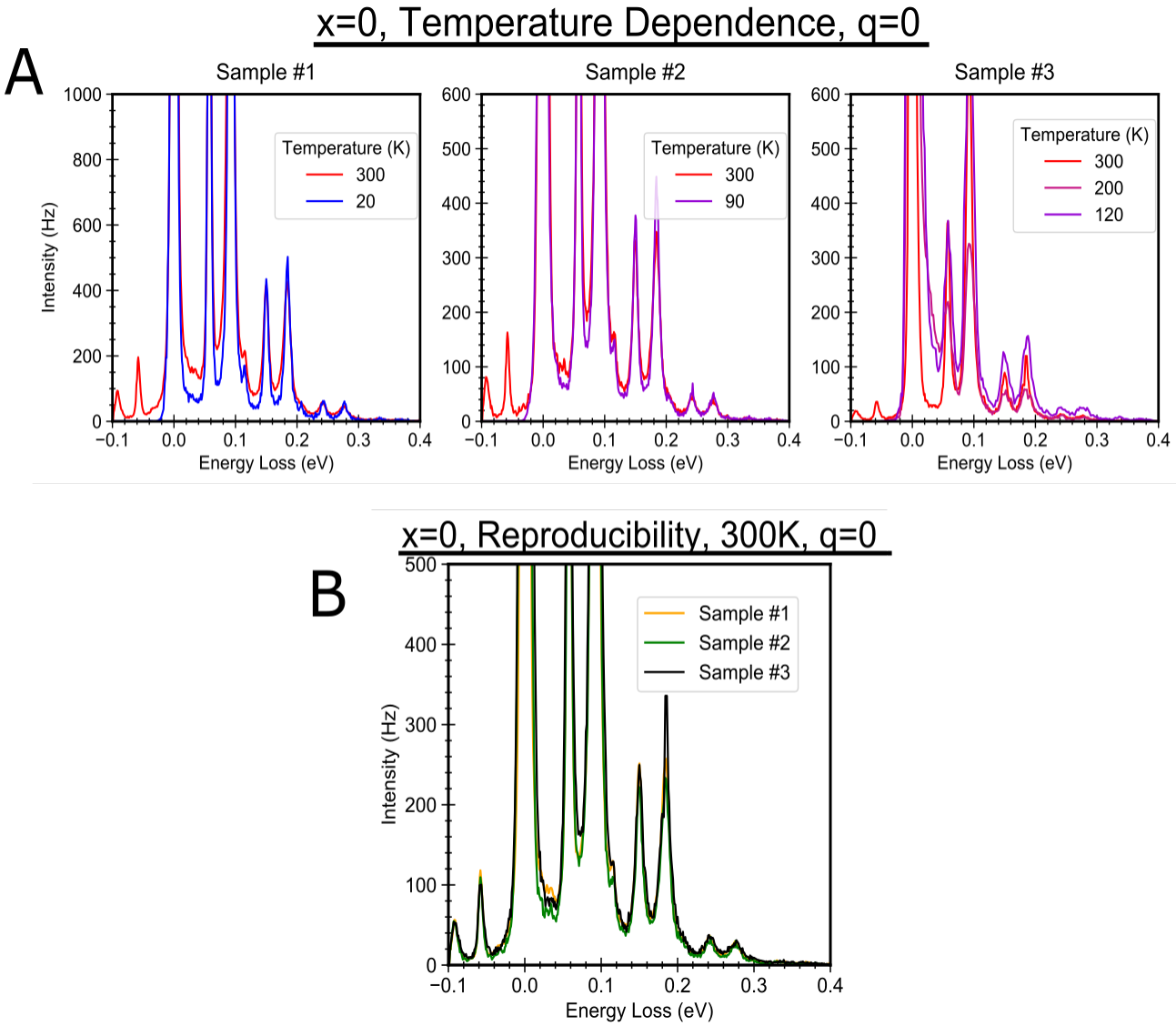

Figure B.1: **Undoped, q=0 Temperature Dependence and Reproducibility of All Datasets** (A) Temperature dependence of M-EELS spectra at q=0 r.l.u. for several temperatures on several cleaved samples. Spectra are scaled to the elastic line and not offset. (B) Sample reproducibility of M-EELS spectra at q=0 r.l.u. and T=300 K for several cleaved samples. Spectra are scaled to the elastic line and not offset.

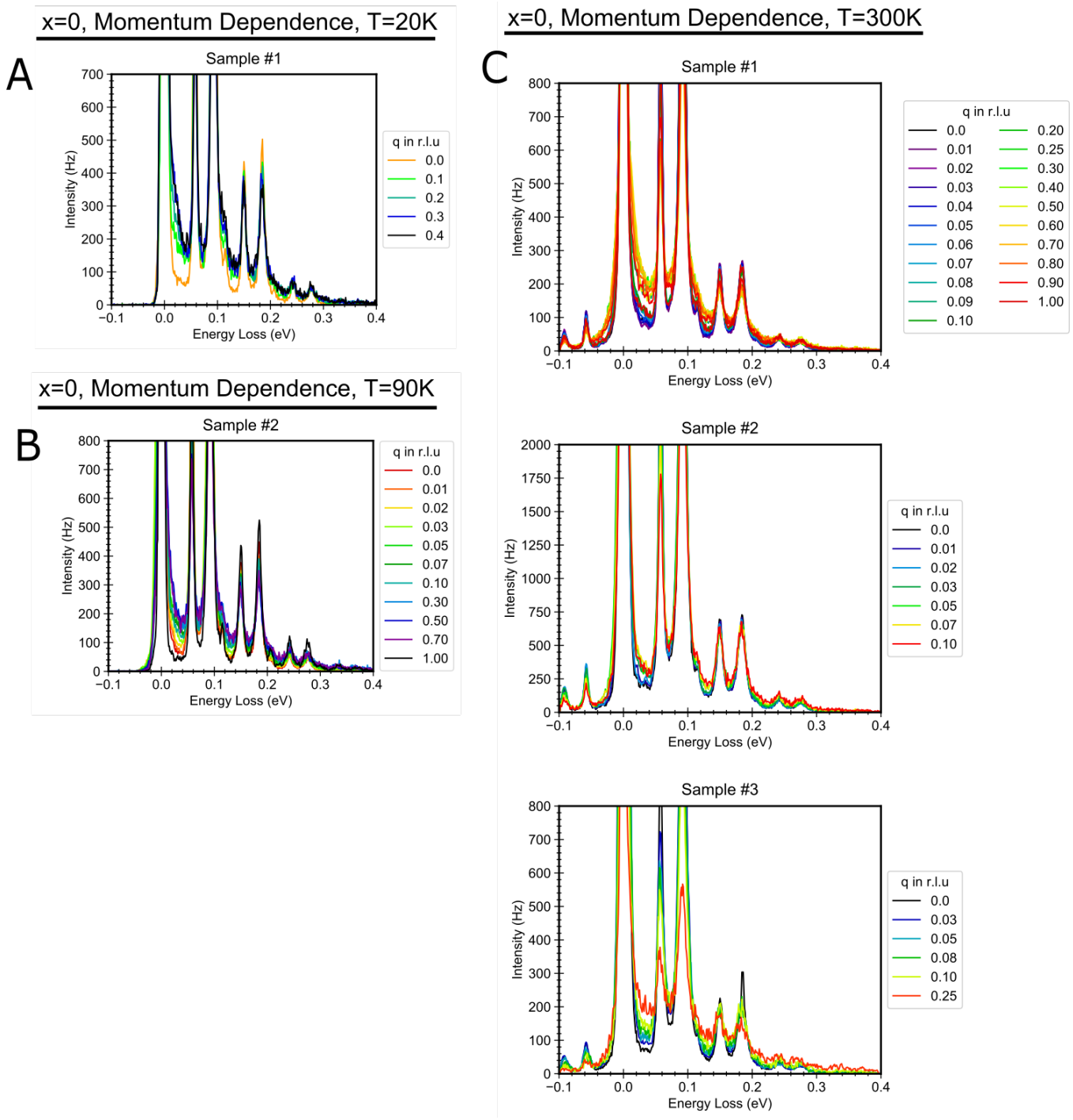

Figure B.2: **Undoped Dispersions of All Datasets at All Temperatures**
Momentum dependence of M-EELS spectra at (A) 20 K, (B) 90 K, and (C) 300 K for several cleaved samples. Spectra are scaled by the f-sum rule and not offset.

Slightly Nb Doped

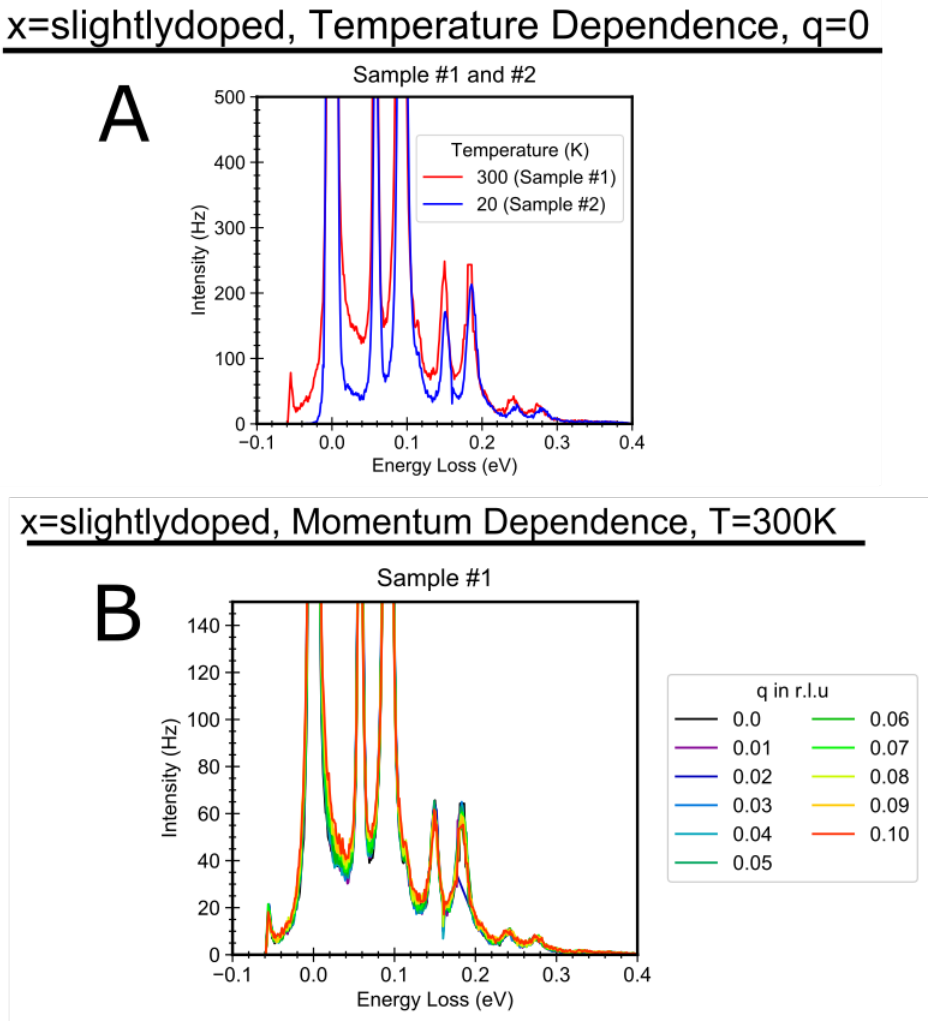

Figure B.3: **Slightly doped, q=0 Temperature and Momentum Dependence of All Datasets** (A) Temperature dependence of M-EELS spectra at q=0 r.l.u. for several temperatures on several cleaved samples. Spectra are scaled to the elastic line and not offset. (B) Momentum dependence of M-EELS spectra at 300 K. Spectra are scaled by the f-sum rule and not offset.

0.2% Nb doped

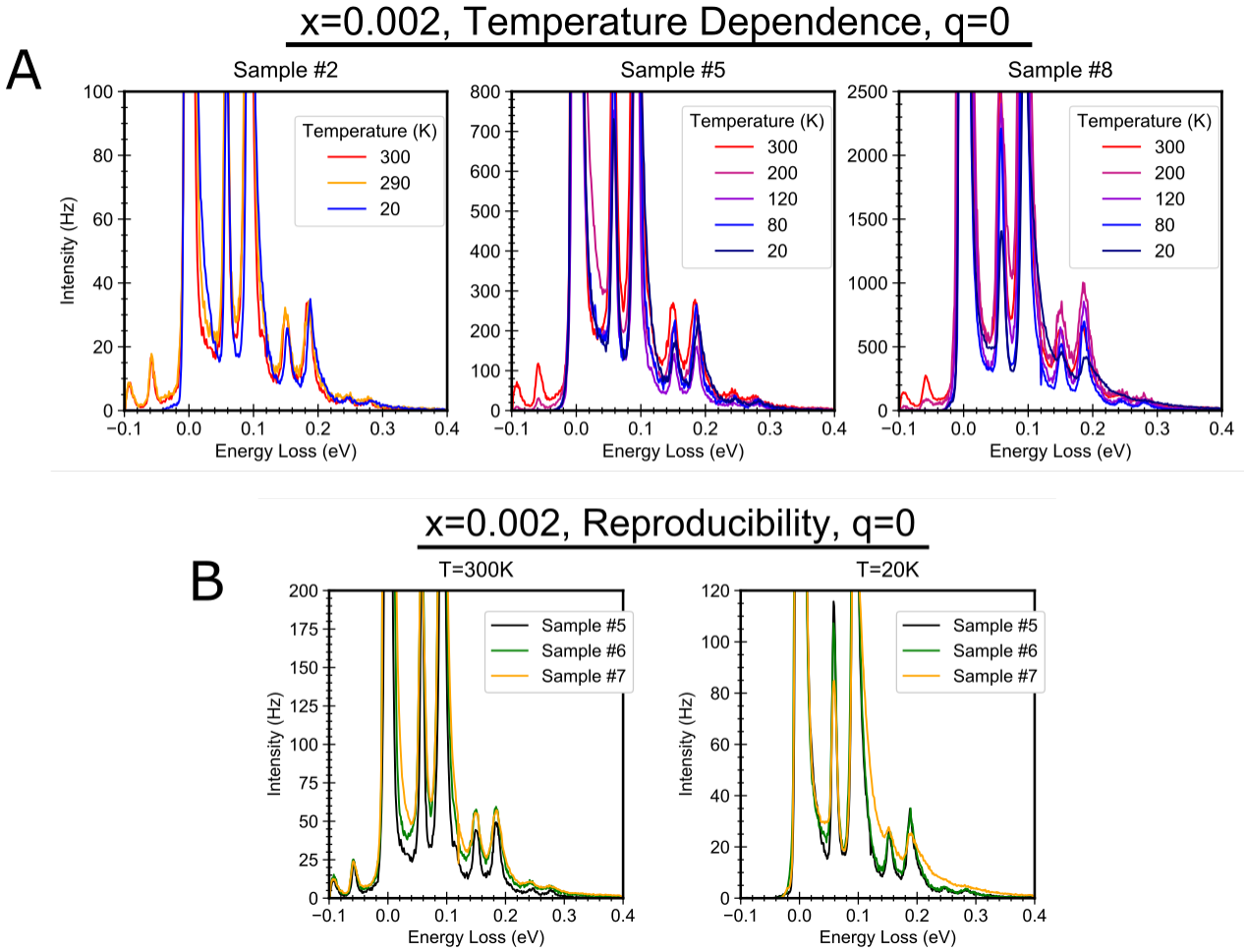

Figure B.4: **0.2% Doped, q=0 Temperature Dependence and Reproducibility of All Datasets** (A) Temperature dependence of M-EELS spectra at q=0 r.l.u. for several temperatures on several cleaved samples. Spectra are scaled to the elastic line and not offset. (B) Sample reproducibility of M-EELS spectra at q=0 r.l.u., T=300 K, and 20 K for several cleaved samples. Spectra are scaled to the elastic line and not offset.

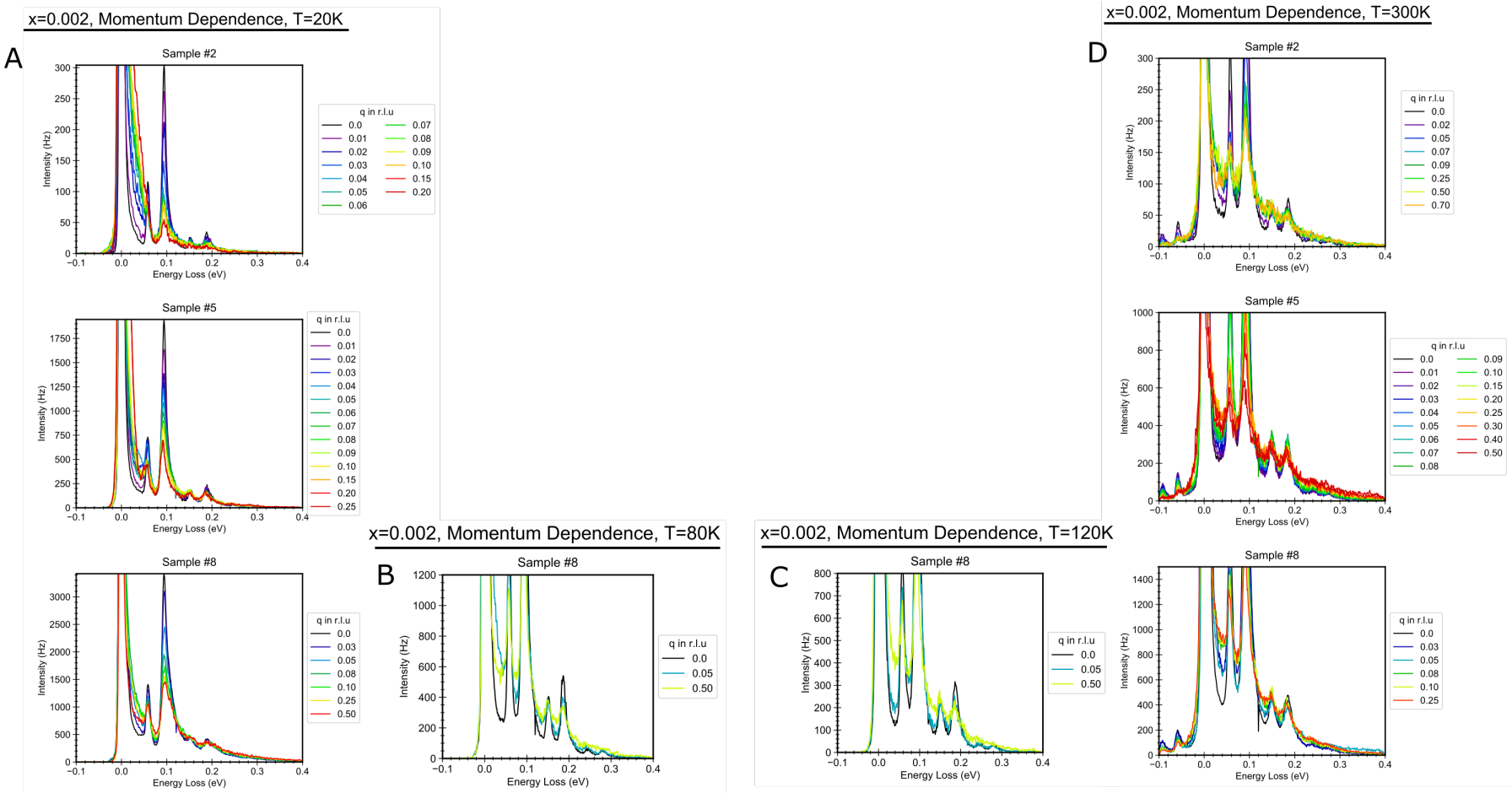

Figure B.5: **0.2% Doped Dispersions of All Datasets at All Temperatures**
Momentum dependence of M-EELS spectra at (A) 20 K, (B) 80 K, (C) 120 K, and (D) 300 K for several cleaved samples. Spectra are scaled by the f-sum rule and not offset.

1% Nb doped

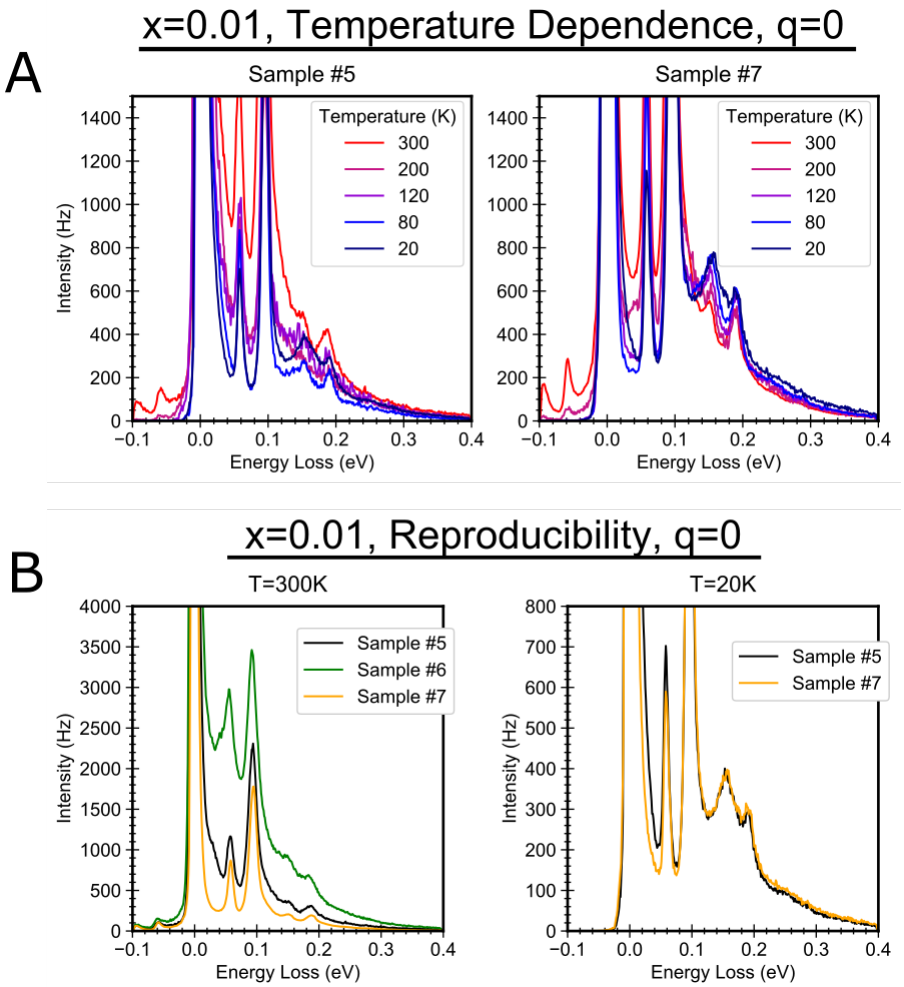

Figure B.6: **1% Doped, q=0 Temperature Dependence and Reproducibility of All Datasets** (A) Temperature dependence of M-EELS spectra at q=0 r.l.u. for several temperatures on several cleaved samples. Spectra are scaled to the elastic line and not offset. (B) Sample reproducibility of M-EELS spectra at q=0 r.l.u., T=300 K, and 20 K for several cleaved samples. Spectra are scaled to the elastic line and not offset.

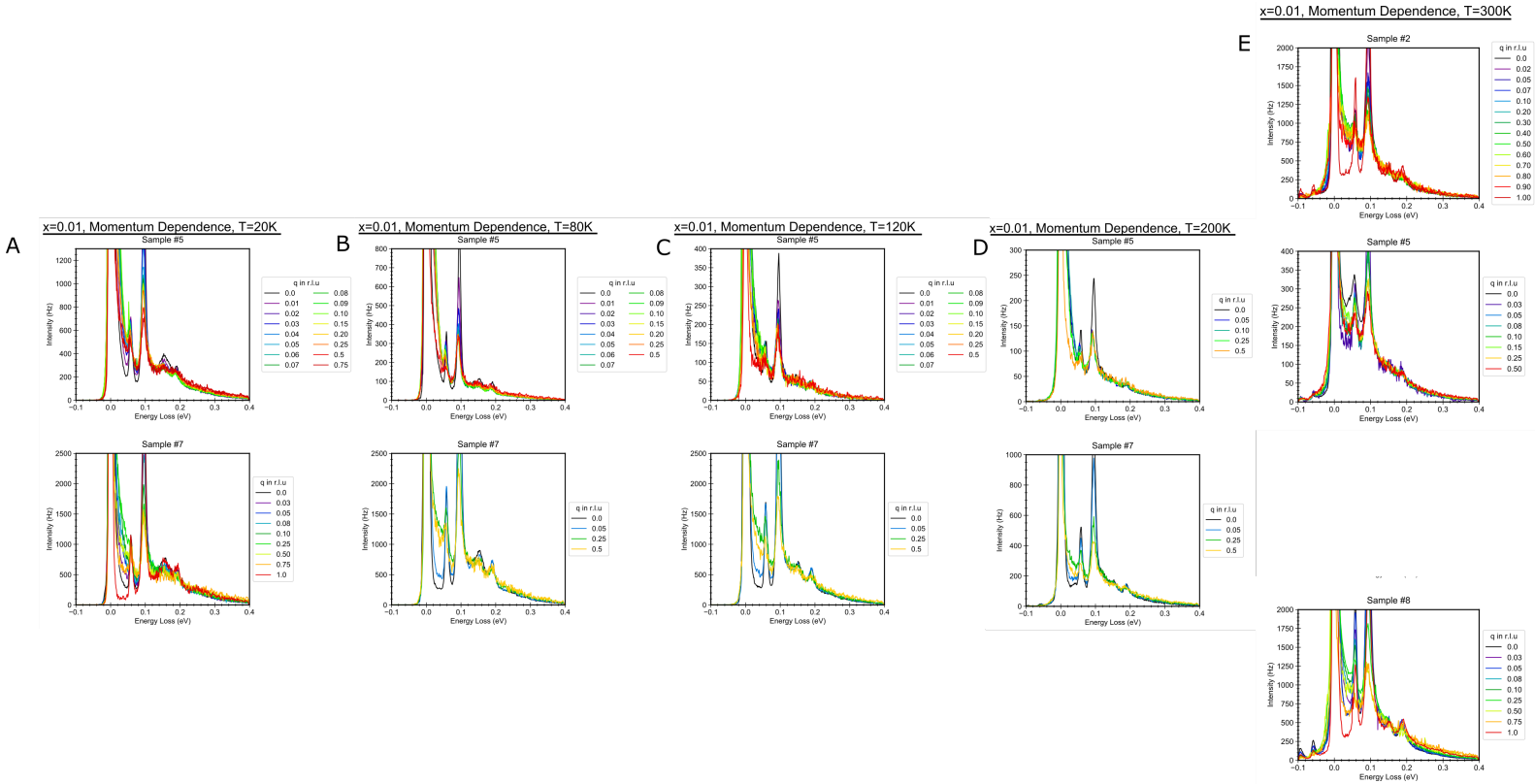

Figure B.7: **1% Doped Dispersions of All Datasets at All Temperatures**
Momentum dependence of M-EELS spectra at (A) 20 K, (B) 80 K, (C) 120 K, (D) 200 K, and (E) 300 K for several cleaved samples. Spectra are scaled by the f-sum rule and not offset.

1.4% Nb doped

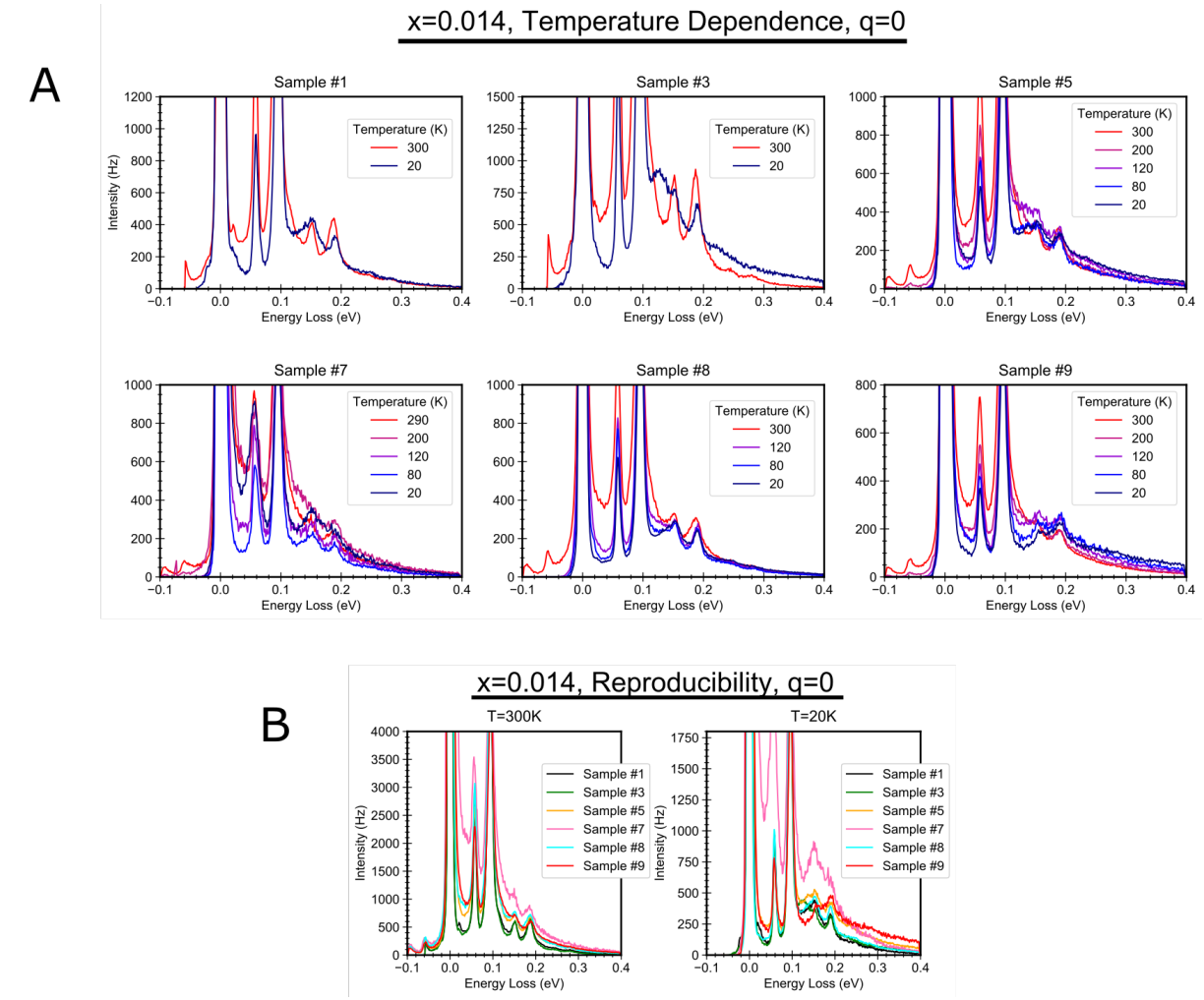

Figure B.8: **1.4% Doped, q=0 Temperature Dependence and Reproducibility of All Datasets** (A) Temperature dependence of M-EELS spectra at q=0 r.l.u. for several temperatures on several cleaved samples. Spectra are scaled to the elastic line and not offset. (B) Sample reproducibility of M-EELS spectra at q=0 r.l.u., T=300 K, and 20 K for several cleaved samples. Spectra are scaled to the elastic line and not offset.

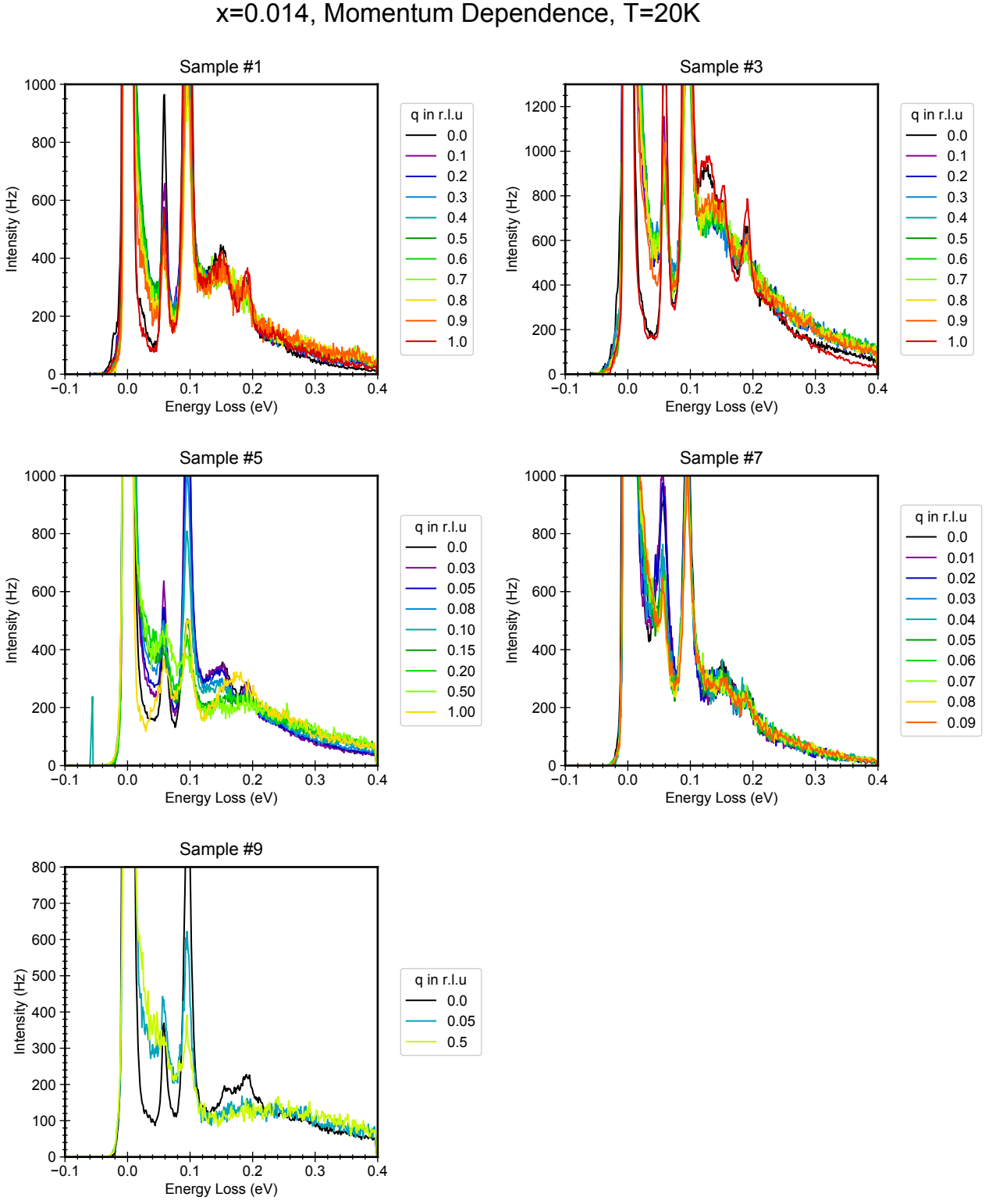

Figure B.9: **1.4% Doped, 20 K Dispersions of All Datasets**
M-EELS spectra at 20 K for several cleaved samples. Spectra are scaled by the f-sum rule and not offset.

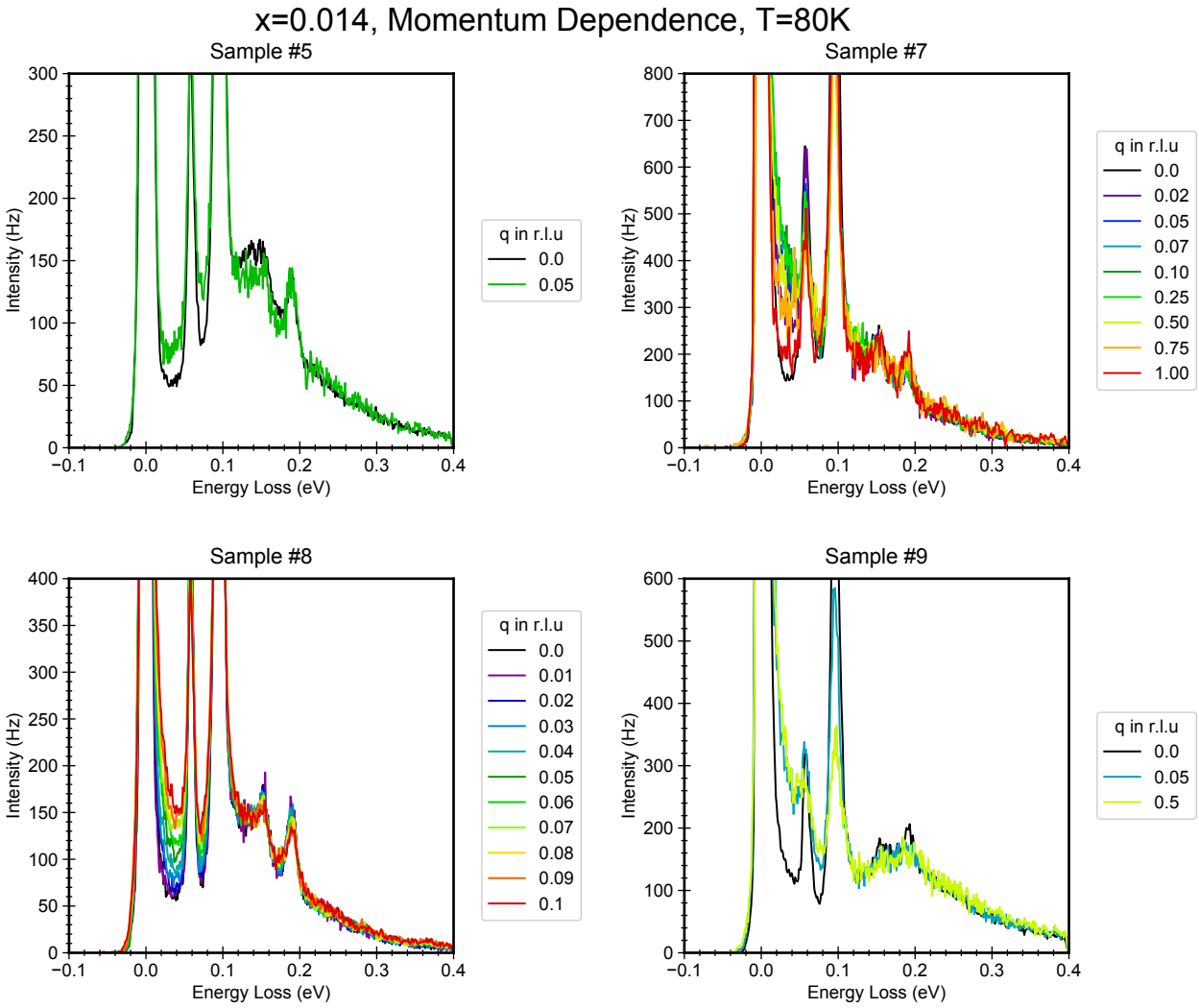

Figure B.10: **1.4% Doped, 80 K Dispersions of All Datasets**
M-EELS spectra at 80 K for several cleaved samples. Spectra are scaled by the f-sum rule and not offset.

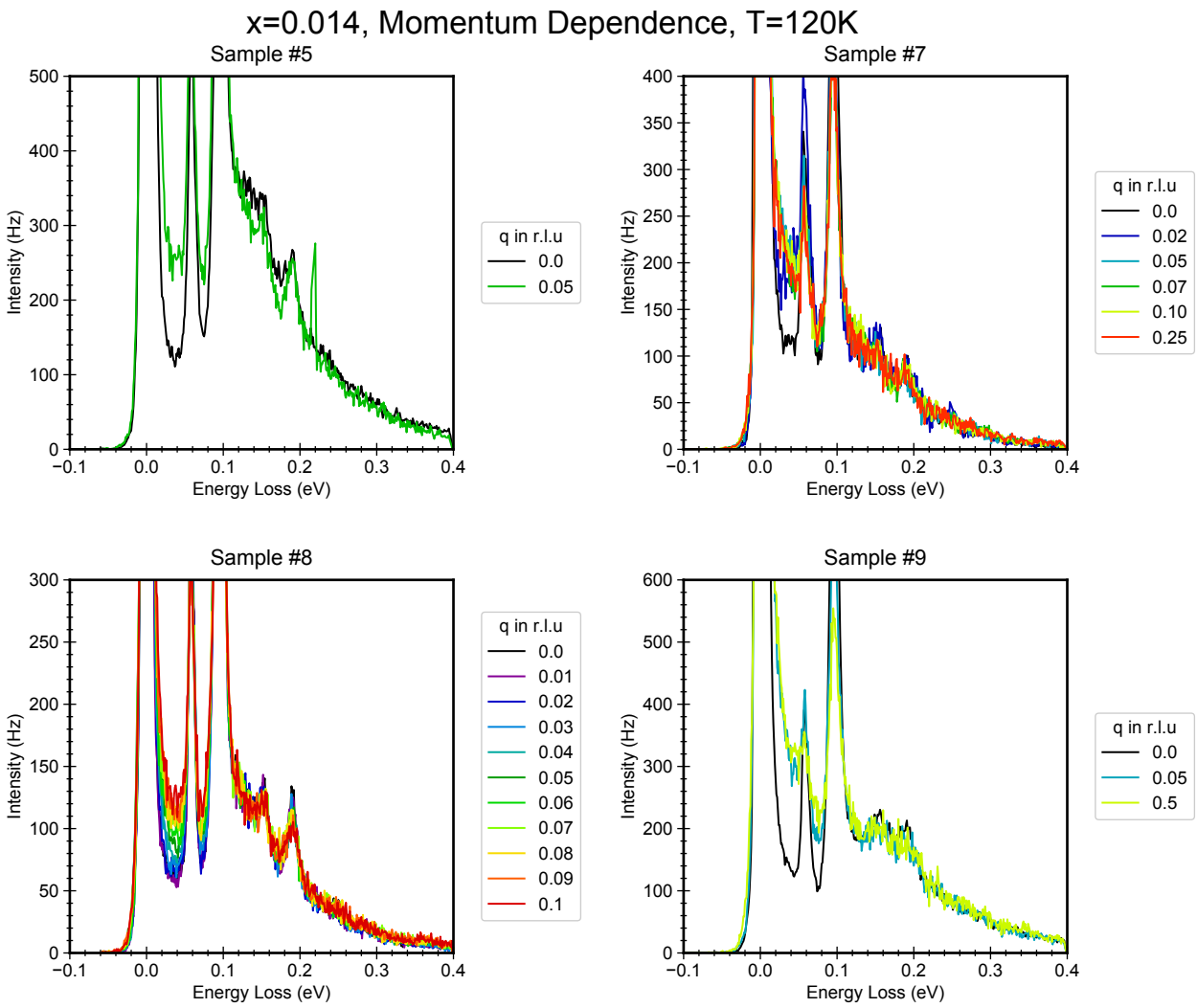

Figure B.11: **1.4% Doped, 120 K Dispersions of All Datasets**
M-EELS spectra at 120 K for several cleaved samples. Spectra are scaled by the f-sum rule and not offset.

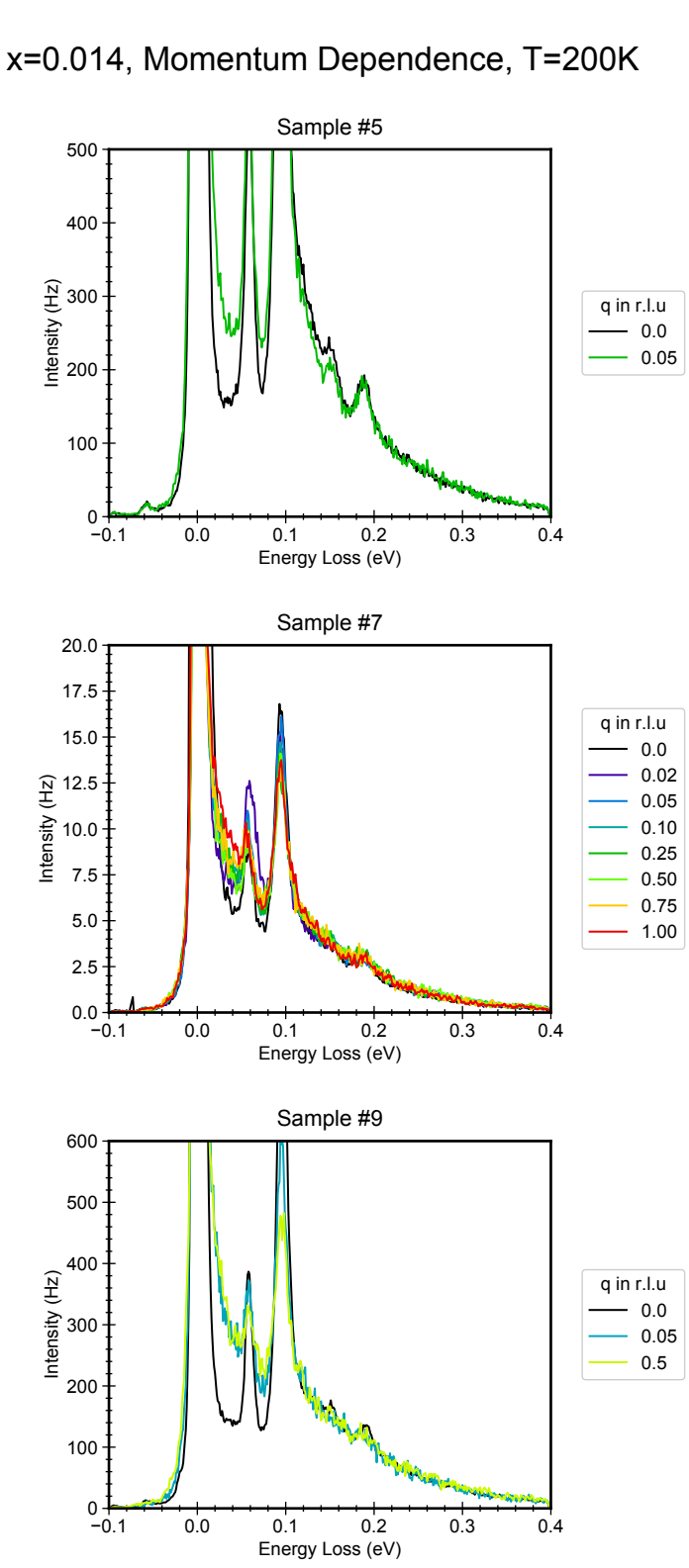

Figure B.12: **1.4% Doped, 200 K Dispersions of All Datasets**
M-EELS spectra at 200 K for several cleaved samples. Spectra are scaled by the f-sum rule and not offset.

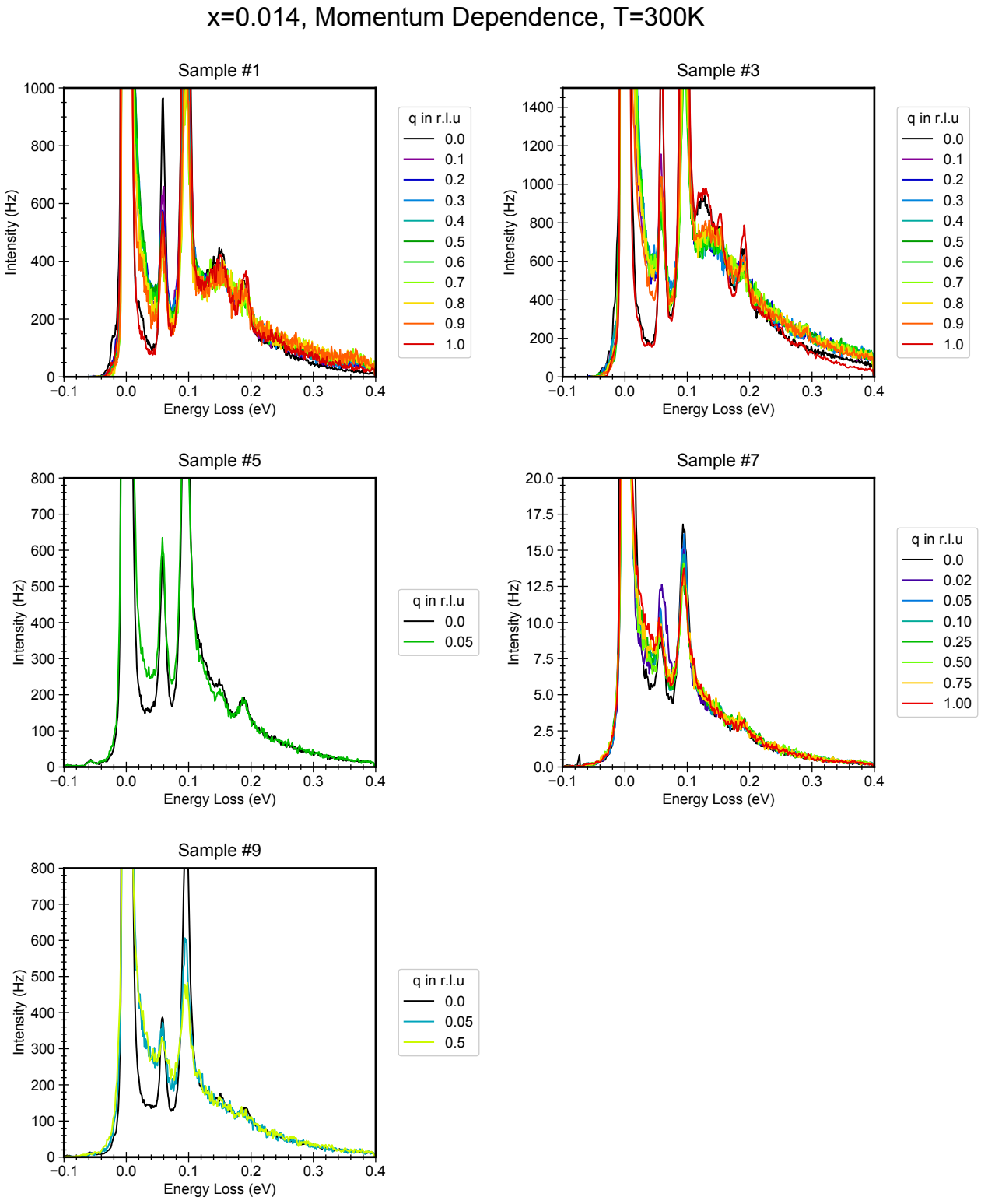

Figure B.13: **1.4% Doped, 300 K Dispersions of All Datasets**
M-EELS spectra at 300 K for several cleaved samples. Spectra are scaled by the f-sum rule and not offset.

References

[1] David Snoke. Spontaneous bose coherence of excitons and polaritons. *Science*, 298(5597):1368–1372, 2002.

[2] J.P. Eisenstein. Exciton condensation in bilayer quantum hall systems. *Annual Review of Condensed Matter Physics*, 5(1):159–181, 2014.

[3] L. V. Keldysh and Y. V. Kopaev. Possible instability of the semimetallic state toward coulomb interaction. *Sov. Phys. Solid State*, 6:2219–2224, 1965.

[4] N. F. Mott. The transition to the metallic state. *Philosophical Magazine*, 6:287–309, 1961.

[5] B. I. Halperin and T. M. Rice. Possible anomalies at a semimetal-semiconductor transistion. *Rev. Mod. Phys.*, 40:755–766, 1968.

[6] W. Kohn and D. Sherrington. Two kinds of bosons and bose condensates. *Rev. Mod. Phys.*, 42:1–11, 1970.

[7] Anshul Kogar, Melinda S. Rak, Sean Vig, Ali A. Husain, Felix Flicker, Young Il Joe, Luc Venema, Greg J. MacDougall, Tai C. Chiang, Eduardo Fradkin, Jasper van Wezel, and Peter Abbamonte. Signatures of exciton condensation in a transition metal dichalcogenide. *Science*, 358(6368):1314–1317, 2017.

[8] A. Kogar, G. A. de la Pena, Sangjun Lee, Y. Fang, S. X.-L. Sun, D. B. Lioi, G. Karapetrov, K. D. Finkelstein, J. P. C. Ruff, P. Abbamonte, and S. Rosenkranz. Observation of a charge density wave incommensuration near the superconducting dome in cu$_x$tise$_2$. *Phys. Rev. Lett.*, 118:027002, 2017.

[9] Chuan Chen, Lei Su, A H Castro Neto, and Vitor M Pereira. Discommensuration-driven superconductivity in the charge density wave phases of transition-metal dichalcogenides. *Physical Review B*, 99(12), 2019.

[10] Chuan Chen. *On the Nature of Charge Density Waves, Superconductivity and Their Interplay in 1T-TiSe*. Springer Theses. Springer International Publishing, 2019.

[11] K. A. Müller and H. Burkard. SrTiO3: An intrinsic quantum paraelectric below 4 K. *Physical Review B*, 19(7):3593–3602, apr 1979.

[12] Xiao Lin, Zengwei Zhu, Benoît Fauqué, and Kamran Behnia. Fermi surface of the most dilute superconductor. *Physical Review X*, 3(2), 2013.

[13] Xiao Lin, Carl Willem Rischau, Lisa Buchauer, Alexandre Jaoui, Benoît Fauqué, and Kamran Behnia. Metallicity without quasi-particles in room-temperature strontium titanate. *npj Quantum Materials*, 2(1):1–8, jul 2017.

[14] Yasutami Takada. Theory of Superconductivity in Polar Semiconductors and Its Application to N-Type Semiconducting Srtio3. *Journal of the Physical Society of Japan*, 49(4):1267–1275, nov 1980.

[15] Jonathan Ruhman and Patrick A Lee. Superconductivity at very low density: The case of strontium titanate. *Physical Review B*, 94(22):224515, 2016.

[16] Lev P. Gor'kov. Back to Mechanisms of Superconductivity in Low-Doped Strontium Titanate. *Journal of Superconductivity and Novel Magnetism*, 30(4):845–852, 2017.

[17] Maria Grazia Betti, U Del Pennino, and Carlo Mariani. Collective and vibrational excitations on the n-doped GaAs(110) surface. *Physical Review B*, 39(9):5887–5891, 1989.

[18] GD Mahan. Many-particle physics, 1990.

[19] Martin Dressel, George Gruener, and George F Bertsch. *Electrodynamics of Solids: Optical Properties of Electrons in Matter*, volume 70. 2002.

[20] W Shülke. *Electron Dynamics by Inelastic X-Ray Scattering*, volume 7. 2007.

[21] Sean Vig, Anshul Kogar, Matteo Mitrano, Ali A. Husain, Vivek Mishra, Melinda S. Rak, Luc Venema, Peter D. Johnson, Genda D. Gu, Eduardo Fradkin, Michael R. Norman, and Peter Abbamonte. Measurement of the dynamic charge response of materials using low-energy, momentum-resolved electron energy-loss spectroscopy (m-eels). *SciPost Phys.*, 3:026, 2017.

[22] G. L. Squires. *Introduction to the theory of thermal neutron scattering*, volume 9781107644. 1996.

[23] E. Morosan, H. W. Zandbergen, B. S. Dennis, Bos J. W. G., Onose Y., T. Klimczuk, A. P. Ramirez, N. P. Ong, and R. J. Cava. Superconductivity in Cu_xTiSe_2. *Nature Physics*, 2:544, 2006.

[24] George Grüner. *Density waves in solids*. CRC Press, jan 2018.

[25] J. Bardeen, L. N. Cooper, and J. R. Schrieffer. Theory of superconductivity. *Physical Review*, 108(5):1175–1204, dec 1957.

[26] M. Maschek, S. Rosenkranz, R. Hott, R. Heid, Michael Merz, D. A. Zocco, A. H. Said, A. Alatas, G. Karapetrov, Shan Zhu, Jasper van Wezel, and F. Weber. Superconductivity and hybrid soft modes in $Tise_2$. *Phys. Rev. B*, 94:214507, Dec 2016.

[27] Clément Collignon, Xiao Lin, Carl Willem Rischau, Benoît Fauqué, and Kamran Behnia. Metallicity and superconductivity in doped strontium titanate, mar 2019.

[28] H. E. Weaver. Dielectric properties of single crystals of SrTiO3 at low temperatures. *Journal of Physics and Chemistry of Solids*, 11(3-4):274–277, oct 1959.

[29] N. E. Hussey, K. Takenaka, and H. Takagi. Universality of the Mott-Ioffe-Regel limit in metals. *Philosophical Magazine*, 84(27):2847–2864, sep 2004.

[30] J. F. Schooley, W. R. Hosler, and Marvin L. Cohen. Superconductivity in semiconducting SrTiO3. *Physical Review Letters*, 12(17):474–475, apr 1964.

[31] J. Georg Bednorz and K. Alex Mller. Perovskite-type oxides - The new approach to high-Tc superconductivity. *Reviews of Modern Physics*, 60(3):585–600, jul 1988.

[32] R. B. Laughlin, G. G. Lonzarich, P. Monthoux, and David Pines. The quantum criticality conundrum, jun 2001.

[33] Om Prakash, Anil Kumar, A. Thamizhavel, and S. Ramakrishnan. Evidence for bulk superconductivity in pure bismuth single crystals at ambient pressure. *Science*, 355(6320), jan 2017.

[34] Ali Abdullah Husain. *Charge Fluctuations of the Strange Metal in Space and Time*. PhD thesis, jun 2020.

[35] Melinda Rak. *Collective modes in strongly correlated electron systems measured with momentum-resolved electron energy-loss spectroscopy*. PhD thesis, jun 2019.

[36] Sean Vig. *Characterization of collective phenomena in cuprate superconductors by momentum-resolved electron energy loss spectroscopy*. PhD thesis, mar 2017.

[37]

[38] E. Evans and D L. Mills. Theory of inelastic scattering of slow electrons by long-wavelength surface of optical phonons. *Physical Review B*, 7(2):853–868, 1972.

[39] D. L. Mills. The scattering of low energy electrons by electric field fluctuations near crystal surfaces. *Surface Science*, 48(1):59–79, mar 1975.

[40] Roger G Newton. *Scattering theory of waves and particles*. Springer Science & Business Media, 2013.

[41] Anshul Kogar, Sean Vig, Yu Gan, and Peter Abbamonte. Temperature-resolution anomalies in the reconstruction of time dynamics from energy-loss experiments. *Journal of Physics B: Atomic, Molecular and Optical Physics*, 47(12):124034, jun 2014.

[42] Joerg Fink. Comment on: Crossover of Charge Fluctuations across the Strange Metal Phase Diagram. 2021.

[43] Yu Gan, Anshul Kogar, and Peter Abbamonte. Crystallographic refinement of collective excitations using standing wave inelastic X-ray scattering. *Chemical Physics*, 414:160–167, mar 2013.

[44] P. Nozieres and D. Pines. *Theory Of Quantum Liquids*. Advanced Books Classics Series. Westview Press, 1999.

[45] M. R. Norman, H. Ding, M. Randeria, J. C. Campuzano, T. Yokoya, T. Takeuchi, T. Takahashi, T. Mochiku, K. Kadowaki, P. Guptasarma, and D. G. Hinks. Destruction of the Fermi surface in underdoped high-Tc superconductors. *Nature 1998 392:6672*, 392(6672):157–160, mar 1998.

[46] Alexander L Fetter and John Dirk Walecka. *Quantum theory of many-particle systems*. Courier Corporation, 2012.

[47] G. Li, W. Z. Hu, D. Qian, D. Hsieh, M. Z. Hasan, E. Morosan, R. J. Cava, and N. L. Wang. Semimetal-to-semimetal charge density wave transition in $1t-tise_2$. *Phys. Rev. Lett.*, 99:027404, 2007.

[48] J. L.M. Van Mechelen, D Van Der Marel, C Grimaldi, A B Kuzmenko, N P Armitage, N Reyren, H Hagemann, and I I Mazin. Electron-phonon interaction and charge carrier mass enhancement in SrTiO3. *Physical Review Letters*, 100(22), 2008.

[49] Andrea Damascelli, Zahid Hussain, and Zhi Xun Shen. Angle-resolved photoemission studies of the cuprate superconductors, apr 2003.

[50] *The interplay of spectroscopy and correlated materials — the University of Groningen research portal*. PhD thesis.

[51] H Ibach and D.L. Mills. *Electron Energy Loss Spectroscopy and Surface Vibrations*. 1982.

[52] Harald Ibach. *Electron energy loss spectrometers: the technology of high performance*, volume 63. Springer, 1991.

[53] Kimball Physics INC. *Single-crystal Lanthanum Hexaboride Cathode*, 2013.

[54] MJ Kristo and CG Enke. Channeltron electron multiplier handbook for mass spectrometry applications, 1991.

[55] Martin Jourdan and Hermann Adrian. Possibility of unconventional superconductivity of SrTiO3-δ. In *Physica C: Superconductivity and its Applications*, volume 388-389, pages 509–510. North-Holland, may 2003.

[56] K Rossnagel. On the origin of charge-density waves in select layered transition-metal dichalcogenides. *Journal of Physics: Condensed Matter*, 23(21):213001, 2011.

[57] F. J. Di Salvo, D. E. Moncton, and J. V. Waszczak. Electronic properties and superlattice formation in the semimetal $TiSe_2$. *Phys. Rev. B*, 14:4321–4328, 1976.

[58] N. Wakabayashi, H. G. Smith, K. C. Woo, and F. C. Brown. Phonons and charge density waves in 1t-$tise_2$. *Solid State Communications*, 28(11):923–926, 1978.

[59] F. Weber, S. Rosenkranz, J.-P. Castellan, R. Osborn, G. Karapetrov, R. Hott, R. Heid, K.-P. Bohnen, and A. Alatas. Electron-phonon coupling and the soft phonon mode in $tise_2$. *Phys. Rev. Lett.*, 107:266401, 2011.

[60] D. Qian, D. Hsieh, L. Wray, E. Morosan, N. L. Wang, Y. Xia, R. J. Cava, and M. Z. Hasan. Emergence of Fermi Pockets in a New Excitonic Charge-Density-Wave Melted Superconductor. *Phys. Rev. Lett.*, 98:117007, 2007.

[61] Y. I. Joe, X. M. Chen, P. Ghaemi, K. D. Finkelstein, G. A. de la Peña, Y. Gan, J. C. T. Lee, S. Yuan, J. Geck, G. J. MacDougall, T. C. Chiang, S. L. Cooper, E. Fradkin, and P. Abbamonte. Emergence of charge density wave domain walls above the superconducting dome in 1t-$tise_2$. *Nature Physics*, 10:421, 2014.

[62] L. J. Li, C. T. O. O'Farrell, K. P. Loh, G. Eda, B. Özyilmaz, and A. H. Castro Neto. Controlling many-body states by the electric-field effect in a two-dimensional material. *Nature*, 529:185, 2016.

[63] Martin Dressel and George GrÃner. *Electrodynamics of Solids: Optical Properties of Electrons in Matter*. Cambridge University Press, 2002.

[64] G. Li, W. Z. Hu, J. Dong, D. Qian, D. Hsieh, M. Z. Hasan, E. Morosan, R. J. Cava, and N. L. Wang. Anomalous Metallic State of $Cu_{0.07}TiSe_2$: An Optical Spectroscopy Study. *Phys. Rev. Lett.*, 99:167002, 2007.

[65] G. Wu, H. X. Yang, L. Zhao, X. G. Luo, T. Wu, G. Y. Wang, and X. H. Chen. Transport properties of single-crystalline Cu_xTiSe_2 ($0.015 \leqslant x \leqslant 0.110$). *Phys. Rev. B*, 76:024513, Jul 2007.

[66] J. F. Zhao, H. W. Ou, G. Wu, B. P. Xie, Y. Zhang, D. W. Shen, J. Wei, L. X. Yang, J. K. Dong, M. Arita, H. Namatame, M. Taniguchi, X. H. Chen, and D. L. Feng. Evolution of the electronic structure of 1$t-cu_x tise_2$. *Phys. Rev. Lett.*, 99:146401, 2007.

[67] S. V. Dordevic, M. S. Wolf, N. Stojilovic, Hechang Lei, and C. Petrovic. Signatures of charge inhomogeneities in the infrared spectra of topological insulators Bi2Se3, Bi2Te3 and Sb2Te3. *Journal of Physics Condensed Matter*, 25(7):075501, jan 2013.

[68] Tao Dong, Rui Hua Yuan, You Guo Shi, and Nan Lin Wang. Temperature-induced plasma frequency shift in Bi2Te 3and CuxBi2Se3. *Chinese Physics Letters*, 30(12):127801, dec 2013.

[69] Giovanni Bertoni, Jo Verbeeck, and Fons Brosens. Fitting the momentum dependent loss function in eels. *Microscopy Research and Technique*, 74(3):212–218, 2011.

[70] Chuan Chen, Bahadur Singh, Hsin Lin, and Vitor M Pereira. Reproduction of the Charge Density Wave Phase Diagram in 1T-TiSe2 Exposes its Excitonic Character. *Physical Review Letters*, 121(22):226602, 2018.

[71] C Monney, E F Schwier, M G Garnier, N Mariotti, C Didiot, H Beck, P Aebi, H Cercellier, J Marcus, C Battaglia, H Berger, and A N Titov. Temperature-dependent photoemission on 1T -TiSe2: Interpretation within the exciton condensate phase model. *Physical Review B - Condensed Matter and Materials Physics*, 81(15), 2010.

[72] M. Mitrano, A. A. Husain, S. Vig, A. Kogar, M. S. Rak, S. I. Rubeck, J. Schmalian, B. Uchoa, J. Schneeloch, R. Zhong, G. D. Gu, and P. Abbamonte. Anomalous density fluctuations in a strange metal. *Proceedings of the National Academy of Sciences*, 115(21):5392–5396, 2018.

[73] James A Noland. Optical Absorption of Single-Crystal Strontium Titanate Hall. *Phys. Rev*, 2:753, 1954.

[74] A Mooradian and G B Wright. Observation of the Interaction of Plasmons with Longitudinal Optical Phonons in GaAs. *Physical Review Letters*, 16(22):999–1001, 1966.

[75] H Vogt. Hyper-Raman tensors of the zone-center optical phonons in SrTiO3 and KTaO3. *Physical Review B*, 38(8):5699–5708, 1988.

[76] Shuyuan Zhang, Jiaqi Guan, Xun Jia, Bing Liu, Weihua Wang, Fangsen Li, Lili Wang, Xucun Ma, Qikun Xue, Jiandi Zhang, E W Plummer, Xuetao Zhu, and Jiandong Guo. Role of SrTiO3 phonon penetrating into thin FeSe films in the enhancement of superconductivity. *Physical Review B*, 94(8), 2016.

[77] Robert A Evarestov, Evgeny Blokhin, Denis Gryaznov, Eugene A Kotomin, and Joachim Maier. Phonon calculations in cubic and tetragonal phases of SrTiO3: A comparative LCAO and plane-wave study. *Physical Review B - Condensed Matter and Materials Physics*, 83(13):134108, 2011.

[78] Hiromi Unoki and Tunetaro Sakudo. Electron Spin Resonance of Fe3+ in SRTiO3 with Special Reference to the 110K Phase Transition. *Journal of the Physical Society of Japan*, 23(3):546–552, dec 1967.

[79] A Spinelli, M A Torija, C Liu, C Jan, and C Leighton. Electronic transport in doped SrTiO3: Conduction mechanisms and potential applications. *Physical Review B - Condensed Matter and Materials Physics*, 81(15), 2010.

[80] Xiao Lin, German Bridoux, Adrien Gourgout, Gabriel Seyfarth, Steffen Krämer, Marc Nardone, Benoît Fauqué, and Kamran Behnia. Critical doping for the onset of a two-band superconducting ground state in SrTiO3-δ. *Physical Review Letters*, 112(20), 2014.

[81] P. G. de Gennes and P. A. Pincus. *Superconductivity of metals and alloys*. CRC Press, jan 2018.

[82] Hassel Ledbetter, Ming Lei, and Sudook Kim. Elastic constants, debye temperatures, and electron-phonon parameters of superconducting cuprates and related oxides. *Phase Transitions*, 23(1):61–70, 1990.

[83] Xiao Lin, Benoît Fauqué, and Kamran Behnia. Scalable T2 resistivity in a small single-component Fermi surface. *Science*, 349(6251):945–948, aug 2015.

[84] D. Eagles, M Georgiev, and P. Petrova. Explanation for the temperature dependence of plasma frequencies in using mixed-polaron theory. *Physical Review B - Condensed Matter and Materials Physics*, 54(1):22–25, 1996.

[85] A. Ohtomo and H. Y. Hwang. A high-mobility electron gas at the LaAlO3/SrtiO3 heterointerface. *Nature*, 427(6973):423–426, jan 2004.

[86] N. Reyren, S. Thiel, A. D. Caviglia, L. Fitting Kourkoutis, G. Hammerl, C. Richter, C. W. Schneider, T. Kopp, A. S. Rüetschi, D. Jaccard, M. Gabay, D. A. Muller, J. M. Triscone, and J. Mannhart. Superconducting interfaces between insulating oxides. *Science*, 317(5842):1196–1199, aug 2007.

[87] A. F. Santander-Syro, O. Copie, T. Kondo, F. Fortuna, S. Pailhés, R. Weht, X. G. Qiu, F. Bertran, A. Nicolaou, A. Taleb-Ibrahimi, P. Le Fvre, G. Herranz, M. Bibes, N. Reyren, Y. Apertet, P. Lecoeur, A. Barthélémy, and M. J. Rozenberg. Two-dimensional electron gas with universal subbands at the surface of SrTiO 3. *Nature*, 469(7329):189–194, jan 2011.

[88] Kamran Behnia. The fragility of distant Cooper pairs: The discovery of superconductivity in bismuth is a challenge to standard theory, jan 2017.

[89] J T Devreese, S N Klimin, J. L.M. Van Mechelen, and D Van Der Marel. Many-body large polaron optical conductivity in SrTi1-xNb xO3. *Physical Review B - Condensed Matter and Materials Physics*, 81(12), 2010.

[90] A. L. Ahmad, N. F. Idrus, and M. R. Othman. Preparation of perovskite alumina ceramic membrane using sol-gel method. *Journal of Membrane Science*, 262(1-2):129–137, oct 2005.

[91] TeYu Chien, Nathan P. Guisinger, and John W. Freeland. Survey of fractured SrTiO3 surfaces: From the micrometer to nanometer scale. *Journal of Vacuum Science & Technology B, Nanotechnology and Microelectronics: Materials, Processing, Measurement, and Phenomena*, 28(4):C5A11–C5A13, jul 2010.

[92] Nathan P. Guisinger, Tiffany S. Santos, Jeffrey R. Guest, Te Yu Chien, Anand Bhattacharya, John W. Freeland, and Matthias Bode. Nanometer-scale striped surface terminations on fractured SrTiO 3 surfaces. *ACS Nano*, 3(12):4132–4136, dec 2009.

[93] A D Baden, P A Cox, R G Egdell, A F Orchard, and R. J.D. Willmer. Observation of surface optical phonons on SrTiO3(100). *Journal of Physics C: Solid State Physics*, 14(34):L1081, dec 1981.

[94] Fengmiao Li and George A Sawatzky. Electron Phonon Coupling versus Photoelectron Energy Loss at the Origin of Replica Bands in Photoemission of FeSe on SrTiO3. *Physical Review Letters*, 120(23), 2018.

[95] Francois Gervais, Jean Louis Servoin, Alexis Baratoff, Johannes G Bednorz, and Gerd Binnig. Temperature dependence of plasmons in Nb-doped SrTiO3. *Physical Review B*, 47(13):8187–8194, 1993.

[96] C Z Bi, J Y Ma, J Yan, X Fang, B R Zhao, D Z Yao, and X G Qiu. Electron-phonon coupling in Nb-doped SrTiO3 single crystal. *Journal of Physics Condensed Matter*, 18(8):2553–2561, feb 2006.

[97] Gabriel Antonius, Yang-Hao Chan, and Steven G Louie. Polaron spectral properties in doped ZnO and SrTiO 3 from first principles. *Physical Review Research*, 2(4):43296, 2020.

[98] Xing He, Dipanshu Bansal, Barry Winn, Songxue Chi, Lynn Boatner, and Olivier Delaire. Anharmonic Eigenvectors and Acoustic Phonon Disappearance in Quantum Paraelectric SrTiO3. *Physical Review Letters*, 124(14), 2020.

[99] M. Iizumi, K Gesit, and J. Harada. Dispersion relations of the normal vibrations in strontium titanate. *Journal of Physics C: Solid State Physics*, 6(21):3021–3023, 1973.

[100] Jin Jian Zhou, Olle Hellman, and Marco Bernardi. Electron-Phonon Scattering in the Presence of Soft Modes and Electron Mobility in SrTiO3 Perovskite from First Principles. *Physical Review Letters*, 121(22), 2018.

[101] W. G. Stirling and R. Currat. Experimental verification of the phonon dispersion curves of strontium titanate. *Journal of Physics C: Solid State Physics*, 9(19), 1976.

[102] W G Nilsen and J G Skinner. Raman spectrum of strontium titanate. *The Journal of Chemical Physics*, 48(5):2240–2248, 1968.

[103] U. Balachandran and N. G. Eror. Raman Spectra of Strontium Titanate. *Journal of the American Ceramic Society*, 65(4):c54–c56, apr 1982.

[104] D A Tenne, I E Gonenli, A Soukiassian, D G Schlom, S M Nakhmanson, K M Rabe, and X X Xi. Raman study of oxygen reduced and re-oxidized strontium titanate. *Physical Review B - Condensed Matter and Materials Physics*, 76(2), 2007.

[105] D Van Der Marel, J. L.M. Van Mechelen, and I I Mazin. Common Fermi-liquid origin of T2 resistivity and superconductivity in n-type SrTiO3. *Physical Review B - Condensed Matter and Materials Physics*, 84(20):205111, 2011.

[106] Jacobus Lodevicus Martinus Van Mechelen. *Charge and Spin electrodynamics of SrTiO3 and EuTiO3 studied by optical spectroscopy*. PhD thesis, 2010.

[107] Clément Collignon, Phillipe Bourges, Benoît Fauqué, and Kamran Behnia. Heavy Nondegenerate Electrons in Doped Strontium Titanate. *Physical Review X*, 10(3), 2020.

[108] Guo Qiang Hai, Nelson Studart, and Gilmar E Marques. Plasmon-phonon coupling in δ-doped polar semiconductors. *Physical Review B - Condensed Matter and Materials Physics*, 55(3):1554–1562, 1997.